Search for scalar top quarks decaying into scalar tau leptons with ATLAS at √s = 8 TeV

Butti, P.

STOP INTO STAU

Search for scalar top quarks
decaying into scalar tau leptons
with ATLAS at $\sqrt{s}$ = 8 TeV

Pierfrancesco Butti

Search for scalar top quarks decaying into scalar tau leptons with ATLAS at $\sqrt{s} = 8$ TeV

ACADEMISCH PROEFSCHRIFT

ter verkrijging van de graad van doctor aan de Universiteit van Amsterdam
op gezag van de Rector Magnificus prof. dr. ir. K.I.J. Maex
ten overstaan van een door het College voor Promoties ingestelde commissie,
in het openbaar te verdedigen in de Aula der Universiteit op
Vrijdag 6 Oktober 2017, te 13 uur
door

PIERFRANCESCO BUTTI

Geboren te Empoli, Italië

PROMOTOR:	Prof. dr. ir. P. J. de Jong	Universiteit van Amsterdam
COPROMOTOR:	Prof. dr. A.P. Colijn	Universiteit van Amsterdam

OVERIGE LEDEN:	Prof. dr. E.L.M.P. Laenen	Universiteit van Amsterdam
	Prof. dr. ir. E.N. Koffeman	Universiteit van Amsterdam
	Prof. dr. M. P. Decowski	Universiteit van Amsterdam
	dr. H.M. Gray	Berkeley LBNL
	dr. W. Verkerke	FOM/Nikhef
	Prof. dr. S.J. de Jong	Radboud Universiteit Nijmegen
	dr. H.L. Snoek	Universiteit van Amsterdam

Faculteit der Natuurwetenschappen, Wiskunde en Informatica

Contents

Contents

Introduction

The Standard Model of particle physics (SM), completed by the discovery of the Higgs boson in 2012 at the Large Hadron Collider, provides a description of the known particles and their strong, weak and electromagnetic interactions. The Standard model is a quantum field theory incorporating both quantum mechanics and special relativity and encapsulates in its mathematical formulation the known fundamental symmetries of nature. All the known matter is composed of elementary half-spin particles (*fermions*) whose interactions are mediated by integer spin particles (*bosons*). The SM theory, however, is thought to be far from being complete. In fact it only incorporates three of the four fundamental interactions leaving gravity out of the picture. In addition it is unable to explain a series of observations such as the presence of Dark Matter in the Universe and the matter-antimatter asymmetry. Among several theories that tried to solve the SM shortcomings, *Supersymmetry* (SUSY) is a theory which extends the symmetries of the SM theory allowing the interchange of fermions into bosons, predicting the existence of a *superpartner* for each SM particle. The fact that no superparticles have been observed yet implies that Supersymmetry, if it exists, has to be a broken symmetry at the energy scale we have been able to probe so far and the superpartner particles are thought to be heavier than their SM counterpart.

The search for Supersymmetry has been carried out for many years now in a large variety of possible scenarios and at various particle colliders with different initial states. The current most powerful particle collider is the Large Hadron Collider (LHC), a two-ring superconducting, circular proton or heavy ion collider located at CERN, across the border between Switzerland and France, with a design proton-proton collision centre of mass energy of $\sqrt{s} = 14$ TeV. The "A Toroidal LHC ApparatuS" (ATLAS) experiment is one of the four experiments which records the collisions delivered by the LHC. During 2012 it recorded a 20.3 fb^{-1} dataset of $p - p$ collisions delivered at a centre of mass energy of $\sqrt{s} = 8$ TeV and in 2015 a dataset of 3.2 fb^{-1} at $\sqrt{s} = 13$ TeV. The LHC is foreseen to run for many years from now and an upgrade to the High-Luminosity LHC (HL-LHC) is foreseen in 2026, bringing the expected size of the collected $p - p$ collisions dataset by ATLAS to 3000 fb^{-1}. Therefore, the LHC and ATLAS provide an excellent experimental setup to probe the existence of physics beyond the Standard Model in the so far unexplored phase space.

However, the quality of the results of an experimental physics analysis does not depend only on the size of the collected data or the centre of mass energy. Within the ATLAS experiment a lot of attention is dedicated to the understanding of the experimental setup in order to provide the best possible reconstruction chain from raw data recorded by the detector to final high-level physics analyses. The study and the improvement of the performance of the detector is a fundamental area of research whose results have a great impact on the whole experiment and its physics program.

Outline of the thesis and author's contributions

The work presented in this thesis is divided in two main parts. The first part presents the results of the Alignment of the ATLAS Inner Detector during 2012, the LHC Shutdown (2013-2014) and the early Run-2 data taking (2015). The second part presents a Supersymmetry search in the context of the Gauge Mediated Supersymmetry Breaking framework which was not covered by the ATLAS search program so far. The content of the thesis is divided in 8 chapters. For each chapter a brief introduction is given here as well as the author contribution.

- **Chapter 1** gives an overview of the Standard Model of particle physics and provides an introduction of Supersymmetry focusing on the Gauge Mediated Supersymmetry Breaking phenomenology and on scalar top squark searches in this scenario.

- **Chapter 2** provides a general overview of the Large Hadron Collider and a description of the ATLAS experiment and its subsystems. Particular focus is dedicated to the description of the structure and mechanics of the Insertable B-Layer (IBL).

- **Chapter 3** provides a description of the algorithms and methods used in the ATLAS experiment for reconstruction and identification of the particles produced in $p - p$ collisions.

- **Chapter 4** describes the Inner Detector Alignment procedure and algorithm. I have contributed to expand the ATLAS alignment framework to compute and visualise the alignment corrections for the IBL.

- **Chapter 5** reports the results of the Inner Detector Alignment procedure during Run-1 and Run-2. I contributed to the validation of the alignment results in Run-1. During Run-2, I measured the distortion of the Innermost B-Layer (IBL) as a function of the operating temperature and I had a key role within a Task Force dedicated to the study of this effect. I have been co-convener of the Inner Detector Alignment group and contributed to the calculation of the alignment constants during the data taking.

- **Chapter 6** presents a general overview of the methodologies used in Supersymmetry searches focusing on the strategies used for $\tilde{t} \rightarrow \tilde{\tau}$ search in GMSB models.

- **Chapter 7** describes the details of the Run-1 $\tilde{t} \rightarrow \tilde{\tau}$ search. I contributed to the analysis as principal analyser of the channel with the final state characterised by two hadronically decaying τ leptons.

- **Chapter 8** presents the results of the Run-1 $\tilde{t} \rightarrow \tilde{\tau}$ search which is also published in [1]. I contributed to the exclusion limits calculation and setting. In addition, a brief summary of the results of the early Run-2 $\tilde{t} \rightarrow \tilde{\tau}$ search is presented.

1 Physics beyond the Standard Model

1.1 Introduction to the Standard Model

The Standard Model (SM) [2–5] is a Yang-Mills theory [6] based on the gauge symmetry group

$$SU(3)_C \ \otimes \ SU(2)_L \ \otimes \ U(1)_Y, \qquad (1.1)$$

where C indicates the colour charge, L the weak isospin and Y the hypercharge. The theory describes the properties of the subatomic half-integer spin particles (*fermions*), which compose the so far known matter, and their strong and electroweak (EW) interactions, which are mediated by integer spin particles (*bosons*). The strong force is carried by the massless gluon g, the weak force is mediated by the massive bosons $W^\pm$ and Z, while the photon γ is responsible for the electromagnetic interaction.

The matter content of the SM is composed of three families of fermions which are organised in two classes: *leptons*, that are subject only to the electroweak force, and *quarks* that also interact strongly. The leptons and quarks are organised in $SU(2)_L$ doublets and singlets for the left-handed and right-handed chirality states, respectively. In the SM the neutrino is assumed to be massless and no right-handed chirality state is present. In addition, quarks carry three possible colour charges, *red*, *green* or *blue*, and are organised in $SU(3)_C$ triplets, while leptons, being colourless, are organised in $SU(3)_C$ singlets. In Tab. 1.1 the particles composing the SM and some of their basic properties are summarised.

1.1.1 Standard Model Lagrangian

The complete Lagrangian of the Standard Model can be factorised in terms that describe the electroweak interactions, the Higgs sector, the Yukawa terms for the fermion masses and the strong interactions:

$$\mathcal{L}_{SM} = \mathcal{L}_{EW} + \mathcal{L}_H + \mathcal{L}_{strong} + \mathcal{L}_{Yukawa}. \qquad (1.2)$$

In this subsection the various terms composing the SM theory are briefly introduced and to help the readability, the usual convention of summing over repeated indices is implicitly used.

Electroweak Lagrangian Terms

The electroweak theory describes the interactions between the particles due to the

Fermions					
Leptons			Quarks		
Flavour	Charge (e)	Mass (GeV)	Flavour	Charge (e)	Mass (GeV)
ν_e	0	–	u	2/3	$2.2 \cdot 10^{-3}$
e	-1	$511 \cdot 10^{-6}$	d	-1/3	$4.7 \cdot 10^{-3}$
ν_μ	0	–	c	2/3	1.27
μ	-1	$105.7 \cdot 10^{-3}$	s	-1/3	0.096
ν_τ	0	–	t	2/3	173.21
τ	-1	1.777	b	-1/3	4.6

Bosons				
	Spin	Charge (e)	Mass (GeV)	Interaction
γ	1	0	0	Electromagnetic
W^+, W^-	1	± 1	80.385 ± 0.015	Weak
Z		0	91.188 ± 0.002	
g	1	0	0	Strong
h^0	0	0	$125.09 \pm 0.21 \pm 0.11$	

Table 1.1: Summary of the particle content of the Standard Model, with their masses and some of their basic properties. The mixing of the neutrino flavour eigenstates implies the existence of three light neutrinos ν_i with masses such that $\sum\limits_{i=1,2,3} m_{\nu_i} < 1$ eV [7].

electromagnetic and weak forces. The fields are separated into left-handed and right-handed chirality states and are arranged into $SU(2)_L$ doublets or singlets:

$$L_i = \begin{pmatrix} \nu_i \\ \ell_i \end{pmatrix}_L , \quad \ell_{i,R} \qquad Q_i = \begin{pmatrix} u_i \\ d_i \end{pmatrix}_L , \quad u_{i,R}, d_{i,R} \tag{1.3}$$

where the index i runs over the three generations of leptons and quarks.

The electroweak Lagrangian is invariant under $SU(2)_L \otimes U(1)_Y$ and can be written as [8]

$$\mathcal{L}_{EW} = \sum_{flavours} i \left(\bar{L} \slashed{D} L + \bar{Q} \slashed{D} Q + \bar{\ell}_R \slashed{D} \ell_R + \bar{u}_R \slashed{D} u_R + \bar{d}_R \slashed{D} d_R \right)$$
$$- \frac{1}{4} B_{\mu\nu} B^{\mu\nu} - \frac{1}{4} W^a_{\mu\nu} W^{\mu\nu}_a \tag{1.4}$$

where the fields are organised in $SU(2)_L$ doublets and singlets respectively.

D is the covariant derivative, $\slashed{D} = D^\mu \gamma_\mu$, with γ the Dirac matrices and $W^a_{\mu\nu}$ and $B_{\mu\nu}$

are the the gauge field kinetic terms defined as:

$$W^a_{\mu\nu} = \partial_\mu W^a_\nu - \partial_\nu W^a_\mu + g\epsilon^{abc}W^b_\mu W^c_\nu$$
$$B^a_{\mu\nu} = \partial_\mu B_\nu - \partial_\nu B_\mu \tag{1.5}$$

where the fact that the structure constants for SU(2) are represented by the component of the three dimensional Levi-Civita tensor ϵ^{abc} with $\epsilon^{123} = 1$ has been used and g is the coupling constant for the weak isospin. The covariant derivative in Eq. 1.4 is defined by:

$$D_\mu = \partial_\mu - \frac{1}{2}ig'YB_\mu + \frac{1}{2}ig\tau^a W^a_\mu \tag{1.6}$$

where τ^a are the Pauli matrices and Y the hypercharge. Since the right handed fermions are singlets under SU(2), the term proportional to the weak isospin vanishes. The hypercharge value is fixed by the Gell-Mann-Nishijima relation $Y/2 = Q - T_3$, where Q is the electric charge and T_3 is the eigenvalue of the third component of the weak isospin.

Spontaneous Symmetry Breaking and Yukawa interactions

In a Yang-Mills theory, Dirac or Majorana mass terms for fermions and gauge bosons are not admitted because they would break the gauge invariance. Therefore, all particles in the theory need to be massless in contrast with experimental observations. This problem was solved theoretically in the 60's by the Brout-Englert-Higgs (BEH) mechanism of Electroweak Spontaneous Symmetry Breaking [9–15]. In this mechanism, the Electroweak part of the SM gauge symmetry group is spontaneously broken by the introduction of an $SU(2)_Y$ complex field doublet ϕ contributing with the Lagrangian terms

$$\mathcal{L}_H = (D_\mu\phi)^2 - \mu^2\phi^2 - \lambda\phi^4 \tag{1.7}$$

where it is required that $\mu^2 < 0$ and $\lambda > 0$ such that the ϕ field has a non-vanishing vacuum expectation value given by

$$v = \sqrt{\frac{-\mu^2}{\lambda}}. \tag{1.8}$$

The choice of the vacuum state is arbitrary and breaks the EW symmetry group into the electromagnetic group $U(1)_Q$, where Q is the electric charge, giving in this way mass to the weak force carrier bosons and leaving the photon massless, at the cost of the introduction of an extra physical scalar field h. The physical gauge boson fields are obtained by linear combination of the W^1_μ, W^2_μ, W^3_μ and B_μ fields

$$W^\pm_\mu = \frac{(W^1_\mu \mp W^2_\mu)}{\sqrt{2}}$$
$$A_\mu = \sin\theta_W W^3_\mu + \cos\theta_W B_\mu \tag{1.9}$$
$$Z_\mu = \cos\theta_W W^3_\mu - \sin\theta_W B_\mu$$

where the mixing angle θ_W is called Weinberg angle and is defined by the condition $\sin \theta_W = g'/\sqrt{g'^2 + g^2}$.

The masses of the physical states of Eq. 1.9 are given by

$$M_W^\pm = \frac{1}{2}vg \quad M_Z = \frac{M_W}{\cos \theta_W} \quad M_A = 0 \tag{1.10}$$

showing that the gauge bosons responsible of the weak interactions gain mass while the photon remains massless. The extra physical field is called the *Higgs* field and has a corresponding mass given by $M_h = \sqrt{2\lambda}v$.

A mass term for the fermions can also be obtained through the BEH mechanism in a way that preserves gauge invariance adding to the EW Lagrangian the Yukawa terms [8]. Considering a single generation, such terms have the form

$$\mathcal{L}_f = \left(-\lambda_e \bar{E}\phi e_R - \lambda_d \bar{Q}\phi d_R - \lambda_u \epsilon^{ab} \bar{Q}_a \phi_b^\dagger u_R + h.c.\right) \tag{1.11}$$

where ϵ^{ab} is the two dimensional total anti-symmetric tensor with $\epsilon^{12} = 1$ and λ_e, λ_u and λ_d are arbitrary parameters. Due to the spontaneous symmetry breaking the fermions assume masses given by

$$m_e = (1/\sqrt{2})\lambda_e v \quad m_e = (1/\sqrt{2})\lambda_u v \quad m_u = (1/\sqrt{2})\lambda_d v \tag{1.12}$$

The validity of this mechanism has been established only in 2012, with the observation of a physical Higgs boson of mass $125.09 \pm 0.21 \pm 0.11$ GeV by the ATLAS and CMS collaborations [16–18].

Strong interaction Lagrangian Terms

The strong interactions are described by a theory called *Quantum Chromodynamics* (QCD). As discussed above, such theory is based on the $SU(3)_C$ gauge symmetry group. Quarks are arranged in triplets and have colour charges while leptons, that do not interact strongly, are represented as colour singlets. The $SU(3)$ group has 8 generators T^a, which can be related to the Gell-Mann matrices λ^a in the fundamental representation of the group. Therefore eight gluon fields are present that carry themselves the colour charge of the strong interaction.

The QCD Lagrangian terms can be written as

$$\mathcal{L}_{strong} = \sum_q \bar{\psi}_{q,i} \left(i\displaystyle{\not}D_{ij} - m_q \delta_{ij}\right) \psi_j - \frac{1}{4}G_{\mu\nu}^a G_{\mu\nu}^a \tag{1.13}$$

where $\psi_{q,i}$ is the fermion field of flavour q and colour i and the covariant derivative operator D^μ and the gluon fields kinetic terms $G_{\mu\nu}^a$ are given by:

$$\begin{aligned} D^\mu &= \partial_\mu + ig_s t^a G_\mu^a \\ G_{\mu\nu}^a &= \partial_\mu G_\mu^a - \partial_\nu G_\mu^a - g_s f^{abc} G_\mu^b G_\nu^c \end{aligned} \tag{1.14}$$

where g_s is the strong running coupling constant and f^{abc} are the SU(3) structure constants given by commutation relations between the group algebra generators $[t^a, t^b] = if^{abc}t^c$. The non-vanishing last term for the gluon fields kinetic terms allows interactions between three and four gluons among themselves. The dynamics of the $SU(3)$ gauge group leads to two important properties of strong interactions. The first is called *asymptotic freedom* [19] and states that the strong coupling constant becomes smaller when interactions happen at greater energy scales, making perturbative theory applicable at high energies while at low energies analytical calculations are not possible. The second important property is called *confinement* and states that quarks are bound into colourless states called *hadrons*. There are two type of hadrons: *mesons* which are composed by a quark-antiquark pair and *baryons* which are composed by three quarks or three anti-quarks. This important property leads to the fact that when quarks are pulled apart, their interaction becomes so strong that quark-antiquark pairs are created from the vacuum. This is at the origin of the *hadronisation* process that leads to the creations of sprays of hadronic particles, called *jets*, as products of $p - p$ collisions at the LHC.

1.1.2 Shortcomings of the Standard Model

In the last decades the Standard Model has revealed itself as a theory capable to describe and predict the behaviour of the subatomic particles with great precision. However, the SM is a theory far from being complete as it does not include the gravitational interaction and there are fundamental issues that lead to the search for *Physics beyond the Standard Model* (BSM). A few of these open questions are reported here in short.

Dark Matter

A large number of astrophysical observations [20–26] have shown the presence of more matter in the Universe than what is predicted by the SM theory. This matter, whose origin and composition is unknown, is called *Dark Matter* and can only interact weakly or gravitationally with the ordinary matter. A possible dark matter candidate is a particle with a mass corresponding to the weak energy scale that interacts weakly with the SM matter (WIMP). In the Standard Model there is no particle candidate for Dark Matter that can account for the current cosmological and astrophysical observations.

Gauge Couplings Unification

Inspired by the unification of the electromagnetic and weak forces into the EW interaction, theorists are exploring the possibility to unify the strong and the EW forces together.

This is done by a *Grand Unified Theory* that embeds the $SU(3)_C \otimes SU(2)_L \otimes U(1)_Y$ group into a larger one that is broken at very high energy scales. The strength of the EW and strong couplings by the *Renormalisation Group equations* becomes very similar when computed at an energy scale of $\Lambda_{GUT} \approx 10^{15}$ GeV, but does not completely coincide. In

some BSM models the complete unification is possible with the insertion of new particles with mass at the TeV scale [27].

Hierarchy Problem

This problem is of a different nature as it is not related to a physics phenomenon that can not be explained by the SM, but rather to the level of the fine tuning of some of the free parameters of the theory.

The physical value of the Higgs boson mass, like all the masses of the other particles of the theory, is affected by quantum loop corrections due to the coupling with the other elementary particles. The corrections to the Higgs mass arising from the coupling with fermions are proportional to

$$\delta m_h^2 \sim \lambda_f^2 \Lambda^2 + \mathcal{O}\ln(\Lambda) \tag{1.15}$$

where λ_f is the Yukawa coupling to the fermion f ($\lambda_f \approx 1$ for the top quark) and Λ is a cutoff scale introduced to regularise the divergence. Since the SM does not predict any new physics up to the Planck scale, the cut off can be taken as $\Lambda = M_{pl} \approx 10^{19}$ GeV, where gravity would have the same strength as the strong and electroweak forces. The bare mass of the Higgs boson has to be such that it cancels the divergence of Eq. 1.15, in order to give a physical mass of about 125 GeV. Even if it is theoretically allowed, such level of fine tuning up to the 17th digit appears rather unpleasant at the eyes of a large fraction of the theorists at the present moment. The presence of new scalar particles at the TeV scale cancels these divergencies reducing by far the fine tuning needed (see Sec. 1.3.2).

1.2 Supersymmetry

Theorists have worked on possible extensions of the SM in order to solve the shortcomings mentioned above. One promising theory is *Supersymmetry* (SUSY) [28–36], a model where bosons and fermions are interchanged through a symmetry transformation, generalising the space-time symmetries of quantum field theories [37, 38]. In SUSY, space-time is extended to a *superspace* formed by the four space-time coordinates and anti-commuting fermionic coordinates. In this formulation, the fields describing bosons and fermions, which are a function only of space-time, are organised in *supermultiplets*. The supersymmetry operators transform the bosonic members of the supermultiplets in the fermionic member and vice-versa, modulo additional space-time translations and rotations. The supersymmetry algebra only closes when the classical equations of motion are satisfied. In order to ensure that supersymmetry is realised also off-shell, a set of chiral fields, F, and gauge fields, D, are introduced in the supersymmetric Lagrangian. These fields are called *auxiliary* fields and vanish on-shell [39]. The supersymmetry algebra operators commute with the internal gauge symmetries of the theory and with the square of the four-momentum operator. Hence, in a non broken supersymmetric theory, the members of the supermultiplets have the same mass and the same gauge quantum numbers.

Particle content of the MSSM						
		Supermultiplets		Quantum numbers		
	Sparticle mass eigenstates	Sparticle fields	Particle fields	$SU(3)_C$	$SU(2)_L$	$U(1)_Y$
gluino/gluon	$\tilde{g}$	$\tilde{g}$	g	8	1	0
gaugino/gauge	$\tilde{\chi}_{1,2}^{\pm}$	$\tilde{W}^{\pm}, \tilde{W}^0$	$W^{\pm}, W^0$	1	3	0
	$\tilde{\chi}_{1,2,3,4}^0$	$\tilde{B}$	B	1	1	0
higgsino/higgs	h^0, H^0	$(\tilde{H}_d^0, \tilde{H}_d^-)$	(H_d^0, H_d^-)	1	2	-1
	$A, H^{\pm}$	$(\tilde{H}_u^+, \tilde{H}_u^0)$	(H_u^+, H_u^0)	1	2	1
slepton/lepton	$\tilde{\nu}_e, \tilde{e}_1$	$(\tilde{\nu}_e, \tilde{e})_L$	$(\nu_e, e)_L$	1	2	-1
	$\tilde{e}_2$	$\tilde{e}_R$	e_R	1	1	-2
squark/quark	$\tilde{u}_1, \tilde{d}_1$	$(\tilde{u}, \tilde{d})_L$	$(u, \tilde{d})_L$	3	2	1/3
	$\tilde{u}_2, \tilde{d}_2$	$\tilde{u}_R$	u_R	3	1	4/3
		$\tilde{d}_R$	d_R	3	1	-2/3

Table 1.2: The field content of the MSSM and their gauge quantum numbers. Only the first generation of leptons and quarks is listed for brevity. The supersymmetric particle fields mix to give mass eigenstates. For the scalar quarks and scalar leptons, the subscripts R and L do not indicate a chirality state but only to which fermion they are partnered. Table adapted from [7].

Since no supersymmetric particle has been experimentally observed yet, the masses of the superpartners are thought to be much larger of the SM particles, implying that SUSY must be a broken symmetry. The mechanisms that lead to supersymmetry breaking are not known at the present moment. More details on this topic are given in Sec. 1.2.2.

SUSY is of particular interest for experimental physicists. In fact, even if not theoretically necessary, a realisation of SUSY at the TeV scale is very intriguing since it would cancel the quadratic divergencies in radiative corrections of the Higgs mass [40]. In addition, some of the possible theory configurations provide a natural candidate for the Dark Matter [41] and correct the value for the running coupling constants such that they assume the exact same value at the GUT scale [42]. The work presented in this dissertation is performed in the *Minimal Supersymmetric Standard Model* (MSSM) framework, that represents the minimal way to create a supersymmetric model starting from the SM theory. Details on the theoretical formulation of the MSSM are given in [7, 39, 43] and here only the aspects inherent to the analysis described in this dissertation are summarised.

1.2.1 MSSM Fundamentals

The MSSM is the supersymmetric extension of the SM that is obtained through the introduction of the minimum number of supersymmetric fields that satisfy the $SU(3)_C \otimes$

$SU(2)_L \otimes U(1)_Y$ gauge invariance and maintain the $B - L$ conservation, where B and L are the baryonic and leptonic numbers, respectively. A summary of the particle content of the MSSM is given in Tab. 1.2. The matter content of the MSSM is formed by the SM fermions, quarks and leptons, with the addition of their scalar super partners, conventionally named *scalar quarks* (*squarks*) and *scalar leptons* (*sleptons*), respectively. There are two scalar quarks $\tilde{q}_R$ and $\tilde{q}_L$ ($q = u, d, c, s, t, b$) and two scalar leptons $\tilde{\ell}_R$ and $\tilde{\ell}_L$ ($\ell = e, \mu, \tau$) that correspond to the superpartners of the two chirality states of the SM quarks and massive leptons. Since neutrinos are assumed massless by the SM, there is only one scalar neutrino $\tilde{\nu}_\ell$ for each lepton flavour. After SUSY breaking, discussed in Sec. 1.2.2, the chirality states of the scalar superpartners of the SM fermions can mix into mass eigenstates which are usually denoted with numerical subscripts. For example, given a SM fermion f, the mass-eigenstates of its superpartners are denoted as $\tilde{f}_1$ and $\tilde{f}_2$, with the first one being the lightest. Since the mixing coefficients depend on the mass of the SM fermion, the mixing in the third generation sector is largest, leading to top squarks being typicaly the lightest of the supersymmetric quarks [44].

The superpartners of the SM gauge bosons are called *gauginos* and are eight *gluinos* $\tilde{g}$, three *Winos* $\tilde{W}^\pm, \tilde{W}^0$ and one *Bino* $\tilde{B}$.

The Higgs sector of the MSSM is composed by two Higgs supermultiplets with opposite hypercharge. They are formed by two scalar Higgs doublets, $H_u = (H_u^+, H^0)$ and $H_d = (H_d^0, H_d^-)$, with their corresponding fermionic superpartners $\tilde{H}_u = (\tilde{H}_u^+, \tilde{H}^0)$ and $\tilde{H}_d = (\tilde{H}_d^0, \tilde{H}_d^-)$ called *higgsinos*. The presence of two supermultiplets is required by the fact that every renormalisable theory must realise the exact cancellation of gauge anomalies [45] that would be broken if only a single scalar Higgs field with an associated fermionic superpartner would be present in the theory. Furthemore, two scalar Higgs doublets are necessary to simultaneously give mass to up- and down-type quarks. The two scalar Higgs doublets introduce eight real degrees of freedoms. While three of them are used to give masses to the SM $SU(2)_L$ gauge bosons, five give rise to two CP-even neutral scalars, h^0 and H^0, one CP-odd scalar A^0 and two charged scalar $H^\pm$ particles.

After the EW breaking mechanism in the MSSM, in a similar fashion to the mixing that occurs for the W_3 and B to give the Z boson and photon physical states in the SM Higgs mechanism, the higgsinos and the electroweak gauginos mix in order to give rise to four neutral and four charged mass eigenstates. The charged higgsinos ($\tilde{H}_u^+$ and $\tilde{H}_d^-$) mix with the charged electroweak gauginos ($\tilde{W}^\pm$) to form the *charginos* $\tilde{\chi}_{1,2}^\pm$ eigenstates. The neutral higgsinos ($\tilde{H}_u^0$ and $\tilde{H}_d^0$) mix with the bino $\tilde{B}$ and the neutral wino $\tilde{W}^0$ to form the so called *neutralinos* $\chi_{1,2,3,4}^0$. The same convention on the mass subscripts is maintained where $\chi_1^\pm$ and χ_1^0 indicate the lightest chargino and neutralino respectively. The choice of the SUSY breaking parameters have not only an impact on the masses of the charginos and neutralinos, but also on their mixing composition, leading to different strengths in their interactions with the other particles in the MSSM theory [44].

Within the MSSM it is possible to define the *R-parity* quantity for each particle

$$R \equiv (-1)^{3B+L+2S} \tag{1.16}$$

where S is the spin of the particle [46, 47]. Standard Model particles have $R = +1$ while all their supersymmetric partners have $R = -1$. As a consequence of $B - L$ conservation,

R-parity is multiplicatively conserved with a great impact on the MSSM phenomenology. Firstly, only pairs of supersymmetric particles can be produced in particle colliders that make use of SM particles in the initial state. Secondly, the lightest supersymmetric particle (LSP) is stable and has to be produced at the end of every decay chain of every heavier and unstable supersymmetric particle. Cosmological constraints impose that the LSP has to be colour and electrically neutral [41], therefore such a particle can interact only weakly, or gravitationally, with ordinary matter.

1.2.2 Supersymmetry breaking

As introduced before, *Supersymmetry* must be a broken symmetry since no superpartners of the SM particles have been observed with the same masses. SUSY is expected to be spontaneously broken but the exact mechanism is not known yet. On the other hand, in order for SUSY to provide a solution for the *hierarchy problem*, it has to be broken *softly* [48], i.e. by terms that do not re-introduce quadratic divergencies and that can have mass dimension at most three. In the MSSM, the most general supersymmetry breaking terms, satisfying the constraints defined above, are directly added to the MSSM Lagrangian [43]. The addition of the explicit *Supersymmetry* breaking term brings the introduction of additional 105 free parameters that, even if many of them are constrained by several precision measurements, create an extremely large spectrum of different possibilities for the SUSY particles masses, couplings and decay modes.

In contrast to this approach and in order to understand the origin of the soft SUSY breaking parameters, it is necessary to consider models in which SUSY is spontaneously broken, i.e. the Lagrangian is invariant under gauge transformations but the vacuum state is not. It can be shown [39] that this fact leads to the condition that the expectation values of the chiral auxiliary fields F_i and gauge auxiliary fields D^a, with i being an index that runs over all gauge and flavour degrees of freedom and a being an index running over the adjoint representation of the gauge group, do not vanish simultaneously in the vacuum state but instead assume a finite and positive *Vacuum Expectation Value* (VEV). The spontaneous breaking mechanism of a global symmetry implies the creation of a Nambu-Goldstone mode, which in the case of fermionic SUSY operators is a Weyl fermion called *goldstino*, whose wave function components are proportional to the vector

$$\tilde{\mathcal{G}} = \begin{pmatrix} \langle D^a \rangle / \sqrt{2} \\ \langle F_i \rangle \end{pmatrix} \tag{1.17}$$

which is not null only if the VEV of the auxiliary fields do not vanish. In the rest of the work presented in this dissertation, only the models based on a non-zero F-term VEV, or O'Raifeartaigh models [49], are considered. A way to realise these models is to use a set of chiral supermultiplets $\Phi_i = (\phi_i, \psi_i, F_i)$ and a super potential W such that $F_i = -\delta W^* / \delta \phi^{*i}$ are not all simultaneously vanishing. The simplest example uses three chiral supermultiplets $\Phi_{1,2,3}$ and a superpotential W defined as

$$W = -k\Phi_1 + m\Phi_2\Phi_3 + \frac{y}{2}\Phi_1\Phi_3^2 \tag{1.18}$$

with k,m and y that can be chosen real and positive without loss of generality. It can be shown [39, 50] that the scalar potential V following from Eq. 1.18 has a positive minimum $V_{\mathrm{min}} = k^2$ for a non trivial auxiliary field $F_1 = k$. Unfortunately, terms linear in the supermultiplets are allowed in the superpotential if and only if they are gauge singlet. Since in the MSSM there are no supermultiplets satisfying this condition, an extension of this model is required.

1.2.3 Gauge Mediated Supersymmetry breaking

In order to explain the *spontaneous Supersymmetry breaking*, several models assume the existence of a *hidden sector*, which is usually assumed to be decoupled from the MSSM. In this sector, SUSY breaking is generated and it is then transmitted by some mechanism to the *visible sector* composed by the MSSM particles. At the present day, there is no preferred mechanism among the theorists community and amongst the various possible theoretical scenarios. The analysis presented in this thesis assumes the realisation of the *Gauge mediated Supersymmetry breaking* (GMSB) [51–56]. Only a brief introduction of the basic concepts behind the GMSB mechanism is presented here since the complete treatment is beyond the scope of this thesis. A more complete review can be found in [39, 50].

This GMSB mechanism is based on the assumption that there exists a set of chiral supermultiplets, called *messengers*, that couple directly to the source of supersymmetry breaking in the *hidden sector* and indirectly through quantum loops to the particles of the MSSM via ordinary $SU(3)_C \times SU(2)_L \times U(1)_Y$ gauge interactions. While the Higgs sector is still responsible to give mass to the SM particles, the gauginos and scalar quarks obtain their masses through one and two loops quantum corrections, respectively, due to the interactions with the messenger fields. The supersymmetry breaking terms for the MSSM are proportional to

$$m_{\mathrm{soft}} = \frac{\langle F \rangle}{M_{\mathrm{mess}}} \tag{1.19}$$

where M_{mess} is the mass of the messenger fields and is affected by two boundary conditions and $\langle F \rangle$ is the VEV of the chiral auxiliary field F. The lower limit on M_{mess} is dictated by the requirement that soft supersymmetry breaking should be realised and so the mass of the messenger can not be arbitrarily small. The upper limit instead is placed in order to avoid gravity effects to the computed masses of the super particles. Those limits are chosen to be [50]:

$$10^4 \lesssim M_{\mathrm{mess}} \lesssim 10^{15} \quad \mathrm{GeV} \tag{1.20}$$

As discussed in the previous section, as a result of the SUSY breaking, a massless spin-1/2 goldstino is added to the physical particle content. This is valid when SUSY is a global symmetry but when it is promoted to a local symmetry, necessary to include gravity within the theory [57], the goldstino provides the longitudinal modes of the spin-3/2 partner of

the graviton, the *gravitino*. The mass of the gravitino is given by [58, 59]

$$m_{3/2} = \frac{\langle F \rangle}{k\sqrt{3}M_P} = \frac{1}{k} \left(\frac{\sqrt{\langle F \rangle}}{100 \text{ TeV}} \right)^2 \cdot 2.4 \text{ eV,} \tag{1.21}$$

where $M_P = (8\pi G_N)^{-1/2} = 2.4 \times 10^{18}$ GeV is the reduced Planck mass, k is a parameter lower than one that varies within different GMSB models and depends on the strength of the couplings between the hidden and the messenger sectors. Therefore the gravitino is the LSP in GMSB models for any relevant value of $\langle F \rangle$. In the following section, the phenomenology of GMSB models will be introduced and briefly discussed.

1.2.4 GMSB phenomenology

The supersymmetric particle mass spectrum within GMSB theories is determined by a small set of parameters including the supersymmetry-breaking scale m_{soft}, the messenger mass M_{mess} and $\tan\beta = \frac{v_u}{v_d}$, where v_u and v_d are the VEV of the two Higgs doublets. Gauge mediated models have the advantage to be highly constrained and very predictive for the superparticles mass spectrum and detailed analyses have been carried out and presented in [50, 60].

As discussed in Sec. 1.2.3, the LSP for GMSB models is the *gravitino* $\tilde{G}$ whose mass can be neglected for kinematic purposes. In the case of R-parity conserving supersymmetry, every super particle has to eventually decay into a gravitino, either directly or through a decay chain. The decay rate of any particle $\tilde{X}$ into its SM partner X plus a gravitino $\tilde{G}$ is given by [50]

$$\Gamma(\tilde{X} \rightarrow X\tilde{G}) = \frac{m_{\tilde{X}}^5}{16\pi \langle F \rangle^2} \left(1 - \frac{m_X^2}{m_{\tilde{X}}^2} \right)^4 \tag{1.22}$$

where m_X and $m_{\tilde{X}}$ are respectively the mass of the SM particle and its superpartner. From Eq. 1.21 and Eq. 1.22 it is possible to see that the decay width becomes larger for smaller $m_{3/2}$, if the other masses are fixed. While this decay mode is usually negligible with respect to the other particle decays, it is the only one allowed in the case of $\tilde{X}$ being the next-to-lightest supersymmetric particle (NLSP). Even if in principle any of the MSSM superparticles could be the NLSP, in GSMB models this role can be covered usually by a neutralino, a charged slepton or, in a very restricted phase space, a sneutrino [50]. In the case of a charged slepton being the NLSP, this role can be taken by more than one super particle as the generated square masses for $\tilde{e}_R$, $\tilde{\mu}_R$ and $\tilde{\tau}_R$ are identical. However, when computing the mass eigenstates, one has to consider the mixing with $\tilde{e}_L$, $\tilde{\mu}_L$ and $\tilde{\tau}_L$. In analogy with what has been discussed for the top squark in Sec. 1.2.1, the off-diagonal term of the mixing matrix depends strongly on the Yukawa coupling. Therefore, while the effects are very small for the two generations of sleptons which can be considered degenerate in mass, the $\tilde{\tau}_R$ and $\tilde{\tau}_L$ have a large degree of mixing to a level that the lightest mass eigenstate $\tilde{\tau}_1$ can be easily the lightest slepton with a mass that strongly depends on $\tan\beta$. The work presented in this thesis assumes a scalar tau as NLSP that, by virtue of Eq. 1.22 and Eq. 1.21 has a decay rate in $\tau + \tilde{G}$ given by:
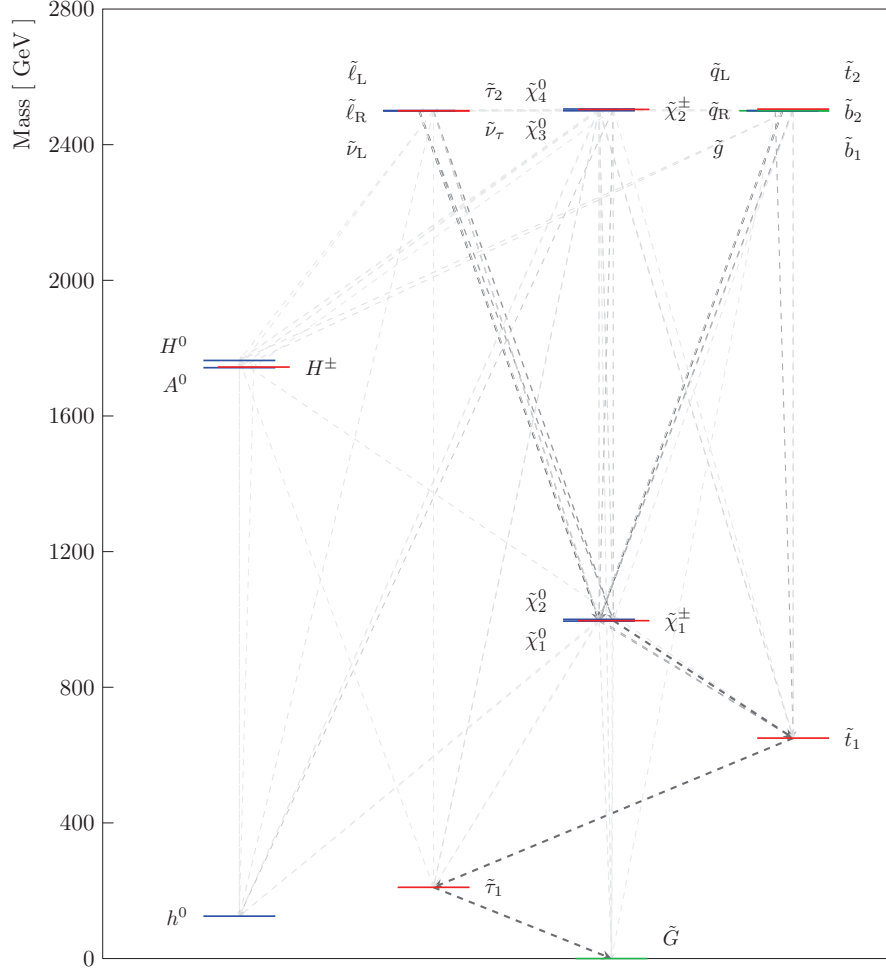
Figure 1.1: Illustrative example of the particle masses spectrum and decay BRs for the model discussed in the text. Thicker and darker dotted lines indicate larger decay branching ratios. The spectrum is obtained via the `pyshla` package [61].

$$\Gamma(\tilde{\tau} \to \tau \tilde{G}) = \frac{k^2 m_{\tilde{\tau}}^5}{16\pi \langle F \rangle^2} = 2k^2 \left(\frac{m_{\tilde{\tau}}}{100 \text{ GeV}} \right) \left(\frac{100 \text{ TeV}}{\sqrt{F}} \right)^4 \times 10^{-3} \text{ eV}. \tag{1.23}$$

This decay rate has an important impact on the signature expected in the ATLAS experiment. From Eq. 1.23 it is possible to obtain the average distance travelled by a $\tilde{\tau}$ when produced with energy E

$$\bar{d} = \left(\frac{100 \text{ GeV}}{m_{\tilde{\tau}}} \right)^5 \left(\frac{\sqrt{F/k}}{100 \text{ TeV}} \right)^4 \sqrt{\frac{E^2}{m_{\tilde{\tau}}} - 1} \times 10^{-2} \text{ cm}. \tag{1.24}$$

The value of $\sqrt{F/k}$ drives the behaviour of the NLSP at particle colliders experiments. If the value is larger than $\sim 10^6$ GeV, the NSLP decays outside the detector and behaves like a stable particle. A value of $\sqrt{F/k} \sim 10^6$ GeV produces a $\tilde{\tau}$ that has a measurable

decay length and it is registered by the detector as a displaced vertex, while in the cases where $\sqrt{F/k} \lesssim 10^6$ GeV, the $\tilde{\tau}$ decays promptly producing a τ lepton and a gravitino that escapes detection. In the analysis work presented in this thesis, the latter case is assumed to be realised, hence prompt taus are expected to be produced. Another assumption that has been made is that the mass of the messengers has to be of the order of 10 TeV in order to minimise the level of fine tuning [62]. This choice is driven by Eq. 1.19, where $\langle F \rangle$ is of the order of 10^6 GeV and m_{soft} is required to be up to the TeV scale. In this scenario the first and second generation squarks and sleptons can assume very large masses while the third generation is required to be at the weak scale. Even if these results imply that in the simplest gauge-mediated models, the predicted Higgs boson mass is lower than the current measured value of 125 GeV [63, 64], a set of mechanisms can raise the theoretical value of the Higgs mass to make it compatible with the observed value [65–67]. An illustrative example of the particle spectrum obtained applying the assumptions discussed above is shown in Fig. 1.1.

Given the phenomenology discussed above, it is possible to probe GMSB models at the energies available at the LHC collider and with the data collected by the ATLAS experiment.

1.3 Search for Supersymmetry at LHC

1.3.1 Particles production at the LHC

During Run-1, LHC reached an energy in the centre of mass of 8 TeV, making it possible to probe the existence of new particles at the TeV energy scale. However, in order to understand the production of particles through proton collisions it is important to give a brief description of protons composition first.

Parton model and parton density functions

A proton is a very complex object composed by *valence* and *sea* quarks as well as gluons responsible for the strong interactions. The constituents of the protons are called *partons*. The *valence* quarks are, in the case of protons, two up quarks and a down quark and are the ones defining the quantum numbers of the protons. The *sea* quarks are extremely short living quark/anti-quark pairs created by random vacuum fluctuations, but that can still interact with the partons in the colliding proton. Each of the partons carries a fraction of the proton's momentum x, defined mathematically as the ratio between the magnitude of the parton momentum over the magnitude of the proton momentum. Using the *factorisation* approach [69], the cross section between two protons can be written as

$$\sigma_{pp} = \sum_{i,j} \int dx_i dx_j f_i(x_i, Q^2) f_j(x_j, Q^2) \sigma_{partons}(x_i, x_j) \qquad (1.25)$$

where a sum is carried over all the types of possibly interacting partons i and j and the integral is carried over the possible momentum fractions that these partons carry and

Value of xf(x, Q²) versus x
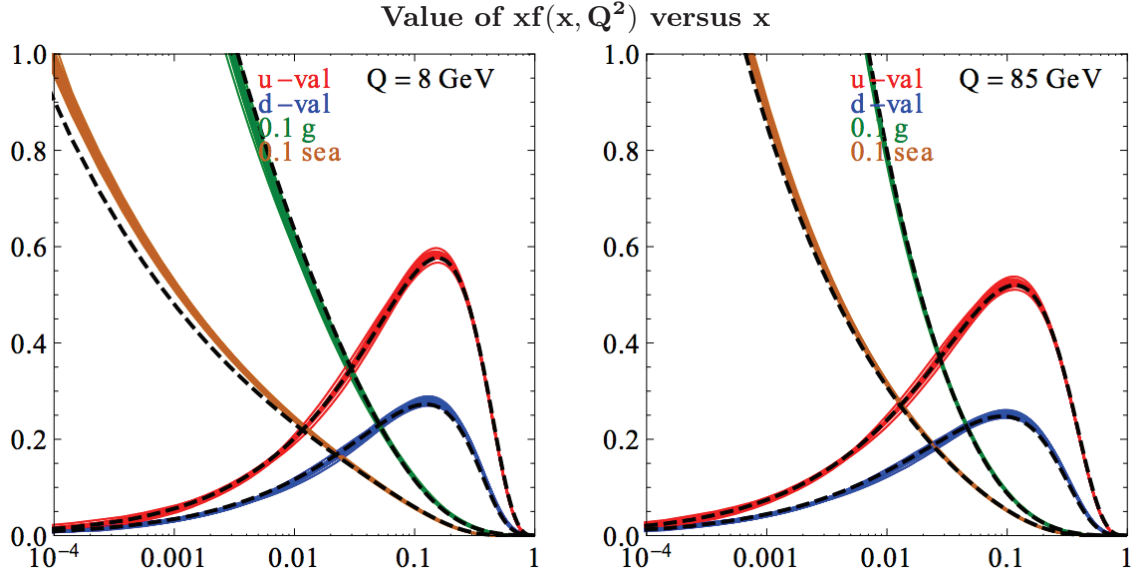
Figure 1.2: The distribution of $xf(x, Q^2)$ for the CT10NNLO parton distribution function at two different interaction scales, for valence quarks, sea quarks and gluons. The coloured bands show the systematic uncertainties.[68].

$\sigma_{partons}(x_i, x_j)$ is the interaction cross section between two partons at proton momentum fraction x_i and x_j, respectively. The functions $f_k(x_k, Q^2)$ are called *parton distribution functions* (PDFs) and parametrise the probability that a certain parton of type k with momentum fraction x_k can interact and they depend on the energy scale Q^2 at which the interaction occurs. The PDFs are measured experimentally in deep inelastic scattering [70, 71] , Drell-Yan [72] and $pp \rightarrow$jets [73] processes. Several collaborations such as MSTW [74], HERAPDF [75], NNPDF [76], CT10 [68] and CTEQ [77] compute the PDF sets at different orders for the processes occurring at the LHC. In Fig. 1.2 the CT10 PDFs at the next-to-next-to-leading order are shown. The remaining partons that do not contribute to the hard scattering will create a set of low momenta particles denominated the *underlying event*. Both initial and final state partons can also radiate photons or undergo hadronisation processes that are called *initial* (ISR) and *final state radiation* (FSR).

Production cross sections of SUSY particles

In the framework of R-parity conserving supersymmetry models, superparticles are produced in pairs from parton interactions during proton-proton collisions. The production cross section for pairs of supersymmetric particles is larger for those that couple strongly to the matter constituents, such as gluinos and squarks, and lower for the processes that instead involve EW interactions, such as pair production of gauginos or leptons. The calculation of the cross sections for the production of pairs of SUSY particles is made using the `Prospino` software [79]. The results are reported in Fig. 1.3 and show that gluinos and squark pairs are expected to be the most abundantly produced. This fact led the
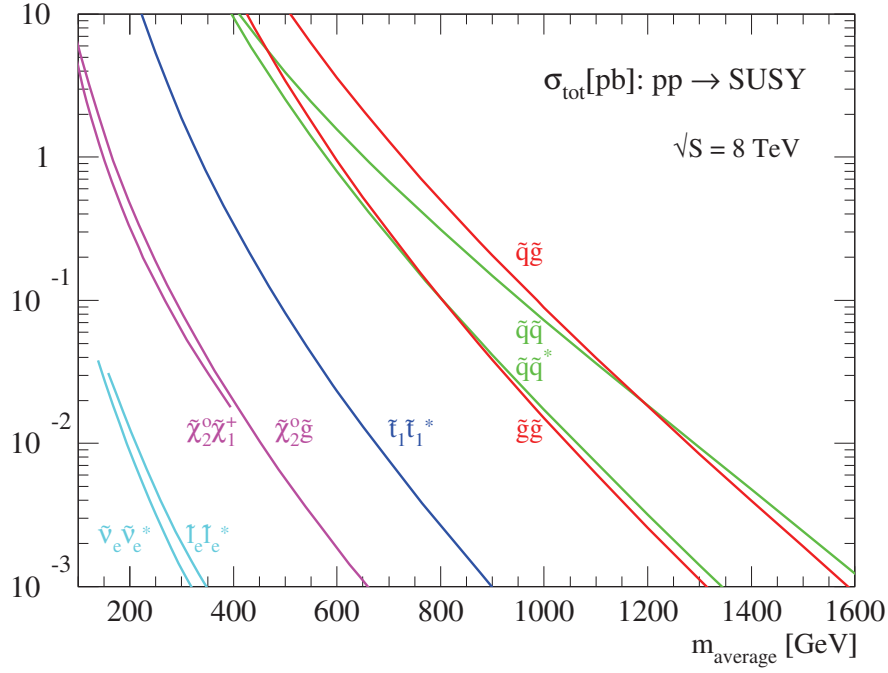
Figure 1.3: Supersymmetric particles pair production cross section (in picobarn) at LHC for $\sqrt{s} = 8$ TeV as a function of their mass. Figure taken from [78].

ATLAS experiment to focus in the early stage on inclusive searches characterised by a large hadronic activity in the final state [80–83], whose results place limits on these particles masses above the TeV scale. With increased statistics, such as the full dataset collected at $\sqrt{s} = 8$ TeV, the interests shifted to the pair production of third generation scalar quarks, and in particular of scalar top quarks, despite the harder challenges presented by such searches due to a lower cross section and final states very similar to other SM processes.

1.3.2 Scalar top pair searches

Searches for production of scalar top quarks represent an area of major interest for the ATLAS experiment. Considering R-parity conserving SUSY models, top squark pairs are produced by quark/anti-quark annihilation or gluon fusion processes and the leading order Feynman diagrams are shown in Fig. 1.4. Scalar top pairs are produced with a cross section that is an order of magnitude smaller than the other two generations of squarks and gluinos. This is due to the fact that top quarks are not present in the initial state and the $t-$channel diagram is suppressed. The production cross section in $p-p$ collisions depends on the top squark mass as shown in Fig. 1.3. For top squark masses ranging between 400 and 800 GeV, the pair production cross section varies between about 1pb to 3fb.

In this section a brief summary of the motivation for the searches for top squark searches is presented, together with a summary of the searches performed in ATLAS at the time of the work presented in this thesis. Finally the motivations for a scalar top search in the context of GMSB is given.
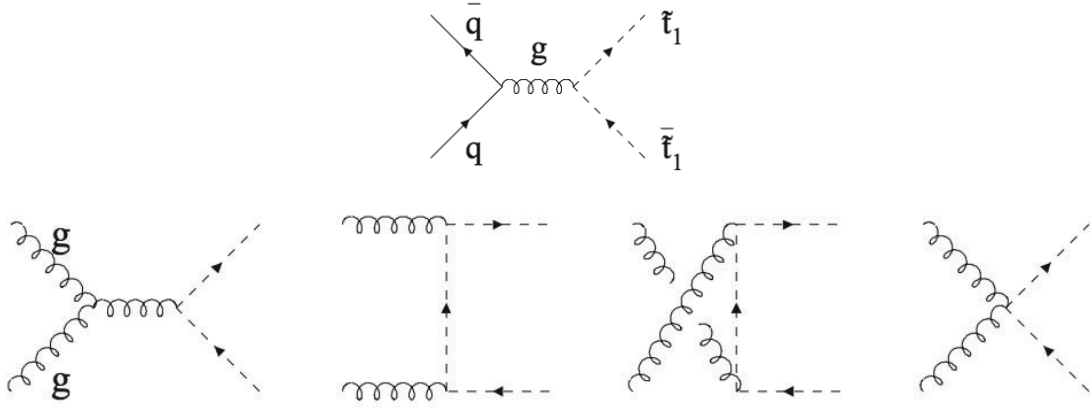
Figure 1.4: Quark/anti-quark annihilation and gluon fusion leading order Feynman diagrams for the production of pairs of scalar top particles [84].

Motivation for scalar top searches

One of the strongest motivations for searching for the production of scalar top particles comes from the role that top squarks play in giving a solution for the *hierarchy problem*. Recalling Eq. 1.15, due to the fact that top squarks share the same Yukawa coupling of top quarks, the corrections to the Higgs mass δm_h^2 become

$$\delta m_h^2 \sim \lambda_t (m_{\tilde{t}}^2 - m_t^2) \ln(\Lambda^2/m_{\tilde{t}}^2), \tag{1.26}$$

showing that only logarithmic divergence is left. If the level of fine tuning has to be kept low such that supersymmetry provides a solution for the *hierarchy problem*, the masses of top squarks are expected to be at the TeV scale and so these particles can be produced at the LHC and discovered by the ATLAS experiment. In addition, the large Yukawa coupling for top quarks and scalar top quarks is responsible for large off-diagonal terms in the mass mixing matrix expressed in the gauge eigenstates $\tilde{t}_R$ and $\tilde{t}_L$ [39]. Such terms induce a large mass splitting between the two mass eigen states $\tilde{t}_1$ and $\tilde{t}_2$, in contrast to the squarks belonging to the first and second generations, which are expected to be almost degenerate, and several models often predict that $\tilde{t}_1$ is the lightest amongst all squarks.
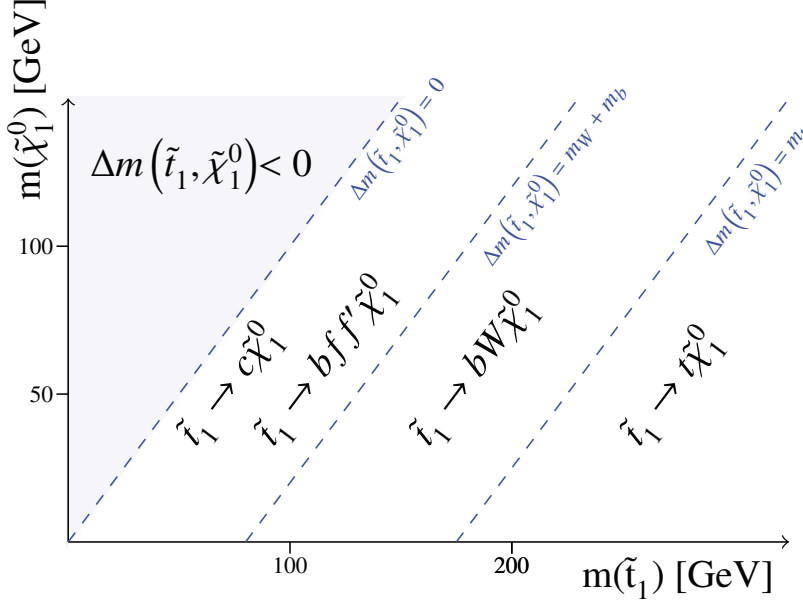
Figure 1.5: Schematic illustration of various top squark decay modes in the plane defined by the top squark mass $m_{\tilde{t}}$ and the lightest neutralino mass $m_{\tilde{\chi}_1^0}$, where the lightest neutralino is assumed to be the LSP. The dashed blue lines separate the regions where particular processes dominate.

Scalar top searches performed in ATLAS

The top squark is characterised by a very rich phenomenology and various decay modes are accessible depending on the spectrum of a particular SUSY model considered. The ATLAS experiment performed an extensive program of searches for third generation scalar quark pair production over the years. While a complete summary is beyond the scope of this thesis, a full review can be found in [85]. At the time of the work presented in this thesis, the ATLAS experiment focused on searches that assumed that the LSP was a stable neutralino $\tilde{\chi}_1^0$, and not the gravitino $\tilde{G}$ leading to a scalar top quark phenomenology that depends over the quantity $\Delta m(\tilde{t}, \tilde{\chi}_1^0) = m_{\tilde{t}} - m_{\tilde{\chi}_1^0}$. In Fig. 1.5 the main regions that are taken into account by the searches performed are shown. Cases where the scalar top decay involved additional SUSY particles in the decay chain have been considered. For example, when the lightest chargino $\tilde{\chi}_1^\pm$ is assumed to be the NLSP, the top squark tends to assume a significant branching ratio for $\tilde{t} \to b\tilde{\chi}_1^\pm$. The presence of additional particles in the decay chain however introduces additional freedom on the choice of the masses of the particles involved. Several scenarios have been considered with the most common ones based on gauge-universality which assume a relation between the mass of the chargino and the one of the neutralino $m_{\tilde{\chi}_1^\pm} = 2m_{\tilde{\chi}_1^0}$ [86–89].

Several dedicated analyses targeting specific top squark final-state topologies have been optimised under the assumptions that the top squarks decay chains involve only one or two possible channels. No analysis found evidence of any excess of measured data over the
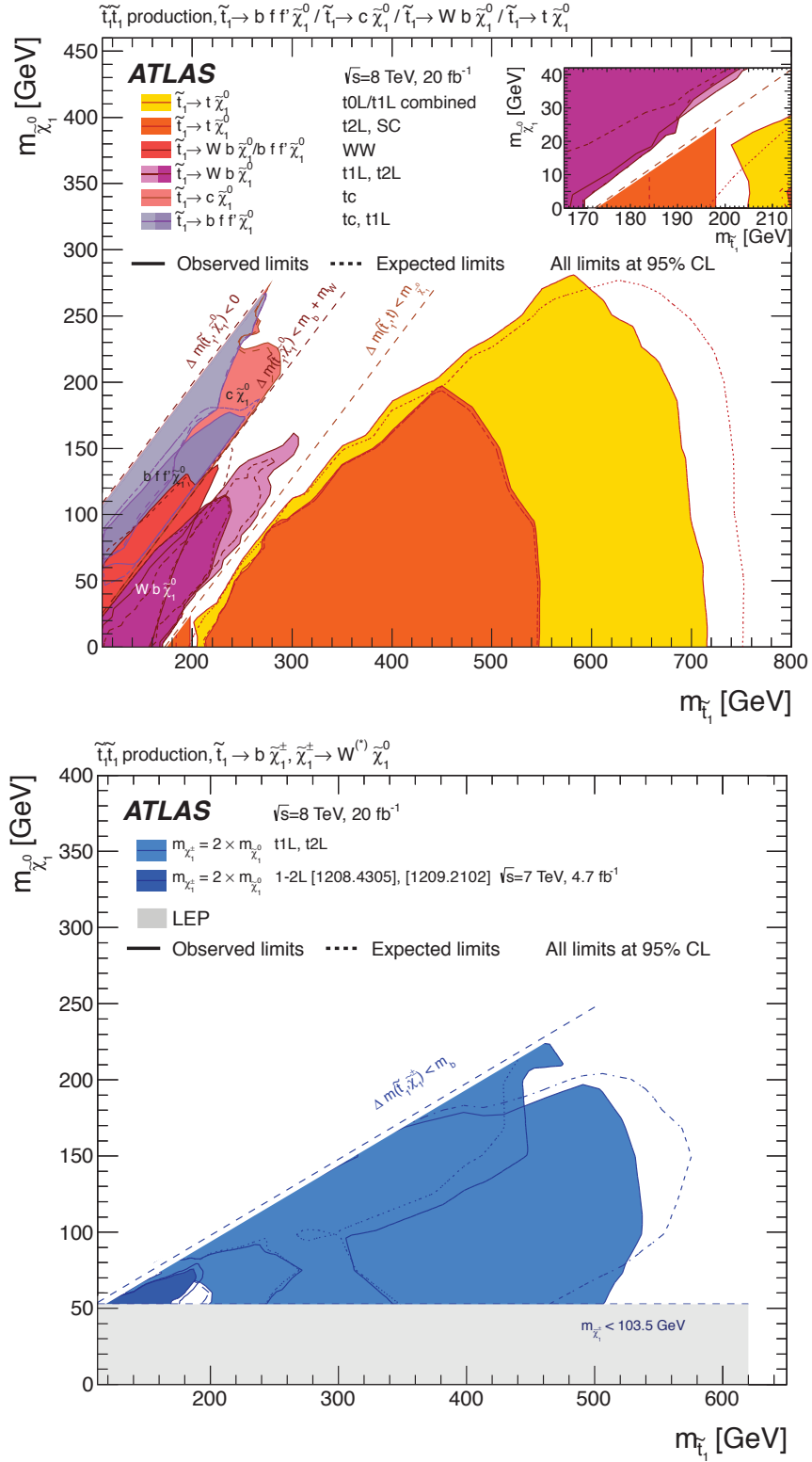
Figure 1.6: Summary of the ATLAS Run 1 searches for top squark pair production under the assumption that $\tilde{\chi}_1^0$ is the LSP. The 95% Confidence Levels limits are shown in the $(m_{\tilde{t}}, m_{\tilde{\chi}_1^0})$ plane. The top figure shows the limits obtained where no supersymmetric particle other than the $\tilde{t}_1$ and the $\tilde{\chi}_1^0$ are involved. The bottom figure shows the limits under the assumption of $\tilde{t}_1 \rightarrow b\tilde{\chi}_1^\pm$ with $\tilde{\chi}_1^\pm \rightarrow W^*\tilde{\chi}_1^0$ in a scenario based on gauge universality with $m_{\tilde{\chi}_1^\pm} = 2m_{\tilde{\chi}_1^0}$ [85].
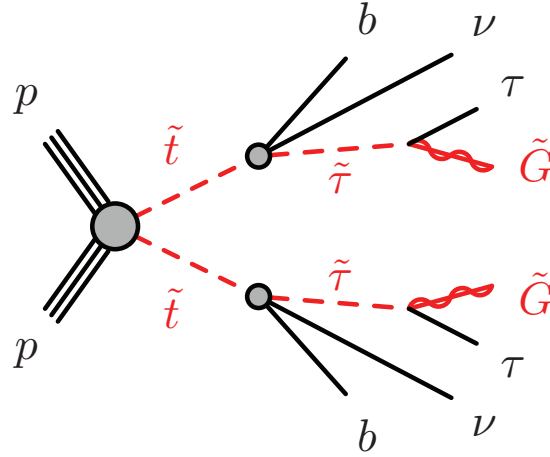
Figure 1.7: Diagram showing the decay topology of the signal process considered in this thesis

SM prediction, hence a combined set of exclusion limits (see Sec. 6.5) at 95% confidence level (CL) has been set. Figure 1.6 shows the combined limits over the two main scenarios discussed above. Depending on the neutralino mass and the model considered top squark masses up to around 720 GeV have been excluded.

Motivation for the search for scalar top decaying into scalar taus

The work presented in this thesis focuses on a set of possible SUSY scenarios arising from the GMSB mechanism discussed in Sec. 1.2.4 that assumes a massless gravitino as LSP, a stau lepton as NLSP and the top squark as the lightest squark. In the models considered, the other supersymmetric particles have very large masses and do not contribute to the top squark decay chain. The only open decay channel of the top squark is the three body decay

$$\tilde{t} \to b\tilde{\tau}\nu_\tau \quad \text{with} \quad \tilde{\tau} \to \tau\tilde{G}. \tag{1.27}$$

This model is not probed by the searches discussed above which consider neutralinos and charginos in the top squark decay chain, neither by other searches with scalar top decaying into gravitinos performed by ATLAS [90] which do not include the scalar tau into the decay chain. The work presented in this thesis presents a dedicated search for pair production of scalar tops in the final state with two tau leptons, two jets that contain a b-hadron and two very light gravitinos that escape detection. The topology of the signal considered is shown in Fig. 1.7. Two distinct analyses are reported in this dissertation that focus on orthogonal final states with one hadronically decaying tau and a muon or an electron in the final state or two hadronically decaying tau leptons, respectively.

2 The Large Hadron Collider and the ATLAS detector

2.1 The Large Hadron Collider

2.1.1 The accelerator complex

The Large Hadron Collider (LHC) is a two-ring superconducting, circular proton or heavy-ion collider. It is located at CERN, near Geneva and across the border between France and Switzerland. The LHC is hosted in the former LEP [91] underground tunnel of 27 km circumference and located approximately 100m below soil. The LHC is designed to operate at a proton-proton centre-of-mass energy of $\sqrt{s} = 14$ TeV. While the delivered energy was $\sqrt{s} = 7$ TeV during 2010 and 2011 and $\sqrt{s} = 8$ TeV during 2012, in 2015 it has been raised to $\sqrt{s} = 13$ TeV. The increase of the centre-of-mass is well justified by the bigger increment in production cross section for heavy particles, such as those predicted by supersymmetry, over the increased background rates. In this thesis, the data recorded at $\sqrt{s} = 8$ TeV and $\sqrt{s} = 13$ TeV is interpreted.

Before injection into the LHC, the hadrons pass through a pre-accelerator chain, as shown in Fig. 2.1. First, the valence electrons are stripped off from the hydrogen atoms and the remaining protons are collected and accelerated up to 50 MeV in the Linear Accelerator 2 (LINAC2). They are subsequently injected into the Proton Synchrotron Booster (PSB), the first of a serie of three circular pre-accelerators, that increase their energy up to 1.4 GeV. The other two accelerators, the Proton Synchrotron (PS) and the Super Proton Synchrotron (SPS), boost the protons to energies of 25 GeV and 450 GeV respectively. The protons are organised in bunches containing 1.1×10^{11} particles with a time spacing between two consecutive bunches down to 25 ns. The protons are then injected into the LHC ring where they are accelerated to the designed centre-of-mass energy by sixteen 400MHz superconductive radio frequency (RF) cavities. This system accelerates the beams through oscillating electromagnetic fields; the cavities are operated at a temperature of 4.5K and a potential of 2 MV. The accelerating field within the cavities is 5 MV/m. The proton beams are kept confined in the LHC ring through the use of 1232 superconducting dipole magnets. Each magnet is kept at a temperature of 1.9K and is operated with a current nominally (for 14 TeV) of 11700 A, producing a magnetic field of 8.3 T. Additional 392 quadrupole magnets are installed in order to stabilise and focus the particle beams.

The proton beams cross each other in four straight sections of the LHC ring, where particle detectors are placed in order to study the products of the collisions. ATLAS [92] is a general purpose experiment designed to primarily study the Electroweak Summetry Breaking and the Higgs Mechanism, precisely measure the SM parameters and look for new physics beyond the SM. ATLAS shares its location with LHCf, an experiment dedicated
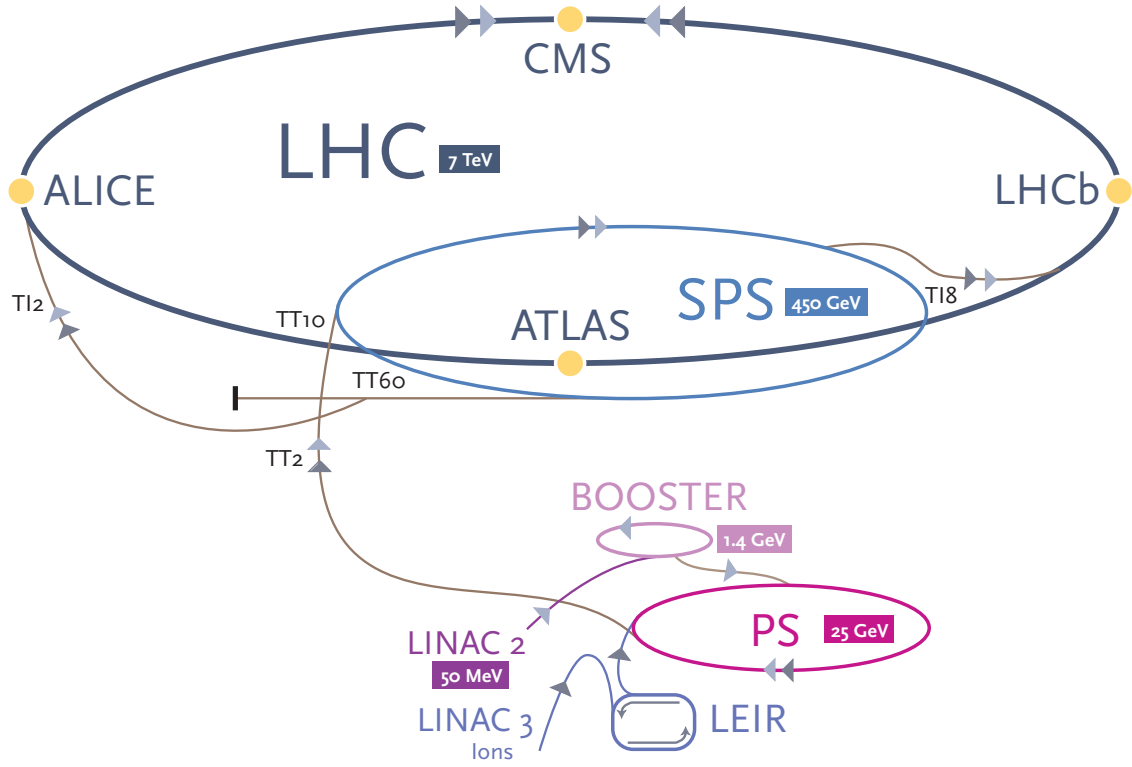
Figure 2.1: The CERN accelerator complex.

to the measurement of the forward production of neutral particles in $p - p$ collisions.

2.1.2 Luminosity

The LHC event production rate is given by $n = L \cdot \sigma$, with σ being the production cross section of a particular process, depending on the centre-of-mass energy, and L being the instantaneous luminosity. The latter depends only on the beam parameters and, assuming a Gaussian beam distribution, can be written as [93] :

$$L = \frac{N_p^2 n_b f_{\text{rev}}}{4 \epsilon_n \beta^{IP}} F \tag{2.1}$$

where N_p is the number of particles per bunch, n_b is the number of bunches per beam, f_{rev} is the revolution frequency, ϵ_n is the normalised transverse beam emittance, β^{IP} is the beta function[1] at the interaction point and F is a luminosity reduction factor due to the geometry of the beams at the crossing point. This factor is defined, in Gaussian approximation of the beam distribution, as

$$F = \left(1 + \left(\frac{\theta_c \sigma_z}{2 \sigma_T} \right)^2 \right)^{-\frac{1}{2}} \tag{2.2}$$

---

[1]The beta function is defined as $\beta^{IP} = \pi \sigma_T^2 / \epsilon_n$, where σ_T is the transverse size of the beam, and represents the beams focusing at the interaction point.

Parameter	2012	2015	Design
Maximum centre-of-mass energy [TeV]	8	13	14
Peak Intantaneous Luminosity [10^{33} cm^{-2}s^{-1}]	7.73	5.02	10
Delivered Integrated Luminosity [fb^{-1}/year]	23.1	4.2	80-120
ATLAS recorded Integrated Luminosity [fb^{-1}/year]	21.7	3.9	-
Maximum number of colliding bunches	1380	2232	2808
Minimum bunch time spacing [ns]	50	25	25
Typical number of protons per bunch [$\times 10^{11}$ protons]	1.6	1.21	1.15
Average number of interactions $\langle \mu \rangle$	20.7	13.6	19.0

Table 2.1: LHC parameters during the proton-proton collisions data taking of 2012 and 2015, corresponding to the datasets analysed in this document. The parameters showing the best achieved performance for that year are taken from [98] and are compared to the design parameters extracted from [99].

where θ_c is the beams crossing angle, σ_z is the longitudinal bunch length, and σ_T is the transverse size of the beam. The total number of generated events is given by integrating the production rate over time. The integrated luminosity, defined as $\mathcal{L} = \int L \mathrm{d}t$, is commonly expressed in inverse barns (1 barn $= 1$b $= 10^{-28}$m^2). In Fig. 2.2a and Fig. 2.2c the integrated luminosities delivered by the LHC machine and recorded by ATLAS during stable beams proton-proton collisions for 2012 and 2015 are shown.

The events of interest at the LHC for searches for physics beyond the SM, come from the hard scattering of two protons. However during each bunch crossing a variable number of inelastic $p - p$ collisions, called *in-time* pileup[2] events take place, following a Poisson distribution with the mean value μ calculated as:

$$\mu = \frac{L\sigma_{\mathrm{inel}}}{n_b f_{\mathrm{rev}}} \tag{2.3}$$

where σ_{inel} is the total inelastic proton-proton cross section. The theoretical cross section obtained by PYTHIA [94, 95] is 73 mb for $\sqrt{s} = 8$ TeV and 78.4 mb for $\sqrt{s} = 13$ TeV. The measured value of the cross section is 74.7 ± 1.7 mb at $\sqrt{s} = 8$ TeV obtained by TOTEM [96], while ATLAS measures 73.1 ± 7.7 mb by using an extrapolation of the fiducial measurement in the acceptance of the forward scintillators [97]. In Fig. 2.2b and Fig. 2.2d the luminosity weighted distributions of the mean interactions per bunch crossing for 2012 and 2015 data taking respectively are shown. In Table 2.1 the main LHC parameters recorded during stable beam data acquisition are reported, comparing them to the design values.

2.2 The ATLAS detector

The ATLAS experiment investigates a broad range of particle physics phenomenology. In particular, its aim is to reveal the presence of new physics as well as precisely measuring the Standard Model parameters. The ATLAS detector, shown in Fig. 2.3, has a cylindrical

---

[2]There is a second type of pileup events, the *out-of-time* pileup, originating from the interactions in neighbouring bunch-bunch crossings and contributing to the detector occupancy.

(a)

(b)

(c)

(d)
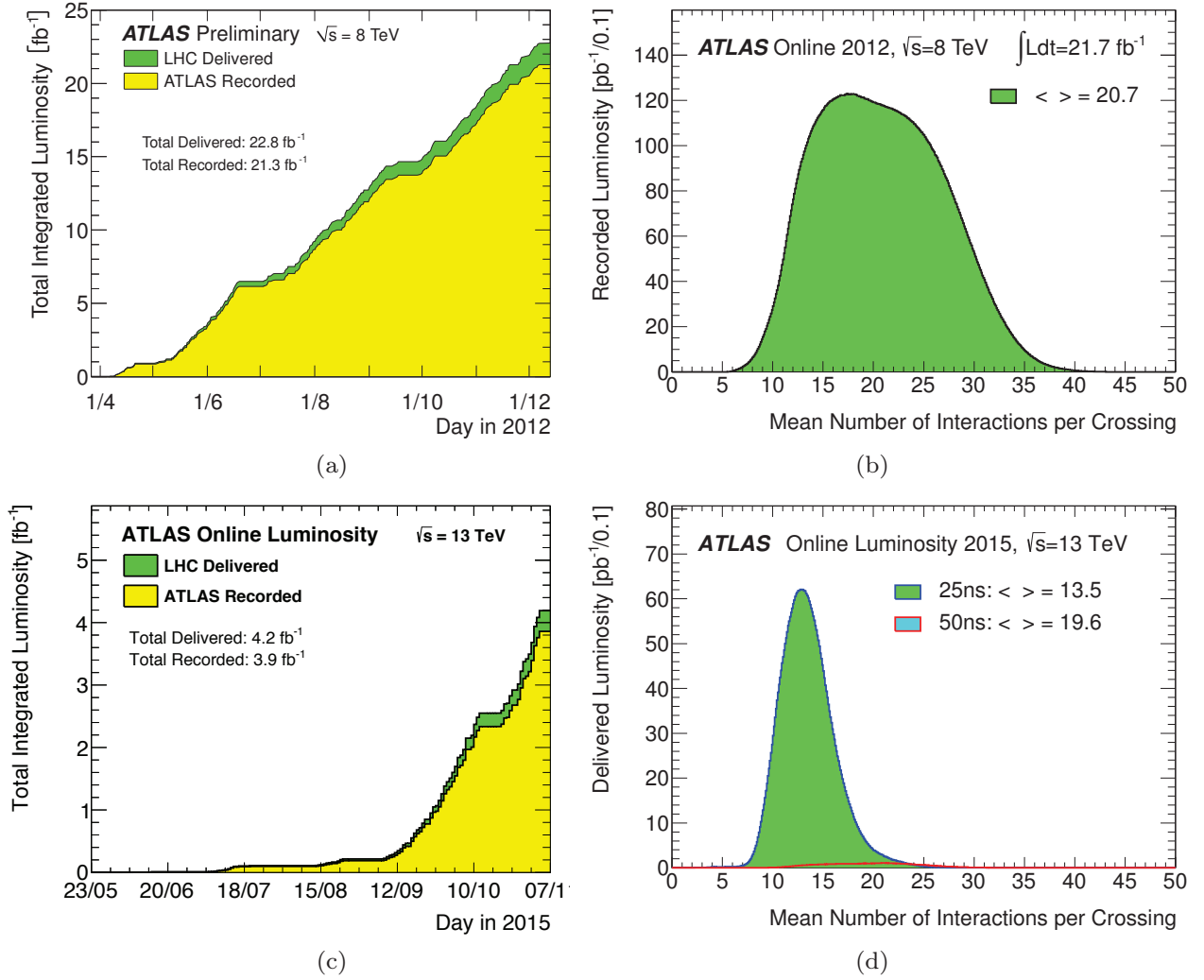
Figure 2.2: Delivered and recorded integrated luminosity in the ATLAS experiment versus operation day for the 2012 (a) and 2015 (c) $p-p$ collisions during stable beams condition. The ATLAS recorded (b) and delivered (d) integrated luminosity versus the mean number of interactions per crossing for 2012 and 2015 is shown, respectively. The value of the total integrated luminosity and the average $\langle\mu\rangle$ are given in the figures. The mean number of interactions per crossing are calculated as the mean of the Poisson distribution of the number of inelastic interactions per bunch crossing. Figures taken from [98].

shape around the beam pipe, it is centred around the crossing point of the beams and it has a forward-backward symmetry with respect to the interaction point. An almost full coverage of the solid angle around the interaction point is achieved thanks to a various set of sub-systems organised in layers, in order to capture essentially all the detectable particles produced in $p-p$ and heavy ions collisions. Starting from the sub-system closer to the LHC beam pipe, the ATLAS detector is composed of an Inner Detector (ID), embedded in a 2T axial magnetic field, the Electromagnetic Calorimeter (ECal), the Hadronic Calorimeter
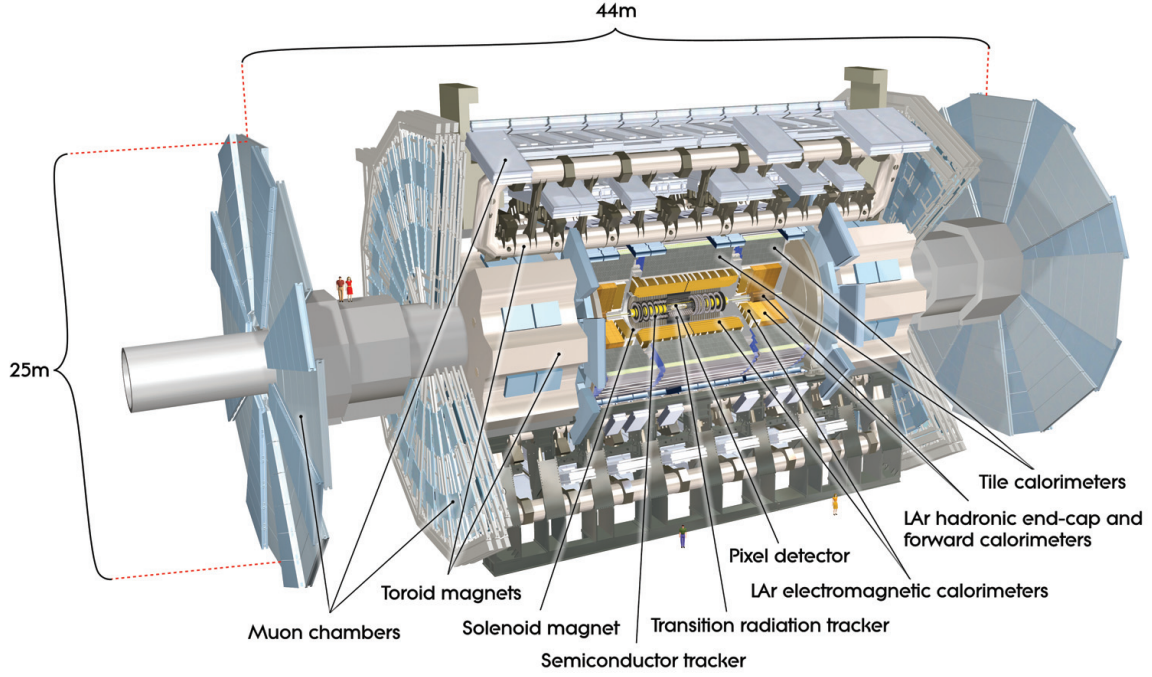
Figure 2.3: Computer generated image of ATLAS, showing the various sub-systems and the size of the whole detector. The figure is taken from [92].

(HCal) and the Muon Spectrometers, surrounded by three toroidal magnets. These subsystems are described in the following sections of this Chapter, concentrating primarily on the Inner Detector details. The upgrade performed on the ATLAS detector during the Long Shutdown One (LS1), that took place between the Run1 and Run2, are also discussed with particular focus on the description of a new Pixel layer: the Insertable B-Layer (IBL).

2.2.1 Coordinate System

The ATLAS reference frame is a right-handed Cartesian coordinate system, where the origin is at the nominal p–p interaction point, corresponding to the centre of the detector. The positive x-axis points to the centre of the LHC ring, the positive y-axis points upwards and the positive z-axis points along the beams direction. Justified by its rotational symmetry around the z-axis, the experiment uses a cylindrical coordinate system to describe the ATLAS detector itself and trajectories of the produced particles. The azimuthal angle $\phi \in (-\pi, \pi]$ is defined as the angle with the x-axis with $\phi = 0$ corresponding to the positive x-axis direction. The polar angle $\theta \in [0, \pi]$ is defined with respect to the z-axis with $\theta = 0$ corresponding to the positive z-axis direction. Instead of the θ angle, the pseudorapidity $\eta = -\ln \tan(\theta/2)$ is used to indicate the polar direction of the particles, with the advantage that differences in this quantity are invariant under Lorentz boosts along the z-axis[3].

---

[3]For massive objects as jets, the rapidity $y = \frac{1}{2} \ln \left(\frac{E+p_z}{E-p_z} \right)$ is used. For massless objects the two formulas are equivalent.

Angular distances between two objects are expressed in terms of $\Delta R = \sqrt{(\Delta\phi^2 + \Delta\eta^2)}$. Of particular importance in the description of the kinematics of the events, is the plane transverse to the beam direction (x–y) where the transverse momentum $p_T = p\sin\theta$ and the missing transverse momentum $E_{\mathrm{T}}^{\mathrm{miss}}$, are calculated.

2.2.2 Inner Detector

The ATLAS Inner Detector [101, 102] provides efficient and robust track reconstruction of the charged particles produced by the LHC collisions. It consists of three sub-detectors: a Pixel detector, the Semiconductor Tracker and the Transition Radiation Tracker. The Pixel and SCT are silicon detectors using different technologies, pixels and micro-strips, respectively. The TRT, a drift chamber composed of gas-filled straws[4] is located in the outer part of the ID volume. The three sub-systems provide a full coverage in ϕ and up to $|\eta| \leq 2.0$, while the two silicon detectors alone cover up to $|\eta| \leq 2.5$. The sub-detectors are organised in a barrel, formed by separated layers of increasing radius, and two end-caps. The Pixel and SCT end-caps are formed by disks, while the TRT end-caps are split into separated wheels. A 3D visualisation of the structure of the ID is shown in Fig. 2.4. The ID volume is embedded in a 2T axial magnetic field generated by a superconducting solenoidal coil. During the Long Shutdown after the 8 TeV run in 2013-2014 , a number of upgrades have been performed for the ATLAS ID. The Pixel detector was extracted from the detector and brought above ground, where several service systems and sensitive modules have been refurbished. The beam pipe itself was replaced by a new one with a smaller radius and on the new beam pipe a silicon pixel detector, the Insertable B-layer [103] was mounted, reducing the distance of the first sensitive layer to the interaction point from 5 cm to 3.3 cm. The insertion of the IBL has several purposes, e.g. the better determination of the track impact parameters due to a closer positioning from the interaction point and the maintenance of high tracking performance in the case of failures of some modules of the B-Layer, the former innermost pixel layer (see Sec. 2.2.2).

The search for supersymmetric scalar top quarks presented in this document is characterised by the presence of objects such as hadronically decaying tau leptons, electrons, muons and jets originating from b-quarks. The Inner Detector plays a fundamental role in providing accurate information on the above mentioned objects. In particular, hadronic tau decays are efficiently separated from jets combining tracking information, such that the precise measurement of their decay length, impact parameter significance and number of tracks associated to the decay, with calorimetric measurements using a multivariate technique. For events where the τ leptons decay leptonically in electrons and muons, highly efficient identification of those particles is required, as well as an accurate measurement of their transverse momenta. The decays of heavy flavour hadrons in jets are distinguished from the decays of light flavour hadrons through the precise evaluation of the transverse impact parameters of tracks within the jet cone and the position of secondary vertices. The ATLAS Inner Detector is constructed to fulfil these requirements.

In Table 2.2 the main characteristics and the intrinsic resolution[5] of the sub-detectors

---

[4]In Run-1 the TRT was filled with a Xenon mixture gas, while in the first part of Run-2 some parts of the detector were filled with an Argon based mixture.

[5]The intrinsic resolution refers to the pitch size divided by $\sqrt{12}$. Refined clustering algorithms can be
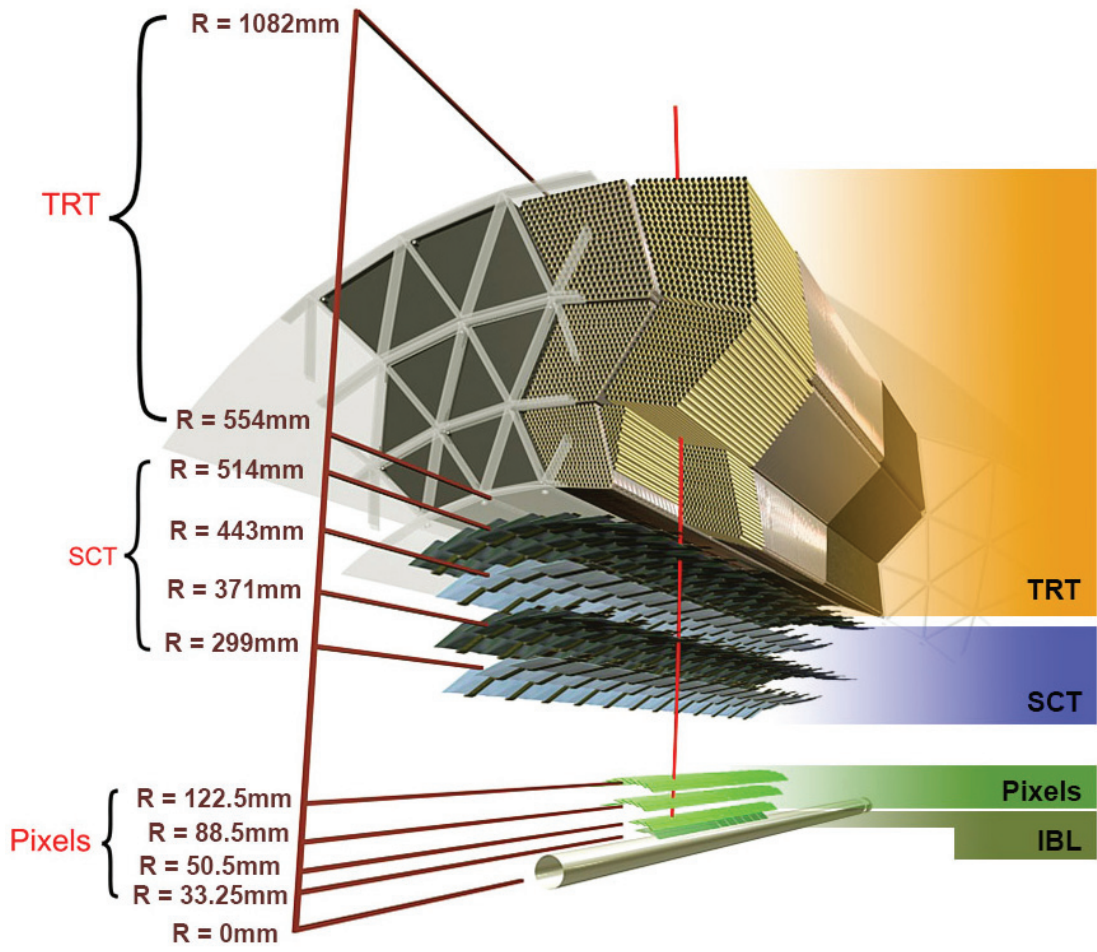
(a)
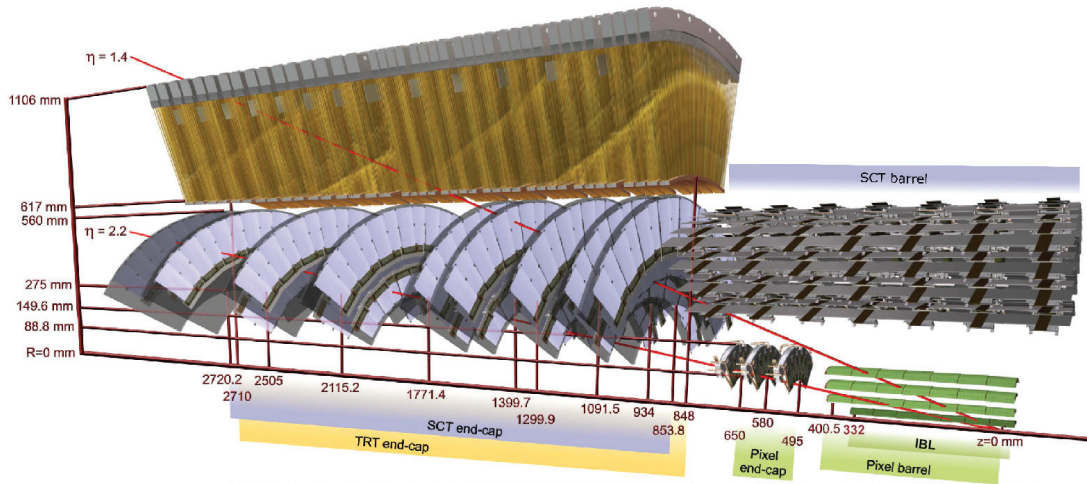
(b)

Figure 2.4: A 3D visualisation of the structure of the barrel (a) and the endcap (b) of the Inner Detector. In the picture the beam pipe, the IBL, the Pixel layers, the Semiconductor Tracker and the Transition Radiation Tracker are shown [92, 100].

composing the ATLAS ID are summarised. A description of the tracking algorithms used for the reconstruction of the trajectories of the charged particles is given in Chapter 3, together with an extensive description of the alignment techniques used to precisely determine ID geometry.

Subdetector	Element size	Intrinsic resolution [μm]	Radius barrel layers [mm]
IBL	$50\,\mu$m$\times 250\,\mu$m	8×40	33.2
Pixel	$50\,\mu$m$\times 400\,\mu$m	10×115	50.5, 88.5, 122.5
SCT	$80\,\mu$m	17	299, 371, 443, 514
TRT	$4\,$mm	130	from 554 to 1082

Table 2.2: Some basic characteristics of the ID subdetectors. The intrinsic resolution of the IBL and the Pixel detector is reported along r–ϕ and z, while for the SCT and the TRT it is reported only along r–ϕ. For SCT and TRT the element sizes refer to the spacing of the readout strips and the diameter of the straw tubes, respectively. The values for the Pixel, SCT and TRT are extracted from [92], while those for the IBL are taken from [103].

Pixel detector

The Pixel detector consists of 1744 silicon pixel modules arranged in three barrel layers and two end caps with three disks each. The barrel layer closest to the beam line is called *Pixel B-Layer*, while the outer layers are called *Layer-1* and *Layer-2*. The pixel modules are formed by 16 front-end (FE) chips, each one with 2880 read-out channels and a n-type pixel sensor with a thickness of 250 μm and a size of 50×400 μm^2. The intrinsic hit resolution of each module is 10 μm in the transverse direction and 115 μm in the longitudinal one, i.e. z and r for the barrel and end-caps respectively.

In Run-2 the instantaneous luminosity is expected to exceed 2×10^{34} cm^{-2} s^{-1} causing more radiation damage to the Pixel detector and a higher number of pileup events, implying a degradation of the accuracy of the measurements of the impact parameters and a decrease of the hit reconstruction efficiency due to the saturation of the data transmission. For these reasons, the Pixel Detector has been dismounted from its location and equipped with the new Service Quarter Panel (nSQP) during the LS1 [104, 105]. This permitted to repair the problems appeared during Run-1, reducing the fraction of dead modules from 5% at the end of Run-1 to 1.9% and to double the speed of the data transmission via optical fibers for the second layer. The Pixel Detector in Run-2 has also been upgraded to a four layer sub-system with the addition of a new innermost layer closer to the beam pipe, called the Insertable B-Layer, described in detail in Section 2.2.3.

---

used to improve the spatial resolution of the sensitive modules

Semiconductor Tracker

The SCT consists of 4088 silicon micro-strip modules, arranged in four barrel layers and two end caps with nine disks each, for a total of 6.3 million readout channels. The barrel modules have a rectangular shape with an area of 64.0×63.6 mm^2 housing 768 strips with a pitch of 80 μm, while the ones mounted on the end-caps are radially fanned out and have a trapezoidal shape with a pitch size variable from 56.9 μm to 94.2 μm. The SCT modules are formed by up to four strip sensors that are glued back to back with a stereo angle of 40 mrad in order to obtain information on the z-coordinate along the strip length and provide a 3D measurement in space. The intrinsic resolution of the SCT modules is of 17 μm in the transverse direction in the barrel and 580 μm in the longitudinal direction.

In order to cope with the increase in the expected luminosity of Run-2, during LS1 the number of SCT Read-Out Drivers[6] (RODs) was increased from 90 to 128, and the mapping between RODs and the modules was re-optimised, ensuring the data transfer rate required by the trigger rate [106].

Transition Radiation Tracker

The TRT is the outermost of the ID sub-detectors and is made of 350848 straws filled with a $Xe/CO_2/O_2$ gas mixture (70/27/3) covering up to $|\eta| \leq 2.0$. The tubes are 4 mm in diameter and have a 31 μm diameter gold plated tungsten wire as anode. The straws are placed parallel to the beam line and organised in 73 modules of length 144 cm and interleaved with polypropylene fibres in the barrel, while they are arranged radially in the end caps and organised in 160 layers interleaved with polypropylene foils. The signal on each wire is amplified and discriminated against two adjustable thresholds, named low- and high-thresholds, to simultaneously provide hits for tracking information and particle identification. In fact, relativistic charged particles traversing the dielectric material embedding the tubes produce transition radiation (TR) photons that are absorbed by the TRT gas mixture producing high-threshold hits. Since the amount of transition radiation depends of the Lorentz factor γ of the particles, the amount of high-threshold hits along the track trajectory provides discrimination power for separating electron tracks from hadronic tracks. This sub-detector compensates the lower number of read-out channels with respect to the silicon sub-detectors with a larger number of hits, in average 34 in the $|\eta| < 1.7$ region, and larger trajectories that contribute to the track transverse momentum measurement resolution. The TRT provides only a 2D hit information along $r - \phi$ with an intrinsic resolution of about 130 μm.

2.2.3 The Insertable B-Layer

The IBL [103] is the fourth and innermost layer of the ATLAS Pixel Detector that has been inserted between the Pixel B-Layer and the new beam pipe. It is formed by 14 staves that ensure a full hermetic coverage in ϕ with an overlapping angle of 1.82 degrees, and a total length of $z = 72.4$ cm. Due to spatial constraints, the IBL modules are not tilted

---

[6]See Section 2.3

Figure 2.5: *top*: Transverse view of the design of the IBL detector transverse section. The figure has been taken from [103] *bottom*: Design of an IBL stave showing the positions in *z* of the planar modules and of the 3D ones. The figure has been taken from [107]. Distances are expressed in mm.

along the *z* direction. Therefore, there is no overlap in η contrary to the other Pixel layers. The staves are attached to the Inner Positioning Tube (IPT) by two mounting points and are constrained to each other via a central ring which is placed in the middle of the stave. Further details on the mechanical layout of the stave structure will be discussed in the next section.

On each stave a total of 20 modules with two different silicon technologies are mounted: the central 12 modules use planar silicon sensors while 4 modules on each side of the staves mount 3D pixel sensors [108] as depicted in Fig. 2.5 (*bottom*), for a total of 12M pixels. Each stave has in total 32 new generation IBM C-MOS FE-I4 front-end chips, two for the planar modules and one for the 3Ds modules, which are connected to the readout service bus, referenced as Stave Flex and mounted on the side of the stave opposite to the sensitive surface. The IBL detector uses a CO_2 cooling system [109] due to the gas capability of high heat transfer and low material budget, which is fundamental to reduce multiple coulomb

scattering effects on tracking. The cooling system, originally designed at Nikhef, can take 1.5 kW of heat away, providing a very stable detector operation temperature between $+20°C$ and $-40°C$.

The main purpose of the IBL is to provide tracking performance robustness against the increase of luminosity of the LHC during Run-2, it is planned to operate up to the full ATLAS tracker upgrade planned for the high luminosity LHC in 2024-2026. Thanks to this new pixel layer, the Run 2 tracking performance exceeds the one of Run-1 in terms of reconstructed track accuracy, primary and secondary vertex reconstruction efficiency and fake tracks reduction[7].

2.2.4 Brief description of IBL staves and conditions monitoring

A detailed description of the material composing the IBL staves and their design is given in [103]. This section wants to just give a qualitative overview of the IBL mechanical structure and properties, in order to introduce the results presented in Chapter 5. As shown in Fig. 2.6, each stave is made of carbon foam with an outer shell of carbon finer laminate and has a triangular cross section with at the centre the titanium cooling pipe. The readout service bus, hereafter referred as *stave flex*, is glued on the back of one of the sides while the pixel sensors are glued on the basis of the stave. The staves are fixed on the IPT at both ends with two different fixation mechanisms, shown in Fig. 2.7. For the C-side, the position of the stave is fixed to the IPT using a screw, while for the A-side it is held by a pin inserted in a larger rectangular hole, allowing it to move in the z-direction by ±0.5mm. This flexibility is justified in order to absorb potential displacement or manufacturing uncertainty of the staves. Finally, the middle-stave ring constrains radial displacement of the staves but allows for movements in the azimuthal direction. The assembly of the staves took place at room temperature and metrology studies are performed to asses their shape and actual positioning of the modules [110], but the evaporation of the coolant can take place at temperatures as low as $-40°C$, meaning that the stave structure is subject to a thermal load of up to $-60°C$. The different materials composing the staves have different *Coefficients of Thermal Expansion* (CTE) and such mismatch has a significant impact on the stresses induced when the staves are cooled down. The CTE mismatch between the materials, together with a non-uniform stave cross section, could lead to deformations of the stave. For example, the CTE mismatch between the cooling pipe and the carbon foam induces a bowing in the vertical plane as discussed in [103]. Another significant CTE mismatch is between the carbon foam and the polyimide-copper-aluminium stave flex and its consequences are summarised in the following sections and publicly reported in [111]. The IBL staves are very high technology structures and their conditions are monitored closely by the Detector Control System (DCS) [112], which provides constant read-out of the Inner Detector status in terms of temperature, power consumption, low and high voltage of the sensitive elements and other important conditions. For the IBL staves three different temperatures can be defined:

- **Cooling pipe temperature:** This is the CO_2 cooling temperature. It is monitored by DCS both at the inlet, where the liquid CO_2 is injected in the pipe, and at the out-

---

[7]For a detailed description of the ATLAS ID Tracking performance, see Section 3.1
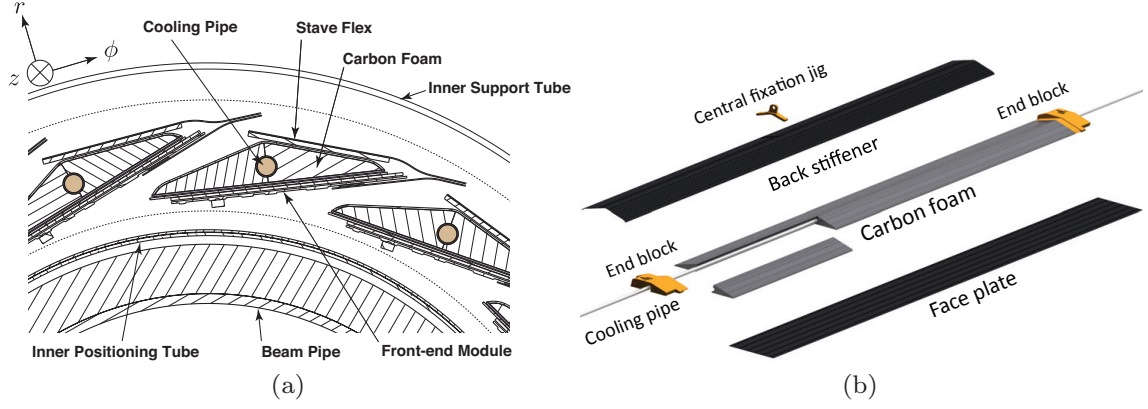
Figure 2.6: Cross section of the IBL Layout (a) and schematic representation of the composition of a stave (b).
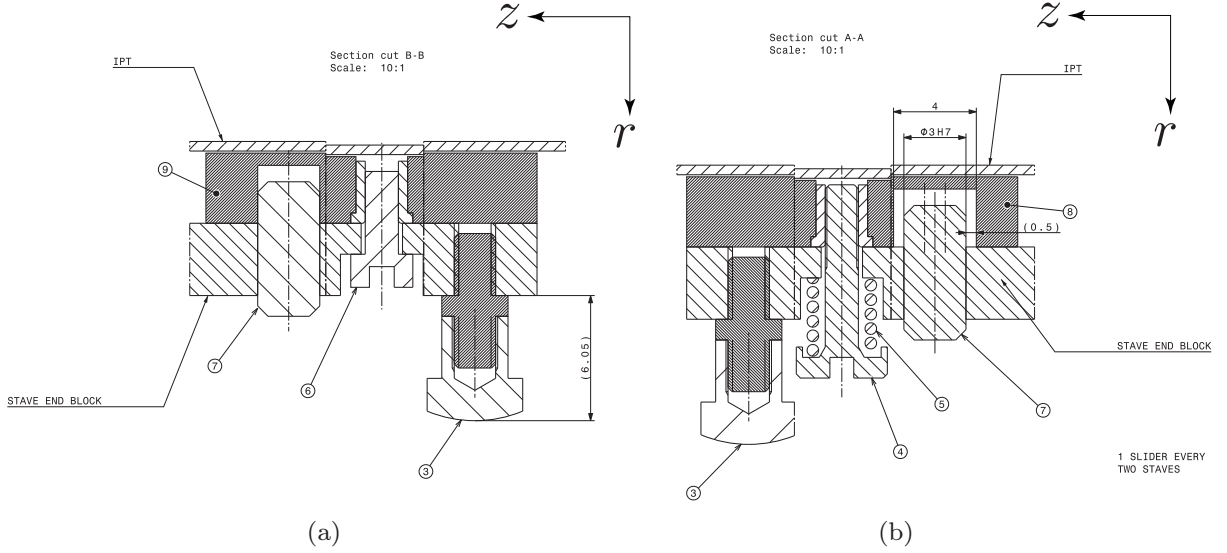
Figure 2.7: IBL stave fixation mechanism for the positive z direction side (A-side) (a) and the negative z direction side (C-side) (b).

let, where the bi-phase system is full established. Here after, the *set-point temperature* T_{set} indicates the outlet reading, more representative of the stave temperature

- **Module temperature:** Each module has a sensor to check for temperature changes. The module temperature T_{mod} strongly depends on the power consumption which varies with the total ionisation dose deposited during data taking. Even in absence of collisions, the module temperature is higher with respect to the set point temperature due to the powering system.

- **Stave Flex temperature:** This is the temperature at the stave flexible bus T_{flex} which is the most representative temperature of the stave, it is not directly monitored by the DCS system and it is correlated to the T_{mod} and T_{set}. Considering a
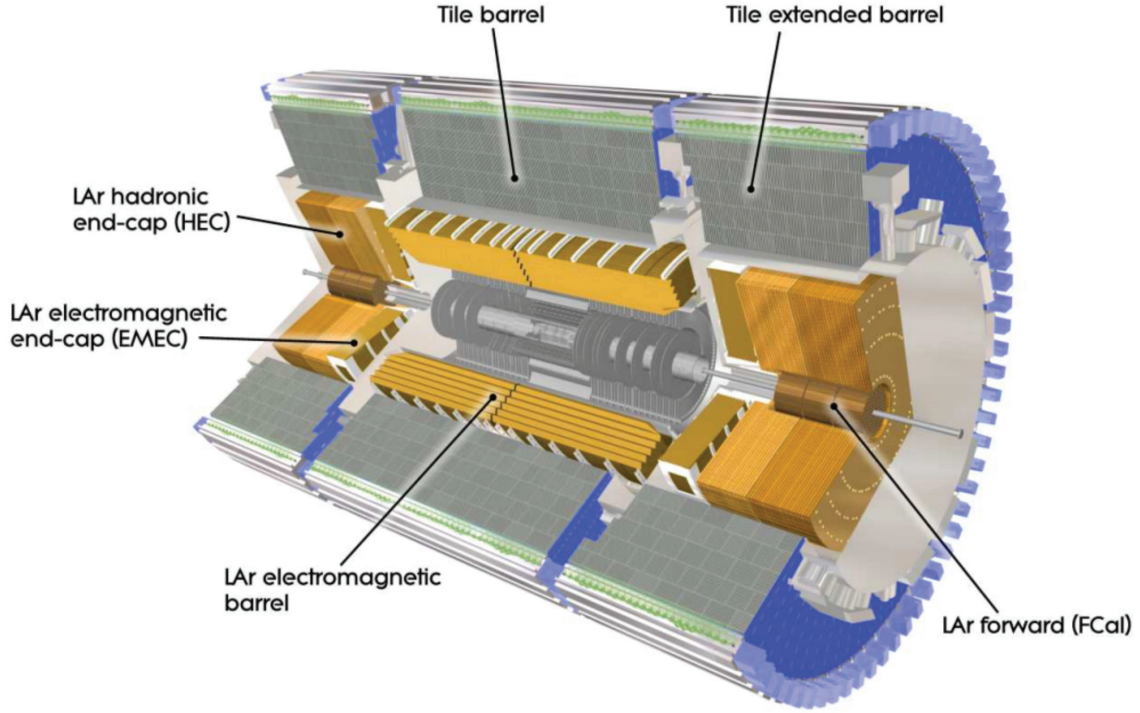
Figure 2.8: Cut away view of the ATLAS calorimeter system [92]

stave as a very simple 1-dimensional static thermo-conducting system and the power consumption at the modules proportional to the power consumption of the stave flex, is possible to express T_{flex} as:

$$T_{\text{flex}} = (1 - k)T_{\text{set}} + kT_{\text{mod}} \tag{2.4}$$

where k is a constant parameter that is determined by the thermal coupling inside the stave and evaluated through a Finite Element Analysis (FEA) simulation (see Sec. 5.3.2).

In the following sections the temperatures considered are either the T_{set} or the T_{mod} since these are the ones directly and precisely monitored by the DCS system.

2.2.5 Calorimeters

The calorimeter system is placed outside the volume of the Inner Detector and the solenoid. It consists of an inner high granularity liquid-argon (LAr) electromagnetic (EM) calorimeter [113] and an outer hadronic sampling calorimeter [114], as shown in Fig 2.8. The calorimeters are separated in barrel, end-cap and forward structures covering a pseudo-rapidity region up to $|\eta| < 4.9$, with a transition region between $1.37 < \eta < 1.52$. The central EM calorimeter has a finer $\eta - \phi$ segmentation with respect to the hadronic one and the end-caps regions in order to provide a precise measurement of the energy deposit of electrons and photons.
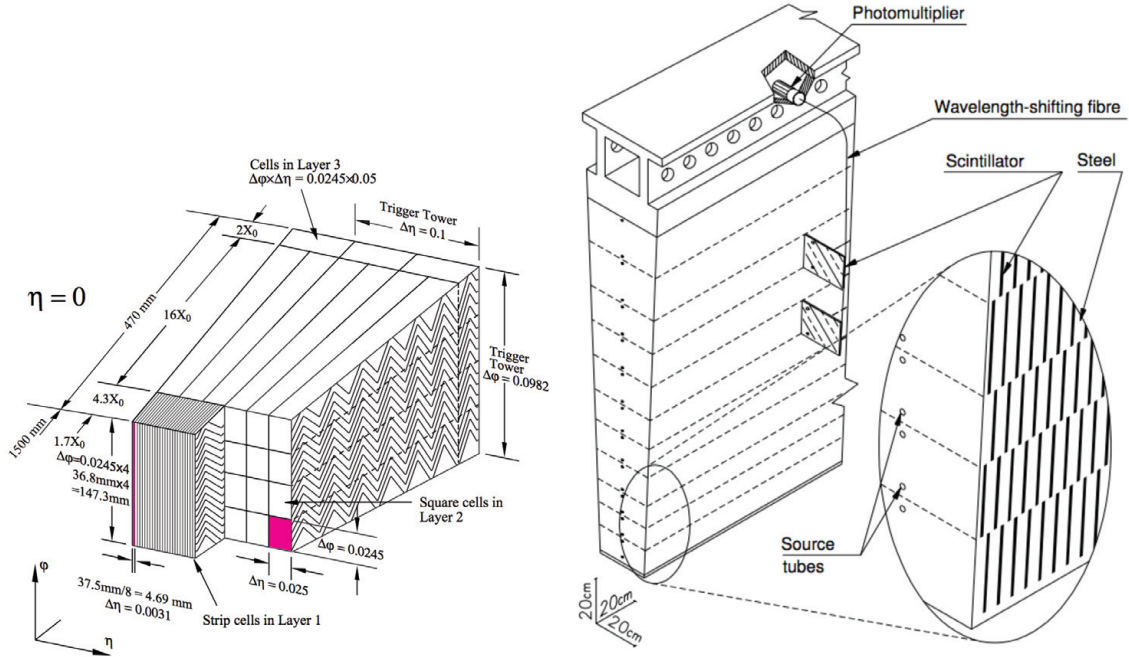
Figure 2.9: Schematic drawing of an ECAL module (*left*) and of a HCAL module (*right*).

Electromagnetic Calorimeter

The electromagnetic calorimeter (ECAL) is a lead-Liquid Argon (LAr) sampling detector with accordion-shaped electrodes and lead plates with thickness and size varying with η in order to provide precise energy measurement. Such a geometry provides a full coverage in ϕ without any cracks and a fast signal extraction from the electrodes. The design energy resolution of the ECAL is $\sigma_E/E = 9\%/\sqrt{E} \oplus 0.3\%$. The ECAL is organised in a barrel, composed of two identical structures separated by a gap of 4 mm at $z = 0$ and covering up to $|\eta| < 1.5$, and two end-caps, each one divided into two co-axial disks covering the region $1.32 < |\eta| < 3.2$. Both of the structures are equipped with LAr presampler detectors [115] in order to provide shower sampling and better energy resolution.

The ECAL barrel modules are constituted by three layers, as shown in Fig. 2.9. The first layer is around 4 radiations length (X_0) deep but has a very fine fragmentation in $\Delta\eta \times \Delta\phi = 0.003 \times 0.1$, in order to provide precise measurement of the energy deposited by electrons and photons used as input for their identification. The middle layer of the module is about 16 X_0 deep, accounting for most of the thickness of the calorimeter and absorbing most of the EM showers. It has a granularity of $\Delta\eta \times \Delta\phi = 0.025 \times 0.025$. The last layer is only 2 X_0 deep and is designed to collect the tail of the EM showers in the calorimeter, therefore has a broader segmentation of $\Delta\eta \times \Delta\phi = 0.05 \times 0.025$. The end-cap modules have an accordion geometry, three longitudinal layers and similar thickness in terms of radiation length as the barrel ones.

Hadronic Calorimeter

The HCAL is placed outside the volume of the ECAL and consists of different sampling calorimeters following different technologies according to the physics performance requirements as a function of the pseudorapidity.

- The *Tile sampling calorimeter* consists of a central barrel structure covering the region $|\eta| < 1.0$ and two extended barrels that cover the region $0.8 < |\eta| < 1.7$ and it's composed of a steel absorber combined with scintillating tiles as active material. The signal from the scintillating tiles is read out by wavelength shifting fibres and directed to photomultipliers that convert the light into current pulses, as shown in Fig. 2.9 (right). Similar to the structure of the ECAL, the tile sampling calorimeter is composed of modules segmented in three layers with different thickness of approximately 1.5, 4.1 and 1.8 interaction lengths (λ_I) for the central barrel and 1.5, 2.6 and 3.3 λ_I for the extended barrel.

- The *LAr hadronic end-cap calorimeter* (HEC) is made of two independent wheels covering the region $1.5 < |\eta| < 3.2$. Each wheel is divided into four layers in depth and is built from 32 wedge-shaped modules, formed by absorbing copper plates interleaved with 8.5 mm LAr gaps as active material.

- The *LAr forward calorimeter* (FCal) is composed of two end-caps made of three modules each: the first uses copper as absorber, for more precise EM energy deposit measurements, while the other two use tungsten and are optimised for hadronic interactions. All three modules use LAr as active material and the total depth of each end-cap is about 10 λ_I.

The design resolution of the HCAL is $\sigma_E/E = 50\%/\sqrt{E[\text{GeV}]} \oplus 3\%$ for the tile sampling calorimeter and the end-caps up to $|\eta| < 3.2$, while it is $\sigma_E/E = 100\%/\sqrt{E[\text{GeV}]} \oplus 10\%$ for the forward calorimeter.

2.2.6 Muon Spectrometer

The Muon Spectrometer (MS) [116] forms the outer part of the ATLAS detector as shown in Fig. 2.10, with the purpose to identify and measure the momenta of the muons that escape the calorimeter systems. Its central part is enclosed by the coils of three toroidal magnets, one for the barrel and one for each end-cap, that provide an azimuthal magnetic field with a bending power from 1.0 to 7.5 Tm, according to the $|\eta|$ region, within the MS volume. The design resolution of MS standalone muon transverse momentum measurement is $\sigma_{p_T}/p_T = 10\%$ at $p_T = 1$ TeV and muon candidates can be identified in the p_T range between 3 GeV to 3 TeV in the range $|\eta| < 2.7$.

The MS is formed by three barrel layers and six end-cap disks mounting fast triggering chambers, the *Resistive Plate Chambers* (RPC) and the *Thin Gap Chambers* (TGC), and precision tracking chambers, the *Monitored Drift Tubes* (MDT) chambers and the *Cathode Strip Chambers* (CSC). Similar to the ID, the design resolution is achieved trough
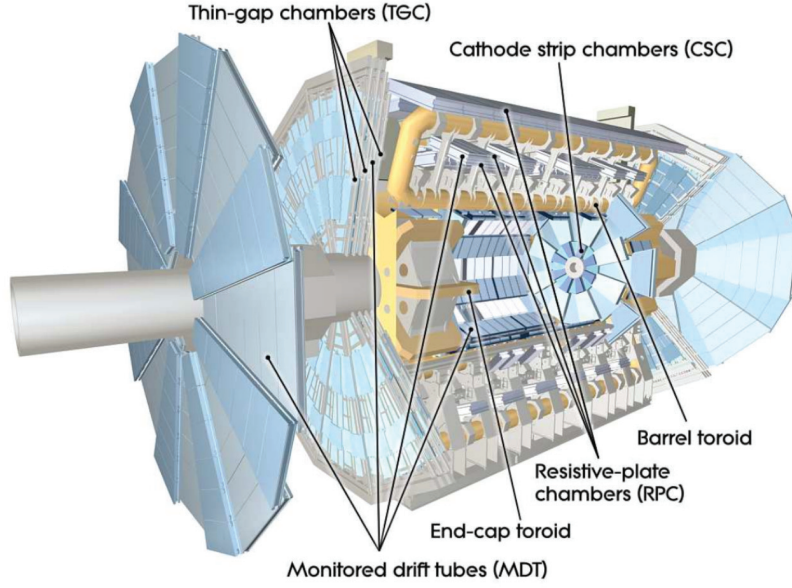
Figure 2.10: Cut away schematic view of the ATLAS Muon Spectrometer

an accurate measurement of the sensitive element positions through the combination of high-precision laser based alignment and track-based alignment algorithms.

Precision Tracking Chambers

The majority of the precision tracking chambers are constituted by MDT chambers that cover the range up to $|\eta| < 2.0$. The sensitive element is an aluminium tube with a diameter of 30 mm and a length that ranges between 1 m and 6 m filled with an Ar/CO_2 gas mixture (93/7) with a tungsten-rhenium anode $50\mu m$ of diameter. The tubes provide a 2D measurement in the plane transverse to the tube, with a single hit resolution of 80 μm. In order to improve the accuracy, each chamber is made of three to eight layers of drift tubes. In the range $2.0 < |\eta| < 2.7$, the MS is equipped with CSCs with finer granularity, higher acceptance rate and time resolution to cope with the larger number of traversing particles. The CSCs are wedge-shape multi-wire proportional chambers filled with an Ar/CO_2 gas mixture (80/20) and equipped with two orthogonal cathode strips. They provide a 3D measurement with a resolution of 40 μm in the $r - z$ plane and 5 mm in the non bending plane.

Fast Trigger Chambers

The MS is equipped with a set of chambers aimed to provide complementary information to the precision tracking chambers, in particular measuring the coordinate of the track in the direction along the MDT tubes, to give information about the bunch crossing and to identify and to trigger on muons. The region $|\eta| < 1.05$ is equipped with three layers

of RPCs, while the end-caps $1.05 < |\eta| < 2.4$ contain four TGC stations. The RPCs are formed by two resistive plates separated by two insulating spacers that form a gap filled with $C_2H_2F_4$/Iso-C_4H_{10}/SF_6 (94.7/5/0.3) gas mixture and with two orthogonal copper strips as readout. The RPCs provide a 2D measurement in both the $\eta - \phi$ directions with a spatial resolution of ~ 10 mm and a time resolution of 1.5 ns. The TGCs are multi-wire proportional chambers with a reduced cathode-anode distance in order to give a very fast timing information. The TGCs provide a 2D measurement in both the radial direction and in the orthogonal one with a varying resolution of 2-7 mm and a drift time measurement with a resolution of 1.5 ns.

During the LS1 the MS design was completed adding a set of chambers in the barrel to end-caps transition region $1.0 < |\eta| < 1.4$. In order to improve the muon reconstruction efficiency of the MS with respect to Run1, four additional RPC-equipped MDT chambers have been placed inside the two elevator shafts, [8] and new MDT chambers have been equipped with smaller radius tubes.

2.3 Trigger system

The LHC event rate depends on the average number of proton-proton collisions per bunch crossing and on the bunch spacing. Under the 2012 LHC conditions, see Tab. 2.1, ATLAS was operating in a very high occupancy environment due to an interaction rate of around 400 MHz. These experimental conditions prohibit to record every single event on disk with the present technology, due to the current limitation in data transfer speed and data storage. The event recording rate is reduced to few hundred Hz through a trigger system that is designed to select only interesting events for ATLAS physics purposes. During Run I the trigger system was organised in three separated stages: Level 1, Level 2 and the Event Filter (EF). The Level 1 trigger is a hardware based system that uses a coarser information from the calorimeter system and from the trigger chambers of the MS and reduces the event rate to 75 kHz, with a processing time of 2.5 μs. The Level 1 selects a Region of Interest (RoI), defined as the $\eta - \phi$ region of the detector where the system identified interesting activity, including all the information regarding the selection criteria that have been satisfied. The RoI is then passed to the Level 2 trigger, a software based system that performs a partial event reconstruction through an analysis of all the available data with full granularity within the RoI, which corresponds to few percent of the full event detector information. The Level 2 is designed to reduce the event rate to approximately 3.5 kHz with a latency of 40 ms. The events that pass the Level 2 selection are then passed to the EF, which performs a full analysis of the event using procedures close to the offline reconstruction and reducing the event rate to 400 Hz, with a latency of 4 s.

During LS1, the ATLAS trigger system underwent a set of upgrades in order to cope with the increased detector occupancy due to higher centre of mass energy of the collisions and higher peak luminosity [117]. The Level 1 selection rules have been updated in order to maintain an output rate of 100 kHz and a latency of 2.5 μs through the raising of selection

---

[8]The elevator shafts are located in the feet of the ATLAS support structure, leading to holes in acceptance when not covered.

thresholds, adding hadronic or electromagnetic isolation requirements. In addition, a new Level 1 Topological Processor (L1Topo) has been introduced to allow further selection cutting on topological properties of the collision events. The Level 2 and EF farms have been merged into a single grid referenced as High Level Trigger (HLT) together with an update and optimisation of the selection algorithms to improve the use of the available computing resources. The final output rate during 2015 data taking was typically 1 kHz.

3 Event Reconstruction

The particles produced by proton-proton collisions in the LHC travel outwards through the ATLAS detector leaving different signatures in the various sub-systems. This raw information is collected and combined in order to identify the nature of the outgoing particles and measure their physical properties. The process of constructing *high-level objects*, such as tracks or particles candidates, from the digitised detector response is commonly referred to as *event reconstruction*. Particles that interact only weakly with the detector material, such as neutrinos, are not directly reconstructed in ATLAS, but their transverse momentum is inferred imposing the momentum conservation in the plane transverse to the beams direction, after the full reconstruction of the visible objects composing the event.

In this chapter, a brief description will be given of the reconstruction algorithms and techniques used to identify the objects used in the Inner Detector alignment studies, described in Chapter 5, and in the $\tilde{t} \to \tilde{\tau} b \nu_\tau$ search, detailed in Chapter 7. Since this thesis contains analyses on both the Run-1 and the Run-2 data, a brief overview of the improvements and the new algorithms used in Run-2 is discussed, focusing only on the physics objects used in the 2015 data analysis, such as tracks, vertices, electrons and muons candidates.

3.1 Tracks and Primary Vertices

The $\tilde{t} \to \tilde{\tau}$ analysis presented in this work makes direct use of electrons, muons, hadronically decaying tau leptons and jets. In order to identify these objects, the ATLAS detector relies on the Inner Detector (ID), described in Section 2.2.2, for the reconstruction of the trajectories of charged particles, the measurement of their transverse momentum and impact parameters, and the determination of the position of the hard scatter interaction.

This section aims to give a small description of the reconstruction procedures and algorithms used by the ATLAS tracking system, with particular focus on the comparison between Run 1 and early Run 2 performance.

3.1.1 Track Reconstruction

Due to the presence of the axial magnetic field along the z direction, charged particles originating from the proton-proton collisions follow helicoidal trajectories that can be parametrised by five parameters. The representation used by the ATLAS reconstruction is

$$\boldsymbol{\tau} = (d_0, z_0, \phi_0, \theta, q/p). \tag{3.1}$$

where d_0 and z_0 are the distances from the point of closest approach to a chosen reference in the transverse plane and along the z axis, respectively. The angles ϕ_0 and θ are defined
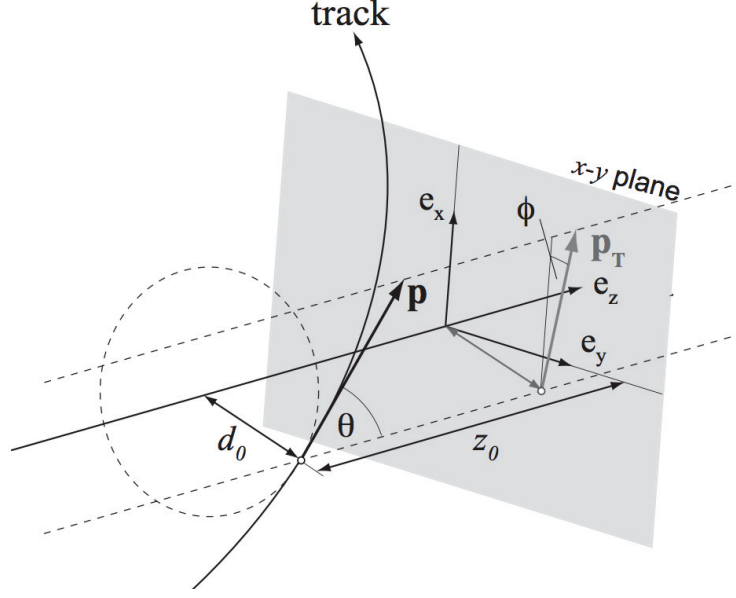
Figure 3.1: Graphical view of the track parameters at the perigee. Figure taken from [119].

as the azimuthal and the polar angle of the track at its perigee[1], respectively. Finally, the ratio q/p defines the orientation and the curvature of the helix trajectory. The charged particles trajectories are identified in the ATLAS ID using a set of local and global pattern recognition algorithms, referred to as New Tracking[118], aiming to reconstruct tracks originating from the proton-proton hard scatter (*primary tracks*), from the decays of long-lived particles (*secondary tracks*) and from the interaction of particles with the material (*conversion tracks*).

Primary tracks are defined as the trajectories of the charged particles with a mean lifetime greater than 3×10^{-11} s or originated by the decay products of particles with a shorter lifetime than this value. They are required to have a $p_T > 400$ MeV and are reconstructed in the region $|\eta| < 2.5$ using a *inside-out* algorithm. This algorithm starts with the identification of triplets of hits in separate layers of the silicon sub-detectors, commonly referred to as *seeds*. Starting from the seeds, measurements in the outwards layers of the silicon detector, that are compatible with the track hypothesis, are added through a combinatorial Kalman Filter [120, 121]. At this stage, a very loose track selection is applied and the hits can be associated with a large set of track candidates. This ambiguity is solved by a scoring algorithm [122] which assigns a weight to each track according to its basic properties as well as the number of *holes* and *shared hits* associated to it. Holes are defined as the sensor elements where a hit is expected by the track fit but none was registered. Shared measurements are defined as hits that are assigned to multiple track candidates. The tracking algorithms exploit a set of artificial neural networks to split the shared hits in the Pixel detector [123] and assign them to the different tracks, improving the track fit quality. Secondary and conversion tracks are then reconstructed using a

---

[1]In charged particles track reconstruction, the perigee is the point of closest approach of a reference point.
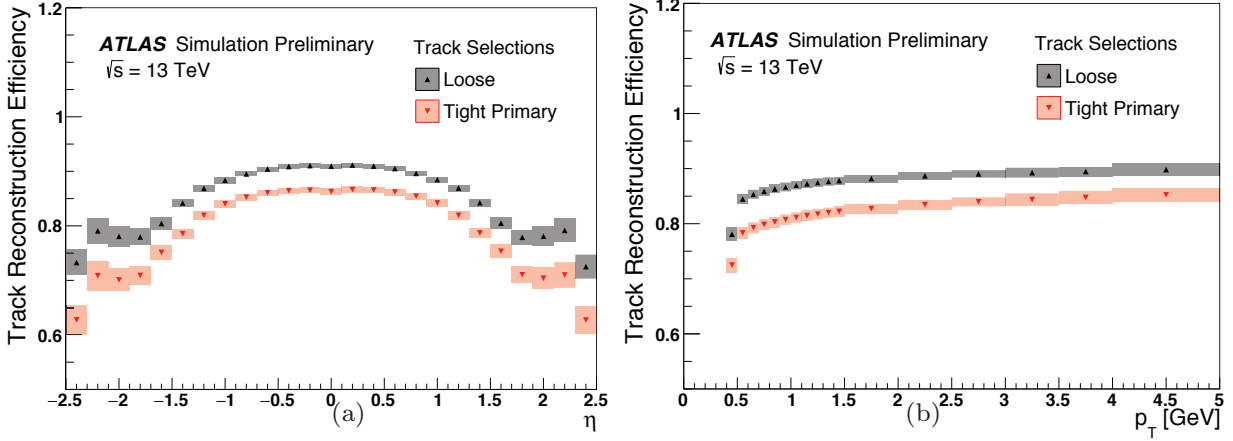
Figure 3.2: Track reconstruction efficiency measured on a `PYTHIA` [126] Minimum Bias [127] MC simulation [128] as a function of η (a) and p_T (b). The error bands represent the total systematic uncertainty. *Loose* indicate the default Run-1 selection. For (a) $p_T > 400$ MeV and for (b) $|\eta| < 2.5$ requirements are applied. Figures taken from [125].

outside-in algorithm starting from TRT segments and extrapolating back adding silicon hits. This procedure is commonly referred to as *back-tracking*.

The track fitting algorithms can lead to the reconstruction of *fake tracks* arising from random combinations of hits that, within the error associated to them, lie on a helix trajectory that can not be matched with primary or secondary tracks. Since the probability to reconstruct fake tracks increases with the Inner Detector occupancy and higher pile-up conditions, the *default* track selection used in 2011, which required at least 7 silicon (Pixel+SCT) hits and at most 2 pixel holes, has been tightened in 2012 data-taking. Tracks are required to pass the *robust* selection, requiring at least 9 hits in the silicon detectors and no holes in the pixel sub-system, in order to reduce the fake tracks rate to negligible levels at higher pile-up values. The track reconstruction efficiency is measured with MC simulation samples using a hit-based track-to-truth charged particle association and it is parametrised as a function of track p_T and η [124].

Following this strategy, in Run-2 the track quality cuts have been re-optimised in order to cope with the expected higher pile-up conditions than Run-1 and with the new geometry of the Inner Detector [125].

Three new sets of quality cuts have been developed for the reconstructed tracks:

- **Loose**: Track selection analogue to the *default* cuts used in Run-1. It targets a very high track reconstruction efficiency at the cost of non-negligible fake rate. Tracks passing this working point are required to have at least 7 silicon hits, at most 2 holes in the silicon detector and at most 1 hole in the Pixel detector and at most one (two) shared hit(s) on track in the Pixel (SCT).

- **Loose-Primary**: Track selection designed to improve the track quality and the impact parameter measurements, maintaining an efficiency as high as possible for
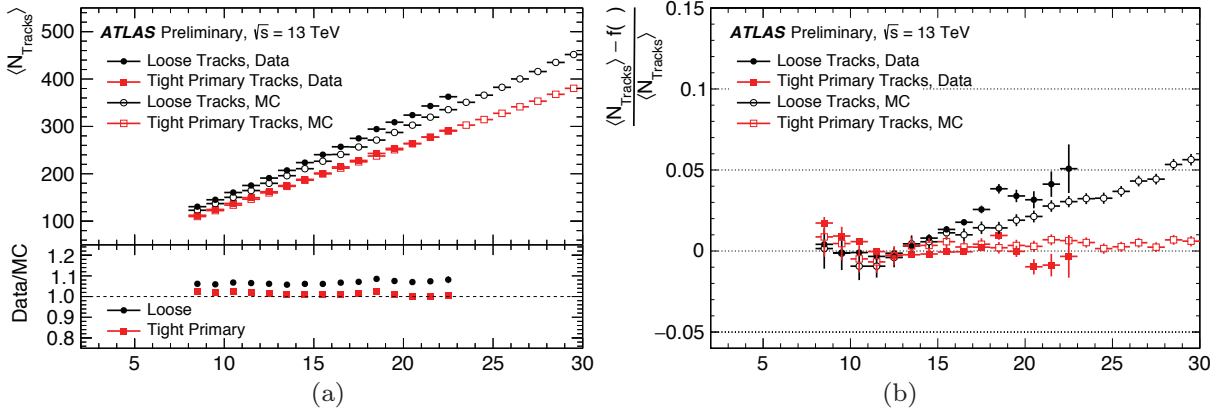
Figure 3.3: Average number of reconstructed tracks $\langle N_{trk} \rangle$ as a function of the average number of collisions per bunch crossing μ with both Loose and Tight Primary selection (a) and the fake rate extracted from the deviation from the linear fit of $\langle N_{trk} \rangle (\mu)$ (b). The statistical errors are reported but too small to be seen. *Loose* indicates the Run-1 default selection. Figures taken from [125].

particles produced before the first measurement plane. It represents a baseline for selecting tracks originating from *b*-hadrons or τ decays. This is achieved requiring, in addition to *Loose* cuts, at least 10 hits in the Pixel and SCT sub-detectors, if there are any shared silicon hits.

- **Tight-Primary**: Track selection designed to reduce the fake track rate to a negligible level at high pileup (below 1% at $<\mu>=40$) at a price of lower track reconstruction efficiency. This is achieved requiring at least a measurement in one of the two innermost layers, no holes on track in the pixel layers and at least 10 silicon hits in the region $|\eta| > 1.65$. Given these requirements, this selection is optimised for primary tracks and for primary vertex reconstruction (see Section 3.1.2) and it is sub-optimal for tracks produced by decays that occur after the first measurement plane. In Fig. 3.2 the track reconstruction efficiency for Tight-Primary tracks is compared with the one obtained with the *Loose* selection, denominated *Loose*

The fake tracks rate can be measured from data and MC simulation under the assumption that the average number of primary tracks increases linearly with pile-up. A linear fit is performed in the region $10 \leq \mu \leq 15$ and extrapolated to higher regions. The fake rate is measured as the deviation from the linear fit as a function of μ. The results are reported in Fig. 3.3 where a fake rate of Tight-Primary tracks is at the sub-percent level for the 2015 dataset.

3.1.2 Primary vertex reconstruction and beam spot determination

Charged particles tracks passing the *robust* requirements are combined in order to reconstruct the spatial position of $p - p$ interaction vertices, using an iterative procedure [129].
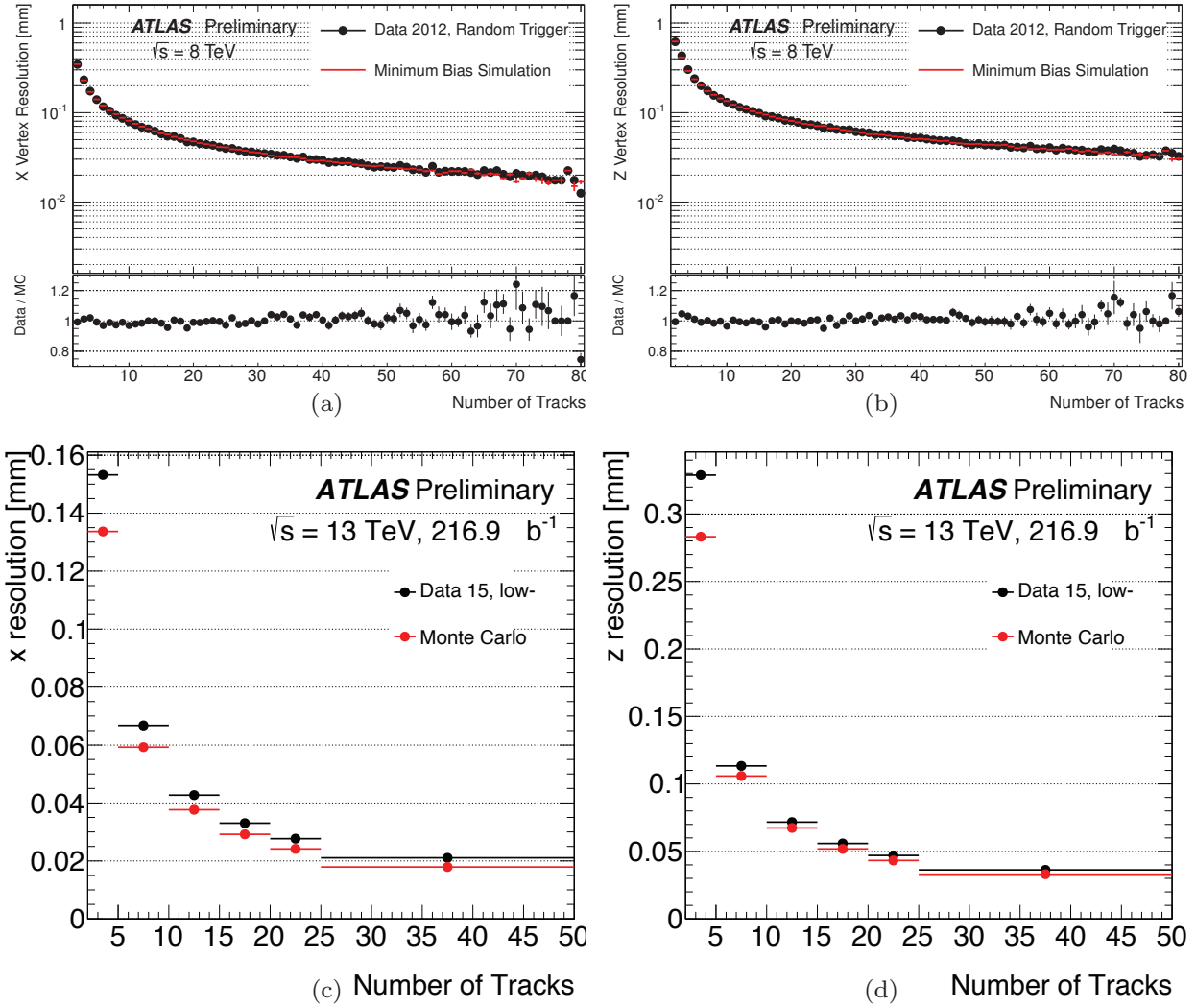
Figure 3.4: Vertex position resolution for data (black) and MC simulation (red) for the x and z coordinates for both 2012 and 2015 data as a function of the number of associated tracks. The tracks used to reconstruct the vertices are required to pass the *robust* selection and the *Tight-Primary* selection in 2012 and 2015, respectively [131, 132].

Firstly, the z coordinate of vertices seeds are selected from the global maximum of the distribution of the z coordinate of the tracks with respect to the interaction point. The seed position and the neighbouring tracks are used by a χ^2 based adaptive vertex fitter [130] that is iterated over a predefined number of steps. The resolution on the vertex position improves as a function of the number of tracks associated to it N_{trk} and with the square sum of their transverse momenta $\sum_i^{N_{trk}} p_{T,i}^2$. The *primary vertex* is the one with highest $\sum_i^{N_{trk}} p_{T,i}^2$ while the other reconstructed vertices are labelled as *pile-up vertices*. In 2015 the *Tight Primary* quality requirement has been applied to select tracks used in vertex reconstruction. In Fig. 3.4 the resolution on the x and z vertex coordinates for both 2012 and 2015 data compared to MC simulation as a function of the number of tracks associated

to the vertex are shown.

The three dimension spatial distribution of the reconstructed vertices reflects the region where the two proton beams are crossing. This region has an ellipsoidal shape and is commonly named *beam-spot*. The centre of the beam-spot is determined through a binned likelihood fit that uses as input the position of the vertices [133] and it is determined both at trigger level, i.e. in order to improve the performance of *b*-jet triggers, and during the offline reconstruction, to improve tracking efficiency and vertex resolution. The offline position of the beam-spot centre is calculated with respect to the ATLAS coordinate system. The precise determination of origin of this coordinate system and the orientation of the axes are defined as the result of the Inner Detector alignment procedure. Therefore, the beam-spot determination occurs after the complete derivation of the alignment constants.

3.1.3 Track impact parameters and momentum resolution

The track impact parameters are important quantities for constraining and reducing background processes that are not generated by the hard scattering. In particular, the transverse impact parameter is of fundamental importance for identifying jets originating from heavy flavour quarks. The presence of the IBL in Run-2 leads to a significant improvement in the impact parameters resolution. A comparison between Run-1 and Run-2 is shown in Fig. 3.5 where the resolution of the transversal and longitudinal impact parameters is shown as a function of the transverse momentum and the pseudo-rapidity for tracks that pass the *LoosePrimary* selection. The impact parameters are calculated with respect to the Primary Vertex and an iterative deconvolution method to subtract the contribution to the impact parameters resolution from the vertex reconstruction [135] has been applied.

The fractional momentum resolution $\sigma(1/p_{\mathrm{T}})/(1/p_{\mathrm{T}})$ for the ID tracks in Run-1 is extracted from $Z \to \mu\mu$ decays and is parametrised as a function of the muon η and p_{T} in Data and MC simulation. The parametrisation takes into account the effects due to multiple Coulomb scattering, fluctuations in energy losses in the material, the description of the detector geometry and the intrinsic spatial resolution of the sensitive elements. Since the parametrised resolution underestimates the measurement on data, a smearing factor ranging up to 12%, depending on the muon pseudorapidity and momentum, is applied in MC simulation. A detailed description of the techniques and results are reported in [136]. In Run-2, a similar procedure is followed using both $Z \to \mu\mu$ and $J/\psi \to \mu\mu$ events. A complete description of the methods and results is given in [137].

3.2 Lepton identification

3.2.1 Reconstruction of Electrons

Electrons are reconstructed in the central region of the ATLAS detector ($|\eta| < 2.47$) by matching EM calorimeter clusters to tracks reconstructed in the ID. The EM clusters are searched for using a *sliding window algorithm* [139, 140] that sums up the calorimeter cells energy deposits in a window of 3×5 towers with size $\Delta\eta \times \Delta\phi = 0.025 \times 0.025$. Clusters with transverse energy greater than 2.5 GeV are then used to define a Region of Interest (RoI) in the ID, where a two-step track reconstruction algorithm is performed. The first
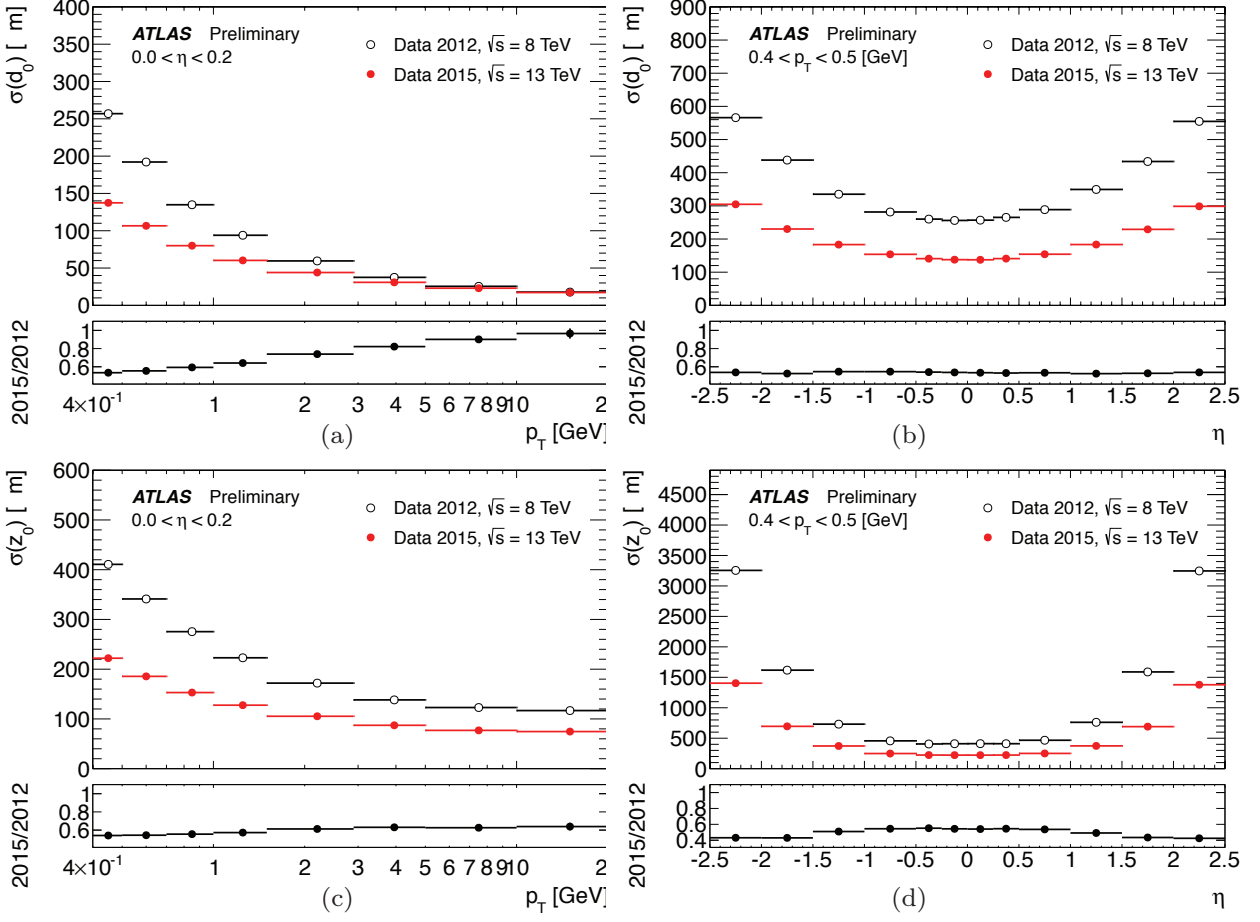
Figure 3.5: Comparison of 2012 and 2015 impact parameter resolution showing the improvement due to the IBL presence. The transverse and longitudinal impact parameter resolution are measured as a function of p_T, for values of $0 < |\eta| < 0.2$ (a,b) and η for values of $0.4 < p_T < 0.5$ (c,d), respectively. Figures taken from [134].

step uses the ATLAS Global χ^2 fit [141] in order to find tracks that could match the EM clusters. The successfully reconstructed tracks are re-fitted using an optimised track fitter designed for electrons candidates, the Gaussian Sum Filter [142], that accounts for non-linear energy losses due to bremsstrahlung. Between all the successfully fitted tracks, the one that best matches the calorimeter cluster is chosen and the electron candidate is built.

However, not all the reconstructed candidates are electrons coming from the hard scattering. Several objects, such as hadronic jets or electrons generated by semileptonic decays of heavy flavour hadrons or photon conversions, can pass the reconstruction algorithm outlined above. Prompt electrons can be selected by a sequential set of cuts on variables describing the ID track properties and the calorimeter shower shape, or by a likelihood discriminant (LH), that combines these variables for a better background rejection for the same identification efficiency in higher pileup experimental conditions. Cut based
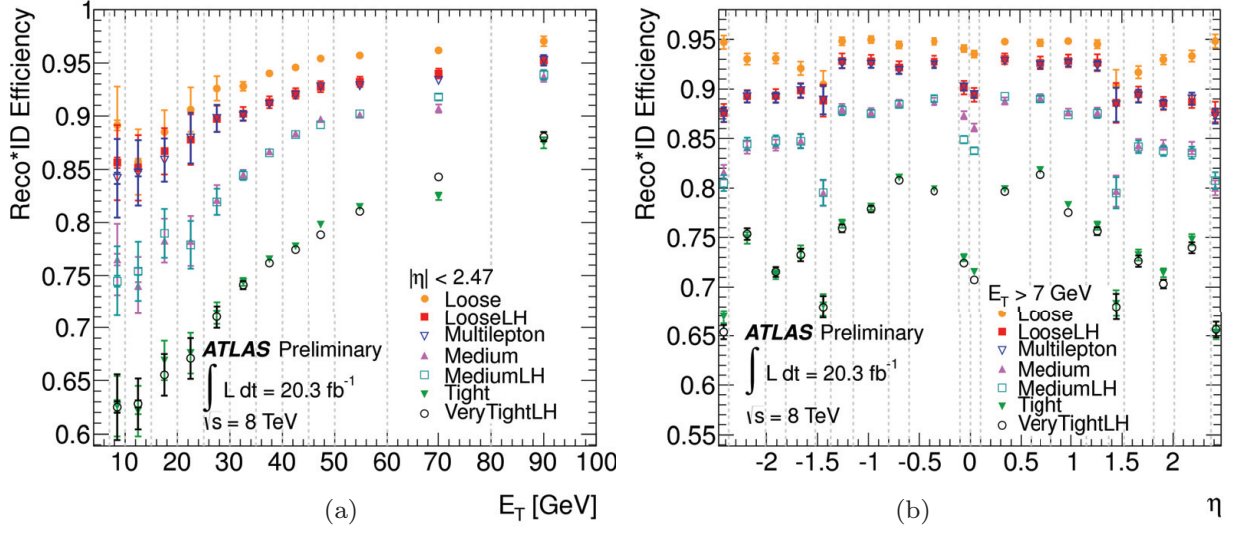
Figure 3.6: Measured combined electron reconstruction and identification efficiency for the cut-based and likelihood working points as a function of E_T (a) and η (b) (with $E_T > 7$ GeV) for the 2012 dataset. The efficiency for data is measured from the data-to-MC efficiency ratio using a $Z \to ee$ simulated sample. The figure has been taken from [138].
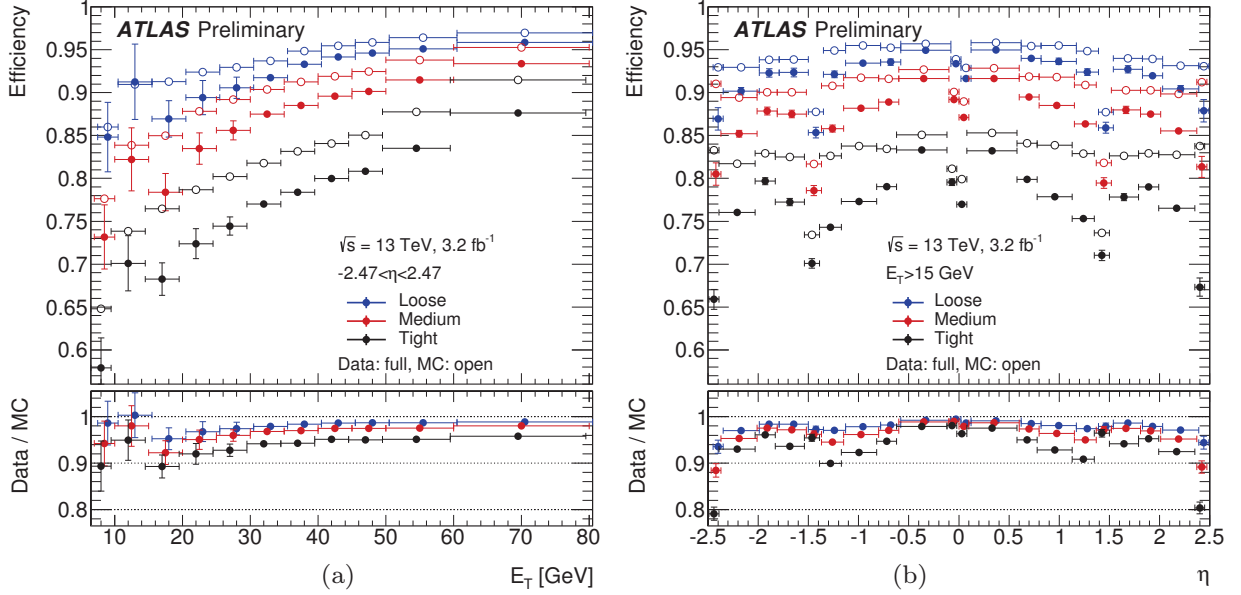
Figure 3.7: Measured electron identification efficiency for the various likelihood working points as a function of E_T (a) and η (b) (with $15 < E_T < 50$ GeV) for the 2015 dataset. The efficiency for data is measured from the data-to-MC efficiency ratio using a $Z \to ee$ simulated sample. The figure has been taken from [143].

identification and LH discriminant criteria have a set of defined working points called *loose, medium, multilepton, tight* and `LOOSE, MEDIUM, VERY TIGHT`, respectively. The electron

identification working point efficiencies for Run-1 and Run-2 data are shown in Fig. 3.6 and Fig. 3.7, respectively.

As the working points range from looser to tighter selection, the background rejection power increases at the cost of a lower efficiency on the electron candidates selection. Loose selections are optimised to discriminate electrons from light flavour jets, while medium and tight selections contain additional variables in order to reject electrons originating from heavy flavour hadrons semileptonic decays or photon conversions. Details on the identification criteria used in 2012 data taking can be found in [138]. The reconstruction and identification efficiency is measured using the *tag and probe* method on a sample of $Z \to ee$ and $J/\psi \to ee$ decays. Strict identification criteria are applied on the first electron (*tag*), while the second electron is identified through a looser selection (*probe*) and is used to perform the efficiency measurement. The efficiency measurement is performed also with simulated MC samples and usually slightly differs from the results obtained from collisions data. This effect is corrected by a multiplicative *scale factor* (SF), defined as the ratio of the efficiency measured in data to the one measured in the MC and calculated in terms of the electron transverse energy and pseudorapidity. The combined reconstruction and identification efficiency measured with the 2012 dataset is shown in Fig. 3.6.

For Run-2 the baseline electron identification algorithm is the likelihood discriminant, with three selection criteria *loose*, *medium* and *tight*, based on an optimised set of variables that take into account the different TRT gas mixture and pileup conditions [144]. The identification efficiency measured using the 25ns dataset of 2015 collisions is shown in Fig. 3.7.

3.2.2 Reconstruction of Muons

Muon reconstruction in ATLAS uses the available information from the ID, MS and EM calorimeter sub-detectors to define four different muon types [145]:

- **Stand Alone (SA)**: Muon tracks are reconstructed only in the MS in the region $|\eta| < 2.7$ and are extrapolated to the beam line taking into account the energy loss and the multiple coulomb scattering in the calorimeters.

- **Calorimeter Tagged muons (CaloTag)**: Muon candidates are reconstructed from a track in the ID that has an EM calorimeter energy deposit compatible with a minimum ionising particle. These muons recover the efficiency at $|\eta| \sim 0$ due to the lack of MS chambers.

- **Segment-Tagged (ST)**: These muons are reconstructed from an ID track with an associated track segment in the first MS station in order to recover low$-p_T$ inefficiencies due to energy losses in the calorimeters.

- **Combined Muons (CB)**: These muons candidates have the highest purity since they are obtained from a combined track fit in both the ID and the MS in the region $|\eta| < 2.5$.

The muon candidates used in physics analyses are reconstructed by three different algorithms, named *chains*, that combine the information from the ID tracks and the MS
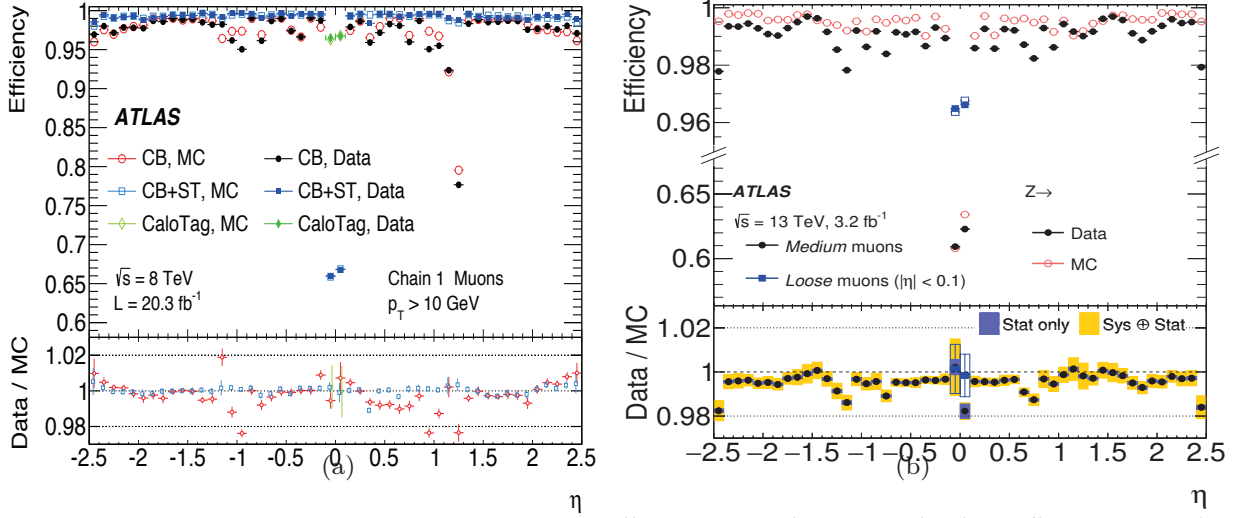
Figure 3.8: Measured muon reconstruction efficiency as a function of η for different type of muons reconstructed using the *Chain 1* algorithm in 2012 (left) and for *Loose* and *Medium* muons selected by the *Chain 3* algorithm in 2015. The figures for Run-1 and Run-2 are taken from [145] and [137], respectively.

track segments. The first chain, called *Staco* or *Chain 1*, statistically combines the ID and MS track candidates using the corresponding track parameters and covariance matrices [146]. The second chain, called *Muid* or *Chain 2*, performs a global Kalman Filter fit of the muon track using hits from the ID and the MS [147]. A third chain has been developed to combine the best results of the other two chains and has been used in parallel to the other two during 2012 data taking. In Fig. 3.8a the reconstruction efficiency for muons reconstructed by the *Chain 1* algorithm is shown.

The muon reconstruction in Run 2 used improved algorithms that were defined as *Chain 3* during 2012. The improvements included a better calculation of the energy loss in the calorimeter, the use of a Hough transformation [148] to increase track-finding efficiency and a better background rejection [137]. In particular, four muon identification selections have been defined to cope with various physics analyses requirements: *Loose*, *Medium*,*Tight* and *High-p_T*. The *Medium* selection is the default muon identification working point for Run-2, with an identification efficiency measured to be above 95% on a $t\bar{t}$ sample. The *Loose* selection has been defined to recover efficiency in the region $|\eta| \sim 0$. The *Tight* working points selects muons with higher purity at the cost of lower selection efficiency. Finally, the *High-p_T*, has been defined to maximise the momentum resolution for muon tracks with transverse momentum above 100 GeV. In Fig. 3.8b the reconstruction efficiency for muons reconstructed by the *Chain 3* algorithm is shown.

In both Run-1 and Run-2, the muon reconstruction efficiency in the region $|\eta| < 2.5$ is calculated using a *tag-and-probe* method using standard candles decays such as $Z \to \mu\mu$ and $J/\psi \to \mu\mu$ that cover a broad muon p_T spectrum. In this method, the *tag* is represented by the muon reconstructed in either the MS or the ID and is used to test the *probe* muon reconstructed in the other system (ID or MS). The differences in the measured reconstruction efficiency in Data and MC are taken into account by multiplicative *Scale*

Factors that differ from unity within a few percent. The drop in efficiency for CB muons at $\eta \sim 1.2$ in the 2012 measurement, Fig. 3.8a, corresponds to the transition region between the barrel and the endcap region where only one layer of MS chambers is present. This feature is not present in 2015 due to the addition of extra muon chambers during the LS1.

Muons used by the SUSY search presented in this dissertation are reconstructed using the combined information from the ID and MS in the $|\eta| < 2.5$ region using the *Chain 1* algorithm. For the $Z \to \mu\mu$ constrained alignment in Run-2, *Chain 3* muons have been used with the *Loose* identification criteria.

3.2.3 Hadronic Taus

In the search for $\tilde{t}$ decaying into $\tilde{\tau}$, tau leptons are produced as final products of the decay chain. With a lifetime of $(290.3 \pm 0.5) \times 10^{-15}$s [149], τ leptons decay either leptonically, denominated τ_{lep}, or hadronically, indicated with τ_{had}, with a branching ratio of 37% and 63% respectively. In the leptonic τ decay, an electron or muon is produced in association with neutrinos. In this case the visible decay products are undistinguishable from prompt electrons or muons and are reconstructed using the techniques described in Section 3.2. In the hadronic τ decay, one or three charged pions are produced in association with τ neutrinos with a branching ratio of 22% and 72%, respectively, while in the majority of the remaining cases kaons are produced instead. In 78% of all hadronic decays, neutral pions are also produced in association with charged hadrons [150]. Hadronically decaying τ leptons are named *1-prong* or *3-prong* in the case of one or three tracks associated to them.

The identification of τ_{had} is a key ingredient for the $\tilde{t}$ decaying into $\tilde{\tau}$ search in order to maximise the discovery, or exclusion, potential of the analysis. A full description of the methods used in ATLAS for τ_{had} reconstruction and identification is reported in [150].

The τ_{had} reconstruction algorithms are seeded by anti-k_t with radius parameter $R = 0.4$ jets (see Sec. 3.3.1) with a $p_{\text{T}} > 10$ GeV and $|\eta| < 2.5$ (see Sec. 3.3.1). An algorithm is used to identify the tau production vertex (TV) using all the tau candidate tracks passing predefined quality criteria in a cone of $\Delta R = \sqrt{(\Delta\phi)^2 - (\Delta\eta)^2} < 0.2$ from the seed direction [151]. Such a vertex is used as a reference point for the tau variables coordinate system in order to determine the τ p_{T} and direction. Tracks are associated to the τ_{had} in a cone with $\Delta R < 0.4$ around the τ direction, but only the ones falling in the *core region*, i.e. within a cone of $\Delta R < 0.2$, are used to classify the τ_{had} as 1-prong or 3-prong. In this region, a π^0 reconstruction algorithm is used to obtain the number of neutral pions associated to the τ_{had}. At this stage, the reconstruction algorithm provides a very small rejection against the large background of quark or gluon jets. A set of variables based on the ID and calorimeters information that show a significant discriminating power against jets, are combined into two Boosted Decision Trees (BDT) [152], each one trained separately for 1-prong and 3-prong on MC simulation and multi-jet data samples. The list of the discriminating variables with a brief description is given in Tab. 3.1.

Three working points that provide a stable signal efficiency as a function of τ_{had} p_{T} and the number of vertices in the event are defined and indicated as *loose*, *medium* and *tight* and are shown in Fig. 3.9. The use of a looser identification working point leads to higher τ_{had} selection efficiency at the cost of a lower background rejection power.

Variable	Description
Central energy fraction f_{cent}	Ratio between the E_{T} deposited in the region $\Delta R < 0.1$ and all energy deposited in the region $\Delta R < 0.2$ around the direction of the τ_{had}
Leading track momentum fraction (f_{track})	Ratio between the p_T of the leading track and the total transverse energy in the core region of a τ_{had}
Track radius (R_{track})	p_{T}-weighted distance of the associated tracks to the τ_{had} direction
Leading track d_0 significance ($S_{\mathrm{leadtrack}}$)	Ratio between the transverse impact parameter of the leading track in the τ_{had} core region with respect to the TV and its estimated error
Number of tracks in the isolation region $N_{\mathrm{track}}^{\mathrm{iso}}$	Number of tracks associated with τ_{had} within $0.2 < \Delta R < 0.4$
Maximum ΔR	Maximum ΔR between an associated track to the τ_{had} candidate and the τ_{had} direction
Transverse flight path significance (S_T^{flight})	The decay length of the secondary vertex in the transverse plane with respect to the TV. Only for multi-track τ_{had}.
Track mass (m_{track})	Invariant mass calculated by the four-momenta of the tracks associated to the core region of a τ_{had}
Track-plus-π^0-system-mass ($m_{\pi^0+track}$)	Invariant mass of the system composed by the tracks and π^0 reconstructed in the core region of τ_{had}
Number of π^0's N_{π^0}	Number of π^0 mesons reconstructed in the core region
Ratio of tracks-plus-π^0-system p_{T} ($p_{\mathrm{T}}^{\pi^0+\mathrm{track}}/p_{\mathrm{T}}$)	Ratio between the p_{T} of the τ_{had} estimated using tracks and reconstructed π^0 and the calorimeter-only measurement

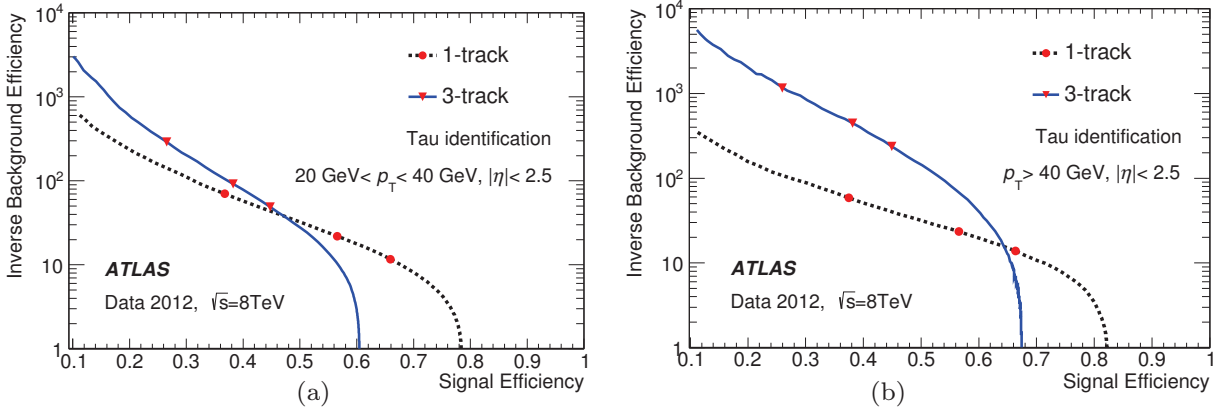Table 3.1: List of the variables used by the τ_{had} identification BDT.

Figure 3.9: The inverse background efficiency is reported as a function of the signal efficiency for (a) low-p_T and (b) high-p_T τ_had, for both 1-prong and 3-prong separately. The red points indicate the three working points described in the text. The signal efficiency doesn't reach unity since it is limited from above by the τ_had reconstruction efficiency [150].

The typical signature of 1-prong τ_had is very similar to the one left in the ATLAS detector by electrons. Therefore, a BDT that uses TRT information on transition radiation and shower shape in the EM+HAD calorimeters is used to reject the electron background. Three working points are defined and labeled as *loose*, *medium* and *tight*, corresponding to 95, 85 and 75% signal efficiency, respectively. Tighter cuts on the electron BDT leads to higher background rejection. Finally, a cut based veto is used to reduce the background arising from the unlikely situation where a muon is misidentified as a τ_had to a negligible level. The signal efficiency for the muon veto is 96%, corresponding to 40% background rejection.

The hadronic tau identification efficiency is measured with a *tag-and-probe* approach in $Z \to \tau_{lep}\tau_\mathrm{had}$ events in both data and MC using a template fit on the number of tracks associated to the τ_had. The differences between the results obtained with simulation and with data are corrected using multiplicative scale factors. Since no significant dependence on the hadronic tau p_T is found, the scale factors are parametrised as a function of η, as shown in Fig. 3.10.

The τ_had energy calibration starts with the correction of the cluster energy to account for out-of-cluster energy deposits and calorimeter inefficiencies. However, this calibration scheme is not optimised for the size of the cone ($\Delta R < 0.2$) used to reconstruct the τ_had momentum. An additional correction, defined as the ratio of the energy at the LCW (see Sec. 3.3.1) scale over the true visible energy obtained from MC simulation, is applied in order to obtain the tau energy scale (TES). The major sources of systematic uncertainties on the tau energy scale are due to detector modelling in MC simulation and pile-up and underlying event effects. The total TES uncertainty ranges between 2% and 3% for 1-prong and 2% and 4% for multiple tracks τ_had, respectively.
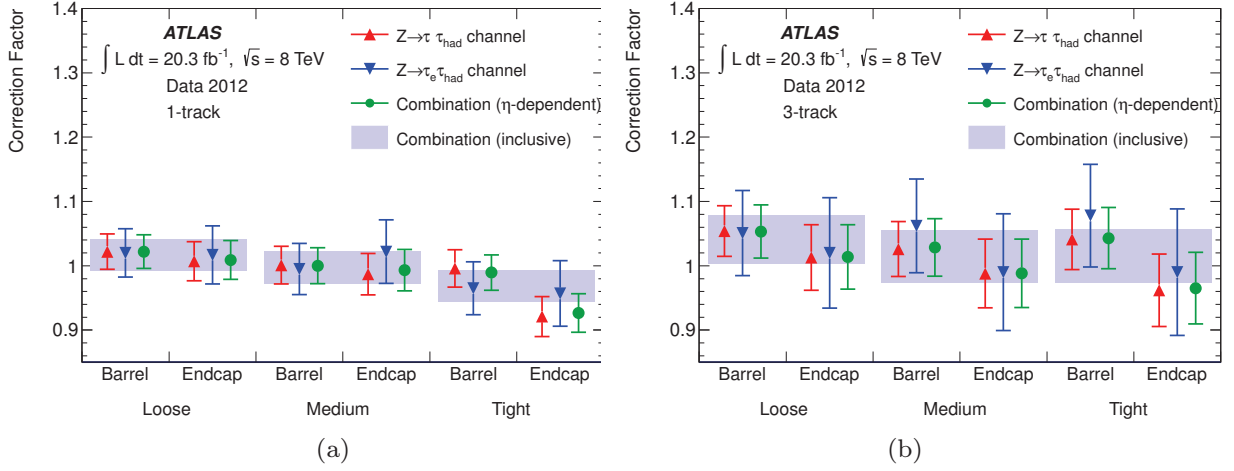
Figure 3.10: Scale factors applied to MC simulation for all working points and as a function of η together with the combined systematic and statistical uncertainty are shown separately for (a) 1-prong and (b) 3-prong τ_{had} [150].

3.3 Jets and Missing Transverse Momentum

3.3.1 Jets

Quarks and gluons produced in the interactions in p-p collisions undergo a fragmentation process, producing a close-by cascade of partons, and a *hadronisation* process, responsible for the formation of colourless hadrons, that together generate a narrow cone of particles around the direction of the original object. Such cone of particles is commonly referred to as a *jet*. The vast majority of proton collisions in the LHC produce quarks and gluons in the final state that produce jets. Therefore it is of key importance to efficiently reconstruct and identify them. From an experimental point of view, they appear in the ATLAS detector as a spray of particles which leave large EM and HAD calorimeter energy deposits associated with collimated charged particles tracks reconstructed in the ID. In ATLAS, jets are reconstructed grouping the calorimeter energy deposits using the anti-k_t sequential clustering algorithm [153], implemented by the `FastJet` [154] program. This algorithm is *collinear* and *infrared safe*, meaning that it is insensitive to collinear splitting of the initial partons and to the extra radiation produced by soft particles not originated by the hard scatter. The calorimeter deposits are merged together depending on the distance d_{ij} between them and from the beam line d_{iB} defined as:

$$d_{ij} = \min\left(k_{Ti}^{2p}, k_{Tj}^{2p}\right) \frac{\Delta R_{ij}^2}{R^2}, \qquad d_{iB} = k_{Ti}^{2p} \tag{3.2}$$

where $\Delta R_{ij}^2 = (\eta_i - \eta_j)^2 + (\phi_i - \phi_j)^2$ and $k_{Ti,j}$, $\eta_{i,j}$ and $\phi_{i,j}$ are the transverse momentum, the pseudorapidity and the azimuthal angle of the objects i and j, respectively. The distance between two topological clusters d_{ij} is compared with d_{iB}: if $d_{ij} < d_{iB}$ the i and j objects are combined together and the algorithm keeps iterating with the other clusters, otherwise i is reconstructed as a jet and removed from the list of objects to be

considered. In the anti-k$_t$ algorithm used in ATLAS, p is equal to -1, ensuring that energy deposits due to soft radiation will be clustered together to the hard object before being merged between themselves and R is equal to 0.4, which defines the size of the jet cone and the minimum distance between two un-merged jets. The calibration of the energy of reconstructed jets is based on a combination of simulated MC samples and data driven techniques. The jet energy is firstly computed at the EM scale [155], providing an accurate measurement of the energy deposits of the showers generated by electrons and photons. A second calibration uses the *local cell signal weighting* (LCW) method [156] to classify the topo-clusters as electromagnetic or hadronic based on their shower properties and apply MC based simulations to the energy deposits due to hadronic calorimetric showers. At this stage the *jet energy scale* (JES) calibrations are applied as a function of the jet energy and pseudorapidity to correct for differences between the truth jet energy and the reconstructed one. These corrections are applied in consecutive steps using both MC simulated samples and in-situ measurements where the jet transverse momentum is compared to the one of a reference object. Firstly, a correction for the average additional energy deposits due to the pile-up is applied. Secondly, the direction of the jet is corrected such that it points to the primary vertex instead of the ATLAS reference point. The energy of the jets is then corrected using the inverse average jet response function $1/R$, computed on MC simulation, defined by

$$1/R^{\text{EM(LCW)}} = E^{truth}_{jet}/E^{\text{EM(LCW)}}_{jet} \tag{3.3}$$

where E^{truth} is the energy of the truth jet matched to the reconstructed jet with energy $E^{\text{EM(LCW)}}_{jet}$ calibrated at the EM (LCW) scale. A similar function is applied also to correct the jet pseudorapidity. A particular correction is applied for the jets originating from b-quarks due to the fact that neutrinos produced by their semileptonic decay cause a lower calorimeter energy response. A correction for semileptonic b-jets decays to muons is derived for MC simulation, correcting the calorimeter response measurement to that of an inclusive sample of b-jets where all the b-quarks decay modes are included following a procedure similar to the EM+JES scheme [157]. The total uncertainty on the JES calibration in 2012, shown in Fig. 3.11 as a function of the jet η (a) and p_T (b), is computed by the square sum of single sources of systematics arising from detector description, pile-up contribution, statistics of the MC and data for the in-situ method and other modelling effects. Reconstructed jets are further selected using the *jet vertex fraction* (JVF), to classify jets coming from the hard scattering from the ones generated by pile-up effects. The JVF variable is defined as the ratio of the scalar sum of the transverse momenta of the tracks within a jet associated to the primary vertex to the total p_T sum of all tracks matched with the jet [158]. Jets with a JVF value close to 1 are likely to be originating from the hard-scatter while those with a value approaching 0 are likely to be pile-up jets. A value of -1 is used for forward jets that are outside the ID coverage and do not have associated tracks.

3.3.2 B-jet tagging

The supersymmetry search presented in this dissertation is characterised by the presence of jets originating from b quarks in the final state, therefore their precise identification is of
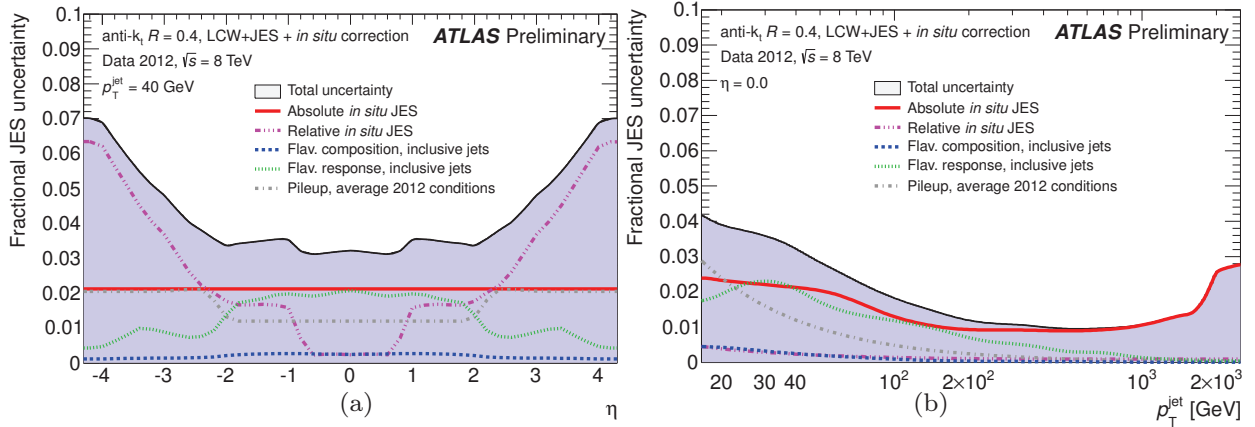
Figure 3.11: Fractional JES uncertainty in 2012 measured as a function of η (a) and p_T (b) [159].
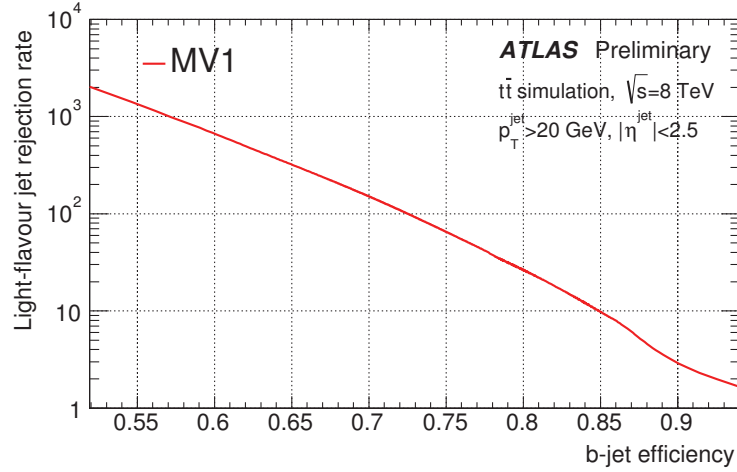
Figure 3.12: Light-flavour jet rejection rate as function of b-jet efficiency for the MV1 tagger in 2012 [161].

key importance for both selecting the SUSY signal and reducing the contribution of some of the expected SM backgrounds. In ATLAS, various algorithms [160–162], based on the information from the reconstructed tracks and displaced secondary vertices in the ID, are used in order to identify b-jets, taking advantage of relatively long lifetime of B hadrons[2].

A first classification is performed by the IP3D [163] algorithm, which exploits the fact that charged tracks within heavy flavour jets have generally larger impact parameters with respect to tracks associated to the primary vertex. To improve the discrimination between heavy flavour and light flavour jets, a full three dimensional reconstruction of a displaced vertex formed by the decay products of b hadrons is performed. This algorithm [164], takes as input a list of tracks that are significantly displaced from the primary vertex and tries

---

[2]The lifetime of B hadrons is of the order of 1.6ps. Considering the mass of a B hadron of 5 GeV and its energy of 30 GeV, the typical flight path is approximately $\sim$ 3 mm.
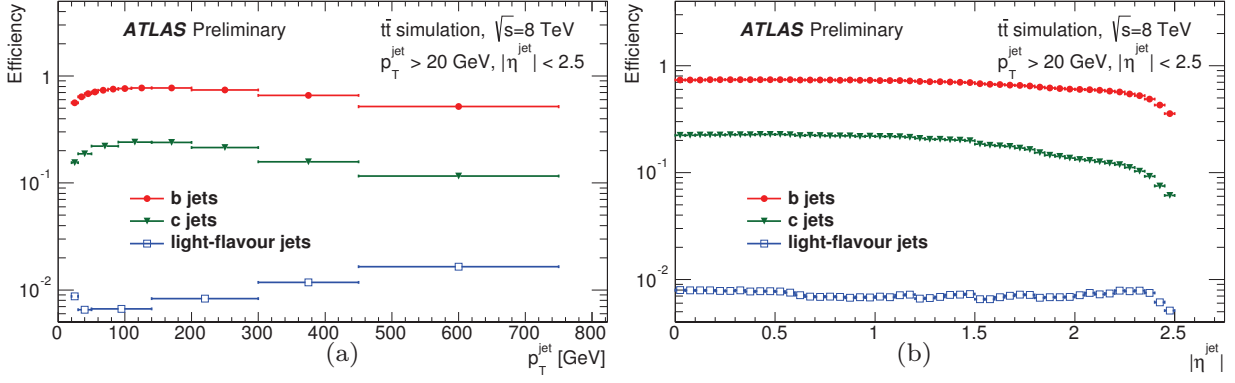
Figure 3.13: Efficiency of the MV1 algorithm to tag b, c and light-flavour jets as a function of jet p_T (a) and η (b) for the 70% working point on simulated $t\bar{t}$ events [161].

to reconstruct vertices from track pairs. Vertices compatible with long lived particles such as K_S or Λ, photon conversions or material interactions are rejected. SV1 [162] is a tagging algorithm based on the reconstruction of displaced secondary vertices. It combines in a likelihood-ratio discriminant quantities such as the *vertex mass*, defined as the invariant mass of the charged particles linked to the secondary vertex, the ratio of the sum of the energies of these tracks to the sum of the energies of all the tracks matched to the jet and the number of two-track vertices. Finally, a Kalman filter is used by the JetFitter [160] algorithm to fully reconstruct the decay chain of B hadrons and further improve the rejection of light flavour jets. The outputs of the IP3D, SV1 and JetFitter algorithms are used as input to an artificial neural network, called MV1 tagger, that combines the different techniques to obtain optimal efficiency in selecting heavy flavour jets and in rejecting light flavour jets. The light-flavour jet rejection as function of the b-jet tagging efficiency for the MV1 tagger is shown in Fig. 3.12. In the analysis described in this thesis, a MV1 operating point of 70% in b-jet efficiency has been chosen. In Fig. 3.13 the MV1 selection efficiency for b-jets, c-jets and light-flavour jets as a function of the jet p_T and η calculated from $t\bar{t}$ simulated events are shown. The MV1 tagger efficiencies for b, c and light-flavour tagged jets are measured using different techniques on data and simulated samples. The b-jet tagging calibration is obtained using a combinatorial likelihood method with selected $t\bar{t}$ dileptonic events [165]. The efficiency of a b-tagging algorithm to tag a c-jet is called *c-tagging* efficiency. For the MV1 tagger, it is measured using a sample of jets containing D mesons, through a comparison of the number of selected yields before and after applying the b-tagging requirement [161]. The probability of a b-tagger to tag a light-flavour jet is called *mistag rate* and it is due to the finite resolution of the ATLAS ID and to tracks originating from displaced vertices or from material interactions. The measurement of the mistag rate for the MV1 tagger is performed in an inclusive jet sample, reverting the sign of the selections for both transverse impact parameter significance and the decay length. The mistag rate deepends on the jet transverse momentum and pseudorapidity and ranges between 1% to about 3% with increasing p_T in the region $|\eta| < 1.2$ [162]. The MV1 tagging efficiencies are measured both in data and Monte Carlo and the differences in the results are corrected through multiplicative scale factors parametrised as a function of the jet

transverse momentum.

3.3.3 Missing Transverse Momentum

Neutrinos and some hypothetical SUSY particles produced by proton collisions will not interact with the ATLAS detector, and thus escape undetected. Indirect information on the presence of these particles can be inferred imposing the momentum conservation in the plane transverse to the beam direction. Since the initial state has zero momentum component in the transverse plane, an imbalance in the total measured transverse momentum in the final state would indicate the presence of an invisible particle being produced. The *missing transverse momentum* $p_{\mathrm{T}}^{\mathrm{miss}}$ is defined as the negative total vectorial sum of the transverse momenta of all the visible objects. There are various missing transverse momentum reconstruction methods that use the ID information, the calorimeter systems or a combination of both [166, 167]. In the supersymmetry search discussed in this work, the missing transverse momentum is a vector quantity computed based on calorimeter information and is commonly referred using the $\mathbf{E}_{\mathrm{T}}^{\mathrm{miss}}$ notation, with $E_{\mathrm{T}}^{\mathrm{miss}}$ being its magnitude. The $\mathbf{E}_T^{\mathrm{miss}}$ is calculated through a vector sum, using energy deposits associated to calibrated high-p_T electrons, photons and jets, or to low momenta hadronic activity and reconstructed muons:

$$\mathbf{E}_T^{\mathrm{miss}} = \mathbf{E}_{T,e}^{\mathrm{miss}} + \mathbf{E}_{T,\gamma}^{\mathrm{miss}} + \mathbf{E}_{T,\mathrm{jet}}^{\mathrm{miss}} + \mathbf{E}_{T,\mathrm{SoftTerms}}^{\mathrm{miss}} + \mathbf{E}_{T,\mu}^{\mathrm{miss}} \tag{3.4}$$

where each contribution is added in this specific order to avoid double counting. The electron and photon contributions, $\mathbf{E}_{T,e}^{\mathrm{miss}}$ and $\mathbf{E}_{T,\gamma}^{\mathrm{miss}}$, are obtained from *medium* electrons and identified photons with $p_{\mathrm{T}} > 10$ GeV and calibrated to the EM scale. The jet component, $\mathbf{E}_{T,\mathrm{jet}}^{\mathrm{miss}}$, is taken from jets with $p_{\mathrm{T}} > 20$ GeV and calibrated using the JES+LCW scheme[3]. The $\mathbf{E}_{T,\mathrm{SoftTerms}}^{\mathrm{miss}}$ term is composed by contributions arising from soft jets with $7 < p_{\mathrm{T}} < 20$ GeV and topoclusters or tracks not associated to any physics object and is calibrated using only the LCW scheme. Finally, the p_{T} of reconstructed muons with a $p_{\mathrm{T}} > 10$ GeV is negatively added to the $\mathbf{E}_T^{\mathrm{miss}}$ computation.

The measurement of the $\mathbf{E}_T^{\mathrm{miss}}$ depends on several components associated with different type of objects. Uncertainties arising from the reconstruction of these objects are combined into an overall systematic uncertainty on the measured missing transverse momentum. Other significant contributions to the measurement of $\mathbf{E}_T^{\mathrm{miss}}$ arise from pile-up effects that have a considerable impact especially on the jet and soft terms. Dedicated methods to reduce the pile up contribution are used such as the jet area method [168] for the $\mathbf{E}_{T,\mathrm{jet}}^{\mathrm{miss}}$ component and scaling the $\mathbf{E}_{T,\mathrm{SoftTerms}}^{\mathrm{miss}}$ term with the soft term vertex fraction (SVTF) [167], i.e. the ratio of the sum of the transverse momenta of tracks associated to the soft term and matched with the primary vertex over the sum of all the tracks associated with the soft term. The systematic uncertainty on the soft term evaluated after applying the pile-up suppression techniques is negligible, while the total systematic uncertainty on the $E_{\mathrm{T}}^{\mathrm{miss}}$ depends on the event topology considered.

---

[3]In general the $\mathbf{E}_{T,\mathrm{jet}}^{\mathrm{miss}}$ term can be divided in two contributions coming from jets and hadronically decaying taus. Even if in principle the τ_{had} contribution should be calibrated at the TES+LCW scale, in the search presented in this thesis this contribution is considered included in the jet term and, therefore, calibrated at JES+LCW scale.

4 Inner Detector Alignment Procedure

In this chapter the ATLAS Inner Detector alignment procedures are outlined. A brief discussion on how to cope with geometrical deformations that are not corrected by the track-based procedure is presented together with a description of the methods to include external constraints in the alignment solution. Finally, the updates performed for the inclusion of the Insertable B-Layer in the alignment framework are discussed.

4.1 Introduction to the Inner Detector Alignment

The accurate reconstruction of the trajectories of charged particles is a fundamental task for the experiments performed at high energy particle colliders and it is crucial for a wide range of physics topics. In ATLAS, these tracking requirements are met with a high resolution Inner Detector by the synergy of three sub-systems using different detection technology. The sensitive elements of the ATLAS ID provide a precise measurement of the position of the hits left by the charged particles at their passage through the tracking devices and the determination of the track parameters through an helicoidal fit. The position measurements are located in space by the relative positions of the sensitive elements with respect to one another in the ATLAS global reference system. The uncertainty on the local measurements is typically of the order of tens of microns for the silicon detectors and of one hundred microns for the TRT, while the relative devices positions are determined from assumptions made from the design and construction of the detector or survey measurements made during the assembly that have much larger uncertainties, limiting the track reconstruction quality [169]. In addition, misplacements of the tracking devices with respect to the assumed position would result in a wrong determination of the track parameters through the trajectory fit.

The accurate determination of the spatial position of the sensitive elements and the precise knowledge of the actual geometry of the ID is crucial to ensure high tracking quality. This procedure is referred to as *Inner Detector Alignment*. Since the ATLAS ID counts more than 300k sensitive elements, the ID Alignment is a challenging task to be performed. However, the three subsystems were constructed and assembled separately and in a modular fashion and then placed together to form the final ATLAS ID. This leads to a natural hierarchy in the levels of alignment [170].

The global movements of the full systems are corrected first, removing in this way correlations between smaller structures misalignments. This step is referred to as *Level 1* (L1) correction. During Run-2, this level has been modified and is called *Level 11* (L11), described in detail in Sec. 4.5.1, where the IBL is considered as a separate structure from the Pixel sub-detector. The second step consists in the corrections of the relative movements of the layers and disks or wheels that constitute the sub-detectors barrel and end caps, respectively. These set of corrections are indicated as *Level 2* (L2). Finally,

Alignment level	Detector	Alignable Structure
Level 1/11	Pixel: barrel and end-caps	1
	IBL: layer (from Run-2)	1
	SCT: barrel and 2 end-caps	3
	TRT: barrel and 2 end-caps	3
	Total	7 (8 from Run-2)
Level 2	Pixel: barrel layers	3
	Pixel: end-caps disks	6
	IBL: layer (from Run-2)	1
	SCT: barrel layers	4
	SCT: end-cap disks	18
	TRT: barrel modules	96
	TRT: end-caps wheels	80
	Total	207 (208 from Run-2)
Level 3	Pixel: barrel modules	1456
	Pixel: end-caps modules	288
	IBL: modules	280
	SCT: barrel modules	2112
	SCT: end-caps modules	1976
	TRT: barrel wires	105088
	TRT: end-cap wires	245760
	Total:	356680 (356960 from Run-2)

Table 4.1: Summary of the main alignment levels for the Inner Detector during Run-2 including the IBL sub-detector.

the final step consists in determining the positions of the single sensitive elements, silicon modules for Pixel and SCT and straws for TRT, individually and it is referred to as *Level 3* (L3) alignment. In Tab. 4.1 the alignable structures corresponding to each level are shown.

For each alignment level, an alignment reference frame is defined depending on the type of alignable structure whose spatial position and orientation need to be determined. These reference frames are indicated as *global* and *local* coordinate systems. The global alignment reference frame that is used for L1 corrections coincides with the ATLAS reference frame described in Sec. 2.2.1. At higher levels, the reference frame describing the position and orientation of the individual alignable structures is a right-handed reference frame with the origin in the geometrical centre of each structure. At *Level 2*, for example, the Pixel end-cap disks reference frame has the axes parallel to the ones of the global reference frame, but the origin located in the centre of the disk. When aligning the single sensitive elements, the local coordinate system (x', y', z') is used. In this reference frame, the x'-axis points along the most sensitive direction of the module. This corresponds to the shorter pitch side for Pixel and IBL modules, perpendicular to the strip-orientation for the SCT, and

perpendicular to both the wire and the radial direction, which is defined from the origin of the global reference frame to the centre of the straw, for the TRT drift-tubes. The y'-axis is along the long side of the module for the silicon devices and along the straw for the TRT elements. Finally, the z'-axis is orthogonal to the $(x' - y')$ plane.

After the alignment procedure, the corrections to the assumed geometrical positions of the detector elements are stored in a database [171] that is accessed by the ATLAS framework during the reconstruction of the recorded $p - p$ collisions events.

4.2 Track-based Inner Detector Alignment

The alignment procedure used in ATLAS to determine the position of the sensitive devices is known as *track-based alignment* [172, 173]. The concept behind this method is that the track fit quality is worsened by the presence of detector sensitive elements misalignments with respect to the assumed geometry. The track fit is based on the minimisation of the track to hit residuals $\boldsymbol{r}$ defined as

$$\boldsymbol{r} = \boldsymbol{m} - \boldsymbol{h}(\boldsymbol{\tau}, \boldsymbol{a}) \tag{4.1}$$

where $\boldsymbol{m}$ are the local measurements on the detector elements and $\boldsymbol{h}$ are the track hypothesis extrapolated to the detector elements surfaces. In a realistic approach to track fitting, the measurement model $\boldsymbol{h}$ does not depend only on the set of track parameters τ, see Sec. 3.1.1, but also on the alignment parameters $\boldsymbol{a}$ that are common to all reconstructed tracks. In fact, the orientation and positioning of a rigid body in space is determined by six degrees of freedom (*d.o.f.*), three translations (T_x, T_y, T_z) and three rotations (R_x, R_y, R_z) with respect to the cartesian axes x, y and z, respectively, of the alignment frame describing the alignable structure[1]. The *track-based alignment* procedure consists in the minimisation of a chi-square defined as

$$\chi^2 = \sum_{tracks} \boldsymbol{r}(\boldsymbol{\tau}, \boldsymbol{a})^{\mathrm{T}} V^{-1} \boldsymbol{r}(\boldsymbol{\tau}, \boldsymbol{a}) \tag{4.2}$$

where V is a matrix containing the detector measurements uncertainty [141]. In general V is not a diagonal matrix due to the contribution of the Multiple Coulomb Scattering which correlates the measurement accuracy on a surface with the hit on the previous one. The sum is performed over a large set of tracks such that large movements due to inaccurate track fits or low hit statistics per sensitive elements are averaged out. The χ^2 defined in Eq. 4.2 has a minimum for the spatial configuration of the detector elements corresponding to the real detector geometry:

$$\left. \frac{d\chi^2}{d\boldsymbol{a}} \right|_{\boldsymbol{a}=\bar{\boldsymbol{a}}} = 2 \cdot \sum_{tracks} \left(\frac{d\boldsymbol{r}}{d\boldsymbol{a}} \right)^{\mathrm{T}} V^{-1} \boldsymbol{r} \Big|_{\boldsymbol{a}=\bar{\boldsymbol{a}}} = 0 \tag{4.3}$$

where $\bar{\boldsymbol{a}}$ is the vector of the alignment parameters which defines the corrections to the assumed geometry. Expanding the first derivative of the alignment χ^2 around the initial

---

[1]In general, it is possible to define additional parameters in order to parametrise the residual dependencies due to modules bending or deformations of collective alignment structures (see Sec. 5.4.1).

assumed geometry $\boldsymbol{a_0}$ one obtains

$$\frac{d\chi^2}{d\boldsymbol{a}} \approx \frac{d\chi^2}{d\boldsymbol{a}}\bigg|_{\boldsymbol{a}=\boldsymbol{a_0}} + \frac{d^2\chi^2}{d\boldsymbol{a^2}}\bigg|_{\boldsymbol{a}=\boldsymbol{a_0}}(\boldsymbol{a}-\boldsymbol{a_0}) \tag{4.4}$$

where a linear approximation is used and the higher order terms have been dropped. Substituting Eq. 4.4 in Eq. 4.3, the detector alignment can be calculated solving

$$(\boldsymbol{a}-\boldsymbol{a_0}) = -\left(\frac{d^2\chi^2}{d\boldsymbol{a^2}}\bigg|_{\boldsymbol{a}=\boldsymbol{a_0}}\right)^{-1}\frac{d\chi^2}{d\boldsymbol{a}}\bigg|_{\boldsymbol{a}=\boldsymbol{a_0}}. \tag{4.5}$$

The linear approximation is necessary to make the problem computationally treatable and holds in the case when the expected misalignments are small and the initial assumed geometry is close to the real detector configuration. This is not true in general and the alignment solution is obtained using the Newton-Raphson method and iterating over the calculated corrections until the solution converges.

In order to simplify the notation, Eq. 4.5 can be rewritten as

$$\delta\boldsymbol{a} = -\mathcal{M}^{-1}\boldsymbol{v} \tag{4.6}$$

where

$$\begin{aligned} \delta\boldsymbol{a} &\equiv (\boldsymbol{a}-\boldsymbol{a_0}) \\ \mathcal{M} &\equiv \left(\frac{d^2\chi^2}{d\boldsymbol{a^2}}\bigg|_{\boldsymbol{a}=\boldsymbol{a_0}}\right) \\ \boldsymbol{v} &\equiv \frac{d\chi^2}{d\boldsymbol{a}}\bigg|_{\boldsymbol{a}=\boldsymbol{a_0}}. \end{aligned} \tag{4.7}$$

The Eq. 4.5 represents a system of equations with the dimension of the number of alignable parameters N, given by the product of the number of allowed number of $d.o.f.$ per structure times the total number of alignable elements considered. The first derivative $\frac{d\chi^2}{d\boldsymbol{a}}$ is a vector with dimension N, while the second derivative $\frac{d^2\chi^2}{d\boldsymbol{a^2}}$ is a matrix with the size $N \times N$ and is usually referred to as *big matrix*.

The next step in the alignment solution relies on the calculation of the total derivatives of the residuals with respect to the alignment parameters. The derivatives can be calculated as

$$\frac{d\boldsymbol{r}}{d\boldsymbol{a}} = \frac{\partial\boldsymbol{r}}{\partial\boldsymbol{\tau}}\frac{d\boldsymbol{\tau}}{d\boldsymbol{a}} + \frac{\partial\boldsymbol{r}}{\partial\boldsymbol{a}} \tag{4.8}$$

which lead to

$$\frac{d\chi^2}{d\boldsymbol{a}} = 2\cdot\sum_{tracks}\left(\frac{d\boldsymbol{r}}{d\boldsymbol{a}}\right)^{\mathrm{T}}V^{-1}\boldsymbol{r} = 2\cdot\sum_{tracks}\left(\frac{\partial\boldsymbol{r}}{\partial\boldsymbol{\tau}}\frac{d\boldsymbol{\tau}}{d\boldsymbol{a}} + \frac{\partial\boldsymbol{r}}{\partial\boldsymbol{a}}\right)^{\mathrm{T}}V^{-1}\boldsymbol{r} \tag{4.9}$$

$$\frac{d^2\chi^2}{d\boldsymbol{a^2}} \approx 2 \cdot \sum_{tracks} \left(\frac{d\boldsymbol{r}}{d\boldsymbol{a}}\right)^{\mathrm{T}} V^{-1} \left(\frac{d\boldsymbol{r}}{d\boldsymbol{a}}\right)$$

$$= 2 \cdot \sum_{tracks} \left(\frac{\partial \boldsymbol{r}}{\partial \boldsymbol{\tau}}\frac{d\boldsymbol{\tau}}{d\boldsymbol{a}} + \frac{\partial \boldsymbol{r}}{\partial \boldsymbol{a}}\right)^{\mathrm{T}} V^{-1} \left(\frac{\partial \boldsymbol{r}}{\partial \boldsymbol{\tau}}\frac{d\boldsymbol{\tau}}{d\boldsymbol{a}} + \frac{\partial \boldsymbol{r}}{\partial \boldsymbol{a}}\right) \tag{4.10}$$

where in Eq. 4.10 the second derivatives of the residuals with respect to the alignment parameters $\frac{d^2\boldsymbol{r}}{d\boldsymbol{a}^2}$ are neglected.

In the alignment framework two possible approaches are used to solve for Eq. 4.5, called *Global* and *Local* χ^2 approaches, described in the following sections.

4.2.1 Global χ^2 alignment

Considering that the alignment parameters are common to all the reconstructed tracks, a way to proceed consists in calculating the track parameters for a particular assumed geometry $\boldsymbol{a_0}$ and calculate their derivatives with respect to the alignment parameters. The track parameters $\bar{\tau}$ are obtained imposing on every single track the following condition

$$\frac{d\chi^2}{d\boldsymbol{\tau}}\bigg|_{\boldsymbol{\tau}=\bar{\boldsymbol{\tau}}} = 2 \cdot \left(\frac{\partial \boldsymbol{r}(\boldsymbol{\tau}, \boldsymbol{a_0})}{\partial \boldsymbol{\tau}}\right)^{\mathrm{T}} V^{-1} \boldsymbol{r}(\boldsymbol{\tau}, \boldsymbol{a_0})\bigg|_{\boldsymbol{\tau}=\bar{\boldsymbol{\tau}}} = 0, \tag{4.11}$$

where the fact that $\frac{d\boldsymbol{r}}{d\boldsymbol{\tau}} = \frac{\partial \boldsymbol{r}}{\partial \boldsymbol{\tau}}$ has been used since the alignment parameters do not depend on the track parameters. Similarly to what is done for 4.4, the solution around the minimum can be expanded linearly in the track parameters and obtain

$$\boldsymbol{\tau} = \boldsymbol{\tau_0} - \left(\frac{d^2\chi^2}{d\boldsymbol{\tau^2}}\bigg|_{\boldsymbol{\tau}=\boldsymbol{\tau_0}}\right)^{-1} \frac{d\chi^2}{d\boldsymbol{\tau}}\bigg|_{\boldsymbol{\tau}=\boldsymbol{\tau_0}} \tag{4.12}$$

where the initial track parameters $\boldsymbol{\tau_0}$ are assumed to be close to the track fit solution. Defining the matrix

$$E = \frac{d\boldsymbol{r}}{d\boldsymbol{\tau}}\bigg|_{\boldsymbol{\tau}=\boldsymbol{\tau_0}} \tag{4.13}$$

it is possible to show [174] that the covariance matrix for $\boldsymbol{\tau}$ is given by

$$C = \left(\frac{d^2\chi^2}{d\boldsymbol{\tau^2}}\right)^{-1} = E^{\mathrm{T}} V^{-1} E \tag{4.14}$$

and taking the derivative of Eq. 4.12 with respect to the alignment parameters one obtains

$$\frac{d\boldsymbol{\tau}}{d\boldsymbol{a}} = -C E^T V^{-1} \frac{\partial \boldsymbol{r}}{\partial \boldsymbol{a}}\bigg|_{\boldsymbol{\tau}=\boldsymbol{\tau_0}}. \tag{4.15}$$

The total derivative of the residuals with respect to the alignment parameters expressed

in Eq. 4.8 becomes

$$\frac{d\boldsymbol{r}}{d\boldsymbol{a}} = \left(\mathbb{1} - ECE^{\mathrm{T}}V^{-1}\right) \frac{\partial \boldsymbol{r}}{\partial \boldsymbol{a}}\bigg|_{\boldsymbol{\tau}=\boldsymbol{\tau_0}}, \tag{4.16}$$

where $\mathbb{1}$ is the identity matrix. The Eq. 4.16 shows that the alignment problem has been reduced to calculating first the partial derivatives of the residuals with respect to the track parameters for a fixed geometry, then the partial derivatives of the residuals with respect to the alignment parameters after each track has been reconstructed.

Due to this result, the procedure to align the ATLAS ID is split in two separate steps:

- **Accumulation**: During this step, tracks are reconstructed with the initial assumed geometry. A tight track selection is applied, both in terms of number of hits-on-track and p_T in order to ensure high quality tracks and minimise the effect of Multiple Coulomb Scattering. Once the tracks are obtained, the vector and matrix of the residual derivatives are computed.

- **Solving**: At this step, the second derivatives matrix is inverted and the Eq. 4.5 is solved to obtain the $\delta\boldsymbol{a}$ corrections to the initial geometry.

A complete calculation of the partial derivatives is carried out in [173] and is not reported here.

4.2.2 Local χ^2 alignment

It is clear that for the whole ATLAS ID system the *big matrix* becomes quite large and computationally challenging to invert, both in terms of CPU time and memory consumption. A way to simplify the problem is to ignore the correlations between alignment parameters of different modules in the detector and neglecting the derivatives of the track-to-hit residuals with respect to the track parameters. This method is referred to as *Local χ^2* [175, 176] and, under these assumptions, Eq. 4.9 and Eq. 4.10 reduce to

$$\frac{d\chi^2}{d\boldsymbol{a}} = \sum_{tracks} \left(\frac{\partial \boldsymbol{r}}{\partial \boldsymbol{a}}\right)^{\mathrm{T}} V^{-1} \boldsymbol{r} \tag{4.17}$$

$$\frac{d\chi^2}{d\boldsymbol{a}^2} = \sum_{tracks} \left(\frac{\partial \boldsymbol{r}}{\partial \boldsymbol{a}}\right)^{\mathrm{T}} V^{-1} \left(\frac{\partial \boldsymbol{r}}{\partial \boldsymbol{a}}\right) \tag{4.18}$$

where the second derivative $d\chi^2/d\boldsymbol{a}^2$ is a 6×6 block diagonal matrix, which is much less CPU-demanding to invert. This method, on the other hand, has a number of disadvantages. The solution is affected by poorly constrained modes since the positions of the single modules are restrained only by the neighbouring ones, there is no direct access to the covariance matrix for the alignment parameters and there is no direct access to the eigenvalues as they are not saved during the solving step. Finally, a larger number of iterations is generally needed to be performed in order to converge to a stable solution with respect to the *Global χ^2* approach.

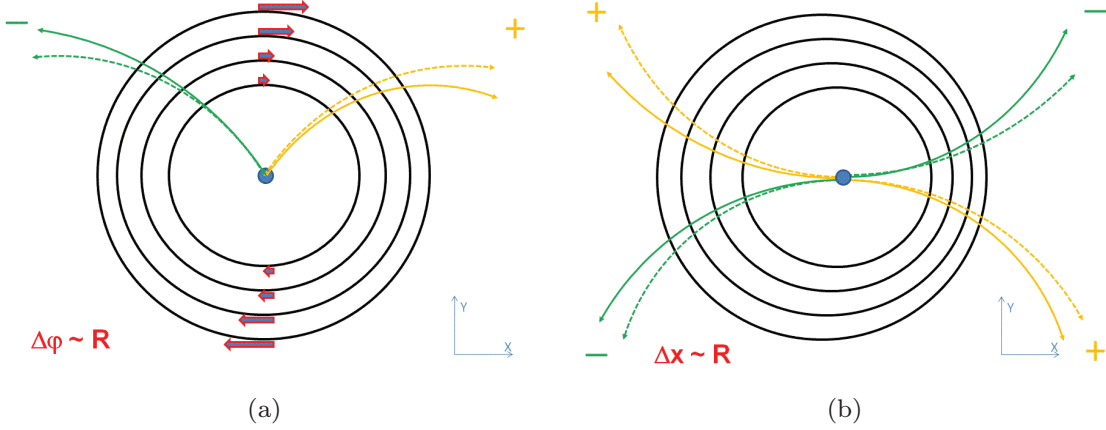(a)   (b)

Figure 4.1: Two examples of basic detector distortions creating a bias in the track recon-
struction without having an impact on the track quality. The *curl* (a) and the
radial (b) distortions affect the track parameters in a charge-antisymmetric and
charge-symmetric way, respectively. The schematic effect on the reconstructed
trajectory (full line) with respect to the true one (dashed line) is shown together
with the detector deformation. Figures taken from [177].

4.3 Alignment solution and Weak Modes

As discussed in the previous sections, the alignment solution involves the inversion of the
alignment second derivative matrix $\mathcal{M}$. Since this matrix is symmetric, it is always possible
to find an orthogonal matrix U such that

$$\mathcal{M} = UDU^{\mathrm{T}} \tag{4.19}$$

where D is a diagonal matrix. The matrix U is composed by the eigenvectors of $\mathcal{M}$, u_i^j
while D is formed by its eigenvalues, d_i. In this basis, the covariance matrix is given by

$$C = UD^{-1}U^{\mathrm{T}} \tag{4.20}$$

$$C_{ij} = \sum l \frac{u_i^l u_j^l}{d_l} \tag{4.21}$$

showing that it depends on the inverse of the eigenvalues, implying that alignment
correction modes that have a very small associated eigenvalue carry a very large uncertainty.
In particular, in the case of vanishing eigenvalues, the alignment *big matrix* needs some
additional regularisation, such as discarding unconstrained modes, in order to be inverted.
These modes are usually referred to as *weak modes* [172, 173] and indicate unconstrained
geometrical distortions to which the track based alignment is not sensitive to since they
leave the χ^2 invariant up to the second order.

Such distortions of the ATLAS ID geometry, which can arise from deformation of the
detector or are pure artefacts of the alignment solution, are particularly dangerous since

they can introduce track parameters biases that can not be determined and removed by just checking the track fit quality [178]. Two examples of possible *weak modes* deformations are shown in Fig. 4.1. In order to constrain *weak modes*, external constraints on the track parameters or the alignment parameters need to be considered. A possibility is to use universal measurements that depend on the track parameters such as the mass of known resonances or calorimeter information [177]. The procedure adopted by the constrained alignment solution is summarised in the following section.

4.4 Alignment with external constraints

The alignment procedure can be carried out considering additional constraints or regularisation procedures, when building the alignment χ^2 or inverting the *big matrix*. External constraints can be added to the procedure adding extra χ^2 terms with linear dependence on either the track parameters, the alignment parameters or both. We focus here only on the constraints used for the results presented in this thesis.

4.4.1 External track parameters constraints

Additional constraints on the track parameters are included in the alignment procedure modifying Eq. 4.2 to

$$
\begin{aligned}
\chi^2 &= \chi^2_{alignment} + \chi^2_{constraints} \\
&= \sum_{tracks} \boldsymbol{r}(\boldsymbol{\tau}, \boldsymbol{a})^{\mathrm{T}} V^{-1} \boldsymbol{r}(\boldsymbol{\tau}, \boldsymbol{a}) + \sum_{tracks} \boldsymbol{R}(\boldsymbol{\tau})^{\mathrm{T}} S^{-1} \boldsymbol{R}(\boldsymbol{\tau})
\end{aligned}
\tag{4.22}
$$

where the vector $\boldsymbol{R}(\boldsymbol{\tau})$ determines the residuals between the track parameters and the constraint and S^{-1} is a matrix parametrising the constraint tolerance. Following the same procedure described in Sec. 4.2.1, it is possible to show [172–174] that the alignment formalism of Eq. 4.6 still holds when applying modifications to the *big matrix* and the vector of the first derivatives that depend on the tolerance matrix S and the matrix

$$
F_\tau \equiv \left. \frac{\partial \boldsymbol{R}(\boldsymbol{\tau})}{\partial \boldsymbol{\tau}} \right|_{\boldsymbol{\tau}=\boldsymbol{\tau_0}}.
\tag{4.23}
$$

The results reported in this thesis make use of the following constraints to the track parameters to reduce the impact of *weak modes*:

- **Fixed track parameters constraints**: this is the most trivial constraint represented by a residual $\boldsymbol{R}(\boldsymbol{\tau}) = \boldsymbol{\tau} - \hat{\boldsymbol{\tau}}$, where $\hat{\boldsymbol{\tau}}$ is a defined set of tracks parameters. In this case the matrix $F_\tau = \mathbb{1}$ corresponds to the identity matrix and the tolerance matrix is a diagonal matrix with the inverse of the square of the constraints uncertainties on the diagonal.

- **Beam spot and primary vertex constraint**: the beam spot position (see Sec. 3.1.2) is used to constrain the transversal impact parameter d_0. The relations between the

track parameters of a track originating from the centre of the beam spot and the beam spot position (x_{bs}, y_{bs}, z_{bs}) is given by

$$d_0 = -(x_{bs} + z_0\alpha_{bs})\sin\phi_0 + (y_{bs} - z_0\beta_{bs})\cos(\phi_0) \tag{4.24}$$

where α_{bs} and β_{bs} are the beamspot tilt with respect to the global x and global y axis, respectively. The matrix of the constraints derivatives assumes the simple form

$$F_{\boldsymbol{\tau}} = \left(1,\ \frac{\partial d_0}{\partial z_0},\ \frac{\partial d_0}{\partial \phi_0},\ 0,\ 0\right) \tag{4.25}$$

and the tolerance matrix is just the σ_{d_0} computed by propagating the uncertainties on the beam spot parameters in Eq. 4.24. The use of the beam spot position in the alignment effectively constrains global translations at *Level 2* in the x and y direction since the transversal size of the beam spot are typically of the order of $\sim 5\mu$m. On the other hand it does not apply any significant constraint in translations along z due to an uncertainty on the longitudinal beam spot size of the order of ~ 40mm. To constrain the T_z *d.o.f.* , the position of the primary vertex (see Sec. 3.1.2) is used, which provides a significant constraint on the z_0 track parameter.

- **Mass resonances**: Some systematic deformations of the ATLAS Inner Detector due to weak modes manifest themselves in biases on the track momentum that can be evaluated by the effect on the reconstructed mass of standard candles, such as the Z boson. Considering the decay of the Z boson into two muons, $Z \rightarrow \mu\mu$, the Z mass is given by

$$m_Z^2 = 2p_1 p_2(1 - \cos\Delta\phi) \tag{4.26}$$

where $\Delta\phi$ is the opening angle of the two ultra relativistic muons of momenta p_1 and p_2. There are two major classes of possible deformations that affect the momentum of tracks [177]: *sagitta* deformations that alter the track curvature in an asymmetric way, such as twist of the barrel detector, or *radial* deformations that are charge symmetric instead. The effect of these distortions can be translated in transformation of the tracks momentum such as

$$\begin{aligned} q/p_T &\rightarrow q/p_T(1 + qp_{\mathrm{T}}\delta_{sagitta})^{-1} &\text{(sagitta)}\\ p_T &\rightarrow p_T(1 + \delta_{radial})^2 &\text{(radial)} \end{aligned} \tag{4.27}$$

where $\delta_{sagitta}$ and δ_{radial} parametrise the effect of the two classes of deformations discussed above. Considering the *sagitta* deformation, the Eq. 4.26 gives

$$\tilde{m}_Z^2 = 2p_1(1 - q_1 p_1 \delta_{sagitta,1})p_2(1 - q_2 p_2 \delta_{sagitta,2})(1 - \cos\Delta\phi) \tag{4.28}$$

which leads to

$$\frac{\tilde{m}_Z^2 - m_Z^2}{m_Z^2} = p_1 q_1 \delta_{sagitta,1} + p_2 q_2 \delta_{sagitta,2} \tag{4.29}$$

where only the terms linear in $\delta_{sagitta}$ are kept. As can be noticed, the two muons are affected in a different way, but since is not possible a priori to determine which of the two muons is biased, half of the mass ratio is used to determine the sagitta deformation to be applied to each muon momentum. This leads to:

$$\delta_{sagitta,i} = \frac{1}{2} \frac{\tilde{m}_Z^2 - m_Z^2}{m_Z^2} \frac{1}{p_1} \qquad i = 1, 2. \tag{4.30}$$

A similar procedure can be applied in the case of radial distortions leading to

$$\delta_{radial,i} = \frac{1}{2} \frac{\tilde{m}_Z^2 - m_Z^2}{m_Z^2} \qquad i = 1, 2. \tag{4.31}$$

The same $Z \rightarrow \mu\mu$ events are also used to constrain the track impact parameters imposing that the two muon tracks must come from the same vertex and therefore must have the same longitudinal impact parameter and opposite transverse impact parameter with respect a reference point. The corrections to the impact parameters become

$$\begin{aligned} \delta_{d_0} &= d_0(\mu^+) - d_0(\mu^-) \\ \delta_{z_0} &= z_0(\mu^+) - z_0(\mu^-) \end{aligned} \tag{4.32}$$

The momentum corrections are expected to depend on the track η and ϕ due to non-uniform detector deformations and are determined using an iterative Gaussian fit procedure. Firstly, the corrections distributions for each $\eta - \phi$ bin are fitted to extract their mean μ and standard deviation σ, then only the region confined in $\mu \pm 1.5\sigma$ is fit again in order to extract the value of the peak of the distribution without being affected by the tails due to muon candidates which have their invariant mass far from the Z boson mass value. This procedure is iterated until the fit values are stable with respect to a chosen uncertainty.

4.4.2 Soft Modes Cut

It is possible to set a constraint directly on the alignment parameters using the results of an external measurement of the positions of the sensitive elements, known as *survey data*, or introducing a *penalty* to the modes that have a large associated uncertainty [173]. In the 2015 Alignment campaign, only the second method, denoted as *Soft Mode Cut*, has been used and consists of adding finite terms to the diagonal of the alignment *big matrix* of the type $\delta_{\text{cut-off}} = 1/\sigma_{SMC}^2$, where σ_{SMC} represents the cut off on the uncertainty allowed on a particular alignment mode. The corrections to the alignment parameters become

$$\delta\boldsymbol{a} = (\mathcal{M} + G_{SMC}^{-1})\boldsymbol{v} \tag{4.33}$$

where G_{SMC} is a diagonal matrix containing the cut-off values. While the eigenvectors are left unchanged, the eigenvalues are transformed to

$$\lambda_i \to \lambda_i + 1/\sigma_{SMC}^2 \tag{4.34}$$

removing the singularities due to weak modes.

4.5 Run 2 Commissioning

During LS1, the ID Alignment framework underwent a series of upgrades consisting of an update of the alignment code and maintenance of the framework configuration to match with the ATLAS reconstruction software developments for Run-2. A major improvement in this context is the introduction of the Insertable B-Layer inside the alignment framework. This task required a set of changes in the ATLAS geometry and the alignment levels definition. In order to check the full functionality of the alignment for Run-2, a commissioning using MC simulated samples is performed.

4.5.1 Insertion of the IBL in the ID Alignment Framework

The Inner Detector subsystems are integrated in the ATLAS conditions database and the alignment corrections to the nominal geometry are stored in two dedicated folders: one for the Pixel and SCT systems and one for the TRT sub-detector. The folder dedicated to the silicon system stores both the corrections to global movements and the corrections to the position of the single active elements with respect to the module local coordinates. These positions get updated in the database according to the level of granularity of the alignment solution. The presence of a new layer of the Pixel detector required an update of the Silicon folder in order to store the dedicated corrections for both global and local reference systems. The following step was to enlarge the alignment vectors and matrix to cope with the additional structures and the granularity levels were extended to the new detector. These changes are relatively straightforward for the high granularity L2 and L3, as the IBL represents just an additional Pixel layer or additional silicon modules, respectively. On the other hand the *Level 1* was modified to treat separately the Pixel subsystem and the IBL Layer. The reason behind treating the IBL as a separate system despite it being part of the Pixel sub-detector, relies in the IBL mounting system and its positioning with respect to the Pixel. The 14 IBL staves are individually mounted on support rings which are glued to the Inner Positioning Tube (IPT) as outlined in Sec. 2.2.3. The rings placed at the end of the staves are fastened to the IBL Support Tube (IST), which is a rigid structure anchored to the Pixel Support Tube, which is connected to the support structure of the rest of the Inner Detector, and its axis is centred using the Inner Support Interlink Structure. Even if in principle the two structures are connected, between the IBL active elements and the Pixel frame there are a series of elements that define their positioning.

At the beginning of Run-2, the position of the IBL with respect to the ID reference frame was known from survey data at the level of $100\mu m$ in z, a much lower accuracy than needed for precision tracking. In addition, to permit the insertion of the IBL, the Pixel detector was to be moved out and subsequently replaced. This operation might have led
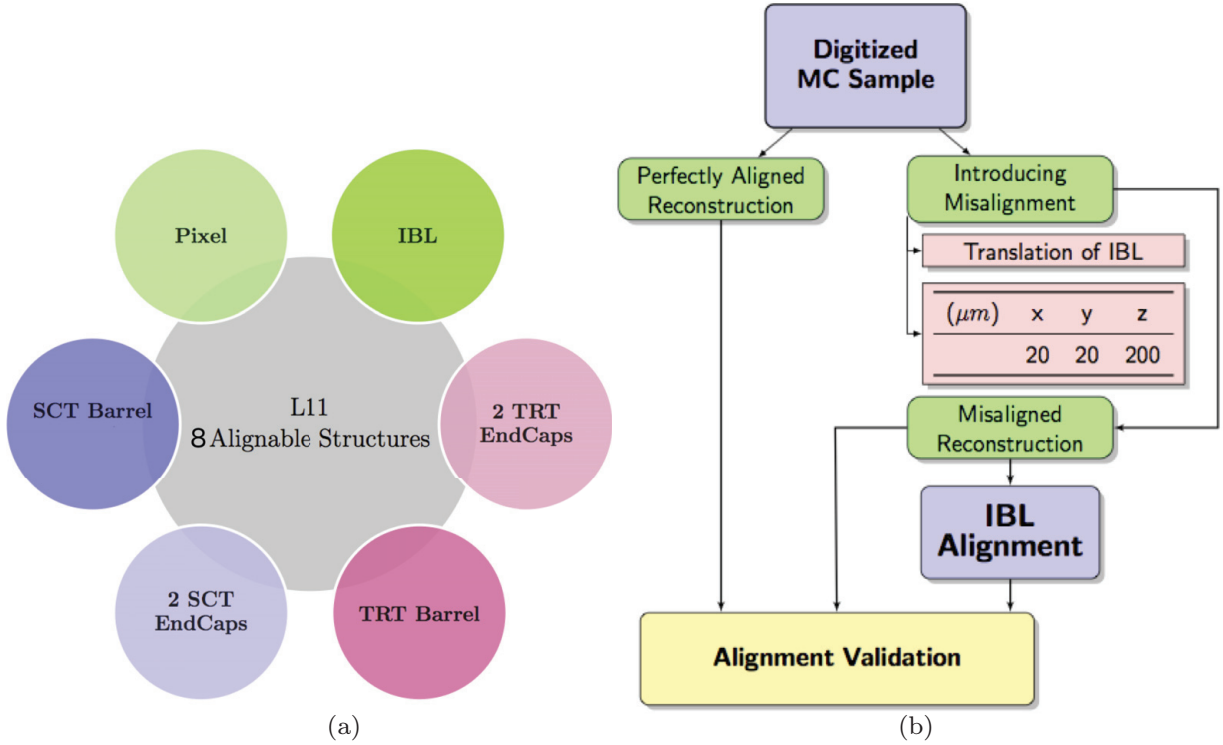
Figure 4.2: Schematic representation of the L11 structures (a). Workflow of the test performed on MC simulation for the IBL integration in the Alignment framework (b).

to significant movements in positioning with respect to the Run-1 geometry. The need of a very accurate determination of the IBL and Pixel position at μm level with respect to the rest of the ID justifies the need of a different treatment of the two sub-systems from an alignment framework point of view. Therefore a new level, called *Level 11* (L11) considers the old Pixel, SCT and TRT as in the L1, with the addition of the IBL as an independent structure. A schematic representation of the L11 alignable structures is given in Fig. 4.2a. In addition, since the IBL is a new type of detector in ATLAS, its behaviour to environmental changes is not known at this stage. The use of the L11 for the run-by-run alignment permits to monitor closely the behaviour of the IBL during data taking, without the risk of introducing weak modes when aligning at higher granularity levels, such as L2.

The first alignment test with the IBL included in the ATLAS geometry for Run-2 has been performed using a MC simulation sample composed of single muons with fixed p_T of [5,15,50,100] GeV in the range $|\eta| < 2.5$. A realistic initial misalignment of the ID structure has been inserted in the simulated geometry assuming a shift of the IBL of 20μm along global x and y and 200μm along the z direction. The MC sample is then reconstructed with both perfect and misaligned geometry using the L11, configured using the SCT barrel as reference. This choice reflects a very realistic choice that can be adopted at the beginning of Run-2. A diagram showing the workflow for this test is shown in Fig. 4.2b. The comparison between the perfect, the misaligned and the aligned geometry is shown in Fig. 4.3. The
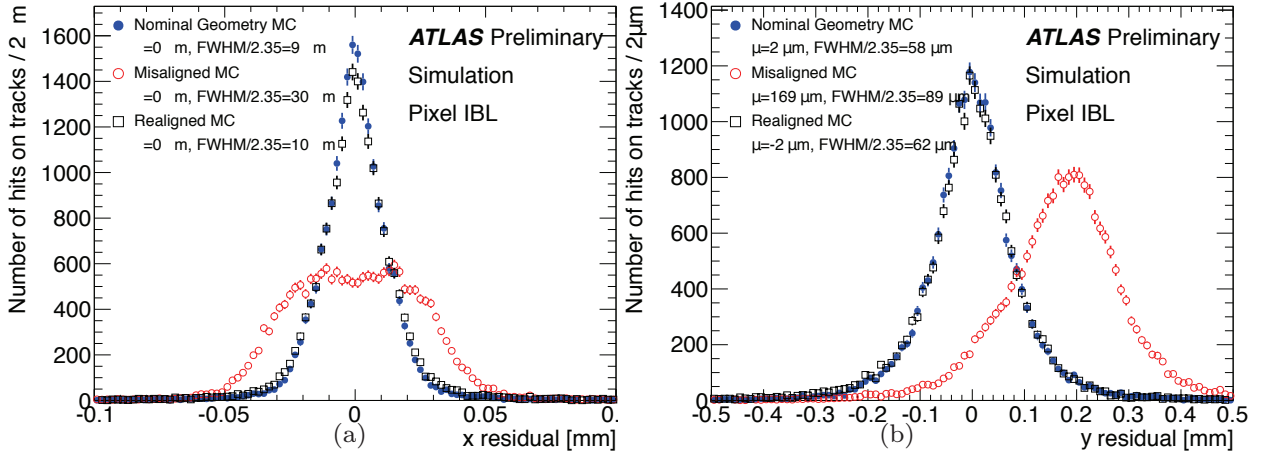
Figure 4.3: Residual distributions for the local x (a) and local y (b) for the IBL detector obtained with nominal ATLAS ID geometry (blue dots), after introducing the misalignment described in the text (red open dots), after re-alignment (white open squares). The hits are integrated all over the 14 staves.

results show that the updated alignment framework is capable to recover the misalignment introduced, substantially improving the resolution of the reconstructed tracks.

4.6 Frequency of the Alignment corrections in ATLAS

As discussed in Sec. 4.1, the alignment procedure in ATLAS is split in three levels of corrections that require increasing computation time and number of accumulated tracks. Therefore the *Level 1*, *Level 2* and *Level 3* corrections are calculated and applied with different frequency during the ATLAS data taking period and calibration.

Level 1 corrections are computed at the end of each run as part of a routine procedure called *Calibration Loop*, where the detector conditions and calibrations are calculated as well as the beam spot position. The frequency of these correction is therefore about one computation per day.

These corrections are calculated with respect to a reference set of alignment constants obtained at *Level 2* and *Level 3* of geometry granularity at the beginning of data taking from calibration runs, such as cosmic rays data or an initial set of collisions runs. The statistics used for the initial baseline corrections is not sufficient for correcting weak modes, hence typically this set of constants does not have a very high quality in terms of residual distributions mean and width and might induce track parameters biases affecting the whole ID resolution. Therefore, *Level 2* and *Level 3* constants are usually re-calculated during technical stops, when larger statistics is available. This happens, typically, only one or two times during data taking.

Finally, at the end of a data taking campaign, new baseline constants up to *Level 3* granularity are re-calculated with larger statistics and a set of external constraints in order to derive a higher quality set of baseline constants. Starting from the re-computed baseline, all the runs collected during the year are corrected at *Level 1* alignment. This procedure

is called *alignment reprocessing* and it is performed once after the completion of the data taking.

5 Inner Detector Alignment in Run-1 and early Run-2

An overview on the state-of-the-art Inner Detector alignment at the end of Run-1 data taking is presented. During the LS1 the alignment framework has been updated to include the IBL as new structure and a new alignment level that is currently used as global structures alignment procedure for Run-2. The techniques and procedures adopted in 2015 to deliver the final alignment constants are discussed.

5.1 Inner Detector Alignment for 2012 data

Since the ID alignment results and performance at the end of Run-1 is described in detail in [136], only a brief summary is given in this section. The alignment constants used as a baseline in 2012 data taking are derived using 4 fb^{-1} of integrated luminosity in a period of time characterised by a very stable detector in terms of global movements. This period is identified by computing the *Level-1* constants periodically during data taking. All levels of alignment have been performed in this period following the procedures outlined in [179]. The description of the Inner Detector geometry in Run-1 includes run-by-run time-dependent displacements occurring due to environmental changes, the determination of the relative positioning of the sensitive devices and the constraint of track parameter biases due to systematic deformations.

5.1.1 Run-by-run corrections

Starting from the fixed reference constants, the *Level 1* corrections are calculated for all each ID sub-systems using the Pixel detector as reference. The T_x global movements of the various subsystems are shown in Fig. 5.1. The TRT and SCT barrel substructures show a level of stability of the order of a few μm. The SCT end-caps and TRT end-caps instead show sudden movements of up to 20 μm in size. These abrupt movements of the sub-systems are related to sudden changes to the environmental conditions such as sub-system cooling temperature changes, power cuts, technical stops during which the detector is turned off, magnetic field changes or gas leakages. Often such abrupt changes are followed by gradual movements which are interpreted as relaxations of the sub-systems to an equilibrium state, that might last up to several weeks before stability as can be noticed in particular for the end-caps subsystems.

5.1.2 Alignment Performance

The ID alignment constants performance is assessed using various techniques. One of these techniques is the study of the *unbiased* track-to-hit residuals and their comparison to a
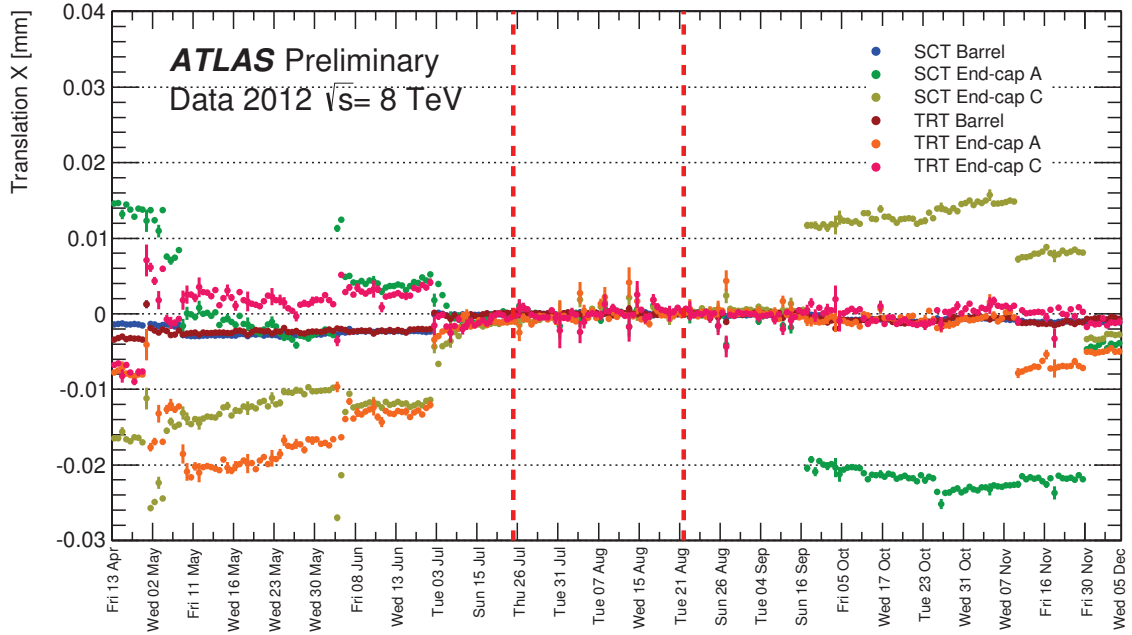
Figure 5.1: Corrections to the T_x global movement of the ID sub-systems with respect to the Pixel detector during 2012. The vertical red dashed lines indicate the period of time used for deriving the reprocessing baseline constants. The uncertainty reported is only statistical. Since the Pixel detector is used as a reference, it does not appear in this figure[136].

perfectly aligned MC sample. A systematic misalignment of a part of a sub-system would manifest itself as a bias in the mean of the track-to-hit residuals of a sub-system, while a random residual misalignment would leave the distribution centred on zero but with a degraded resolution. In addition, standard candles such as J/ψ, K_S or Z that have a very precisely known mass can be used to check, and also correct, eventual momentum or impact parameter biases. These methods are outlined in the following.

Track-to-hit Residuals

Muon tracks originating from $Z \rightarrow \mu\mu$ decays are used to evaluate the track-to-hit residuals both in data, collected by either low-p_T di-muon or high-p_T single muon triggers, and in a MC sample generated using PYTHIA-8.1 [180]. The residual distributions integrated over the Pixel, SCT and TRT barrel are shown in Fig. 5.2. While reasonably good agreement is seen between data and MC for the SCT, in the Pixel larger residual width is observed in data, while the opposite is seen for TRT. The discrepancies between data and MC simulation in the Pixel residual distribution are thought to be due to a mis-modelling of the charge deposition distribution in the Pixel sensors.
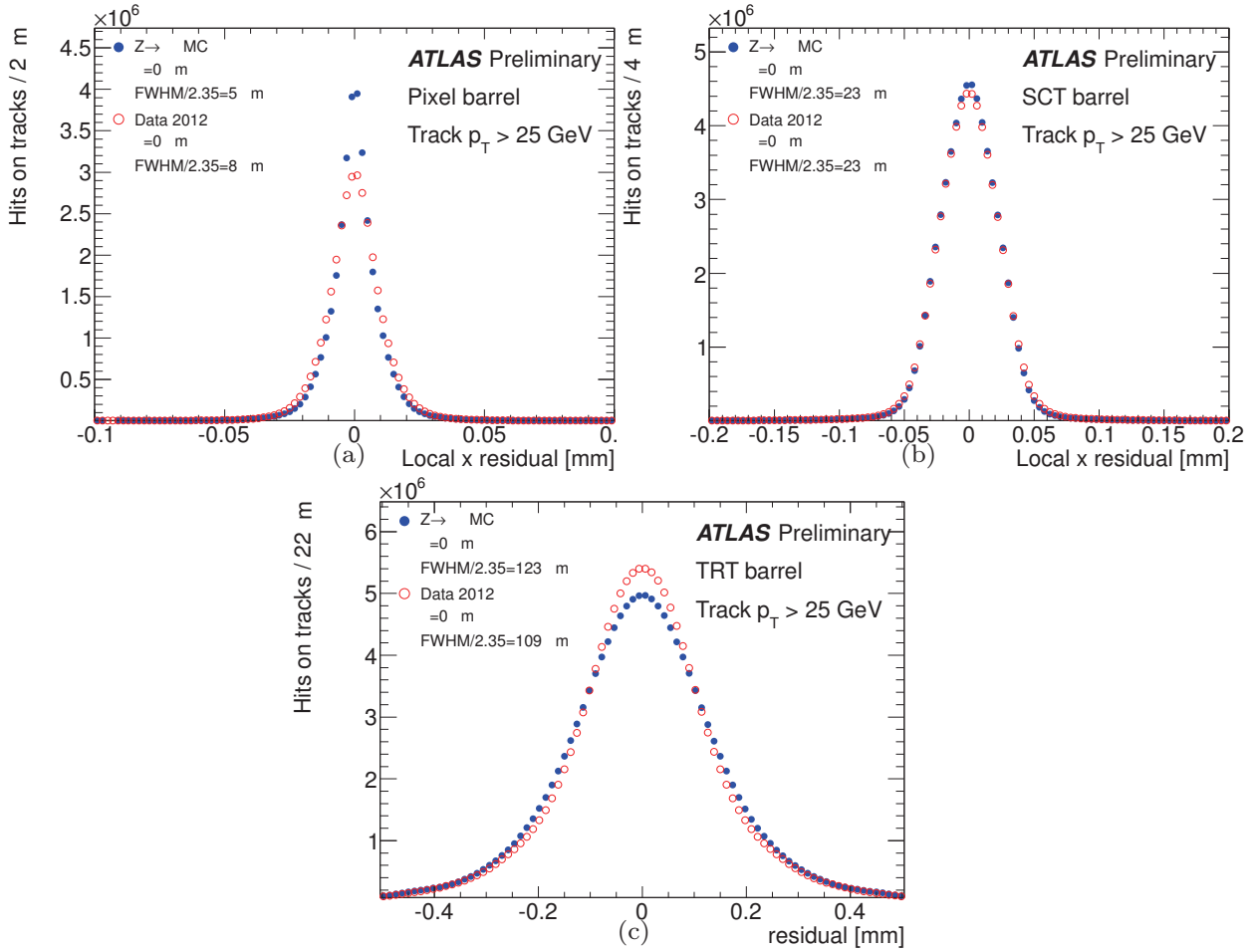
Figure 5.2: The Pixel (a) and SCT (b) local x residual and the TRT (c) local r residual distributions integrated over the barrel. Figures taken from [136].

Track Parameters Biases

In the 2012 alignment reprocessing campaign the track momentum biases have been minimised during the determination of the baseline constants through the introduction of external constraints obtained from the $Z \to \mu\mu$ and E/p methods [177]. The results from the E/p method, which compares the energy of electrons measured in the electromagnetic calorimeter to their momentum measured in the ID, show a residual sagitta bias $\delta_{sagitta}$ (see Eq. 4.27) in the negative endcap region of about -0.6 TeV^{-1}, or 3% at $p_T = 50$ GeV, while the mean sagitta bias is 0.023 TeV^{-1} with an RMS of 0.14 TeV^{-1}, which translates to 0.12% at $p_T = 50$ GeV. The results from the $Z \to \mu\mu$ method are similar with a mean sagitta bias of -0.009 TeV^{-1} and an RMS of 0.12 TeV^{-1}. The difference in the two mean values is attributed to the fact that the global sagitta biases enter as second order in the Z invariant mass. In Fig. 5.3 the sagitta biases results for 2012 reprocessing are shown.

In a similar way to the method used to determine the sagitta biases, the track impact parameter biases can be measured applying the corrections to the measured impact param-
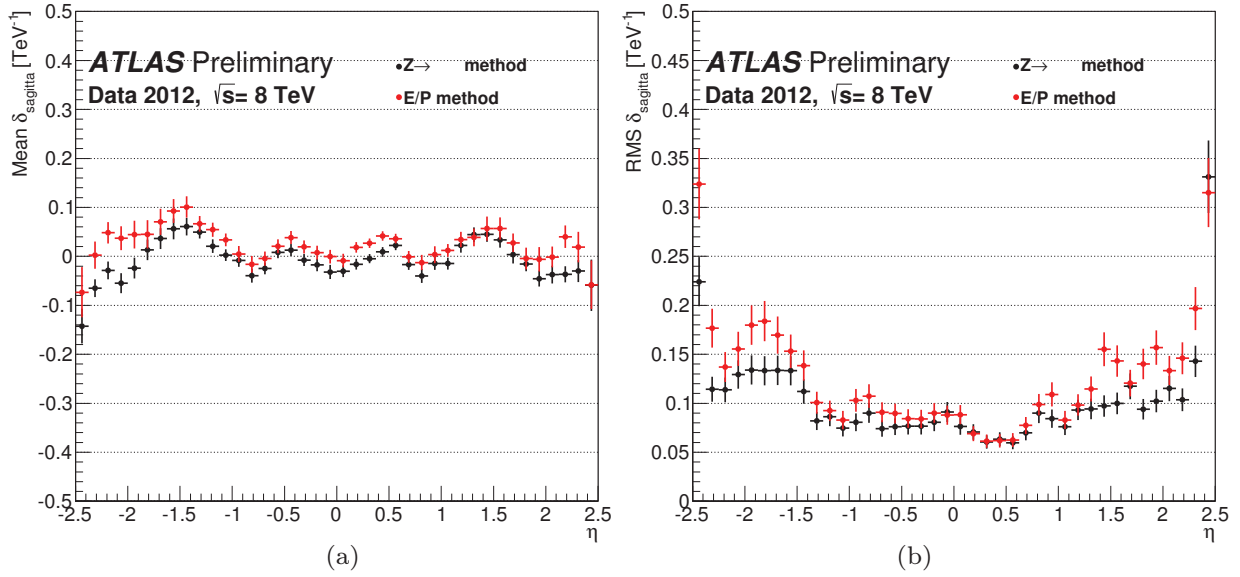
Figure 5.3: Comparison of the measured sagitta biases as a function of pseudorapidity using the $Z \to \mu\mu$ and E/p methods in 2012 data.

eters of the two muons originating from the $Z \to \mu\mu$ decay. The biases are corrected by adding $\eta - \phi$ dependent constraints to the impact parameters of the tracks used to perform the alignment. At the end of the 2012 alignment reprocessing campaign, the bias on the transverse impact parameter has a mean of $\delta_{d_0} = 0.024$ μm and an RMS of 0.8 μm, while the longitudinal impact parameter has a mean $\delta_{z_0} = 1.64$ with an RMS of 6.6 μm.

5.2 Inner Detector Alignment for 2015 data

5.2.1 Cosmic rays data alignment

As stated in the previous chapter, the position of the Pixel detector at the beginning of Run-2 is expected to be within 100μm from the nominal location inside the Pixel support tube thanks to the precision of the accurate mechanical mounting system. In addition, the IBL position is known only from survey data at a similar accuracy level. On the other hand, the SCT and TRT have not been removed during LS1. In order to determine more precisely the positions of all ID sub-systems in preparation for Run-2, a track-based alignment is performed using cosmic ray data recorded with the ATLAS detector. In this campaign, the TRT barrel is used as a reference to extract the alignment corrections. The results discussed in this section are described in higher level of detail in [100].

Cosmic ray data represent a set of data that is used for commissioning of several parts of the ATLAS detector and comprise predominantly events passing through the detector from top to bottom. This feature correlates the top and bottom shells of the ID and is particularly powerful in constraining weak modes in the alignment solution. On the other hand, cosmic ray data do not provide a uniform illumination of the ID modules: lower number of hits are recorded in the end caps and in the barrel modules located in either side,

Level	Description	Structures	DOF
1	IBL	1	All except R_x
	Pixel detector	1	All except R_x
	SCT barrel (end-caps fixed)	1	T_x, R_y, R_z
2	IBL and Pixel barrel split into layers	4	All except R_x
	Pixel end-caps split into discs	6	T_x, T_y, R_z
	SCT barrel split into layers	4	T_x, R_y, R_z
	SCT end-caps split into 2	2	T_x, T_y, R_z
PIX-stave 2	IBL and Pixel barrel split into staves	126	T_x, T_y, R_y
	Pixel end-caps split into discs	6	T_x, T_y, R_z
	SCT barrel split into layers	4	T_x, R_y, R_z
	SCT end-caps split into 2	2	T_x, T_y, R_z
PIX 3	IBL and Pixel barrel modules	1736	T_x, T_y, R_y, R_z
	Pixel end-caps split into discs	6	T_x, T_y, R_z
	SCT barrel split into layers	4	T_x, R_y, R_z
	SCT end-caps split into 2	2	T_x, T_y, R_z

Table 5.1: Alignment levels and degrees of freedoms used during Run-2 cosmic ray data commissioning together with their brief description. The TRT detector is kept fixed during the alignment procedure.

where the cluster sizes are also generally larger due to the large track incident angle. Due to these limitations, depending on the granularity of the alignment level, a full structure or a group of modules as well as some degrees of freedom (DOF) are fixed during the alignment procedure due to a low number of hits-on-track or an expected poor resolution. The cosmic ray data consists of muons created by primary cosmic ray interactions with the Earth's atmosphere and are produced at typically 15 km high in the atmosphere. The mean energy of muons is about 4 GeV at the ground level and the integral intensity for normally incident muons is about 70 $m^{-2}s^{-1}sr^{-1}$.

The alignment campaign uses two data sets recorded in February and March 2015[1] collected using a trigger based on a fast hardware-based logical `OR` of the TRT wires having a hit along a possible muon track path [181]. The trigger has an efficiency of about 90% and an average rate of 4.9Hz. The tracks used by the alignment procedure must pass a series of quality cuts defined in [100]. After the track selection, about $5 \cdot 10^4$ tracks for the February data set and about 10^5 tracks for the March dataset are available for alignment. The two sets have not been combined since large global movements have been measured between the two datasets, but instead two subsequent alignment procedures have been performed. The distributions of the signed transverse momentum $q \cdot p_\mathrm{T}$ and of the pseudorapidity η are shown in Fig. 5.4. The asymmetry in the $q \cdot p_\mathrm{T}$ distribution is due to a

---

[1]The first track-based alignment with cosmic ray data was performed in November 2014, providing a very coarse location of the ID elements, including the IBL. For the sake of brevity, only results that are public are treated in this thesis. The *before alignment* label in the legend of the plots of Sec. 5.2.1 indicates data reconstructed with the constants obtained from this coarse alignment.
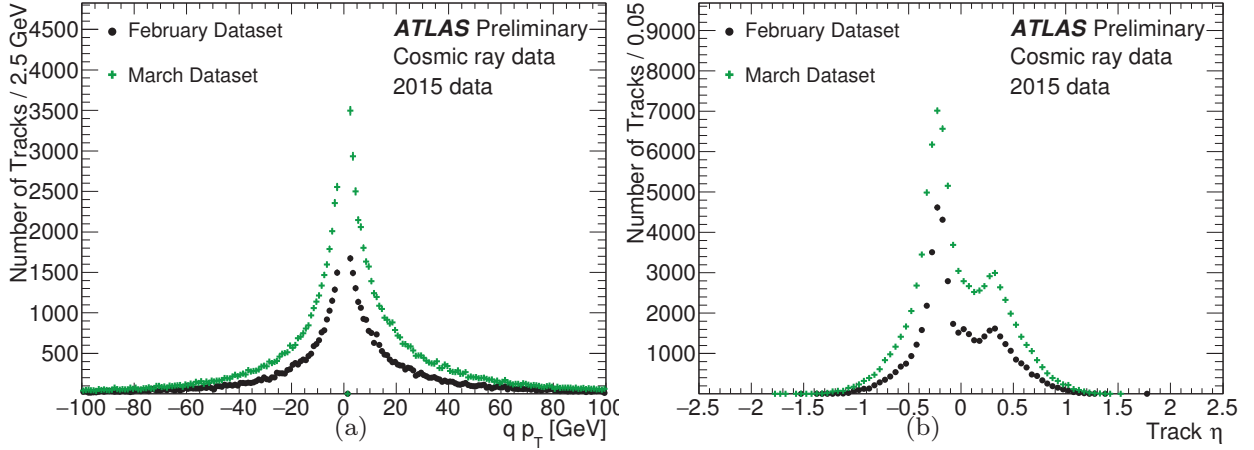
Figure 5.4: Distributions of the $q \cdot p_T$ (a) and η (b) of the collected cosmic ray data in February (black) and March (green) 2015. The two distributions are not normalised to each other to show the different statistics of the datasets.
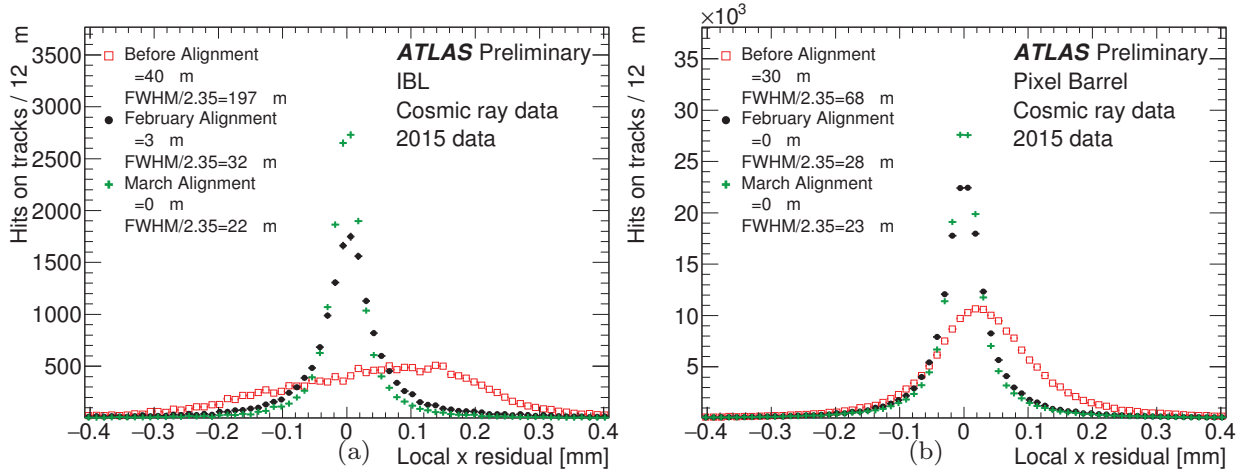

Figure 5.5: Distribution of the local x residuals integrated over the full IBL (a) and the outer three layers of the Pixel Barrel (b). The march distribution has been re-scaled to February's number of entries.

higher flux of atmospheric μ^+, due to a larger fraction of positively charged primary cosmic rays [149], while the double peak distribution of η is due to the construction shafts used to lower the ATLAS detector into the cavern that are open during cosmic ray data taking to allow for higher data collection rate. The local x residual distributions for the IBL and for the outer three layers of the Pixel detector are shown in Fig. 5.5. In order to quantify the improvement on the track parameter resolution, the *split tracks* method is used [100]. The method consists of selecting the hits in the top and bottom shell of the ID from a particular cosmic track and refit them separately into two split track segments. Even if the difference between the track parameters of the top and bottom track segments has to be zero since the two tracklets belong to the same track, detector resolution and biases
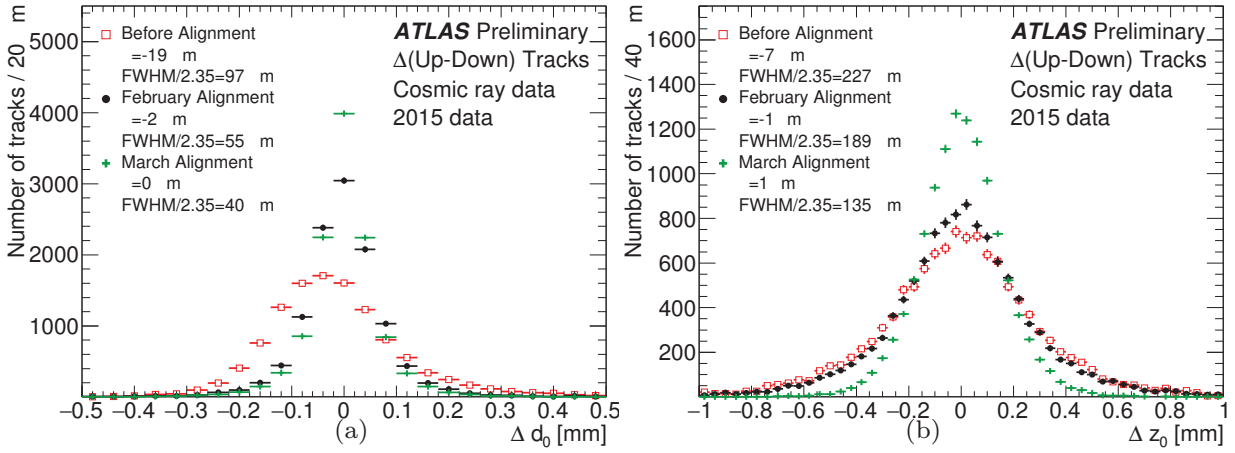
Figure 5.6: Distribution of the difference of the reconstructed track impact parameters Δd_0 (a) and Δz_0 (b) using the *split Tracks* method described in the text.

due to misalignment in different parts of the ID would lead to biases in the distribution and additional smearing. The distribution of the differences between the tracklets impact parameters Δd_0 and Δz_0 are shown in Fig. 5.6, where it is possible to observe a net improvement due to the track-based alignment iterations. A systematic deformation is found in a detailed study of the IBL residual distributions mean shown in Fig. 5.7. In the figure the local x and local y residuals mean are shown as a function of the module location along the stave (η-index) and integrated over all 14 staves[2]. The distribution of the local x residuals mean indicates an in-plane deformation of the IBL staves in the negative local x axis with respect to the flat stave geometry, while the distribution in local y might point to a systematic displacement of the modules along the IBL staves. The IBL modules have been glued on the staves from the stave-center outwards, therefore such a stave elongation with respect to the nominal geometry may be due to a wider gap between neighbouring modules with respect to the nominal positioning. As shown in Fig. 5.7, a L3 alignment of the IBL modules is able to correct for such systematic displacement and recover a flat-stave geometry. The description of the IBL geometry is given in Sec. 2.2.3.

5.3 Causes of the IBL Stave Distortion

Detailed studies have been carried out during 2015 to determine if the IBL systematic deformation depends on the ATLAS detector operation conditions in terms of operating temperature and power consumption. In fact these two conditions are amongst the ones that are more susceptible to changes and fluctuations during data recording within an LHC run. Understanding the stability of the IBL detector is indispensable to ensure high quality reconstructed data.

---

[2]As described in Sec. 2.2.1 and Sec. 4.1, the local x coordinate is along global $r - \phi$ direction, while local y is along global z direction for the Pixel detector. The η-index indicate the position of a module along the Pixel staves along global z direction. Higher absolute values of the η-index indicate modules closer to the extremes of the staves.
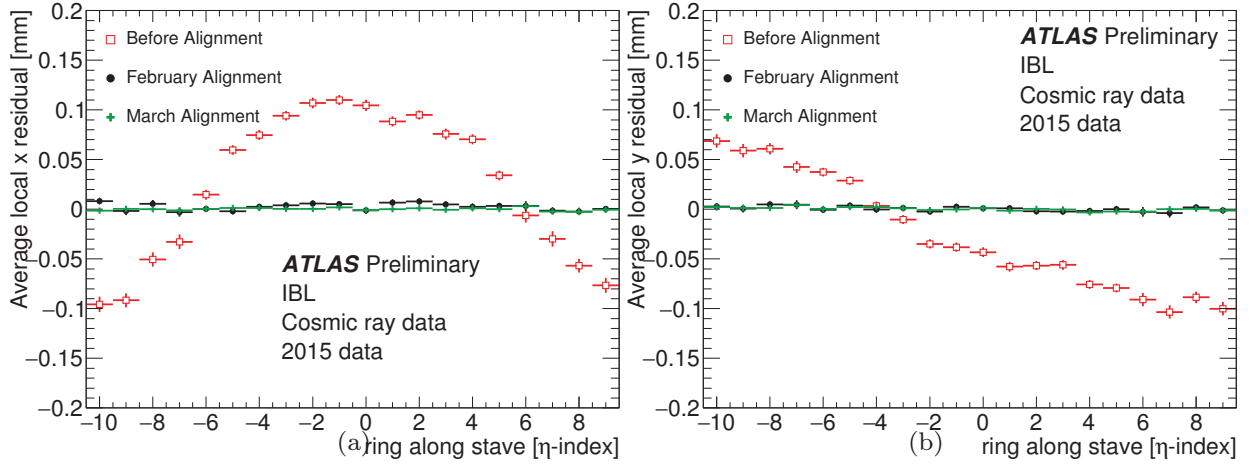
Figure 5.7: The IBL mean of the local x (a) and local y (b) residuals distributions as a function of the η position of the module indicated with its index along the staves and integrated over ϕ.

5.3.1 Measurement of the IBL distortion in Cosmic ray data

A correlation of the IBL operating temperature to the size of the stave distortion is studied in a particular subset of the March cosmic ray dataset collected at different temperature set points as defined in Sec. 2.2.4 ranging between $+15^{\circ}$ C and -20° C as shown in Fig. 5.8. Each run contains more than 5×10^{5} tracks and, after a basic track selection listed in [111], about 17% of the tracks are retained for the distortion studies. In order to demonstrate the effect due to temperature changes, a set of alignment constants with null corrections to the ideal geometry of flat staves is used as reference for the reconstruction. The distribution of the local x residuals integrated over the hits collected on all the staves is shown in Fig. 5.9. From the diagram it is possible to observe that the staves are flat within 10μm at a cooling pipe temperature of $+15^{\circ}$ C, corresponding to a module temperature close to the room temperature of $+20^{\circ}$ C, and strongly distort in the $r\phi$ direction when the temperature is changed.

The measurement of the size of the distortion as a function of the set temperature is obtained from a different baseline set of constants calculated up to *Level 3* using data collected at -20° C, as shown in Fig. 5.10. The averaged local x residual distribution mean displacement r_x is fitted with a parabolic function defined as:

$$r_x(z) = B + M \left(1 - \frac{z^2}{z_0^2} \right) \tag{5.1}$$

where z is the position of the module along the z-axis, $z_0 = 366.5$mm is the fixing point of each IBL stave at both ends, B is the baseline which describes a global overall translation of the stave in the global $r\phi$ direction and M is the magnitude of the stave distortion. In the fit the baseline B has been fixed to zero for all temperature points because the end-blocks of each stave are fixed mechanically and the only free parameter of the fit is the magnitude M. This is justified also by the fact that the baseline B is highly correlated with
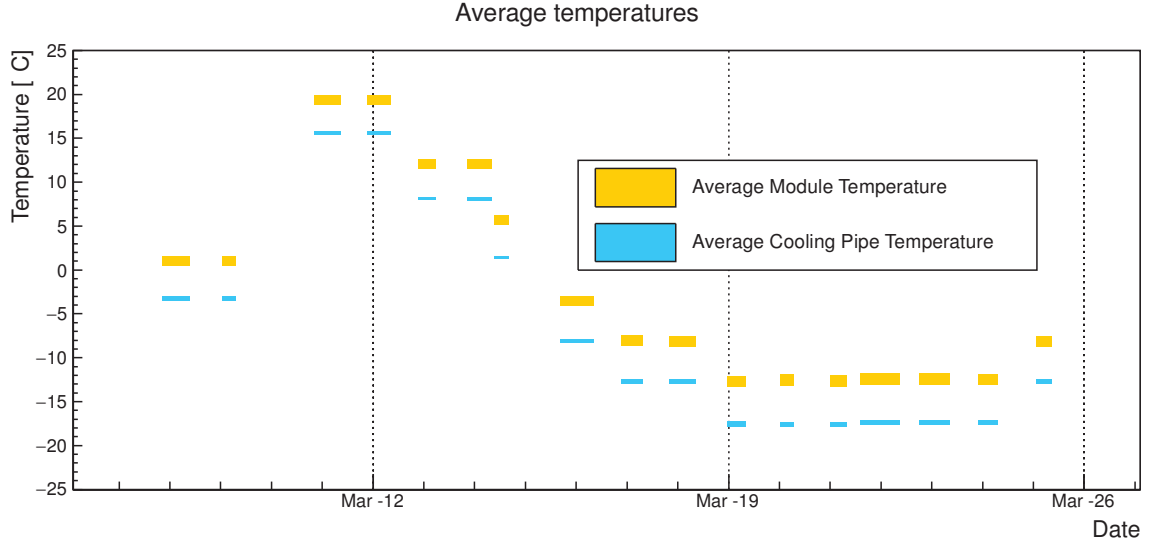
Figure 5.8: IBL module and cooling pipe temperature during the cosmic ray data temperature scan runs in March 2015.
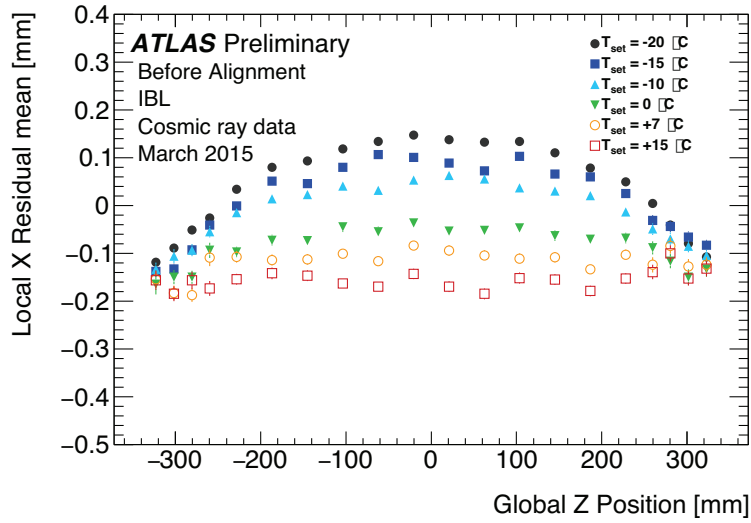

Figure 5.9: IBL track-to-hit residual distribution mean in the local x direction during the temperature scan runs. The residuals mean is averaged over all hits on modules corresponding to the same z position on the stave. No alignment corrections are applied to the IBL modules in the local frame during the track reconstruction. The uncertainty associated to the points is only statistical.

global rotations along z of the IBL detector, that are corrected by the alignment reference constants already at *Level 11*. The magnitude distortion is extracted as a function of the set temperature and a linear dependence is observed. The gradient of the magnitude of
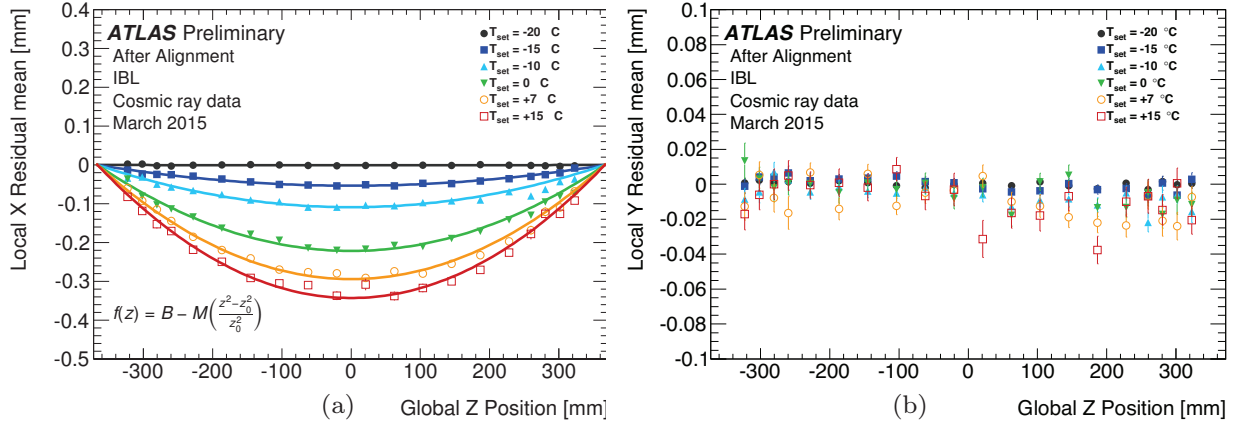
Figure 5.10: The IBL track-to-hit residual distributions mean in the local x (a) and local y (b) direction during the temperature scan runs as a function of the z position on the stave and the parabolic fit. Alignment corrections derived at $-20\ ^\circ$C are applied to the module positions. The uncertainties on the points are only statistical.

the distortion is extracted from a linear fit to be

$$\frac{\mathrm{d}M}{\mathrm{d}T_{\mathrm{set}}} = -10.6 \pm 0.7\ \mu\mathrm{m/K}. \tag{5.2}$$

The linear fit is shown in Fig. 5.11. The uncertainty on the above measurement is due to the statistical uncertainty combined with a systematic uncertainty estimated by performing the same fit without constraining the baseline B. This observation is studied with a set of Finite Element Analysis (FEA) simulations performed on the IBL staves and the results are qualitatively discussed in the next section. No dependence on temperature is observed in z direction within 20μm as shown by the local y residuals distributions in Fig. 5.9 (b).

5.3.2 IBL thermo-mechanics and cause of the the distortion

The coefficient of thermal expansion (CTE) of the stave structure, composed of carbon fibre, can be considered negligibly small, while the CTE of the stave flexible bus glued on the side is measured to be of the order of ~ 30 ppm/K. The observation of a distortion depending on the set point temperature points to the hypothesis that the effect is due to this CTE mismatch, which would easily imply a bowing distortion in the case of a stave with free boundary conditions. In reality, the situation is more complex due to the fixation points at the end of the stave and FEA simulations are used to determine the IBL stave mechanics under temperature changes.

One of the simulations considers an uniform temperature along the stave and a detailed structure of the IBL staves, properly implementing the boundary conditions and constraints. Particular focus is dedicated to the stave ends fastening mechanism. The material composing the end blocks is poly-ether-ether-ketone (PEEK) which is not stiff enough to maintain the stave straight and allows for the edge to distort and assume a finite angle with respect to the beam axis. The screw is not sufficient to provide enough torque
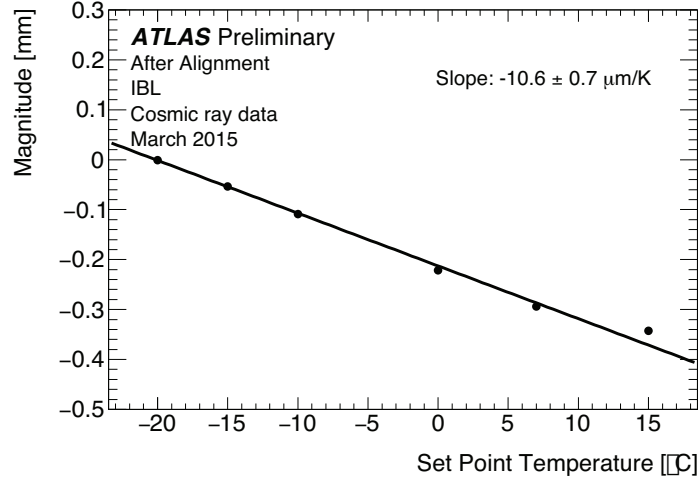
Figure 5.11: The magnitude of the IBL bowing distortion M (see Eq. 5.1) as a function of the temperature set point. The points are averaged among the 14 staves.

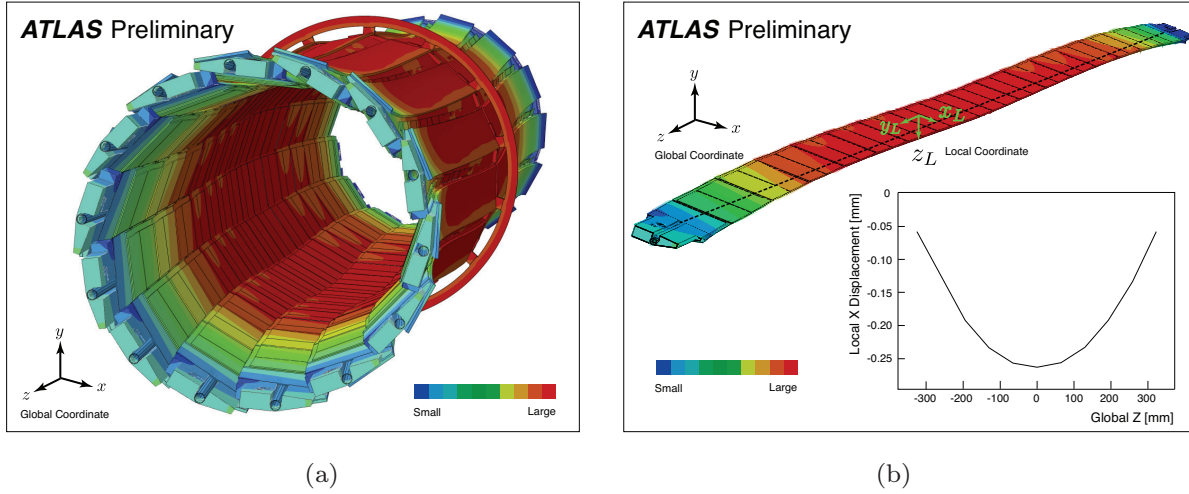|	
(a)	(b)

Figure 5.12: Three dimensional visualisation of the IBL distortion simulated by one of the FEA. The taken temperature change is considered to be $\Delta T = -60\,^{\circ}\mathrm{C}$ and the effect has been magnified by a factor 20 for graphics purposes. The colour scheme indicates the size of the displacement. Both the full IBL detector (a) and a single stave, together with the displacement size r_x as a function of global z, (b) are shown. Figures taken from [111].

to prevent in-plane rotations. In addition, the sliding pin allows for rotation around the anchoring point providing no contrasting force, together with a 0.5mm sliding in z. The central ring does not constrain the staves to move in the $r\phi$ direction, but only radially. A radial distortion of the order of 100μm is considered in the simulation. This is because the stave flex is not glued perpendicularly to the radial direction, so a radial bending component can be present. Finally, the staves are characterised by a non-uniform cross section
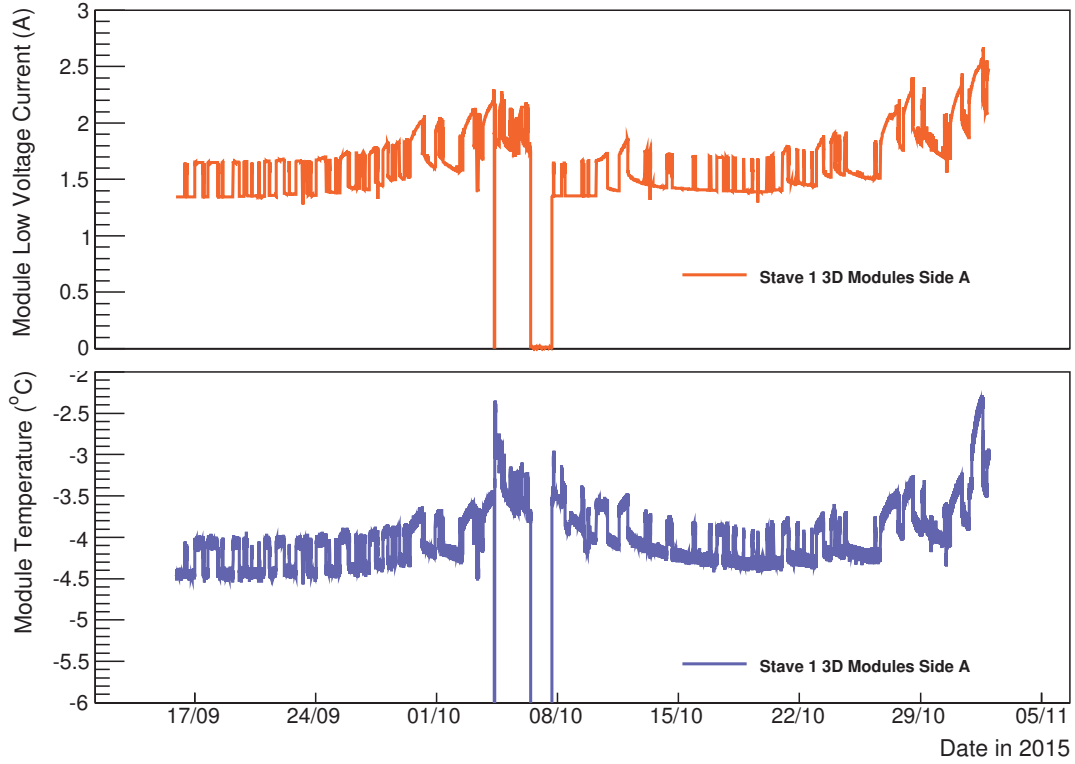
Figure 5.13: The LV current drift (up) and the temperature (down) of the front-end chips of the four 3D modules placed on the A side of one of the IBL staves. The data has been collected from the detector control system [112] from the 16th of September until the 2nd of November 2015. The drops in the shapes indicate temporary shutdown of the ATLAS detector. A similar plot produced by the ATLAS Pixel community is available at [182].

that diminishes toward the end points in order to permit the fixation mechanism. The FEA simulation shows that the staves distort in the negative $r\phi$ direction of the ATLAS global coordinate system when the IBL is cooled down. The results are shown in Fig. 5.12, where it is possible to observe that the magnitude of the *stave bowing* is maximum at the centre of the stave. The shape of the distortion is parabolic and the simulation predicts a magnitude displacement of about -0.27mm for $\Delta T = -60^\circ$C. This number might appear inconsistent with the observation from cosmic ray data. However the relative uncertainty on this estimate is as large as 100% due to the lack of precise information on some material properties and the notorious difficulty in modelling mechanical joints.

Another FEA simulation considers only the stave cross section. It is used to estimate the impact of the power generated in the flexible bus on the flex temperature and thermal gradient in the stave. The results of this simulation are that the average temperature of the stave flex increases linearly with the module power consumption. This result is used to calculate the k constant in Eq. 2.4 obtaining a value of $k \approx 0.6$ [111].

The final assessment of the studies described above is that the IBL detector distorts when a change in the stave temperature occurs. As already discussed in Sec. 5.3.1, such a

ΔT [K]	$\sigma_{x,L}$ [μm]	$\sigma_{y,L}$ [μm]	$\sigma_{z,L}$ [μm]
0.0	13.9 ± 0.2	14.0 ± 0.2	53.3 ± 0.5
+0.2	13.9 ± 0.2	14.0 ± 0.2	53.3 ± 0.5
+0.5	14.1 ± 0.2	14.2 ± 0.2	53.3 ± 0.5
−1.0	14.3 ± 0.2	14.5 ± 0.2	53.3 ± 0.5
+1.0	14.5 ± 0.2	14.6 ± 0.2	53.3 ± 0.5
+2.0	16.9 ± 0.2	16.8 ± 0.2	53.3 ± 0.5

Table 5.2: The reconstructed beam spot sizes $\sigma_{x,L}$, $\sigma_{y,L}$ and $\sigma_{z,L}$ along the x-, y- and z-axis respectively as a function of a change in IBL temperature.

change can be induced by varying the IBL cooling operating temperature.

However, radiation effects have an impact on the IBL low voltage (LV) current with a consequent rise in the module and stave temperature [182, 183].

An example of the LV current rise in some of the IBL modules is observed during 2015 $p - p$ collisions data taking and is shown in Fig. 5.13. The description of the mechanism behind this effect is beyond the scope of this thesis but a detailed treatment of the causes of this effect can be found in [184]. From the same figure, it is possible to observe that the same trend is induced in the module temperature causing changes of up to 0.8°C within a single data taking run. The correlation between the rise in the LV current and the average temperature of the IBL modules follows a linear trend. As previously discussed the change in the module temperature induces a change in the stave temperature according to Eq. 2.4, causing a distortion of the IBL staves.

5.3.3 Impact on physics performance

It is clear that the bias on the residual distributions in the IBL induced by the distortion driven by the CTE mismatch might negatively affect the reconstruction of physics objects as well as the general ID performance. In particular, since the IBL provides the measurement closest to the interaction point, it is expected that the track impact parameters are among the quantities which are mostly affected by such distortion. The impact is evaluated on $p-p$ collision MC simulation reconstructed introducing artificial misalignments corresponding to $\Delta T = 0.2, 0.5, 1.0, 2.0$ K on top of a perfect geometry. The misaligned constants are created moving the IBL modules position according to Eq. 5.2. Only a brief overview on the impact on the reconstruction of the beam-spot position, the tracking performance and on b-tagging algorithms is reported in this section, in order give a context for the necessary alignment framework modifications discussed in Sec. 5.4.2.

Beam Spot

Since the IBL is the detector closest to the interaction point, its measurements have the largest weight in the fit determining the beam spot position, size and rotation. The IBL distortion is expected to have an impact on different beam spot parameters such as:
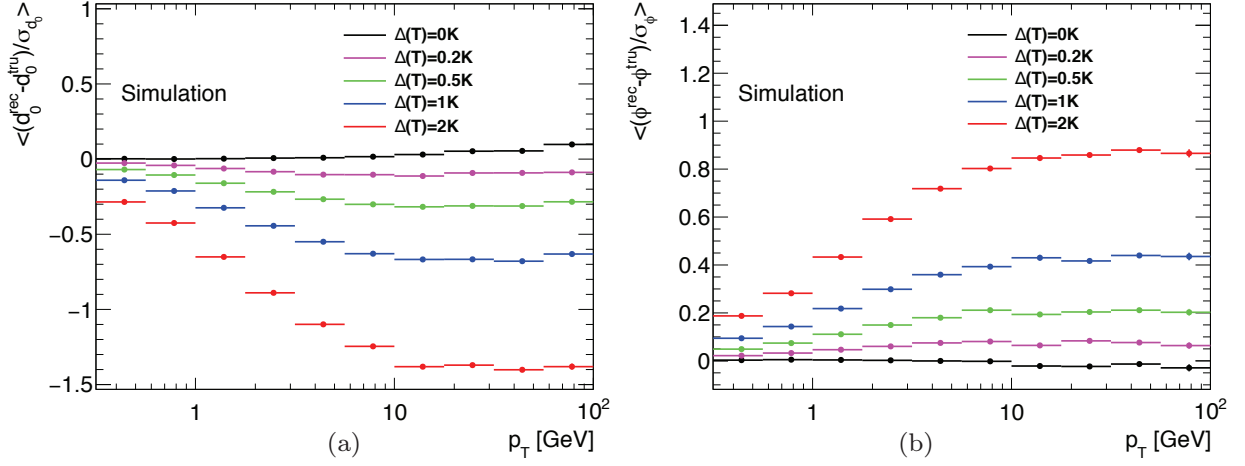
Figure 5.14: The ratio of the bias of the d_0 (a) and ϕ (b) track parameters over its resolution for each p_T bin.

- The rotation of the beam spot in the $x - y$ plane in the case of a non-spheric beam spot shape.

- In the case of a displaced beam spot centre with respect to (0,0) in the transverse plane, an additional shift is expected to be due to IBL distortion.

- The transverse size ($\sigma_{x,L}, \sigma_{y,L}$) of the beam spot is expected to be negatively affected due to a reduced spatial resolution in determining the position of vertices or due to a distortion in the reconstruction of small length scales close to the interaction point.

A MC di-jet sample, reconstructed with the aforementioned set of alignment constants, is used to estimate the impact of these effects. Due to the nature of the simulated sample that assumes a spherical beam spot centred in (0,0) in the transverse plane, only the effect on the beam spot size is studied. The results of the study are reported in Tab. 5.2.

Tracking Performance

The track parameters most affected by local-x residual distribution biases and resolution degradation are the transverse impact parameter d_0 and azimuth ϕ. The impact on tracking performance is studied on a $Z \to \mu\mu$ MC simulated sample. The results were checked also on a $t\bar{t}$ MC simulated sample, reconstructed with the same distorted alignment constants, and no dependence on the signal process is observed. The effect of the IBL distortion on d_0 (ϕ) is quantified in terms of the ratio of the mean bias, obtained by the difference of the reconstructed d_0^{rec} (ϕ^{rec}) with the truth value of d_0^{truth} (ϕ^{truth}), over its resolution σ_{d_0} (σ_ϕ). The results of the study are reported in Fig. 5.14 where it is possible to observe that for $\Delta T < 0.2$ K the bias induced by the IBL distortion is of the order of 10% of the track parameter resolution. The behaviour of the ratio as a function of the track p_T is due to the convolution of two effects. Firstly, the bias between the reconstructed and the truth track
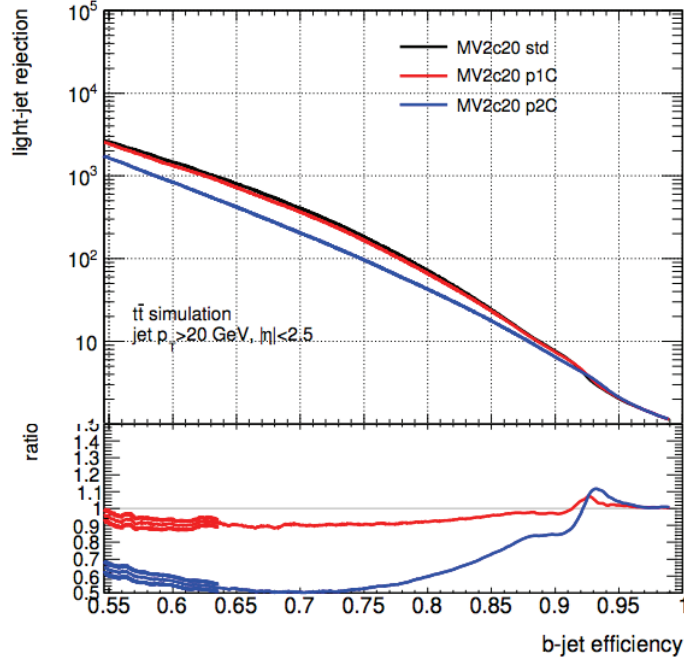
Figure 5.15: Light jet rejection evaluated with the `MV2c20` b-tagging algorithm as function of the *b*-tagging efficiency for the nominal scenario (std) and distorted IBL geometry at $\Delta T = 1$K (p1C) and 2K (p2C).

parameters is bigger at low p_{T} values. Secondly, the resolution on these track parameters gets better with increasing track p_{T}. Therefore, the pulls results show that the relative bias on the track parameters induced by the IBL distortion is more significant for high p_{T} tracks.

B-Tagging performance

Dedicated investigations are performed to assess the impact on *b*-tagging performance using MC simulation of $t\bar{t}$ events at $\sqrt{s} = 13$ TeV that are reconstructed with $\Delta T = 0.2$K, 0.5K, 1K, and 2K. The *b*-tagging performance is evaluated for the `MV2c20` algorithm [185, 186], which is the default for Run 2. The light-jet rejection decreases to 90% (50%) of the nominal case at a *b*-tagging working point of 70% for $\Delta T = 1$K (2K) as shown in Fig. 5.15. In the case of $\Delta T = 0.2$K and 0.5 K the *b*-tagging performance does not deteriorate.

5.4 ID Alignment campaign in early Run-2 collisions

In this section the changes made to the Inner Detector Alignment procedure in order to cope with the distortion of the IBL sub-detector and restore high-quality data reconstruction are discussed. Finally, the procedure used to determine baseline constants for 2015 data processing is presented.
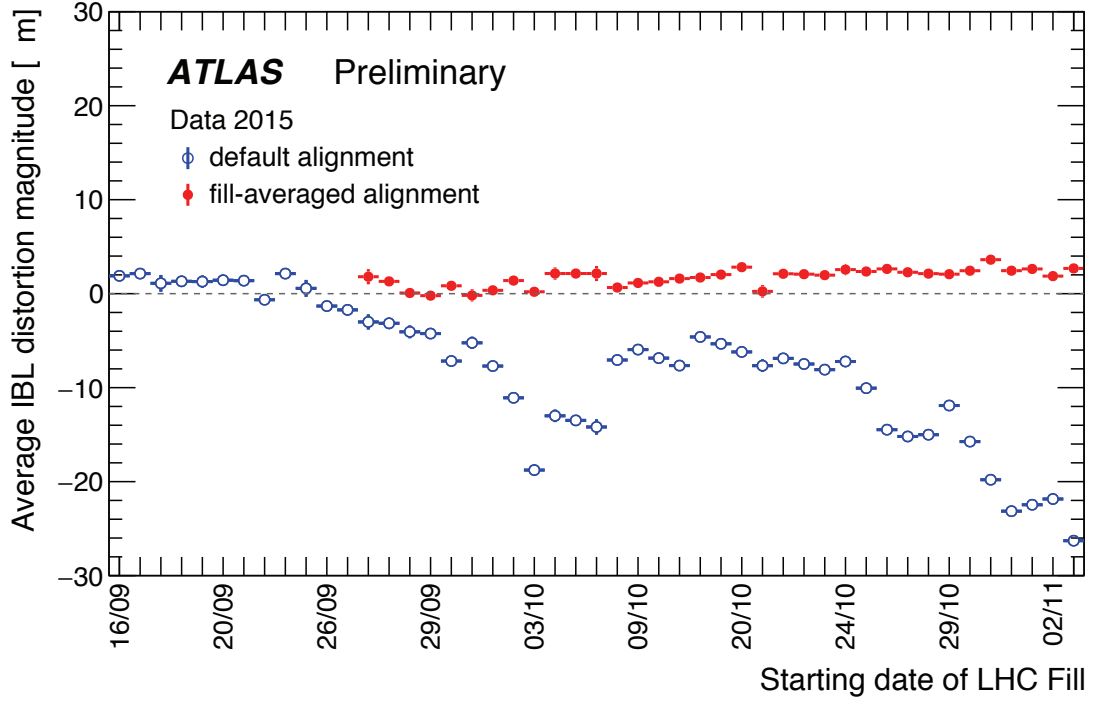
Figure 5.16: The IBL distortion magnitude per LHC fill averaged over the 14 staves and the duration of the correspondent run. The systematic displacement of $1 - 2\mu$m indicates a small, tolerable distortion with respect the initial alignment conditions. The *default alignment* (blue open points) indicates the baseline constants [187], while the *fill-averaged alignment* indicates the constants obtained after the L11 correction averaged on the single run.

5.4.1 Alignment corrections for the IBL distortion

The distortion of the IBL staves was checked for each run during the period between September and November 2015 by the alignment monitoring framework and the drift of the magnitude is shown in Fig. 5.16. The increase in the magnitude in the default alignment corresponds to the behaviour of the module LV current and temperature discussed in Sec. 5.3.2. The distortion is calculated with respect to alignment constants calculated at the beginning of $p - p$ collisions data taking [187]. The corrections to the IBL distortion are calculated introducing a new alignment degree of freedom in the alignment framework that corrects for the collective parabolic distortion of the stave. The bowing *d.o.f.* is coded into two different alignment levels: in *Level 11* the IBL distortion magnitude is averaged over the 14 staves, while a new level, named *Level 16*, corrects for the bowing in each stave independently in the case a stave dependent distortion is observed[3]. The first derivative of the track-to-hit residual with respect to the IBL bowing distortion *d.o.f.* is obtained from

---

[3]The reference frame of this alignment level coincides with the global reference frame. The IBL is considered composed of 14 independent staves, while the other sub detectors, such as the outer three layers of the Pixel detector, the SCT detector and TRT detector, have the same degrees of freedom as L11.

Level 11							
Structure	T_x	T_y	T_z	R_x	R_y	R_z	M
TRT (Barrel)	✓	✓	✗	✓	✓	✓	✗
TRT (End-caps)	✓	✓	✗	✗	✗	✓	✗
SCT (Barrel)	Kept fixed as reference						
SCT (End-caps)	✓	✓	✗	✗	✗	✓	✗
Pixel	✓	✓	✓	✓	✓	✓	✗
IBL	✓	✓	✓	✓	✓	✓	✓
Level 16							
TRT	Kept Fixed as reference						
SCT	Kept Fixed as reference						
Pixel	Kept Fixed as reference						
IBL	✗	✗	✗	✗	✗	✗	✓

Table 5.3: List of the degrees of freedom and structures aligned for the time-dependent IBL distortion correction. During the L16, 14 total *d.o.f.* are aligned corresponding to the bowing magnitude for each IBL stave.

equation Eq. 5.1:

$$\frac{\partial r_x}{\partial M} = \frac{z^2 - z_0^2}{z_0^2} \tag{5.3}$$

where the position along the z axis of the alignable module in the alignment frame, $z_0 = 366.5$mm is the distance between the fixation points and the centre of the stave, M is the IBL stave bowing alignment parameter and r_x is the residual along local-x direction. The baseline of Eq. 5.1 is determined at L11 by a global rotation around the z axis, R_z, and by the translation along the x axis, T_x, at L16. Finally, the derivative of the residual along local y is set to zero, since negligible dependence from this *d.o.f.* is observed. The L11 alignment correction with the bowing *d.o.f.* included has been applied from the end of September 2015 in order to correct the average drift of the IBL distortion and the results are shown in Fig. 5.16. It is possible to observe that the average IBL bowing distortion is corrected within 2μm. However, as shown in Fig. 5.17, the run averaged alignment is not able to correct for movements within the run itself and it becomes necessary to derive alignment constants with a finer time granularity. During Run-2, the alignment correction to the bowing distortion has been calculated every 100 luminosity blocks (LBs)[4] on top of the L11 global movements corrections for each data-taking run. The configuration of the alignment is reported in Tab. 5.3 showing the *d.o.f.* used to align the ID at the various alignment levels. The results of the real-time alignment are shown in Fig. 5.17. The distributions of the local x unbiased residuals integrated over all hits of the IBL sub-detector are shown in Fig. 5.18 with the default alignment constants, the run averaged alignment correction to the global IBL bowing and the time dependent corrections to the bowing of each stave.

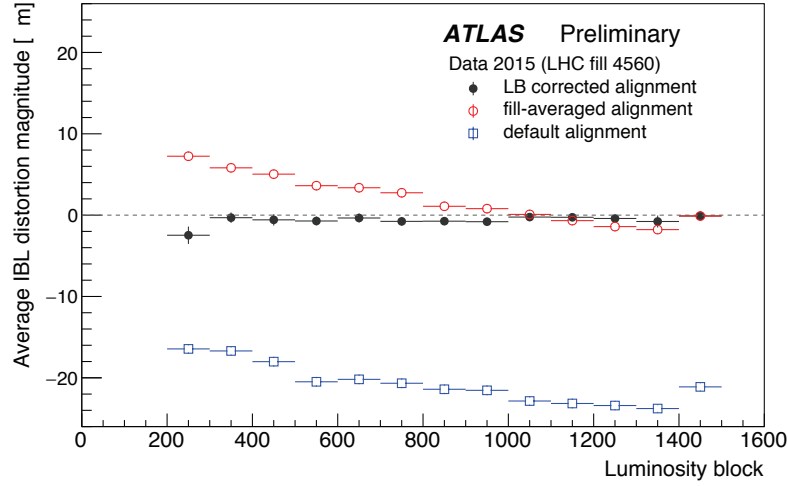[4]A luminosity block corresponds to one minute of data-taking.

Figure 5.17: The IBL distortion magnitude averaged over the 14 staves for the LHC fill 4560. The *default alignment* indicates the baseline constants derived in [187], the *fill-averaged alignment* the constants obtained after the L11 correction and *LB corrected alignment* the time-dependent L16 correction.
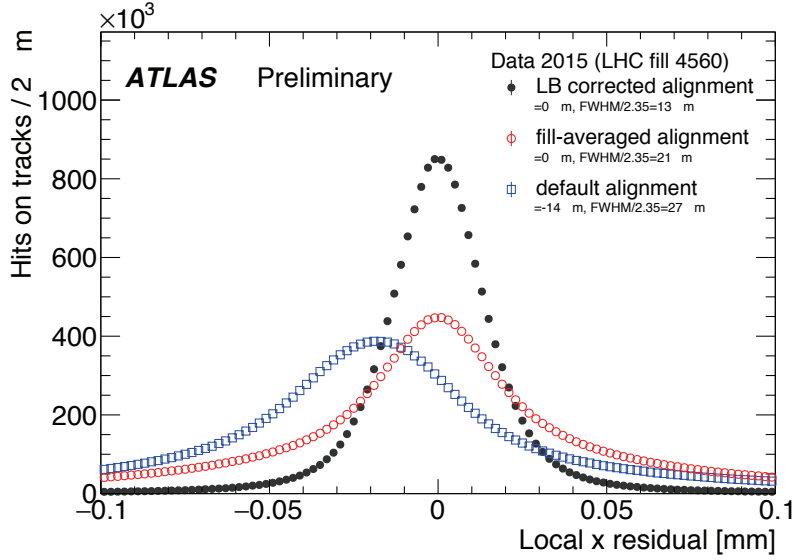
Figure 5.18: The local-*x* unbiased residual distributions integrated over all hits-on-track in the IBL layer modules. The *default alignment* indicates the baseline constants derived in [187], the *fill-averaged alignment* the constants obtained after the L11 correction and *LB corrected alignment* the time-dependent L16 correction.

5.4.2 Alignment of full 2015 $p-p$ collisions dataset

The alignment of the full 2015 $p-p$ collisions at $\sqrt{s} = 13$ TeV has been recomputed at the end of the data-taking. A similar procedure to the one discussed in Sec. 5.1 is followed. The full alignment reprocessing of the data collected during 2015 is performed in two steps. Firstly a baseline set of constants is derived and a set of time dependent corrections to

Level	Description	Structures	DoF	Constraints
11	IBL	1	All	
	Pixel	1	All	SCT Barrel Fixed
	SCT barrel + 2 end-caps	2	All	
	TRT barrel + 2 end-caps	3	All but T_z	
2 Si-Only	IBL	1	All	
	Pixel barrel layers	4	All	d_0 from beam-spot position
	Pixel 3 end-caps disks	6	T_x, T_y, R_z	q/p_T fixed
	SCT barrel layers	4	All	$z0$ fixed
	SCT endcaps disks	16	T_x, T_y, R_z	
3 Si-Only	IBL	280	All	
	Pixel barrel	1456	All	d_0, z_0 from $Z \to \mu\mu$
	Pixel end-caps	288	T_x, T_y, R_z	Sagitta bias from $Z \to \mu\mu$
	SCT barrel	2112	All	Soft cut
	SCT end-caps	1976	T_x, T_y, R_z	
1 TRT-Only	TRT Barrel	1	All but T_z	Silicon Fixed
	TRT end-caps	2		
2 TRT-Only	TRT Barrel modules	96	T_x, R_z	Silicon Fixed
	TRT end-caps wheels	80	T_x, T_y, R_z	

Table 5.4: Summary of the alignment configurations used in deriving the baseline constants for the 2015 dataset. Only tracks reconstructed in the silicon detectors have been used for the Si-Only alignment, while the full ID tracks have been used for the TRT-Only alignment.

correct both run-by-run global movements and the within-run IBL bowing distortion is applied.

Reprocessing baseline constants

The baseline alignment constants are derived using hadronic tracks passing the *Tight Primary* selection with $p_\mathrm{T} \geq 5$ GeV collected during a particular LHC run between the 11th and the 12th of September 2015, for a total integrated luminosity of 67 pb^{-1}. The alignment chain used for the derivation of the alignment constants makes use of the beam spot position, soft mode cut technique [188] and the Z mass external constraints, using events from $Z \to \mu\mu$ events. The $Z \to \mu\mu$ data sample used for the alignment validation and track parameters bias correction is selected from a period of data taking during which the Inner Detector sub-systems are stable with respect to global movements relative to the Pixel barrel, that is chosen as fixed reference. This period corresponds to the data collected between the 8th and the 14th of September 2015, for a total integrated luminosity of 178 pb^{-1} when selecting exclusively events that pass the necessary Data Quality requirements. The various steps of the alignment chain performed are summarised in Tab. 5.4 and the performance is compared to a perfectly aligned Monte Carlo $Z \to \mu\mu$ sample in Sec. 5.4.3.

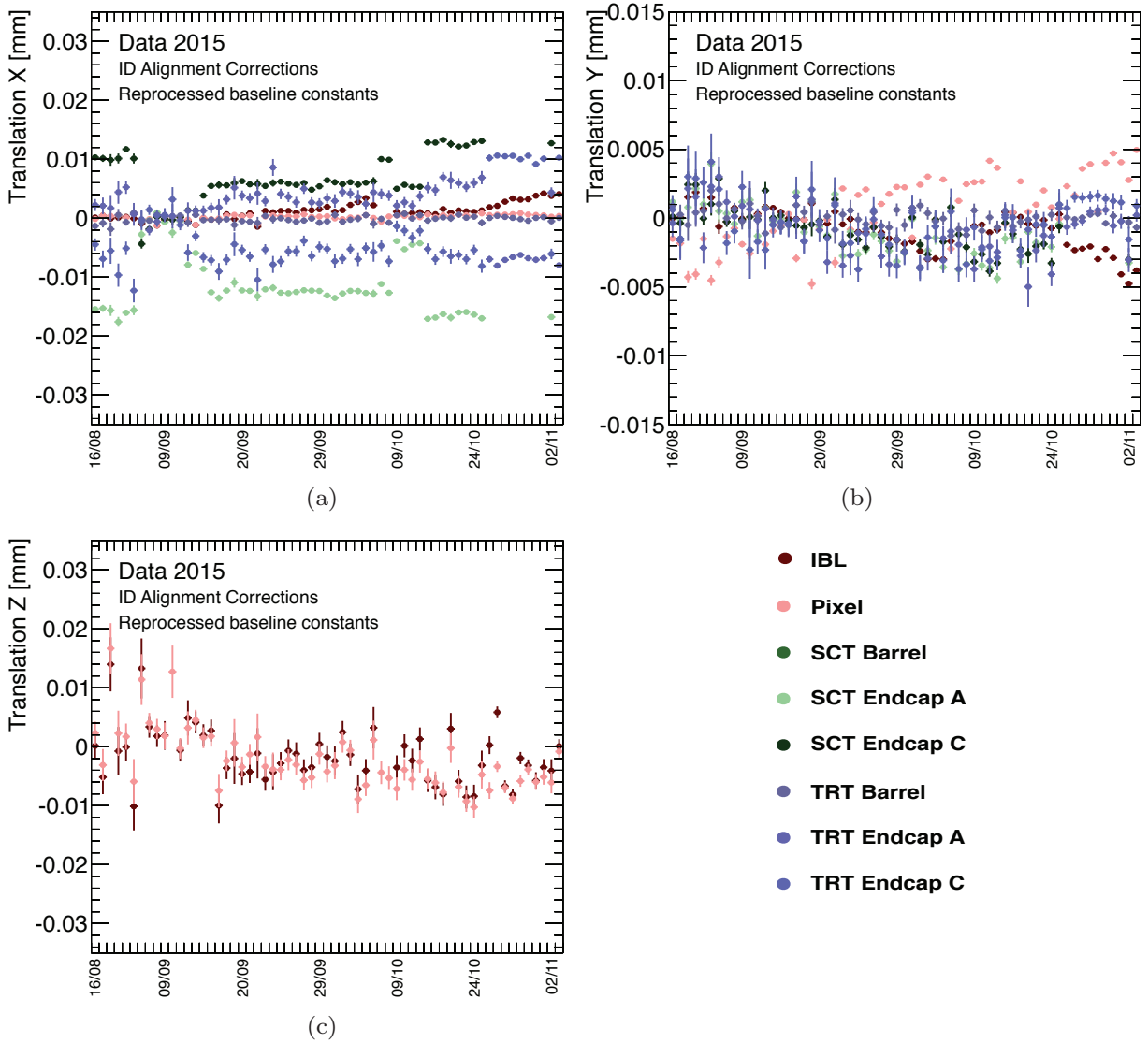**Run-by-run and within run corrections**

Figure 5.19: *Level 11* run-by-run alignment corrections performed on the 2015 runs on top of the baseline constants for the translations with respect to the global x (a), y (b) and z (c) axes. The SCT Barrel is used as fixed reference, therefore no correction is applied to it, while the corrections to the other sub-systems are applied according to Tab. 5.3.

Starting from the fixed set of baseline constants, a L11 alignment is performed for each ATLAS run to correct for significant global movements of the Inner Detector subsystems. The alignment configuration for these corrections is the same as of Fig. 5.3. In Fig. 5.19 and Fig. 5.20 the corrections for the translations and the rotations together with the IBL bowing for all the runs used for data analysis in 2015 are shown. By convention, the alignment corrections are expressed relative to the SCT barrel, which is kept fixed as a reference, and are reported as a function of time. Changes to the environmental conditions of the Inner Detector, such as magnetic field strength, cooling failures, gas leaks or changes
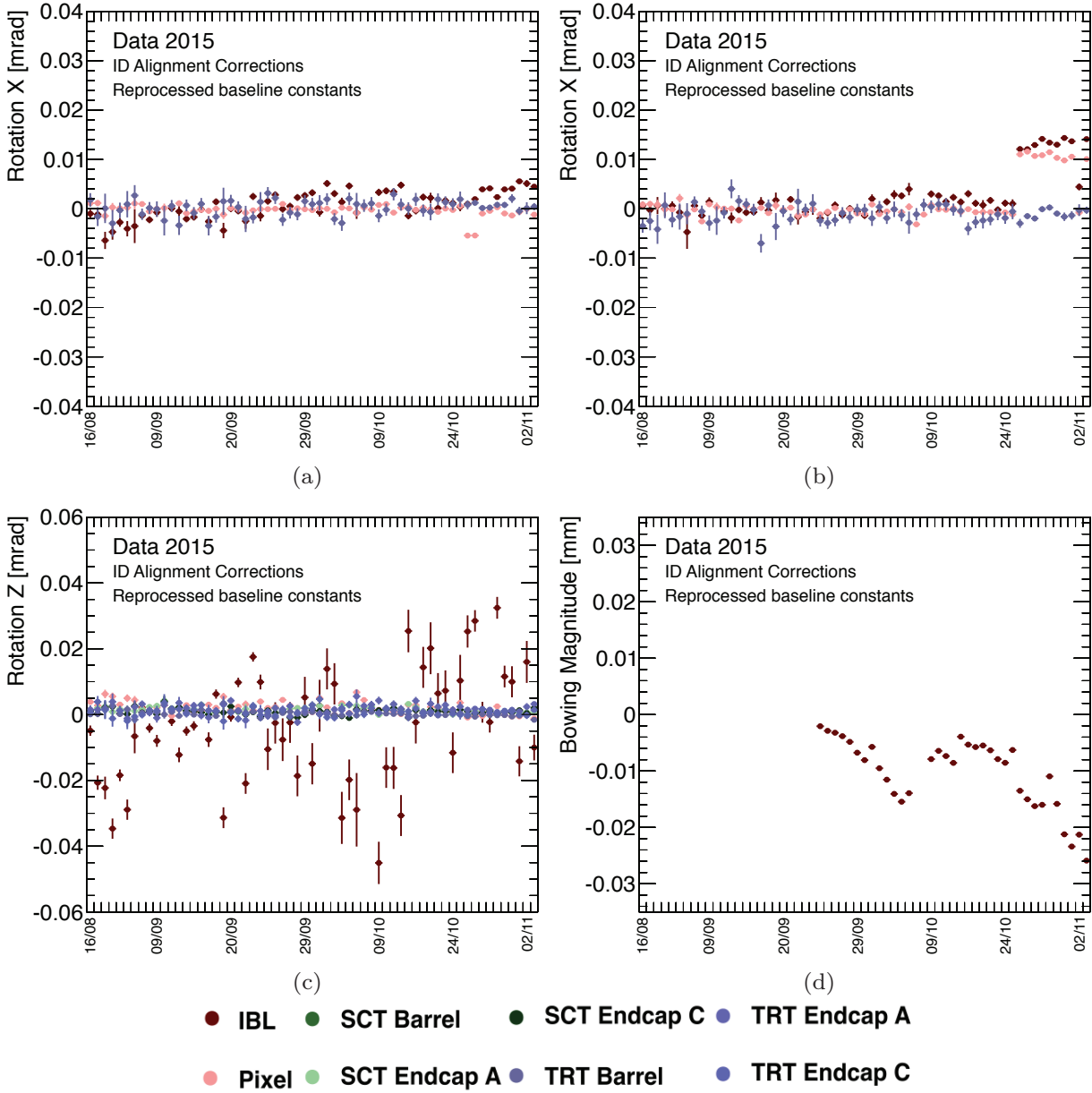
Figure 5.20: *Level 11* run-by-run alignment corrections performed on the 2015 runs on top of the baseline constants for the rotations with respect to the global x (a), y (b) and z (c) axes and the IBL bowing correction (d). The SCT Barrel is used as fixed reference, therefore no correction is applied to it, while the corrections to the other sub-systems are applied according to Tab. 5.3.

in operating temperature, lead to significant movements of the various subsystems [174]. In addition, slow drifts of the sub-detectors that are due to mechanical relaxations that might take a few weeks before stabilisation are corrected. Such a procedure for global movements correction is of great importance for improving the momentum resolution and especially reduce the ϕ dependence of the sagitta biases [136]. On top of the run by run
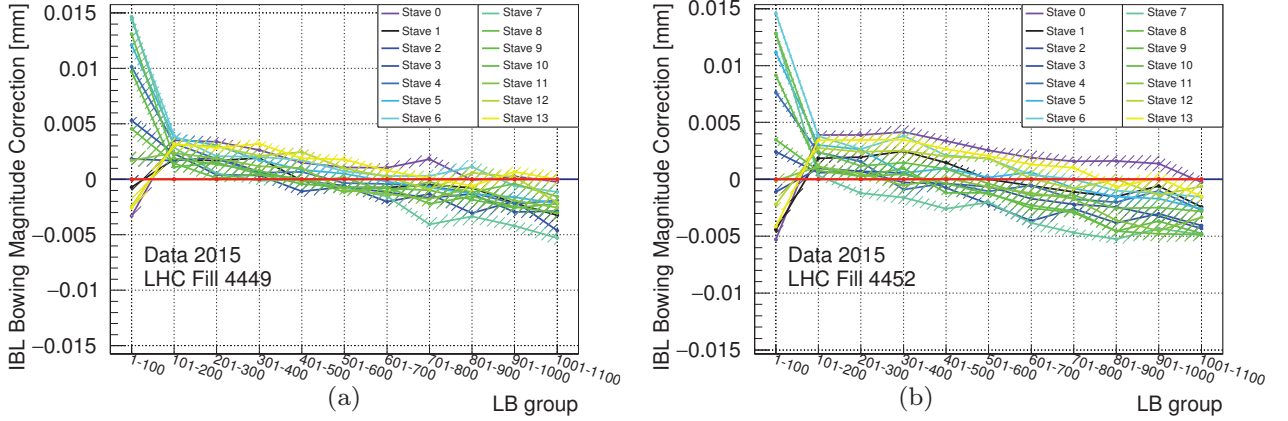
Figure 5.21: *Level 16* within-run alignment corrections to the IBL sub detector performed on the LHC Fills 4449 (a) and 4452 (b) on top of the run-by-run corrections. All the other sub-systems are kept fixed as outlined in Tab. 5.3.

movements global corrections, the dynamic correction of the IBL stave distortion has been applied with the configuration outlined in Tab. 5.3. In Fig. 5.21 the alignment correction to the bowing magnitude for two LHC fills is shown. The first 100 LB are dominated by the movement of the outer layers of the Pixel detector along T_y that were already observed and described in [133]. It is possible to notice that in this case the alignment produces artificial corrections to the IBL bowing which are ϕ dependent, as it would be expected when instead a global vertical movement is present. After the outer pixel layers relaxation, it is possible to notice that the corrections for the bowing magnitude follows a very similar trend for all the staves, as it is expected due to the central support rings that introduce a mechanical constraint. These dynamic corrections are of major importance to ensure good tracking performance as discussed in Sec. 5.3.3.

5.4.3 Alignment Validation and systematics

The alignment validation is performed using $Z \to \mu\mu$ events that are selected requiring exactly two muon candidates reconstructed by a combined fit using both the hits in the ID and in the MS system with a *Loose* identification working point (see Sec. 3.2.2). The data is compared to a MC $Z \to \mu\mu$ simulated data sample.

The muon tracks are required to be isolated imposing that the ratio between the sum of the transverse momentum of all the other tracks around the muon in a cone of radius $\Delta R = 0.4$ over the muon transverse momentum is lower than 0.2. In addition, the two muons invariant mass is required to be close to the Z boson mass in the window defined as $70 \leq M_{\mu^-\mu^+} \leq 110$ GeV and the angular separation between the two muons is required to be $\Delta R = \sqrt{(\Delta\eta)^2 + (\Delta\phi)^2} > 0.2$. The track reconstructed in the Inner Detector associated with the muon candidate is required to have a hit in the IBL, if a hit is expected, at least two hits in the Pixel detector and at least 6 hits in the SCT, including dead modules and at most one hole in the silicon sub-detectors. This selection is required to ensure good quality tracks with a precise reconstruction of the track parameters. The plots used
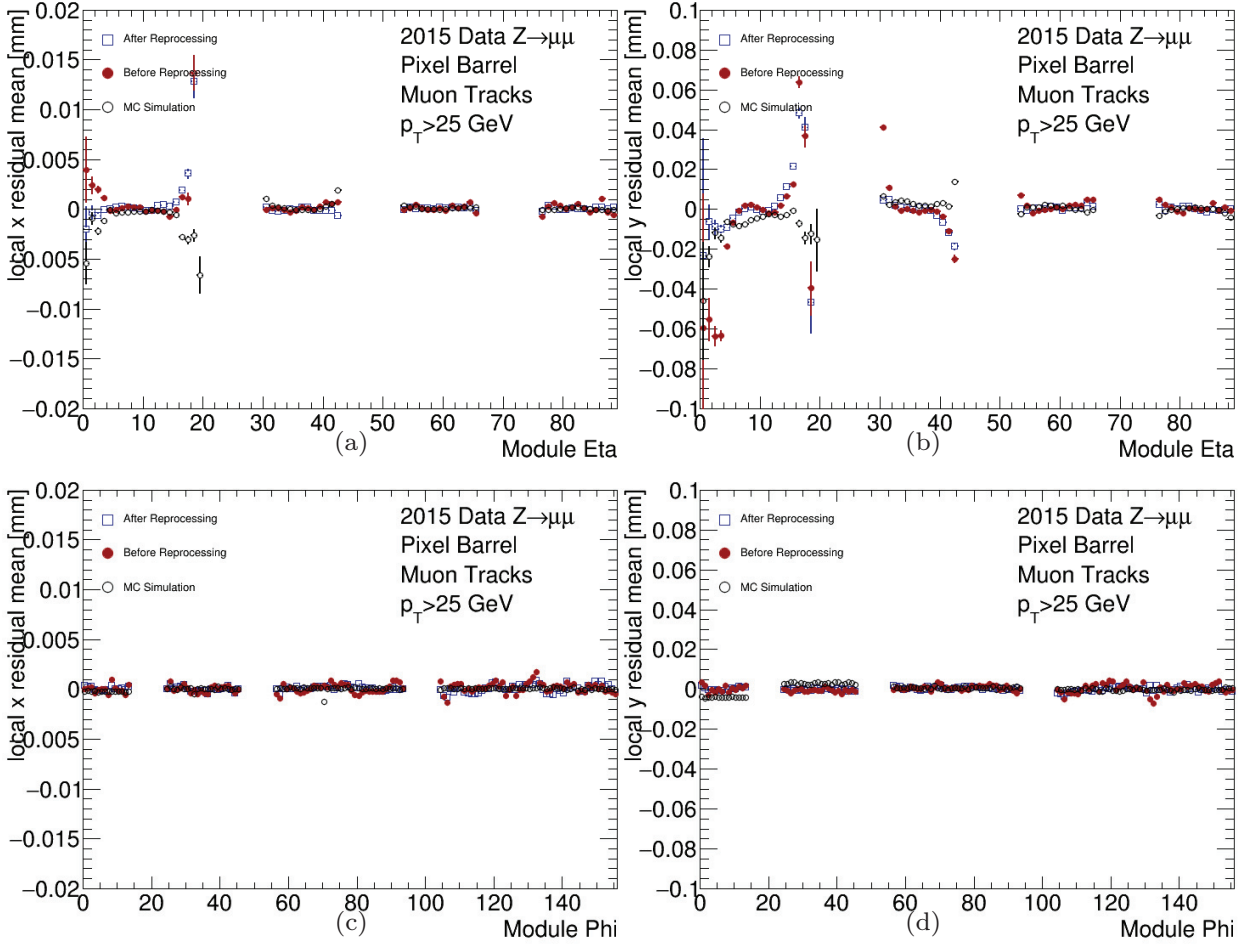
Figure 5.22: Data and Monte Carlo comparison between the distributions of the mean of the local-x and local-y residuals as a function of the η-index (a,b) and of the ϕ-index (c,d) of the Pixel modules, respectively. The η-index corresponds to the module position along the stave while the ϕ-index corresponds to the stave number. The distributions are grouped together by each Pixel layer: the first group corresponds to the IBL detector, the second to the B-Layer, the third to the Layer 1 and the last to Layer 2.

to check the performance of the alignment in the silicon detector are the mean of the residual distributions as a function of the module eta and phi index, which represents the positioning of the modules along the stave and the stave number, respectively. The results for the Pixel barrel and the SCT barrel sub detectors are shown in Fig. 5.22 and Fig. 5.23, respectively. In Fig. 5.22 the mean of the residuals are grouped together by each Pixel layer: the first group corresponds to the IBL detector, the second to the B-Layer, the third to the Layer 1 and the last to Layer 2. Similarly, in Fig. 5.23 the mean of the residuals are grouped together by each SCT barrel layer. Larger misalignments are present only for the IBL 3D modules which are affected by the lack of statistics since they are located outside the nominal track reconstruction η-range. Such misalignments are expected to have a
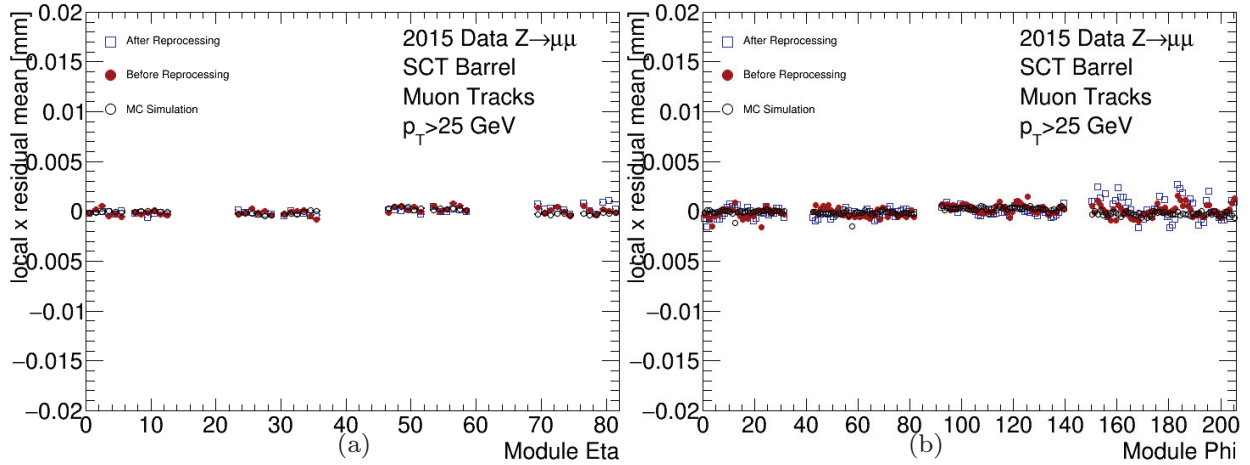
Figure 5.23: Data and Monte Carlo comparison between the distributions of the mean of the local-x residuals as a function of the η-index (a) and of the ϕ-index (b) of the SCT modules, respectively. The η-index corresponds to the module position along the stave while the ϕ-index corresponds to the stave number. The distributions are grouped together by each SCT layer.

negligible impact on physics and no particular efforts have been carried out to correct for them. The constants shift of $\approx 1\mu$m in the mean of the local-y residual distributions in the MC simulation is due to a small bias present in the determination of the centre of the pixel cluster when using the Neural Network algorithm to find the hit position [189]. Such bias is not observable in data due to the alignment corrections that cancel it. The comparison between data and MC simulation distributions of the mean of the residuals as a function of the TRT barrel modules index is reported in Fig. 5.24 and shows within layer misalignments of the order of 5μm. The reason behind these biases is due to an incomplete alignment at *Level 2* performed using only 3 degrees of freedom, T_x, T_z and R_z, that do not allow for a perfect correction. Due to time constraints in delivering the alignment constants for the data reprocessing, there was no chance to further improve the alignment of the TRT. Given a hit resolution of around 130μm in the TRT, such biases are expected to have a small impact on quantities such as track reconstruction efficiency and momentum resolution.

Finally, the $Z \to \mu\mu$ selected data is used to determine the presence of track parameter biases due to the alignment iterations. The corrections δ_{d_0}, δ_{z_0} and δ_{sagitta} as a function of the muon η and ϕ are shown in Fig. 5.25 for the 2015 dataset, before and after the reprocessing alignment, and for the MC simulation. The biases in the high η regions are due to end-cap misalignments which are partially corrected with a *Level 2* iteration of the Silicon detectors and it is possible to observe an improvement in the large η region, where the sagitta bias is reduced by more than a factor two. The δ_{d0} and δ_{z0} biases were improved performing a constrained L3 alignment. For both the impact parameters, the high η regions get the largest improvement, while in the case of δ_{d_0} a considerable improvement is present also in the barrel region. The distributions reported show the presence of systematic biases in the distributions of the impact parameters in the MC simulation. Data recorded in

2015 is expected to suffer larger sagitta biases and longitudinal impact parameter biases with respect to the 2012 dataset. This is due to the fact that only a single iteration of the constrained alignment has been used due to time constraints at the time of the calculation of the alignment constants.
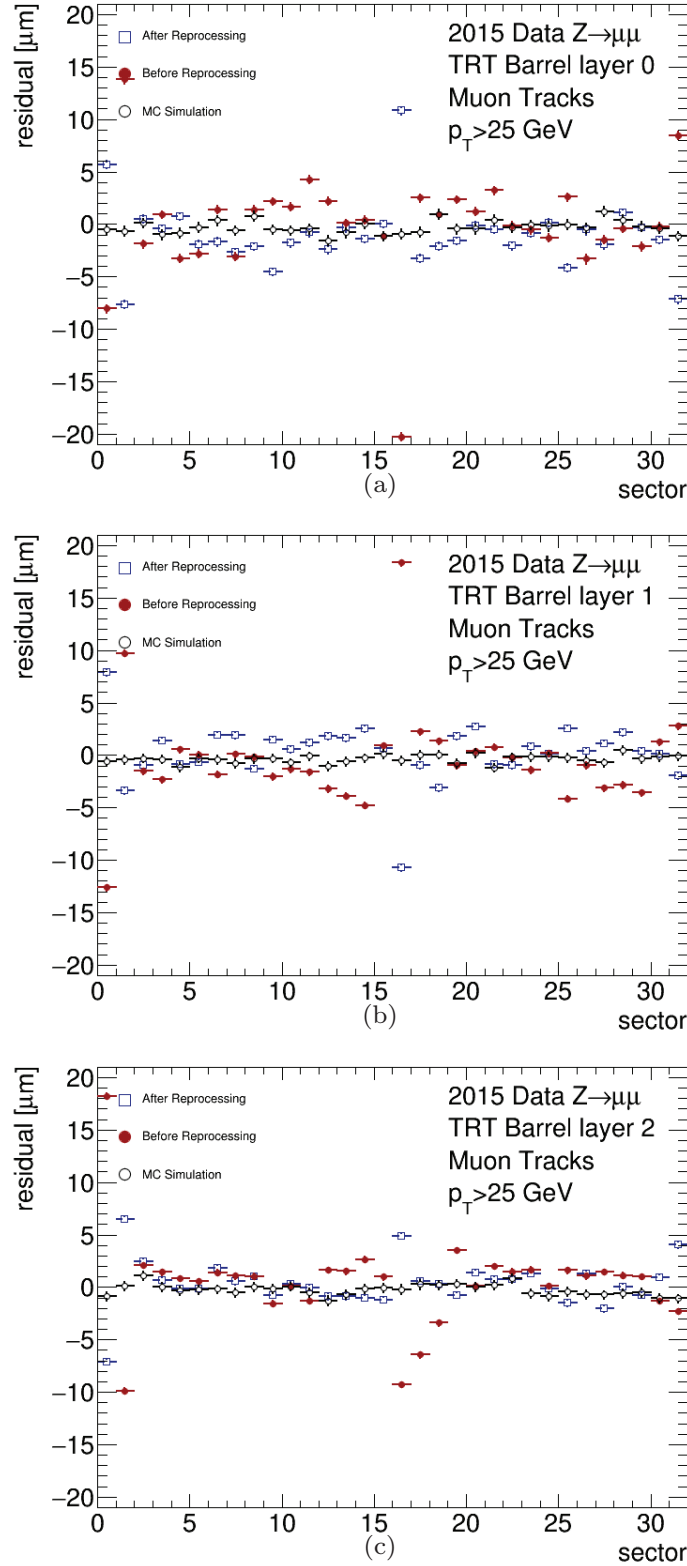
Figure 5.24: Data and Monte Carlo comparison between the distributions of the mean of the local-R residuals as a function of the position of the TRT modules along the barrel ϕ-sector for the first layer (a), the second layer (b) and the third one (c).
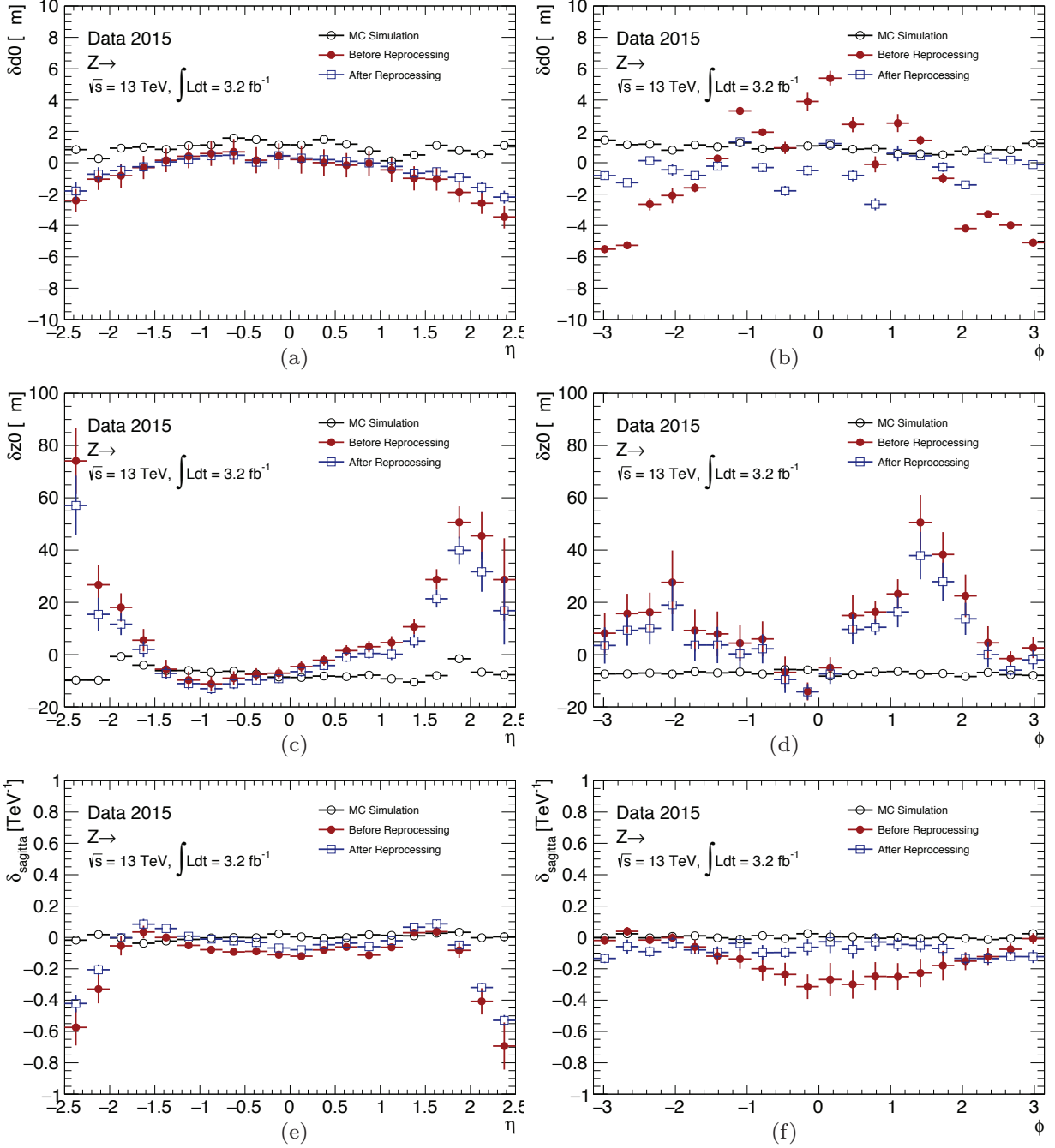
Figure 5.25: The corrections to the track parameter biases δ_{d_0} (a,b), δ_{z_0} (c,d) and $\delta_{\mathrm{sagitta}}$ (e,f) as a function of the muon track η and ϕ, respectively. The 2015 reprocessed $Z \to \mu\mu$ dataset is shown in open black circles, the data reconstructed with the alignment described in [187] is represented in open blue squares, while the MC simulation is in full red circles.

6 Search for a top squark decaying into a scalar tau lepton

6.1 The $\tilde{t} \to \tilde{\tau}$ signal and final state

As described in Chapter 1, the scalar top quark can have a rich variety of decay modes. This search targets the three body decay of the scalar top into a b quark, a scalar tau $\tilde{\tau}$ and a ν_τ, followed by the decay of the $\tilde{\tau}$ into a τ lepton and a gravitino $\tilde{G}$ that is assumed to be massless.

$$\tilde{t} \longrightarrow b\nu_\tau\tilde{\tau} \longrightarrow b\nu_\tau\tau\tilde{G} \tag{6.1}$$

Since R-parity is assumed to be conserved, the scalar top is produced in pairs in $p-p$ interactions. The gravitino is stable and escapes the ATLAS detector undetected since it interacts with matter only gravitationally. Therefore, the topology of the final state of this search is characterised by large missing transverse momentum due to the presence of invisible particles, jets originating from b-quarks and τ leptons. The search is divided in three channels according to the decay modes of the τ leptons:

- **Dileptonic channel**: This channel, also named *lep-lep*, targets final states where both τ leptons decay leptonically. The main handle for this channel is the presence of exactly two isolated light leptons ($ee/\mu\mu/e\mu$) in the final state.

- **Semileptonic channel**: This channel, also named *lep-had*, targets final states where one of the two τ's decays leptonically while the other decays hadronically. The main handle for this channel is the requirement of one isolated lepton, either an electron or a muon, and an identified τ_{had}.

- **Full-hadronic channel**: This channel, referred as *had-had*, aims to analyse final states with both τ leptons decaying hadronically. Exactly two reconstructed and identified τ_{had} are required and a veto over isolated electrons or muons is placed.

The search presented in this thesis is based on a simplified model approach in which the branching ratio (BR) of the scalar top and the scalar tau in the decay modes described above are assumed to be 100%, while the other supersymmetric particles not involved in the decay chain are assumed to be very massive and decoupled. For this approach, the only free parameters are the masses of the scalar top and the scalar tau. Each mass hypothesis corresponds to a different model which is generated by MC simulation. Only pair production of scalar tops has been considered in the simulation, using a scalar top mixing matrix such that the lightest scalar top mass eigenstate is almost a pure partner

of the right-handed top quark. In addition, the lifetimes of the supersymmetric particles involved are assumed to be below 1 ps, such that the decay length is negligible and the decays can be considered prompt (see for example Eq. 1.24).

In this thesis, particular focus will be put on the *had-had* channel. A brief description of the techniques used for the *lep-had* channel is included. The *lep-lep* channel has been investigated using a reinterpretation of a scalar top search with two light leptons in the final state [190]. Therefore, just a brief introduction of this channel is discussed.

6.2 Background processes

A final state containing τ leptons, b-jets and missing transverse momentum can be produced also by a certain number of SM processes acting as backgrounds for this search. The main SM processes contributing to this final state are top quark pair production and single top quark production. The production of vector bosons in association with jets also represents a considerable background. Smaller background contributions arise from the production of two gauge bosons in association with extra jets and top pair production in association with a vector boson. These processes are modelled through Monte Carlo simulation and a brief summary of the used generators, together with a few technical details, is given in Sec. 6.3. Multijet processes have a very high production cross-section but the requirement of one or two isolated leptons together with a hard cut on the $E_{\mathrm{T}}^{\mathrm{miss}}$, makes this background negligible. This is not a-priori true for the *had-had* channel, where jets can be mis-identified as τ_{had}'s with a non negligible probability. Multijet processes are estimated through a data-driven method since no reliable MC simulation is available at present.

6.2.1 Top quark production: $t\bar{t}$, single top

The top quark can be produced at the LHC either in $t\bar{t}$ pairs, through quark or gluon fusion, or singularly through electroweak (EWK) interaction [192]. The former mechanism is the dominant production mode of top quarks at the LHC and the cross section is $\sigma_{t\bar{t}} = 252^{+6.4}_{-8.6}(\text{scale})^{+7.6}_{-7.3}(m_t)^{+11.7}_{-11.7}(\text{PDF} + \alpha_S)$ pb at $\sqrt{s} = 8$ TeV [193–198]. Top quarks decay into Wb with a BR very close to 100% before undergoing any hadronisation process. Since the W boson can decay either leptonically ($W \to \ell\nu_\ell$, with $\ell = e, \mu, \tau$) or hadronically ($W \to q\bar{q}'$), top pair background has a very similar topology to the SUSY signal considered in this search. In fact, this process represents the major background for all three search channels.

The electroweak top production mechanism has a smaller production cross section and represents a sub-dominant background in the search. For a top quark of mass $m_t = 172.5$ GeV, the t-channel cross-section is $87.8^{+3.4}_{-1.9}$ pb [199], while for the Wt-channel it is 22.4 ± 1.5 pb [200] and for the s-channel it is 5.6 ± 0.2 pb [201].

6.2.2 Production of vector bosons in association with jets: W+Jets, Z+Jets

The production of vector gauge bosons in association with jets is a sub-dominant background. Depending on the type of boson produced, these events are named W+jets and Z+jets. The W+jets events represent a sizeable background for the *lep-had* channel, due
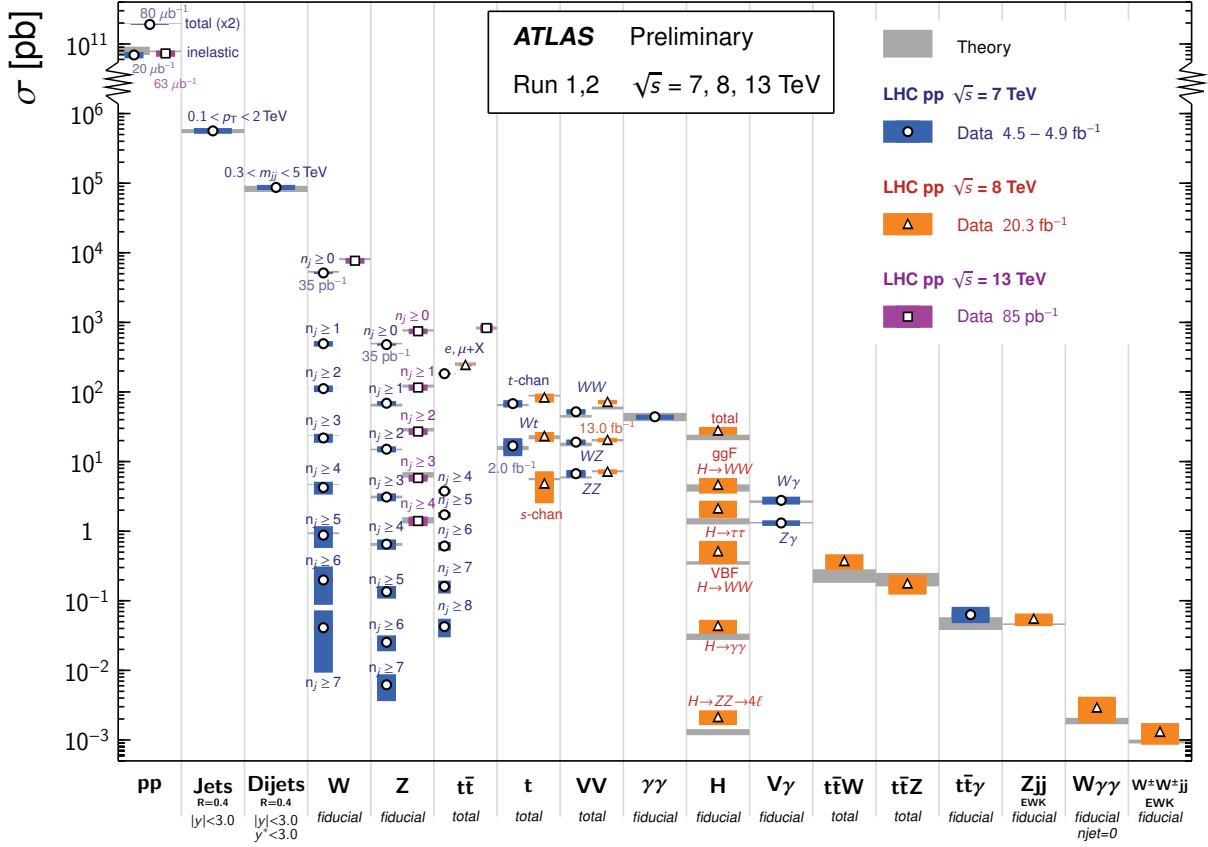
Figure 6.1: Summary of several SM total and fiducial production cross sections measurements, corrected for the leptonic branching ratios and compared to the theoretical expectations calculated at NLO or higher, performed using Run-I and early Run-II data sets. The uncertainties reflect the ones reported in the original ATLAS papers. Figure taken from [191].

to the presence of an isolated lepton, electron or muon, large $E_{\mathrm{T}}^{\mathrm{miss}}$ and jets that can be mis-identified as τ_{had} in the final state. The Z+jets events are a considerable background for *lep-lep* and *had-had* channels due to the presence of two light leptons or τ_{had}'s originating from the Z boson decay, respectively. Background events coming from Z+jets processes are present also in the *lep-had* channel in the case one of the two τ's coming from the Z boson decays hadronically while the other decays leptonically. This type of background can be rejected requiring an invariant mass of the two leptons to not be close to the Z mass.Due to the b-jets in the final state, the major contributions from this type of background events arise from the production of gauge bosons in association with heavy flavour jets.

6.2.3 Other backgrounds: WW, WZ, ZZ and $t\bar{t} + V$

Other sources of electroweak background events are due to the production of pairs of vector bosons. The next-to-leading order cross-sections of these processes for WW, WZ and ZZ production are respectively 66.1 pb, 38.5 pb, 13.1 pb [202]. Despite the relatively large cross section, these processes represent a subdominant background due to the combined requirements of heavy flavour jets and two identified leptons in the final state and large E_T^{miss} in the final state.

Rare SM processes can contribute to background events in a selected phase space targeting SUSY events. Processes like production of a top pair in association with gauge vector bosons, such as $t\bar{t} + W$ and $t\bar{t} + Z$ with a cross section of 0.232 pb and 0.206 pb [203] respectively, can enter the final selection. These processes have a very complex and rich final state that can mimic all the features required by this search. Production of a single top quark in association with a vector boson is included in the simulation for $t\bar{t} + V$ processes and is treated as indistinguishable in the $\tilde{t} \rightarrow \tilde{\tau}$ analysis.

6.2.4 Multijet production

Proton-proton collisions at the LHC can lead to the production of events fully in hadronic final states. In this context, multijet events are characterised by several energetic jets in the final state and no prompt isolated leptons and they are produced with an inclusive cross section of the order of 1 mb. The most common production mode of such events is a $2 \rightarrow 2$ QCD process but additional initial state radiation (ISR) or final state radiation (FSR) can lead to high jet multiplicity in the final state. These events can contain a large amount of E_T^{miss}, due to jet energy mis-measurements, and high-p_T leptons, which are typically non isolated, generated by the decays of heavy flavour hadrons. The combined requirements of one or more isolated light leptons, large E_T^{miss} and additional topological cuts make this background negligible for the *lep-lep* and *lep-had* channel. For the *had-had* mode it is not possible to exclude a priori this channel since there is a non negligible probability of a jet to be mis-identified as a τ_{had} and mimic the fully hadronic final state. In addition, since there is no reliable MC simulation for these processes available, the use of data driven methods is necessary to estimate the contribution of this background in the phase spaces targeted by SUSY searches.

6.3 Selected Data and Monte Carlo samples

The SUSY search discussed in this thesis uses the full $p - p$ collisions dataset of 20.3 fb^{-1} collected in 2012 at $\sqrt{s} = 8$ TeV. Only events that pass the high data quality standards are analysed in order to reject events recorded during periods with sub-detector failures or defects.

A set of MC simulated samples is used to model the signal and background processes considered in the search. The matrix element generator is interfaced to a simulator for the parton showering and fragmentation using various Parton Density function (PDF) sets and Monte Carlo tunes. The MC samples are either generated using the full ATLAS detector simulation [204] based on `GEANT4` [205] or a fast simulation of the electromagnetic

and hadronic calorimeter response and `GEANT4` elsewhere, named ATLAS Fast II (`AFII`) [206]. The normalisation of the background samples are calculated up to the next-to-next-to-leading order (NNLO) in α_s adding the resummation of soft gluon emission up to next-to-next-to-leading logarithm (NNLL) accuracy.

The signal cross sections are calculated to next-to-leading order (NLO) with next-to-leading logarithm (NLL) accuracy and their value and uncertainty are taken from an envelope of different predictions obtained using various PDF sets and renormalisation and factorisation scales [207]. The samples are generated taking into account additional $p - p$ interactions due to in-time and out-of-time pile-up and the simulated events are re-weighted so that the distribution of the average number of interactions matches the one of data. A summary of the programs used to generate the SM background and signal events, together with details on the cross-section normalisation, PDF sets, generator tunes and detector simulation scheme, is reported in Tab. 6.1.

Process	Generator	Parton Shower	Normalisation	PDF set	Generator tune	Detector
$t\bar{t}$	`POWHEG-r2129` [208, 209]	`PYTHIA` 6.426 [180]	NNLO+ NNLL [193–198]	NLO CT10 [68]	Perugia 2011C [210]	`AFII`
single top (Wt/s)	`POWHEG-r1556` [208, 211, 212]	`PYTHIA` 6.426	NNLO+ NNLL [200, 201]	CTEQ6L1 [77]	Perugia 2011C	`AFII`
single top (t)	`ACERMC` 3.8 [213]	`PYTHIA` 6.426	NNLO+ NNLL [199]	CTEQ6L1	Perugia 2011C	FullSim
$t\bar{t} + W/Z$	`MADGRAPH5` 1.3.28 [214]	`PYTHIA` 6.426	NLO [203]	CTEQ6L1	AUET2 [215]	FullSim
WW, WZ, ZZ	`SHERPA` 1.4.1 [216]	`SHERPA`	NLO[202]	NLO CT10	`SHERPA` default	FullSim
$Z/\gamma^*(e/\mu)$+jets	`ALPGEN` 2.14 [217]	`HERWIG` 6.520 [218]	NNLO [219]	CTEQ6L1	AUET2	`AFII`
$Z/\gamma^*(\tau)$+jets	`SHERPA` 1.4.1	`SHERPA` 1.4.1	NNLO [219]	NLO CT10	`SHERPA` default	`AFII`
W+jets	`SHERPA` 1.4.1	`SHERPA` 1.4.1	NNLO [219]	NLO CT10	`SHERPA` default	`AFII`
$\tilde{t}_1\tilde{t}_1^*$	`HERWIG++` 2.6.3 [220]	`HERWIG++` 2.6.3	NLO+ NLL [84, 221, 222]	CTEQ6L1	UE-EE-3 [223]	`AFII`

Table 6.1: Details about the MC generators, parton shower, PDF sets, cross section normalisation, generator tune and detector simulation scheme for the background and signal simulated samples.

6.4 Strategy of the $\tilde{t} \to \tilde{\tau}$ search

The analysis follows a strategy that is common to a large set of SUSY searches performed in the ATLAS experiment. The basic strategy of this search is a so called *cut-and-count* analysis, consisting of selecting a particular kinematic phase space where a significant amount of signal events are expected, evaluate the SM background contamination and compare the total expectation to the collected data. The first step consists of choosing dedicated rectangular cuts on a set of variables able to discriminate between the signal
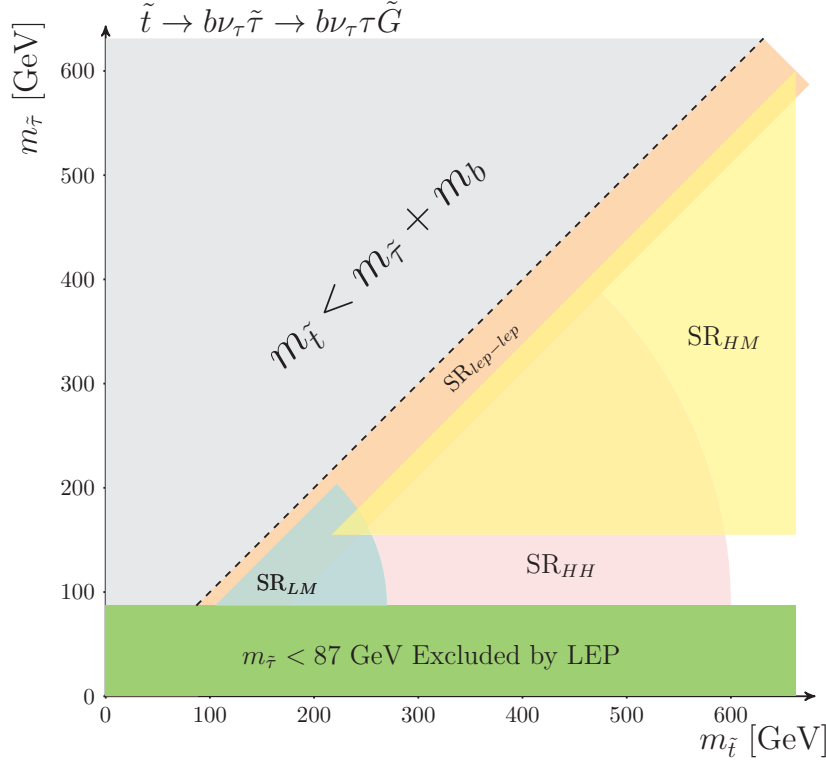
Figure 6.2: A schematic representation of the $m_{\tilde{t}} - m_{\tilde{\tau}}$ plane. The region above the line $m_{\tilde{t}} = m_{\tilde{\tau}} + m_b$ is kinematically forbidden and the region with $m_{\tilde{\tau}} < 87$ GeV has been excluded by searches for direct production of $\tilde{\tau}$'s at LEP [224–228]. The areas targeted by the different SRs described in the text are represented with different colours.

and SM backgrounds. An optimisation procedure is ran in order to choose the best cut value that maximises the signal efficiency and the background rejection. The final set of optimised cuts is referred to as *signal region* (SR). This procedure is performed on Monte Carlo simulation and the amount of data in the SR is kept blinded to avoid biases in the optimisation procedure. The second step consists of evaluating the SM background events that fall into the signal region selection using Monte Carlo simulation and data-driven approaches. Each major background normalisation is constrained to the data via a Likelihood fit in a *control region* (CR), characterised by a selection optimised to enrich the contribution of that particular background process. In addition, the CRs are required to be kinematically close to the SR, statistically independent and with a low signal contamination. The fit on the control region provides normalisation scale factors to be applied to the particular background MC estimate obtained in the signal region. The validity of this extrapolation is checked for each constrained background on a *validation region* (VR), orthogonal to the control region and signal region but kinematically closer to the latter. When this whole procedure is validated, the data is unblinded in the SR and an hypothesis test is run in order to assess if the SM-only hypothesis is statistically

compatible with the data observed or whether there is an excess in data. Details on the statistical treatment of the selected data is given in Sec. 6.5. For each possible $\tilde{t} \to \tilde{\tau}$ final state described in Section 6.1, one or more signal regions are defined, where the analysis sensitivity is maximised. The *lep-lep* channel has been investigated combining a set of SRs described in [190] and indicated as $\mathrm{SR}_{lep-lep}$ and targets the kinematic region close to the kinematic limit $m_{\tilde{t}} = m_{\tilde{\tau}} + m_b$. In this region, referred to as *compressed region*, the final state objects are expected to have soft momenta due to the small difference in mass between the scalar top and the scalar tau. The *lep-had* and *had-had* selections are insensitive to this scenario due to the τ_{had} identification criteria which requires τ_{had} with $p_\mathrm{T} > 20$ GeV to reduce the high jet background rates at lower momenta. The *lep-had* channel makes use of two independent SRs probing low top squark masses, SR_{LM}, and high top squark masses SR_{HM}. The *had-had* channel is covered by a single signal region, SR_{HH}, aiming to extend the sensitivity to low values of $m_{\tilde{\tau}}$. In Fig. 6.2 the accessible phase space in the $m_{\tilde{t}} - m_{\tilde{\tau}}$ plane is shown, together with a sketch of the areas targeted by the different SRs used by the analysis. The phase space region with $m_{\tilde{\tau}} < 87$ GeV has been already excluded by direct τ slepton searches at LEP [224–228].

6.5 Statistical analysis

The search presented in this thesis makes use of statistical data analysis techniques in order to extract both the backgrounds normalisation factors and to test if any eventual excess of number of observed events over the SM expectation is statistically significant. These techniques make use of different Likelihood fits which are briefly summarised in this section. Operatively, all the Likelihood fits performed in this analysis make use of the `HistFitter` package [229, 230], which is based on `RooFit`/`RooStats` framework [231, 232]. A more detailed review of the statistical procedure used in this search is presented in [233].

Likelihood Function

The generic Likelihood function used in this analysis has the following form

$$\mathcal{L}(\mathbf{N^D}|\boldsymbol{\mu}, \boldsymbol{s}, \boldsymbol{B}, \boldsymbol{\theta}) = \prod_{regions} \mathcal{P}_i(N_i^D | N_i^{exp}(\boldsymbol{\mu}, \boldsymbol{s}, \boldsymbol{B}, \boldsymbol{\theta})) \prod_j \mathcal{N}(\theta_j) \tag{6.2}$$

where $\mathcal{P}$ is the Poisson distribution which, for each region i, depends on the number of observed events N_i^D and the number of expected events N_i^{exp}, which is a function of the systematic uncertainties $\boldsymbol{\theta}$, the number of expected signal and background events $\boldsymbol{s}$ and $\boldsymbol{B}$ corrected by normalisation scale factors $\boldsymbol{\mu}$. In each region i, the number of expected events is given by the sum of the scalar top expected events s_i and the total SM expectation B_i and depends on a set of systematics uncertainties $\boldsymbol{\theta}$

$$N_i^{exp} = \mu_s s_i(\boldsymbol{\theta}) + \sum_j \mu_{b,j} b_{j,i}(\boldsymbol{\theta}) \tag{6.3}$$

where the sum extend over all the SM background processes and μ_s and $\mu_{b,j}$ are normalisation factors for the signal and a single background process b_j, respectively. The dependence of the expected number of events on the systematic uncertainty for each pro-

cess N_p, where p indicates the signal process or a particular background process b_j, in the region i is given by

$$N_p^i = N_{nom,p}^i \cdot (1 + \sum_k \Delta_{p,k}^i \theta_k) \tag{6.4}$$

where k indicates every systematic source considered, $\Delta_{p,k}^i$ is the absolute systematic variation from the nominal expected value $N_{nom,p}$ due to the systematic source θ_k. The parameters θ_k are nuisance parameters in the Likelihood function of Eq. 6.2 and are constrained by Normal distributions $\mathcal{N}$, i.e. Gaussian distributions with zero mean and variance equal to one. In each region i, the other free parameters in the Likelihood function are the *signal strength* μ_s, which is the normalisation factor applied to the signal process under examination, and the normalisation factors for each SM background process j, $\mu_{b,j}$.

Background estimate Likelihood fit

In this analysis, a data driven technique is used in order to extract the normalisation of the major SM processes in the signal regions instead of relying directly on the nominal MC expectation. The fit is performed simultaneously on a set of orthogonal control regions defined by a number of kinematic cuts. The input parameters of the Likelihood fit are the number of observed events in each control region and the fit parameters are the normalisation factors of the SM background processes under analysis. The fit is performed assuming that the number of expected signal events in the control region is zero so it is important to design control regions with the lowest possible signal contamination for each superparticle mass hypothesis considered in the simplified model under investigation.

Discovery and exclusion Likelihood fits

A hypothesis test is performed in order to evaluate whether the number of observed data is not compatible with the SM background-only expectation. The test variable used is the Likelihood ratio given by

$$q(\mu_s) = -2 \ln \left(\frac{\mathcal{L}(N^D | \mu_s, \hat{\hat{\boldsymbol{\theta}}}, \hat{\hat{\boldsymbol{b}}})}{\mathcal{L}(N^D | \hat{\mu}_s, \hat{\boldsymbol{\theta}}, \hat{\boldsymbol{b}})} \right) \tag{6.5}$$

where the single hat indicates the values that maximise the Likelihood, while the double hat indicated the values that maximise the Likelihood for a fixed μ_s. Firstly, a *discovery test* is performed. In this test the normalisation factor for the signal is fixed to zero and any signal contamination in the control regions is assumed to be negligible. For this test the Likelihood ratio variable is defined as

$$q_0 = \begin{cases} q(0), & \text{if } \hat{\mu}_s > 0 \\ 0, & \text{if } \hat{\mu}_s < 0. \end{cases} \tag{6.6}$$

The test against the background-only hypothesis is carried out computing a *p-value*

$$p(\mu_s) = p_{\mu_s} = \int_{q_{\mu_s}^{obs}}^{\infty} f(q(\mu_s)|\mu_s) dq_{\mu_s} \tag{6.7}$$

where $f(q(\mu_s)|\mu_s)$ is the probability density function of the test statistic q_{μ_s} given a fixed value of μ_s and the integral extends from the observed value of the test statistic to infinity. The analytical form of $f(q(\mu_s)|\mu_s)$ is not known a priori, so an approximated form is computed with an asymptotic function [233], in the case of signal regions with large statistics, or by generation of pseudo experiments, if the expected statistics is limited. Data is considered incompatible with the background only hypothesis if $p(\mu_s = 0) = p_0 \leq 2.87 \cdot 10^{-7}$, corresponding to the integral over the tails of a Gaussian distribution starting from 5 standard deviations away from the mean. In the case the discovery test fails to reject the background-only hypothesis, a model dependent *exclusion limit* is carried out in order to exclude signal hypotheses with a fixed signal strength and considering the signal contamination in the control regions. The statistic for the exclusion test for a certain μ_s is given by

$$q_{\mu_s} = \begin{cases} q(\mu_s), & \text{if } \mu_s \geq \hat{\mu}_s \\ 0, & \text{if } \mu_s < \hat{\mu}_s. \end{cases} \tag{6.8}$$

In order to exclude the signal models considered in this analysis the signal strength is imposed to be $\mu_s = 1$ and a particular signal model is excluded using the CL_s formalism [234]. First the CL_s is computed as

$$CL_s = \frac{p_1}{1 - p_0} \tag{6.9}$$

where p_1 and p_0 are the *p-values* calculated by Eq. 6.7 using $\mu_s = 1$ and $\mu_s = 0$, respectively. A particular signal hypothesis is excluded at 95% Confidence Level (CL) if $CL_s < 0.05$, alternatively the point is not excluded. In this analysis, the results from the different signal regions have been combined by choosing the signal region yielding the lowest CL_s for a particular signal hypothesis.

7 Signal Selection and background estimate

7.1 Hadron-Hadron Channel

The *had-had* channel targets the $\tilde{t} \to \tilde{\tau}$ final state where both τ-leptons decay hadronically. In the following sections a detailed description of the procedures adopted for the event selection, signal region definition and background estimate and validation is presented.

7.1.1 Trigger selection

The data used by the *had-had* channel is collected using a missing transverse trigger with a a threshold of $E_{\mathrm{T,EF}}^{\mathrm{miss}} > 80$ GeV at event filter level for to a total integrated luminosity of 20.1 fb^{-1}. The turn-on curve of the $E_{\mathrm{T}}^{\mathrm{miss}}$ trigger was extracted using data collected by a muon trigger as a reference and an offline cut on the muon transverse momentum of $p_{\mathrm{T}} > 25$ GeV. A baseline selection of at least two jets, with the leading-jet $p_{\mathrm{T}} > 40$ GeV, exactly one muon with $p_{\mathrm{T}} > 25$ GeV and a medium τ_{had} with $p_{\mathrm{T}} > 20$ GeV is applied before extracting the trigger efficiency. In Fig. 7.1 the trigger efficiency as a function of the offline $E_{\mathrm{T}}^{\mathrm{miss}}$ is shown. The offline $E_{\mathrm{T}}^{\mathrm{miss}}$ has been corrected to match with the online definition, subtracting the muon transverse momentum in both the MC simulation and data. The turn-on curve shows that the trigger is fully efficient at the plateau. A cut at $E_{\mathrm{T}}^{\mathrm{miss}} > 150$ GeV has been used as offline cut for the *had-had* analysis since the trigger plateau is reached.

7.1.2 Discriminating variables and Signal Region

The events that pass the trigger requirement are preliminarily selected applying a set of cuts, called *Preselection*, aiming to select signal-like final states using only loose requirements. Exactly two τ_{had} with $p_{\mathrm{T}} > 20$ GeV are requested passing the *tight* jet-BDT and *medium* electron-BDT working points, respectively. The *tight* jet-BDT working point has been chosen in order to reduce the events where jets could be misidentified as τ_{had}. A veto on isolated leptons, either muon or electron, has been placed, ensuring complete orthogonality with the other channels of the search. The missing transverse momentum is requested to satisfy $E_{\mathrm{T}}^{\mathrm{miss}} > 150$ GeV as discussed in Sec. 7.1.1. At least two jets with $p_{\mathrm{T}} > 20$ GeV are required. The leading jet[1] in the event is imposed to have $p_{\mathrm{T}}^{jet,1} > 40$ GeV, in order to apply the multijet background determination method (see Sec. 7.1.3 for details). Finally a cut on the angular separation between the missing transverse momentum and the leading jets is placed in order to reject possible multijet contamination. In fact, in order to have multijet events passing the very hard cut of $E_{\mathrm{T}}^{\mathrm{miss}} > 150$ GeV, a large mis-measurement

---

[1]In this context *leading jet* indicates the jet with highest p_{T} in the event. The second leading jet is usually referred to as *sub-leading*.
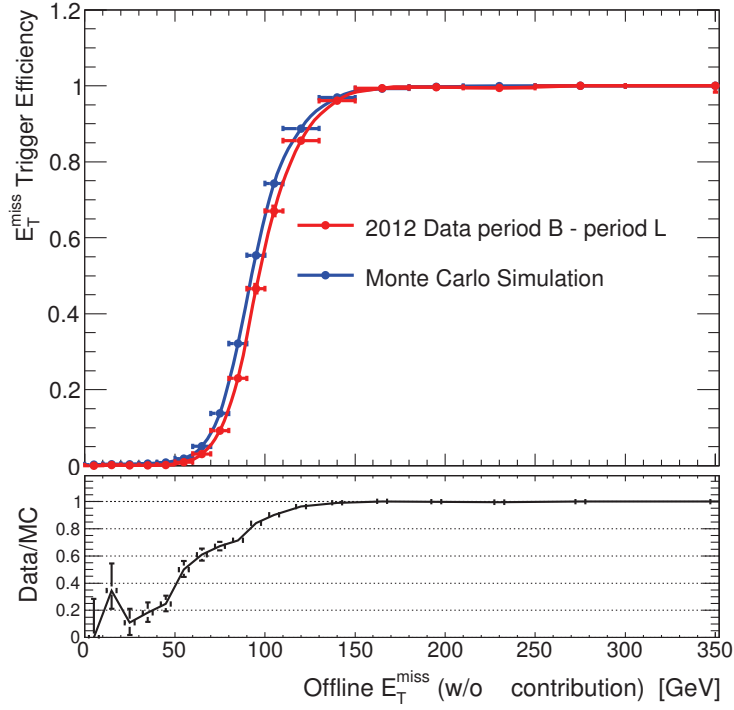
Figure 7.1: Comparison between data and MC simulation of the efficiency of the logical OR between the two E_T^{miss} triggers used for the had-had channel calculated with a muon trigger as reference. The data events shown are limited to the ones where both the triggers are defined, namely for run numbers greater than 203719. The statistical errors are reported in the error bands of the ratio plot.

of the energy of the hardest jets in the event is necessary to produce large amounts of *fake-E_T^{miss}*. Therefore, the *fake-E_T^{miss}* is aligned with the direction of those jets and such events can be removed with a cut on $\left|\Delta\phi(E_T^{\mathrm{miss}}, \mathrm{jet}_i)\right| > 0.5$ with $i = 1, 2$.

Variable		Cut Value
$N_\mu + N_{el}$		$=0$
$N_{\tau_{\mathrm{had}}}$		$=2$
N_{jets}		≥ 2
$\mathrm{jet}^1_{p_T}$		≥ 40 GeV
E_T^{miss}		≥ 150 GeV
$\left|\Delta\phi(E_T^{\mathrm{miss}}, \mathrm{jet}_i)\right|$	$i = 1, 2$	≥ 0.5

Table 7.1: Summary of the Preselection cuts applied for the *had-had* channel.

A summary of the preselection cuts is given in Tab. 7.1. These selections provide a basic rejection of the SM backgrounds to the *had-had* channel and are the starting point for the optimisation studies. A large set of kinematic variables has been studied in order to
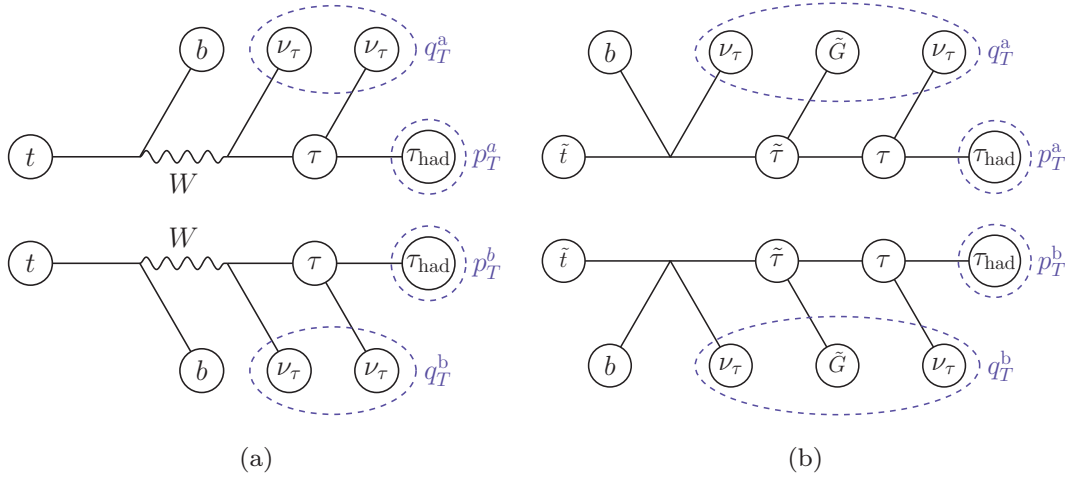
Figure 7.2: Schematic representation of how the decomposition of the $E_\mathrm{T}^\mathrm{miss}$ is performed in the stransverse mass calculation for both $t\bar{t}$ (a) and $\tilde{t} \to \tilde{\tau}$ (b) events. Both the invisible $\left(q_\mathrm{T}^a, q_\mathrm{T}^b\right)$ and the visible $\left(p_\mathrm{T}^a, p_\mathrm{T}^b\right)$ momenta used in the calculation are highlighted in the figure.

obtain a good discrimination between signal and background, but only the most powerful variables are retained. These variables are described in the rest of this section, together with a plot showing the separation between signal and background. In the plots, the total SM prediction includes the combination of statistical and systematic uncertainties[2]. In the plots the systematics are treated as uncorrelated between the processes, leading to an overestimation of the systematic band with respect to the final results. In addition, the SM backgrounds contributions are stacked up, while two signal models are superimposed to show the power of these variables in discriminating different kinematic distribution shapes.

Transverse and Stransverse masses

The transverse mass is a kinematic variable defined as

$$m_\mathrm{T}\,(\mathrm{a,b}) = \sqrt{m_\mathrm{a}^2 + m_\mathrm{b}^2 + 2\left(E_\mathrm{T}^\mathrm{a} E_\mathrm{T}^\mathrm{b} - \mathbf{p_\mathrm{T}^a} \cdot \mathbf{p_\mathrm{T}^b}\right)}\,, \qquad (7.1)$$

where m, p_T and E_T are the object mass, transverse momentum and transverse energy, respectively. In this analysis, the objects used in the m_T calculation are considered massless. In the selected final state the sources of missing momentum are due to multiple invisible particles, i.e. neutrinos coming from the W decays in W+jets and $t\bar{t}$ events and neutrinos produced by the τ lepton decay which are present also in $Z(\to \tau_\mathrm{had}\tau_\mathrm{had})$+jets decays. Since the $\tilde{t} \to \tilde{\tau}$ signal is characterised by two additional gravitinos in the final state, a larger tail in the m_T distribution is expected. Due to the intrinsic ambiguity in the definition of this variable caused by the presence of two τ_had in the final state, two transverse masses are defined using both the leading τ_had $(m_\mathrm{T}(\tau_{had,1}))$ and the sub-leading τ_had $(m_\mathrm{T}(\tau_{had,2}))$,

---

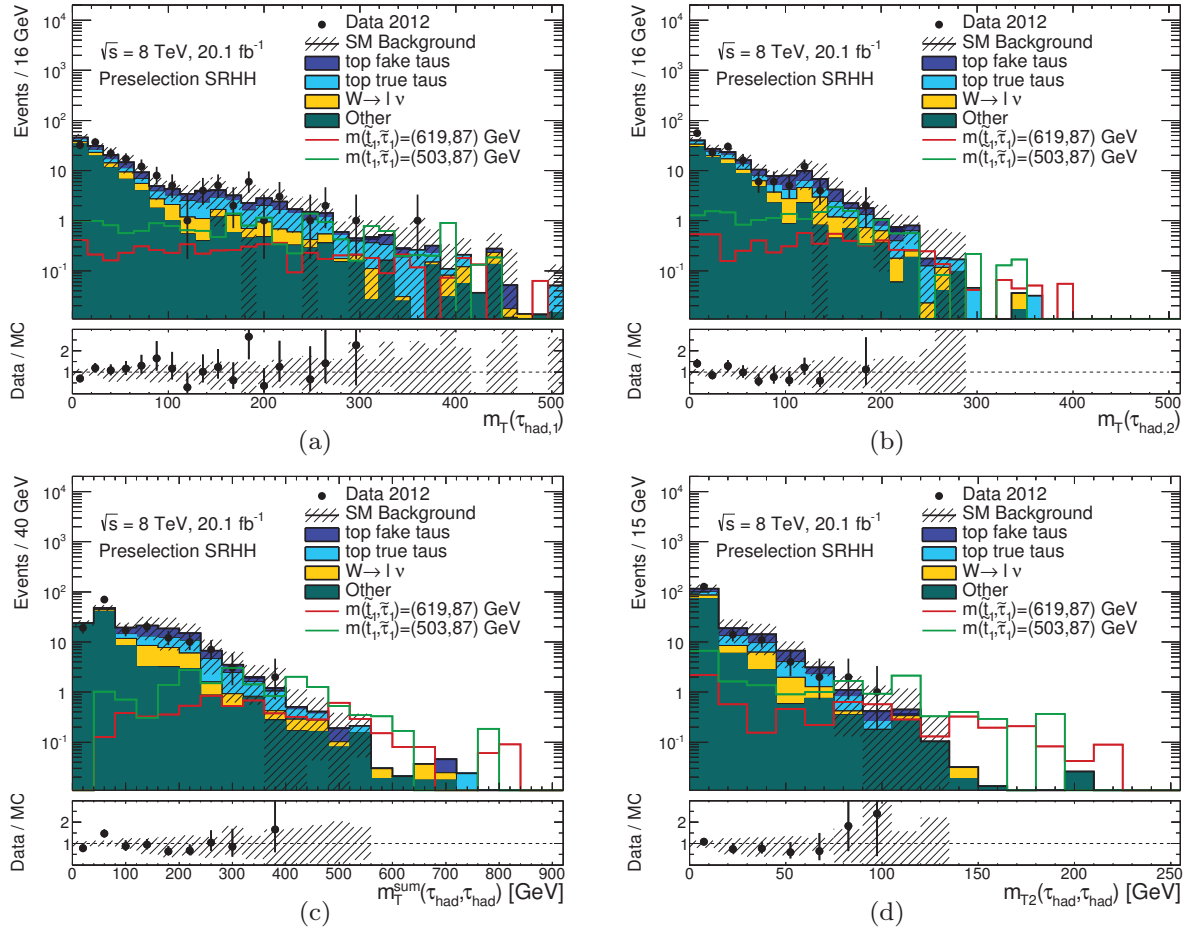[2]A description of all the systematic uncertainties is given in Sec. 8.3.

Figure 7.3: Distributions of the $m_T(\tau_{had,1})$ (a) and $m_T(\tau_{had,2})$ constructed with the leading and sub-leading τ_{had}, of the $m_T^{sum}(\tau_{had}, \tau_{had})$ (c) and $m_{T2}(\tau_{had}, \tau_{had})$ (d) after preselection cuts.

respectively. The discrimination power can be improved considering the sum of the two transverse masses:

$$m_T^{sum}(\tau_{had}, \tau_{had}) = m_T(\tau_{had,1}) + m_T(\tau_{had,2}). \tag{7.2}$$

This variable is particularly powerful in removing the Z+jets background. In fact in order to pass the very hard E_T^{miss} requirement, large missing transverse momentum has to come from the ν_τ coming from the τ decay. This configuration results in low transverse masses since the neutrinos are essentially aligned with the taus. It is possible to extend the transverse mass to a more general case when more than one invisible particles are expected in the final state. The *stransverse mass* [235, 236] is defined as:

$$m_{T2}(a, b) = \sqrt{\min_{\mathbf{q}_T^a + \mathbf{q}_T^b = \mathbf{p}_T^{miss}} \left(\max \left[m_T^2\left(\mathbf{p}_T^a, \mathbf{q}_T^a\right), m_T^2\left(\mathbf{p}_T^b, \mathbf{q}_T^b\right) \right] \right)}, \tag{7.3}$$

where the minimisation is performed over all the possible configurations of the vectors
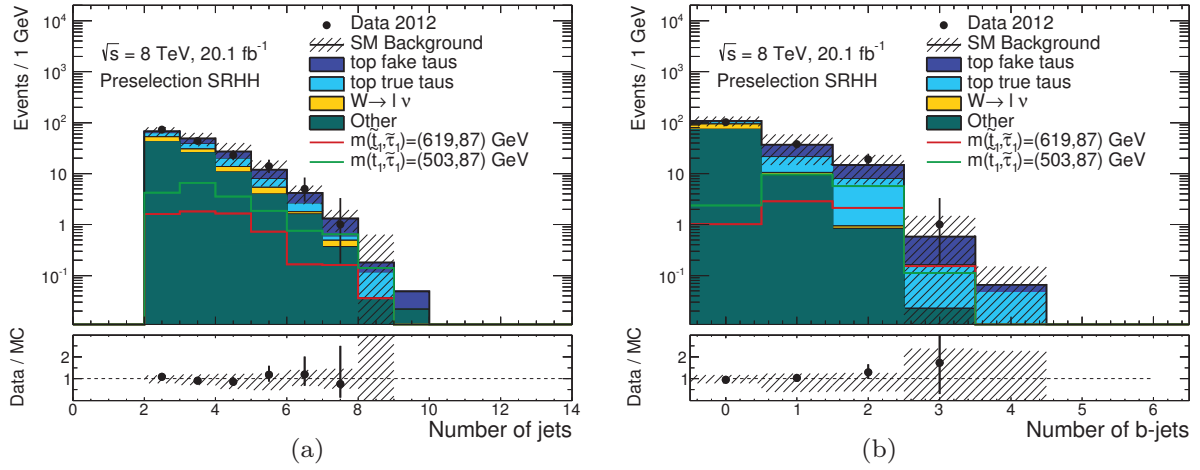
Figure 7.4: Distributions of the number of jets (a) and of the identified b-jets in the final state after the preselection cuts.

$\mathbf{q}_T^a$ and $\mathbf{q}_T^b$ satisfying $\mathbf{q}_T^a + \mathbf{q}_T^b = \mathbf{p}_T^{\text{miss}}$. The stransverse mass in the *had-had* channel is built using the two τ_{had} and the E_T^{miss}, with the hypothesis of invisible massless particles. A schematic representation of the assignment of the object momenta in $t\bar{t}$ and $\tilde{t} \to \tilde{\tau}$ events is given in Fig. 7.2. The stransverse mass calculated in SM processes with an on-shell W has as upper limit the mass of the W boson [237, 238], although this condition is not observed in reality due to detector resolution effects. Due to the presence of two additional gravitinos, signal events have a longer tail and can be selected placing a lower cut on this variable. This m_{T2} has the highest discrimination power and is widely used in all three channels of this search. Alternative definitions of this variable using different decomposition and invisible particles mass hypotheses are used in the *lep-had* and *lep-lep* channel. The kinematic distributions of the transverse masses and of the stransverse mass are shown in Fig. 7.3.

Number of b-jets

The signal final state is characterised by two jets originating from b-quarks, which can provide a strong rejection against several SM processes. In this search the `MV1` *tight* working point, corresponding to 70% of b-jets selection efficiency, is used in order to obtain a set of data with higher purity in the final SR. The distributions of the number of jets and the number of identified b-jets are shown in Fig. 7.4, where it is evident that the request of the presence of b-jets in the selection provides a strong rejection power.

Signal Region Optimisation

The signal region selection for the *had-had* channel is performed with the aim to provide a very good coverage in the phase space region characterised by values of $m_{\tilde{\tau}}$ close to the
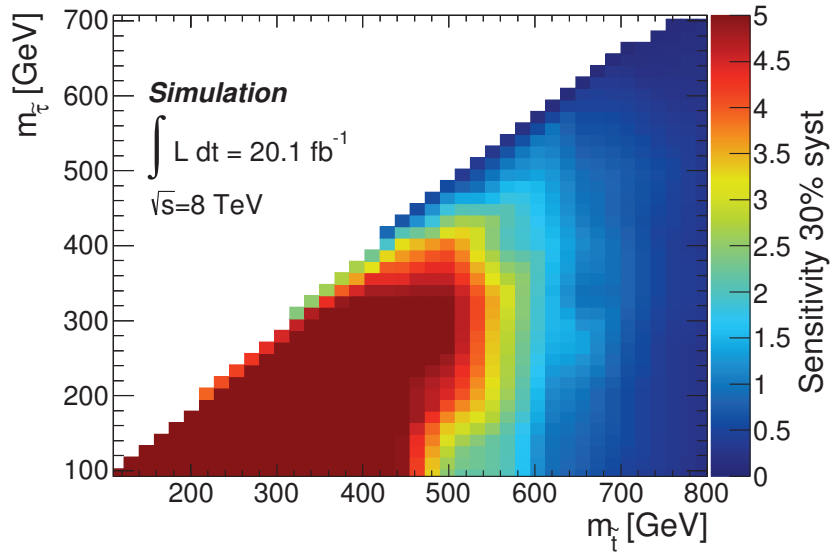
Figure 7.5: Values of the sensitivity $S/\sqrt{B + (0.3B)^2}$ as a function of $m_{\tilde{t}}$ and $m_{\tilde{\tau}}$ for the SR$_{HH}$ selection. A cut-off at sensitivity value equal to 5 has been applied in the plot to improve readability.

LEP limit of 87 GeV [224–228]. A good coverage is also expected in the central region of the $m_{\tilde{t}} - m_{\tilde{\tau}}$ plane where the separation $\Delta(m_{\tilde{t}}, m_{\tilde{\tau}})$ is large enough to permit the reconstruction of τ_{had} that require a minimum $p_{\text{T}} \geq 20$ GeV. The variables used in the optimisation procedure are the number of b-jets in the final state $N_{b-\text{jet}}$, the sum of the τ leptons transverse masses $m_{\text{T}}^{\text{sum}}(\tau_{\text{had}}, \tau_{\text{had}})$ and the stransverse mass $m_{\text{T2}}(\tau_{\text{had}}, \tau_{\text{had}})$. The optimisation has been performed using only MC simulation, since data is kept *blinded* in the procedure in order to avoid biases or artificial fine tuning of the final cuts. A systematic uncertainty of 30% on the total background estimate is considered in the process. Every optimisation strategy needs a figure of merit in order to be able to choose which set of cuts perform best. In this channel a simple figure of merit $\mathcal{S} = S/\sqrt{B + (\sigma_B)^2}$ is used, where S and B are the number of the expected signal and background events and $\sigma_B = 0.3 \times B$ corresponds to a 30% systematic uncertainty. In the procedure it is requested that the optimised set of cuts must satisfy $B \geq 2$, in order to avoid unphysical results and reduce the statistical uncertainty in the final selection. At this stage of the analysis, all the necessary MC weights, such as scale factors for the object reconstruction modelling, pile-up weight and a normalisation weight to reproduce the expectation corresponding to 20.1 fb^{-1} of integrated luminosity, are applied. The results of the optimisation procedure are shown in Fig. 7.5 and the signal region selection is reported in Tab. 7.2.

Signal Region composition

The first step of the analysis is the evaluation of the topology of backgrounds entering the *had-had* Signal Region, denominated SR$_{HH}$ in the following. In Tab. 7.2 the expected

SRHH	
Variable	Cut Value
Charge of τ_{had}	Opposite Sign (OS)
$m_{\mathrm{T}}^{\mathrm{sum}}(\tau_{\mathrm{had}}, \tau_{\mathrm{had}})$	≥ 160 GeV
$m_{\mathrm{T2}}(\tau_{\mathrm{had}}, \tau_{\mathrm{had}})$	≥ 50 GeV
$N_{b-\mathrm{jets}}$	≥ 1

Table 7.2: Cuts applied on top of the preselection defining the SR_{HH}.

SM background events entering the selection are shown. These processes are grouped in three categories through matching the reconstructed τ_{had} to the truth particles produced in simulation. Firstly, truth hadronically decaying taus are selected and their four momenta are corrected subtracting the four momenta of the ν_τ produced in the decay, defining in this way the *visible momentum* $\tau_{\mathrm{had}}^{\mathrm{vis}}$. If $\Delta R(\tau_{\mathrm{had}}, \tau_{\mathrm{had}}^{\mathrm{vis}}) < 0.2$, the reconstructed τ_{had} is considered a *real* tau. In the case both τ_{had} in the final state are matched to the same truth $\tau_{\mathrm{had}}^{\mathrm{vis}}$, the one with smaller value of $\Delta R(\tau_{\mathrm{had}}, \tau_{\mathrm{had}}^{\mathrm{vis}})$ is selected. If a reconstructed τ_{had} is not matched to any truth level τ lepton, it is classified as *fake* τ, originating from the misidentification of an electron or a jet.

Following this procedure, the events entering the SR_{HH} are grouped in three categories. The first contains events with two *real* hadronically decaying taus and consists mainly of $t\bar{t}$, single-top quark, diboson and $t\bar{t} + V$ events. The second category corresponds to one *real* and one *fake* τ_{had} in the final state and is composed by events coming from $t\bar{t}$, single-top and Z+jets events. The third category consists in two *fake* τ_{had} in the final state and is made of events produced mostly by $t\bar{t}$, single-top, $Z(\to \nu_\tau \nu_\tau)$+jets and multijet processes. The composition of the SR_{HH} is shown in Tab. 7.3. The $t\bar{t}$ process represents the major source of background events due to its final state being kinematically very similar to the signal model, followed by single top and dibosons. The majority of the EWK background events belong to the two *real* τ_{had} category (59.4%), followed by the one *real* and one *fake* τ_{had} (37.9%). Finally, the contribution due to two *fake* taus is very small (2.7%) but doesn't include the contribution of multijet events, which has been evaluated with a data driven method.

7.1.3 Multijet background estimate

The multijet background can contribute to the *had-had* channel when jets are mis-identified as *tight* τ_{had} and if large $E_{\mathrm{T}}^{\mathrm{miss}}$ is present in the event due to large jet energy mis-measurement. Even if these two effects have a very low probability to occur, the multijet production cross section is extremely large and a considerable amount of multijet events might enter the signal region selection. In addition, the large cross section of the multijet processes makes it difficult to provide a simulation with sufficient statistics. The probability for a jet to pass the *tight* tau identification criteria is not expected to be reliably described by simulation due to the complications in modelling of the fragmentation processes and of the interactions of hadrons with the detector. The multijet estimate is primarily based on the *Jet Smearing* method, described in details in [239], which consists of two basic steps.

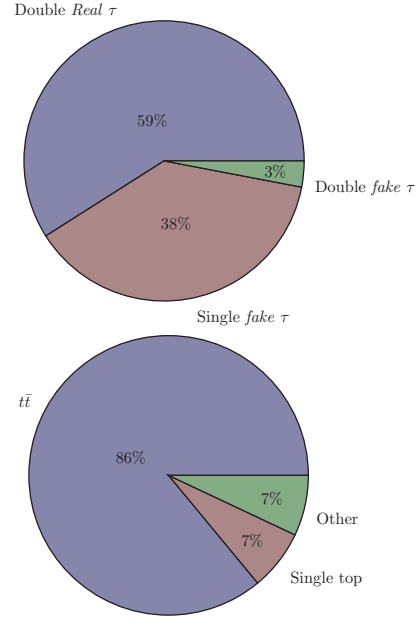|	SR_{HH}
Estimated bkg events	3.7
$t\bar{t}$ real τ_{had}	1.89
$t\bar{t}$ 1-fake τ_{had}	1.23
$t\bar{t}$ 2-fake τ_{had}	0.07
single top real τ_{had}	0.11
single top 1-fake τ_{had}	0.12
single top 2-fake τ_{had}	0.03
W+jets	0.01
Dibosons	0.14
Z+jets	0.04
$t\bar{t} + V$	0.04

Table 7.3: Composition of the background in the SR_{HH} selection estimated by MC simulation. No uncertainty on the estimate is given at this stage since these results are obtained before the background estimate procedure. The pie charts show the composition in term of number of real or fake τ and in term of SM processes.

First, *seed* events with well measured $E_{\mathrm{T}}^{\mathrm{miss}}$ are selected from a data sample enriched in multijet events, with similar kinematics and jet flavour content as the Signal Region. Secondly, the energy of the jets present in each of the seed events is *smeared* according to dedicated functions representing the calorimeter response in order to simulate large amount of $E_{\mathrm{T}}^{\mathrm{miss}}$ originating from detector resolution[3]. In order to obtain smooth multijet pseudo-data kinematic distributions, it is very important that enough statistics is retained in the seed events selection. For this reason, the jet-BDT identification criteria have been dropped for reconstructed τ_{had} and these objects will be indicated as noBDT$-\tau_{\mathrm{had}}$ in the following. The probability for a noBDT$-\tau_{\mathrm{had}}$ to pass the *tight* identification criterion has been calculated in order to estimate the multijet background in the SR_{HH}, where two *tight* τ_{had} are required. The steps to obtain the final estimate are summarised below.

No-BDT to *tight* τ_{had} fake rate

The first step consists of the calculation of the fake rate in a data sample recorded by a single un-prescaled[4] single jet trigger with an online threshold of $p_{\mathrm{T}} > 360$ GeV. A cut of

---

[3]Hadronically decaying taus are smeared as ordinary jets even if their response function might differ due to different *out-of-cone* activity and particle multiplicity. Dedicated smearing functions for this particular type of jets constitute a possible improvement of the method.

[4]The rate of every trigger in ATLAS is scaled down by a multiplicative factor, called *prescale* factor, in order to record events within the allowed bandwidth. During offline reconstruction, each event recorded by a certain trigger obtains a weight equal to the prescale factor. An un-prescaled trigger has a scaling factor equal to one.
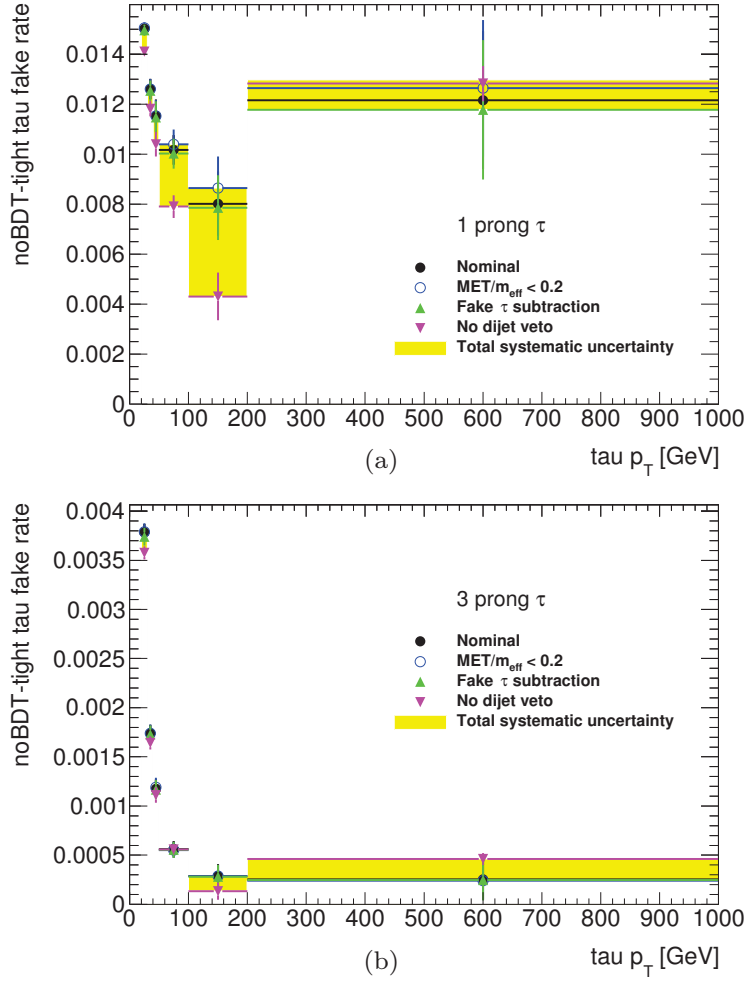
Figure 7.6: Fake rate, defined in Eq. 7.4, as a function of the noBDT$-\tau_{\text{had}}$ p_{T} for 1-prong (a) and 3-prong (b) tau candidates obtained in the selection discussed in the text. The total systematic uncertainty on the fake rate is shown as a yellow band around the central value.

$p_{\text{T}} > 410$ GeV is required offline on both data and MC in order to ensure the trigger plateau. Additionally, events with back to back leading jet and leading noBDT$-\tau_{\text{had}}$ characterised by $\Delta\phi(\text{jet1}, \tau_1) > 2.6$ are vetoed. This kind of back-to-back di-jet events cause an artificial bump around 410 GeV in the p_{T} distribution of the noBDT$-\tau_{\text{had}}$ when imposing the p_{T} cut on the leading jet. The bump is due to the fact that the noBDT$-\tau_{\text{had}}$ p_{T} follows a different turn-on shape than the leading jet p_{T} distribution due to the different energy calibration scheme (see Section 3.2.3). Finally, at least two jets are required in the final state in order to enrich it in multijet topology. The fake rate is calculated as the ratio of the number of taus that pass the *tight* identification over the noBDT$-\tau_{\text{had}}$ selection:

$$F(p_{\text{T}}^\tau) = \frac{N_{\tau,data}^{\text{tight-BDT}} - N_{true\ \tau,MC}^{\text{tight-BDT}}}{N_{\tau,data}^{\text{no-BDT}} - N_{true\ \tau,MC}^{\text{no-BDT}}} \tag{7.4}$$

121

where $N_{true\ \tau,MC}$ is the number of truth matched τ_{had} generated by non-multijet processes. Some possible sources of systematics were investigated for the fake rate measurement. First, the impact of the selection cuts was evaluated removing the di-jet veto and, subsequently, applying an additional cut on the ratio $E_{\text{T}}^{\text{miss}}/m_{\text{eff}} < 0.2$, where m_{eff} is defined as the scalar sum of $E_{\text{T}}^{\text{miss}}$ and the p_{T} of the visible objects. This additional requirement further enriches the selections in multijet events at the cost of a lower statistics for the numerator of Eq. 7.4. Finally, in the calculation of the fake rates, the removal of the truth matched taus assumes that the quark/gluon composition of the numerator of Eq. 7.4 has a smaller effect than the mis-modelling of fake taus in the simulation and therefore has a small impact on the value of the fake rate. This assumption was checked including the fake tau component in the MC background subtraction. The results of the fake rate measurements are shown in Fig. 7.6.

Selection of Seed Events and multijet pseudo data

The seed events were recorded using a logical `OR` between various single jet triggers. The lowest threshold trigger has an online jet $p_{\text{T}} > 25$ GeV requirement, leading to an offline request of $p_{\text{T}} > 40$ GeV to ensure full trigger efficiency. This requirement justifies the need of the cut on the leading jet p_{T} in the *had-had* channel. The use of prescaled single-jet triggers with low transverse momentum is justified by the requirement of selecting seed events with jet kinematics similar to the one of the $\tilde{t} \to \tilde{\tau}$ signal. The correct prescale factors have been considered when merging the data collected by different jet triggers. The selection proceeds requiring at least two jets and at least one b-tagged jet, at least two noBDT$-\tau_{\text{had}}$ and a veto on light leptons. The final step consists of selecting seed events with very well measured $E_{\text{T}}^{\text{miss}}$ placing an upper cut on the $E_{\text{T}}^{\text{miss}}$ significance, defined as:

$$E_{T,\text{sig}}^{\text{miss}} = \frac{E_{\text{T}}^{\text{miss}}}{\sqrt{\sum\limits_{jets} E_{\text{T}} + \sum\limits_{soft\ terms} E_{\text{T}}}} \tag{7.5}$$

The upper cut was chosen to be $E_{T,\text{sig}}^{\text{miss}} < 4$ in order to select a region enriched in multijet seed events with low contamination from other processes. The distribution of the $E_{T,\text{sig}}^{\text{miss}}$ is shown in Fig. 7.7 and the seed selection region is summarised in Tab. 7.4. For each selected seed event, the light jets and b-jets present in the final state were smeared according to the relative calorimeter response functions. As stated above, jets reconstructed as noBDT$-\tau_{\text{had}}$ are treated as jets, since no dedicated calibration functions have been implemented in the *Jet Smearing* software at the time of the analysis. Each event was smeared 2500 times in order to obtain a set of multijet pseudo data with sufficient statistics and smooth kinematic distributions.

The normalisation of the multijet template is obtained from data in a dedicated region enriched in multijet events. This region is obtained requiring $E_{\text{T}}^{\text{miss}}/m_{\text{eff}} < 0.2$ and $\Delta\phi(\text{jet}_2, E_{\text{T}}^{\text{miss}}) < 0.5$. Since these requirements are not sufficient to suppress $t\bar{t}$, $W+$jets and $Z \to \nu\nu$ to a negligible level, three control regions have been defined to check the modelling and the normalisation of these backgrounds. While the top and $W+$jets control
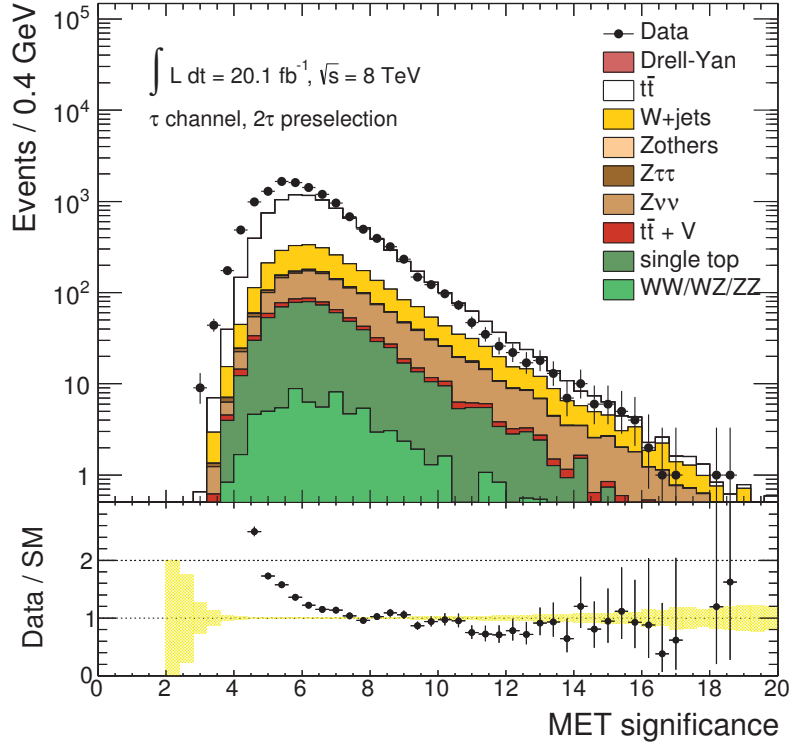
Figure 7.7: Distribution of the $E_{\mathrm{T,sig}}^{\mathrm{miss}}$ in the region where all the cuts of the multijet seed selection are applied apart from the $E_{\mathrm{T,sig}}^{\mathrm{miss}}$ itself. Events are collected using the $E_{\mathrm{T}}^{\mathrm{miss}}$ trigger. The multijet processes contribution is not added to the plot. Only the statistical uncertainty is considered.

regions have been defined through dedicated kinematic cuts, the $Z \to \nu\nu$ control region relies on a slightly more advanced method due to the fact that neutrinos are invisible to ATLAS and there is no trivial way to select this particular process. Firstly, $Z \to \mu\mu$ events have been selected requiring exactly two muons and no b-jets. The final state muons are considered equivalent to two invisible neutrinos ($p_\mu \equiv p_\nu$), with the clear advantage of knowing precisely their four momenta. This assumption is supported by the low mis-identification rate and the low calorimeter energy deposit of relativistic muons. Therefore, the second step consists in recomputing the missing transverse energy of each event adding back the transverse momenta of the visible muons to the $E_{\mathrm{T}}^{\mathrm{miss}}$ calculation. The summary of the selection criteria used for the definition of the CRs to the multijet background is shown in Tab. 7.4. The normalisation of the top, W+jets and $Z \to \nu\nu$ backgrounds is extracted simultaneously in the three control regions by a likelihood fit[5]. The scale factors were found to be:

---

[5]A more detailed description on how this method works for the extraction of scale factors in two control regions is given in Sec. 7.1.4 to the number of observed events. The method can be easily extended to $n \geq 2$ regions.

Seed Region	multijet CR		Top CR	W+jets CR	$Z \to \nu\nu$ CR
single jet triggers			single μ triggers		
$N_\mu < 1$			$N_\mu \geq 1$	$N_\mu = 1$	$N_\mu = 2$
$N_{jets} \geq 2$, $N_{\text{noBDT-}\tau_{\text{had}}} \geq 2$, $N_{electrons} < 1$					
$N_{b-jet} \geq 1$				$N_{b-jet} = 0$	
$E_{\text{T,sig}}^{\text{miss}} < 4$	$\Delta\phi(\text{jet}_2, E_{\text{T}}^{\text{miss}}) < 0.5$ $E_{\text{T}}^{\text{miss}}/m_{eff} < 0.2$ GeV	$E_{\text{T}}^{\text{miss}}/m_{eff} > 0.2$		$E_{\text{T}}^{\text{miss}}/m_{eff} > 0.2$	$p_\mu \equiv p_\nu$

Table 7.4: Criteria defining the seed selection, the multijet, top, W+jets and $Z \to \nu\nu$ control regions that are used for the multijet background estimate.

$$\mu_{t\bar{t}} = 1.06 \pm 0.10 \, (\text{stat} \oplus \text{syst})$$
$$\mu_{W+\text{jets}} = 0.88 \pm 0.08 \, (\text{stat} \oplus \text{syst}) \tag{7.6}$$
$$\mu_{Z \to \nu\nu} = 0.92 \pm 0.08 \, (\text{stat} \oplus \text{syst})$$

where the systematic uncertainty includes the luminosity uncertainty and $t\bar{t}$, W+jets and $Z \to \nu\nu$ cross section uncertainties. Other sources of systematics are neglected because they are expected to have a negligible impact on the multijet normalisation factor. The multijet contamination in these regions has been neglected. As an example of the modelling in the control regions after the scale factor fit, the distributions of the leading and sub-leading τ_{had} are shown in Fig. 7.8. The multijet template normalisation scale factor is extracted constraining the sum of the expected MC processes, scaled by the proper scale factors in Eq. 7.6, and the multijet pseudo data to the observed data in the QCD control region. The scale factor obtained is not informative and has no physics meaning since it strongly depends on the number of seed events, and so on the kinematic cuts such as the $E_{\text{T,sig}}^{\text{miss}}$ cut, and the number of smearing iterations, which is completely arbitrary. The agreement of the MC simulation plus the multijet template to the observed data has been checked in a selection requiring at least two jets, at least one b-jet, at least two noBDT$-\tau_{\text{had}}$ and $E_{\text{T}}^{\text{miss}} > 150$ GeV, which defines the so called *no-BDT preselection*. The distributions of m_{T2} and $m_{\text{T}}^{\text{sum}}$ are shown in Fig. 7.9. Since this selection admits ≥ 2 noBDT$-\tau_{\text{had}}$, these variables have been built with the leading and sub-leading taus only. The agreement has been considered satisfactory to proceed with the extrapolation to the SR_{HH} and the final evaluation of the multijet contamination.

Multijet estimate in the SR_{HH}

The number of estimated multijet events that enter in the SR_{HH} selection is extracted in two steps. First, starting from the *no-BDT preselection*, the other SR_{HH} cuts are imposed: $m_{\text{T2}}(\text{noBDT} - \tau_{\text{had}}, \text{noBDT}-\tau_{\text{had}}) > 50$ GeV, $\left|\Delta\phi(\text{jet}_{1,2}, E_{\text{T}}^{\text{miss}})\right| < 0.5$ and $m_{\text{T}}^{\text{sum}}(\text{noBDT}-\tau_{\text{had}}, \text{noBDT}-\tau_{\text{had}}) > 160$ GeV. This region differs from the *had-had* channel signal region only by the fact that τ_{had} candidates have no identification cut applied and it is expected to be dominated by events where jets are mis-reconstructed as τ leptons.
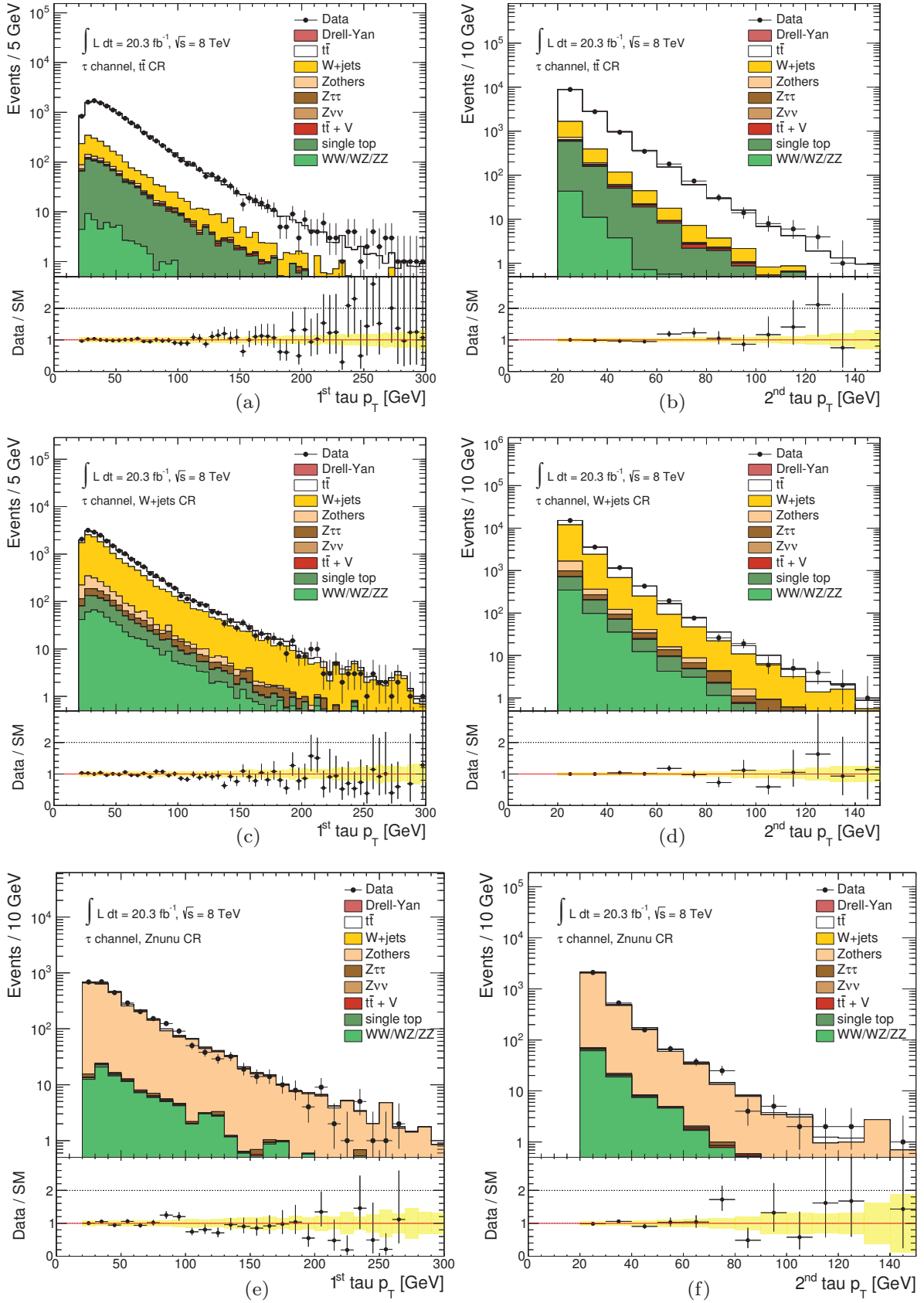
Figure 7.8: Distributions of the leading and subleading noBDT$-\tau_{\mathrm{had}}$ transverse momenta in the $t\bar{t}$ CR ((a),(b)), in the W+jets CR ((c),(d)) and $Z \to \nu\nu$ CR ((e),(f)) for the multijet estimate, respectively. Only the statistical uncertainty is considered.

125

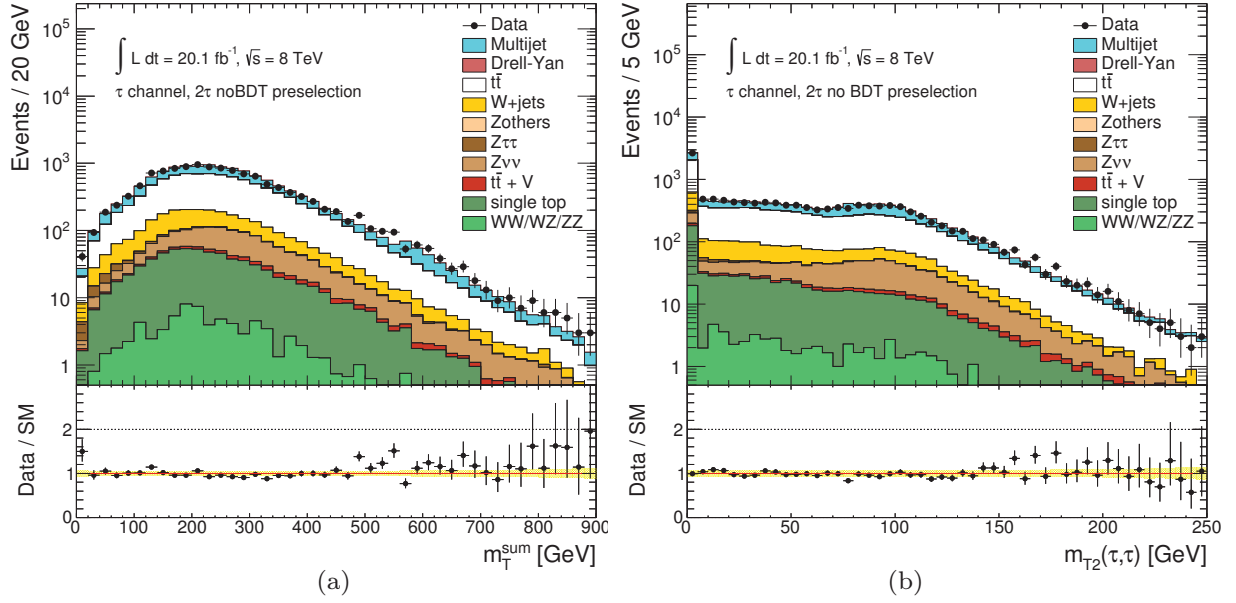Figure 7.9: Distributions of $m_{\mathrm{T}}^{\mathrm{sum}}$ (a) and m_{T2} (b) in the noBDT Preselection region. Only statistical uncertainty is considered.

The number of multijet events entering into this region need to be re-weighted by the probability for each noBDT$-\tau_{\mathrm{had}}$ candidate to pass the τ identification criteria which is given by the *fake rate* defined by Eq. 7.4. Each multijet event selected at this stage gets a different weight depending on the number of noBDT$-\tau_{\mathrm{had}}$ present in the final state. When an event contains exactly two noBDT$-\tau_{\mathrm{had}}$ the event weight is simply $F(p_{\mathrm{T}}^{\tau_1}) \times F(p_{\mathrm{T}}^{\tau_2})$. In the case 3 noBDT$-\tau_{\mathrm{had}}$ are present the weight is computed as:

$$
\begin{aligned}
w_{event} = \quad & F(p_{\mathrm{T}}^{\tau_1}) \times F(p_{\mathrm{T}}^{\tau_2}) \times [1 - F(p_{\mathrm{T}}^{\tau_3})] \times \\
& F(p_{\mathrm{T}}^{\tau_2}) \times F(p_{\mathrm{T}}^{\tau_3}) \times [1 - F(p_{\mathrm{T}}^{\tau_1})] \times \\
& F(p_{\mathrm{T}}^{\tau_3}) \times F(p_{\mathrm{T}}^{\tau_1}) \times [1 - F(p_{\mathrm{T}}^{\tau_2})]
\end{aligned}
\tag{7.7}
$$

and so on for higher noBDT$-\tau_{\mathrm{had}}$ multiplicities. Following this procedure, the number of multijet events that are expected to enter the SR_{HH} is estimated to be $0.0043 \pm 0.0007(\mathrm{stat}) \pm 0.0039(\mathrm{syst})$ and is therefore neglected in the rest of the analysis. As will be discussed in the following section, this result also justifies the fact that the multijet contamination is neglected in the *lep-had* channel control regions due to the extra requirement of a single muon.

7.1.4 Electroweak background estimate

As discussed in Sec. 7.1.2, MC simulation is used to perform the optimisation of the signal region selection and to estimate its composition. However, a data driven technique is used to evaluate the normalisation of the backgrounds processes. This procedure assumes that the events characterised by real taus in the final state are well modelled by MC simulation. This assumption is supported by other SUSY searches performed by the

ATLAS collaboration [240], which find that MC simulation is compatible with data within the estimated uncertainties. On the other hand, the rate of a jet faking a hadronically decaying τ lepton can not be directly taken by MC simulation since the presence of a fake rate mismodelling has been shown in similar SUSY searches with τ_{had} in the final state [240]. Since almost 40% of the background events entering the SR_{HH} fall into the one *real* + one *fake* category, a dedicated background estimate has been performed for this case. Finally, the number of events falling in the two *fake* category has been taken directly from MC simulation. This choice has been driven by two motivations: the first is the lack of statistics when selecting a region enriched in two *fake* taus originating from EWK processes and kinematically close to the SR_{HH} and the second is that this background represents a very small fraction of the expected events which is covered by the total systematic uncertainty.

One *real* + one *fake* τ_{had} background estimate

The procedure followed in this channel aims to calculate a data driven correction to the MC estimate for the rate of reconstructing electrons or jets as hadronically decaying τ leptons. Instead of using a region where two taus are selected, a region with an isolated muon and a τ_{had} has been defined. The assumption behind this approach is that a μ reasonably models the kinematics of a reconstructed *real* τ_{had} with the advantage to be less sensitive to systematics such as τ energy scale and resolution. Even if in principle also an electron sample can be used for the same purpose, the probability that an electron could fake a τ_{had} is not negligible and would lead to extra complications in applying this method. Events passing a single muon trigger are preselected requiring exactly one isolated μ with $p_{\text{T}} \geq 25$ GeV, no loose electrons and exactly one τ_{had} with $p_{\text{T}} \geq 20$ GeV. Additionally, at least two jets with $p_{\text{T}} \geq 20$ GeV, with a leading jet of $p_{\text{T}} \geq 40$ GeV, are requested in order to resemble the requirement applied in the full hadronic preselection. An additional cut on $m_{\text{T}}(\mu, E_{\text{T}}^{\text{miss}}) \geq 40$ GeV is applied to remove possible multijet processes contamination.

The events coming from $t\bar{t}$ and single top are combined in the CRs into a single category called *top background*. This procedure is justified by the fact that the contribution coming from the single top Wt-channel in the SR can be interpreted as $t\bar{t}$ pair production followed by the decay of one of the top quarks into Wb. The top background is then split into two sub-categories through the truth matching procedure: the first category contains events with a muon and either a real τ_{had}, while the second contains a fake τ_{had}. The distribution of the transverse momentum and pseudorapidity of the τ_{had} is shown in Fig. 7.10. A τ_{had} p_{T}-dependent bias has been observed and is due to an over prediction of the fake rate modelling in the W+jets events, while no dependence is seen as a function of τ_{had} pseudorapidity . This effect has already been observed in [240] and a similar procedure to correct for this effect has been followed also in this search in order to avoid over prediction of W+jets events in the Control Regions. The preselection is enriched in W+jets events requiring an additional b-jet veto and the correction is obtained from the ratio of the p_{T}^{τ} between the background-subtracted data and the W+jets, where the subtraction is
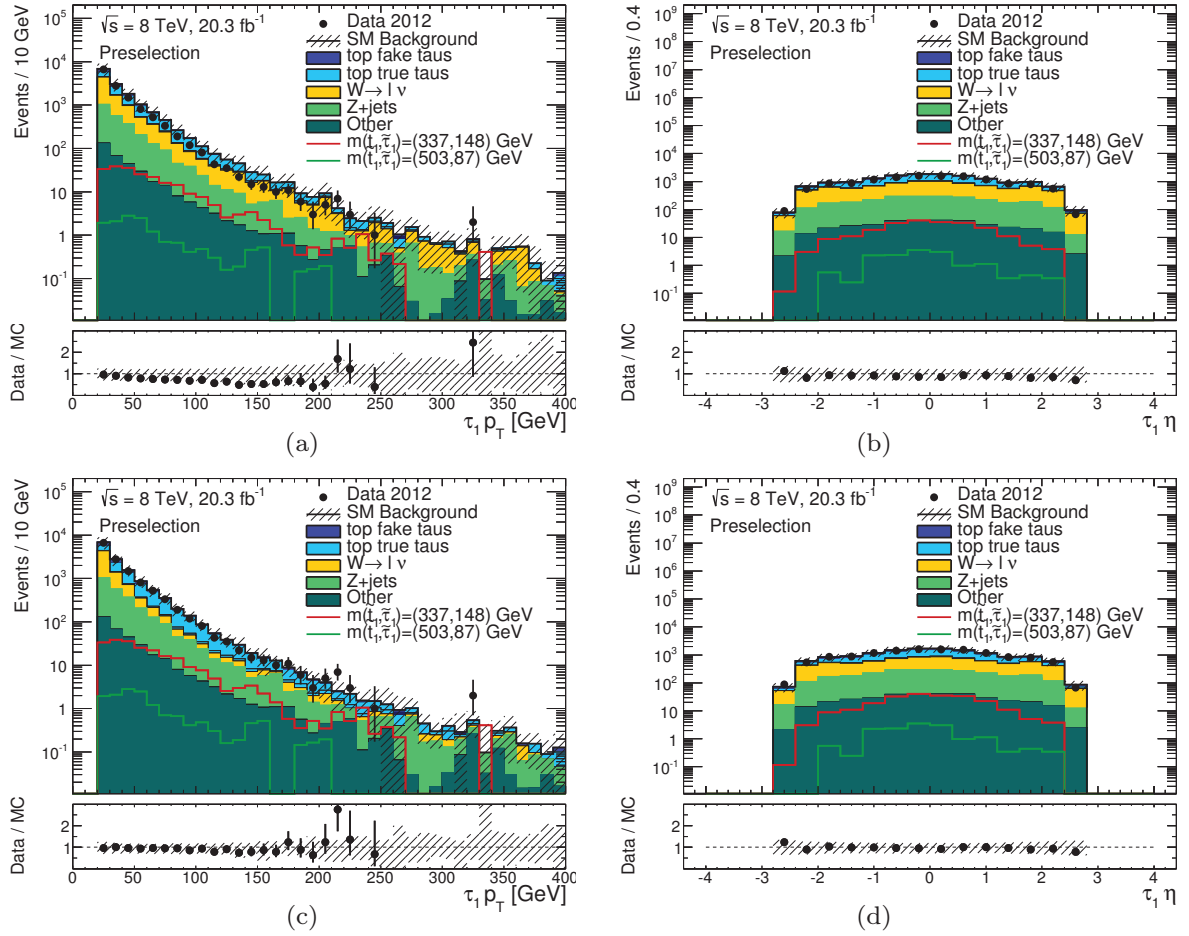
Figure 7.10: Distributions of the transverse momentum (a) and pseudorapidity (b) of the τ_{had} in the $1\mu1\tau$ preselection before the W+jets re-weighting. The same distributions after applying the per events weights are shown in (c) and (d), respectively.

performed on the non-W backgrounds, and an exponential fit is then performed to extract a per-event weight, as shown in Eq. 7.8

$$w(p_{\mathrm{T}}^{\tau}) = \frac{N_{Data}(p_{\mathrm{T}}^{\tau}) - N_{non-W}(p_{\mathrm{T}}^{\tau})}{N_W(p_{\mathrm{T}}^{\tau})}. \tag{7.8}$$

The results of the re-weighting procedure are shown in Fig. 7.10 and show an improved agreement between data and MC simulation in the transverse momentum distribution, without affecting the η distribution.

Control regions for $t\bar{t}$ and W+jets

As already discussed, the major background contribution in the SR is due to $t\bar{t}$ and single
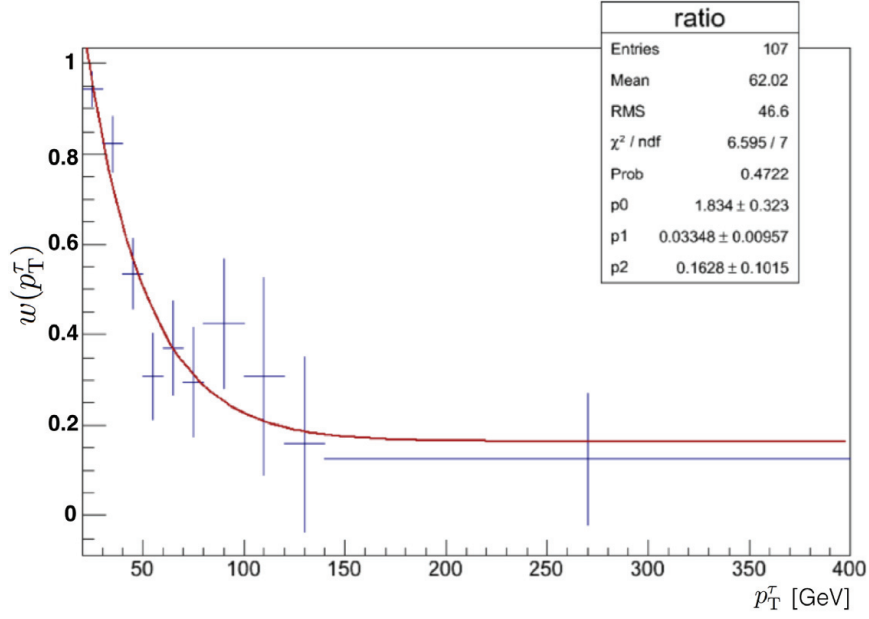
Figure 7.11: Fit on the $N_{data} - N_{nonW}$ over N_W as a function of the τ transverse momentum.

top processes. A region enriched in top production events named $\mathrm{CR}_{t\bar{t}}$ has been defined to be kinematically close and at the same time statistically independent to the SR_{HH}. The orthogonality is ensured by a window cut on $70 \leq m_{\mathrm{T}}^{\mathrm{sum}}(\mu, \tau_{\mathrm{had}}) \leq 120$ GeV that also successfully largely reduces the Z+jets contamination in this region. The $E_{\mathrm{T}}^{\mathrm{miss}}$ cut has been relaxed to 100 GeV in order to have similar kinematics of the SR_{HH} but retain larger statistics to study the background modelling. At least one b-jet is required to enrich the sample in top events and maintain the same flavour topology of the SR_{HH}. After these cuts, the contribution of W+jets events is not negligible relative to the number of top fakes events. Therefore a control region that probes the modelling of the W+jets CR_W was designed requiring a cut on $m_{\mathrm{T2}}(\mu, \tau_{\mathrm{had}}) < 40$ GeV, a window cut on $80 < m_{\mathrm{T}}^{\mathrm{sum}}(\tau_{\mathrm{had}}, \tau_{\mathrm{had}}) < 120$ GeV and a b-jet veto. The summary of the control regions selection criteria is given in Tab. 7.5.

$\mathrm{CR}_{t\bar{t}}$	CR_W
single μ trigger	
N_μ=1, $N_{\tau_{\mathrm{had}}}^{\mathrm{tight}}$=1, $N_{jets} \geq 2$ $E_{\mathrm{T}}^{\mathrm{miss}} > 100$ GeV, $\left\|\Delta\phi(\mathrm{jet}_{1,2}, E_{\mathrm{T}}^{\mathrm{miss}})\right\| > 0.5$	
$N_{b-jet} \geq 1$	$N_{b-jet} = 0$
$70 \leq m_{\mathrm{T}}^{\mathrm{sum}}(\mu, \tau_{\mathrm{had}}) \leq 120$ GeV	$80 \leq m_{\mathrm{T}}^{\mathrm{sum}}(\mu, \tau_{\mathrm{had}}) \leq 120$ GeV $m_{\mathrm{T2}}(\mu, \tau_{\mathrm{had}}) < 40$ GeV

Table 7.5: Criteria defining the $\mathrm{CR}_{t\bar{t}}$ and CR_W that are used for the one *real* + one *fake* background estimate.

Region	CR$_{t\bar{t}}$	CR$_W$
Observed events	98	108
Pre-fit bkg events	113	100
Post-fit bkg events	98 ± 10	108 ± 10
top *real* τ_{had}	57 ± 12	11 ± 4
top *fake* τ_{had}	24 ± 15	9 ± 6
W+jets	10 ± 3	65 ± 13
Z+jets	5.0 ± 0.8	15 ± 4
Other bkgs	1.8 ± 0.3	8 ± 1
	$\mu_{t\bar{t}} = 0.58 \pm 0.41$	$\mu_W = 1.27 \pm 0.27$

Table 7.6: Event yields in the CR$_{t\bar{t}}$ and CR$_W$ for observed data, before and after the normalisation fit. The post-fit results for various SM processes are reported. The *other bkgs* category includes $t\bar{t} + V$, dibosons and Drell-Yan processes. As discussed in the text, $\mu_{t\bar{t}}$ only applies to the top fakes background. The uncertainties quoted include both statistical and systematics and correlation effects between different sources of systematics are taken into account for the uncertainty on the post-fit total number of background events.

The normalisation of the top *fakes* background and W+jets is extracted by constraining the SM expectation to the observed data in the CRs. This approach reduces to solve a system of two equations:

$$\begin{cases} N_D^{\mathrm{CR}_{t\bar{t}}} = \mu_{top} N_{top}^{\mathrm{CR}_{t\bar{t}}} + \mu_W N_W^{\mathrm{CR}_{t\bar{t}}} + N_{other}^{\mathrm{CR}_{t\bar{t}}} \\[2ex] N_D^{\mathrm{CR}_W} = \mu_{top} N_{top}^{\mathrm{CR}_W} + \mu_W N_W^{\mathrm{CR}_W} + N_{other}^{\mathrm{CR}_W} \end{cases} \qquad (7.9)$$

where N_D^{CR}, N_{top}, N_W and N_{other} are the number of observed data and the number of expected events of top, W and other sources of backgrounds for the control region CR, respectively. This system of equations can be solved for the normalisation scale factors for the top *fakes* (μ_{top}) and W+jets (μ_W):

$$\begin{cases} \mu_W = \dfrac{(N_D^{\mathrm{CR}_{t\bar{t}}} - N_{other}^{\mathrm{CR}_W}) \cdot N_{t\bar{t}}^{\mathrm{CR}_{t\bar{t}}} - (N_D^{\mathrm{CR}_{t\bar{t}}} - N_{other}^{\mathrm{CR}_{t\bar{t}}}) \cdot N_{t\bar{t}}^{\mathrm{CR}_W}}{N_W^{\mathrm{CR}_W} \cdot N_{t\bar{t}}^{\mathrm{CR}_{t\bar{t}}} - N_W^{\mathrm{CR}_{t\bar{t}}} \cdot N_{t\bar{t}}^{\mathrm{CR}_W}} \\[3ex] \mu_{t\bar{t}} = \dfrac{(N_D^{\mathrm{CR}_{t\bar{t}}} - N_{other}^{\mathrm{CR}_{t\bar{t}}}) \cdot N_W^{\mathrm{CR}_W} - (N_D^{\mathrm{CR}_W} - N_{other}^{\mathrm{CR}_W}) \cdot N_W^{\mathrm{CR}_{t\bar{t}}}}{N_W^{\mathrm{CR}_W} \cdot N_{t\bar{t}}^{\mathrm{CR}_{t\bar{t}}} - N_W^{\mathrm{CR}_{t\bar{t}}} \cdot N_{t\bar{t}}^{\mathrm{CR}_W}} \end{cases} \qquad (7.10)$$

Even if the above system can be easily solved algebraically, in practice the solution is obtained using a Likelihood fit to the data on both the control regions following a standard procedure used in SUSY searches in ATLAS. The likelihood function is built as a product of poisson distributions where the observed data equals N_D^{CR} and gaussian distributions for the inclusion of the systematic uncertainty sources as described in Sec. 6.5. The advantage

of this approach is the rigorous evaluation of the scale factors taking into account the correlations across the various CRs due to common sources of systematics uncertainties and the cross-contribution of the various SM processes in each CR. The free parameters of the fit are the normalisation scale factor of the constrained backgrounds: top *fakes* and W+jets. The contribution from all other backgrounds is kept fixed to their MC expectation, but are allowed to vary within their uncertainty. The multijet contribution is neglected in the fit. The Likelihood is maximised varying the free parameters, while the systematic uncertainties are left unchanged. The event yields before and after the normalisation fit in the top and W+jets control regions are shown in Tab. 7.6, together with the scale factors. A description of the systematic uncertainties included in the fit is given in Sec. 8.3.

The distributions of the $m_{\mathrm{T}}^{\mathrm{sum}}(\mu, \tau_{\mathrm{had}})$ and $m_{\mathrm{T2}}(\mu, \tau_{\mathrm{had}})$ after applying the calculated scale factors are shown in Fig. 7.12 and in Fig. 7.13 for the $\mathrm{CR}_{t\bar{t}}$ and the CR_W, respectively.

7.1.5 Validation of the procedure

As described in the previous section, the normalisation of the one *real* + one *fake* τ_{had} background is estimated by a likelihood fit to the data in two control regions. The use of the normalisation scale factors in the signal region relies on trusting the MC modelling of the various kinematic quantities and their extrapolation to the signal region. In order to validate this assumption a *Validation Region* is defined for each control region which is kinematically closer to the SR_{HH} and located between, and statistically orthogonal to, the CRs and the SR. The validation regions selection criteria are summarised in Tab. 7.7. The additional cut on the $m_{\mathrm{T2}}(\mu, \tau_{\mathrm{had}}) < 40$ GeV in the $\mathrm{VR}_{t\bar{t}}$ is added to keep the signal contamination as low as possible. For the same reason the cut on the $m_{\mathrm{T}}^{\mathrm{sum}}(\mu, \tau_{\mathrm{had}})$ in the $\mathrm{VR}_{t\bar{t}}$ is kept lower than the one in the VR_W. The cut on the missing transverse momentum has been raised to $E_{\mathrm{T}}^{\mathrm{miss}} > 120$ GeV to better select events with a topology more similar to the one of the SR_{HH}. The total event yields in the VRs before and after the normalisation fit are shown in Tab. 7.8, together with various expected SM process contributions. A summary of the total event yields comparison between data and MC simulation is shown also in Fig. 7.14. The results of the comparison between data and expected MC simulation in both the VRs is considered satisfactory to proceed with the extrapolation of the normalisation scale factors to the SR_{HH}.

$\mathrm{VR}_{t\bar{t}}$	VR_W
single μ trigger	
$N_\mu = 1$, $N_{\tau_{\mathrm{had}}}^{tight} = 1$, $N_{jets} \geq 2$ $E_{\mathrm{T}}^{\mathrm{miss}} > 120$ GeV, $\left\|\Delta\phi(\mathrm{jet}_{1,2}, E_{\mathrm{T}}^{\mathrm{miss}})\right\| > 0.5$	
$N_{b-jet} \geq 1$	$N_{b-jet} = 0$
$120 \leq m_{\mathrm{T}}^{\mathrm{sum}}(\mu, \tau_{\mathrm{had}}) \leq 140$ GeV $m_{\mathrm{T2}}(\mu, \tau_{\mathrm{had}}) < 40$ GeV	$120 \leq m_{\mathrm{T}}^{\mathrm{sum}}(\mu, \tau_{\mathrm{had}}) \leq 150$ GeV $m_{\mathrm{T2}}(\mu, \tau_{\mathrm{had}}) < 40$ GeV

Table 7.7: Criteria defining the $\mathrm{VR}_{t\bar{t}}$ and VR_W that are used for the one *real* one + *fake* background estimate validation.
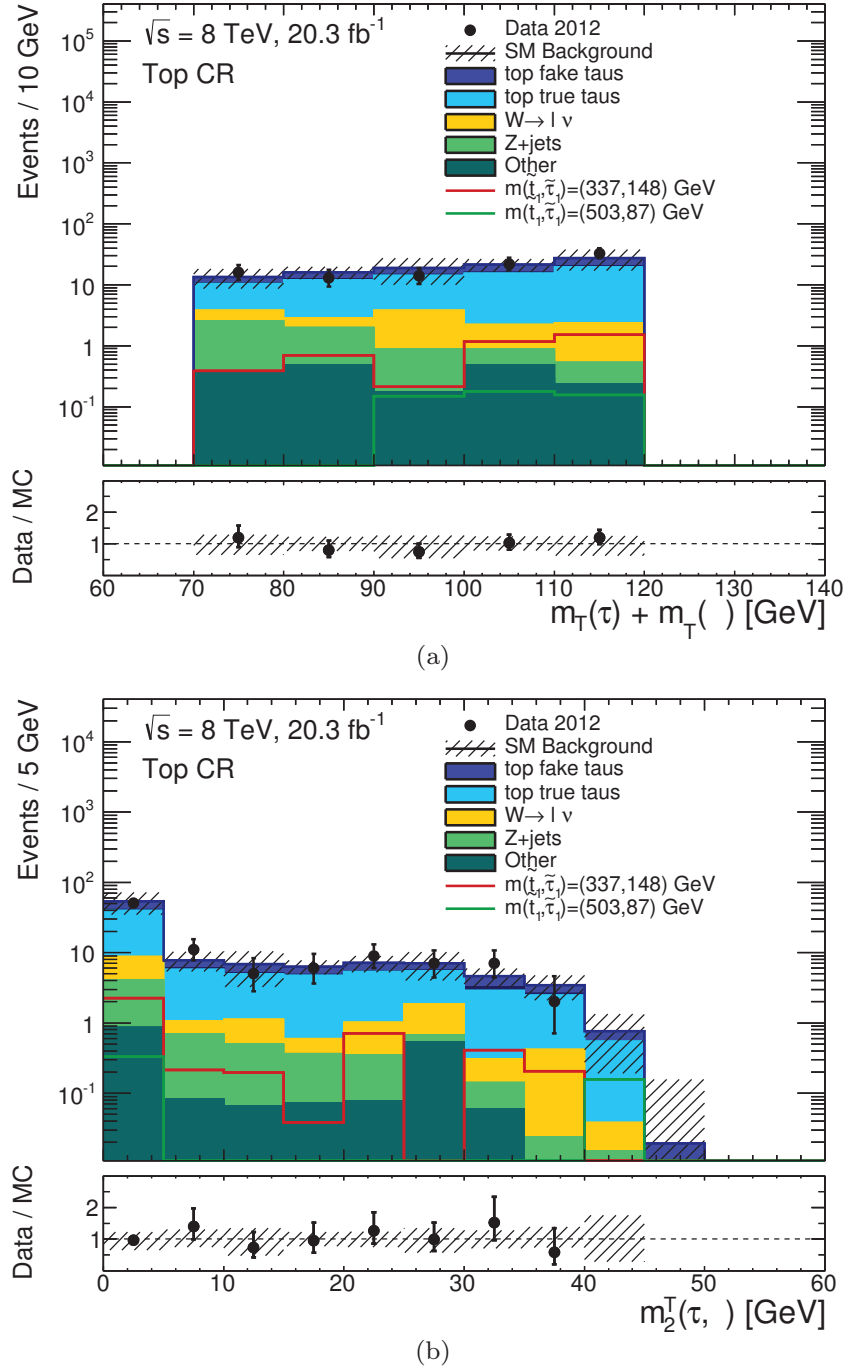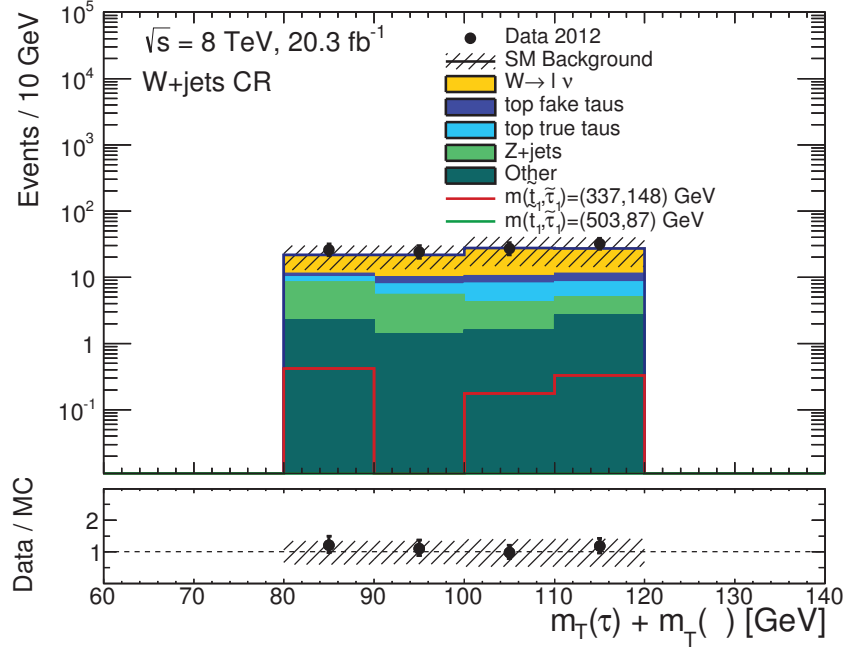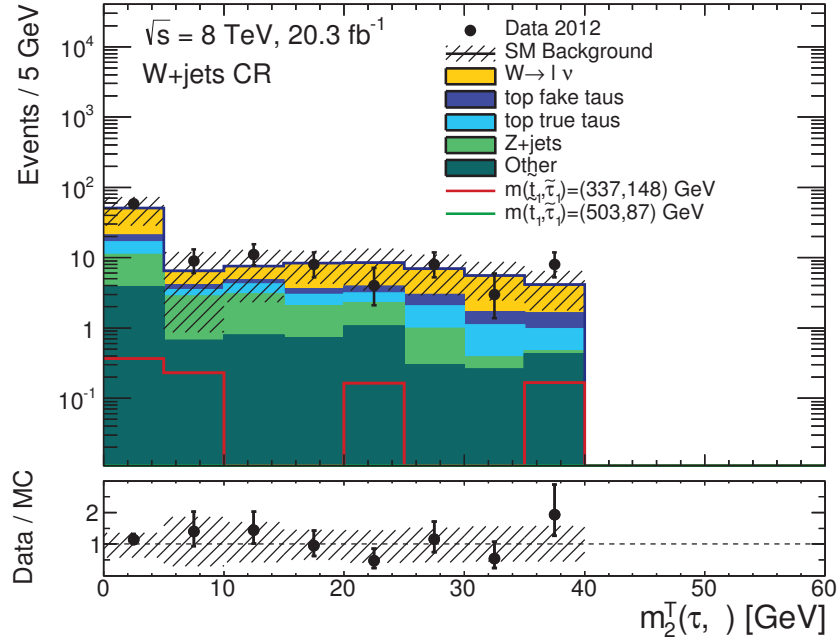
Figure 7.12: Distributions of $m_{\mathrm{T}}^{\mathrm{sum}}(\mu, \tau_{\mathrm{had}})$ (a) and $m_{\mathrm{T2}}(\mu, \tau_{\mathrm{had}})$ (b) in the region enriched in top background events. The top fakes and the W+jets processes are scaled by the factors obtained from the simultaneous likelihood fit.

(a)

(b)

Figure 7.13: Distributions of $m_{\mathrm{T}}^{\mathrm{sum}}(\mu, \tau_{\mathrm{had}})$ (a) and $m_{\mathrm{T2}}(\mu, \tau_{\mathrm{had}})$ (b) in the region enriched in W+jets background events. The top fakes and the W+jets processes are scaled by the factors obtained from the simultaneous likelihood fit.

	$\text{VR}_{t\bar{t}}$	VR_W
Observed events	31	50
Pre-fit bkg events	33	45
Post-fit bkg events	29 ± 4	49 ± 7
top *real* τ_{had}	20 ± 4	7 ± 2
top *fake* τ_{had}	6 ± 4	4 ± 3
$W+$jets	1.7 ± 0.4	32 ± 7
$Z+$jets	0.16 ± 0.06	1.3 ± 0.5
Other bkgs	0.5 ± 0.1	4.2 ± 0.3

Table 7.8: Event yields in the Top VR and $W+$jets VR for observed data, before and after the normalisation fit. The post-fit results for various SM processes are reported. The *other bkgs* category includes $t\bar{t} + V$, dibosons and Drell-Yan processes. The uncertainties quoted include both statistical and systematics effects and correlations between different sources of systematics are taken into account for the uncertainty on the post-fit total number of background events.
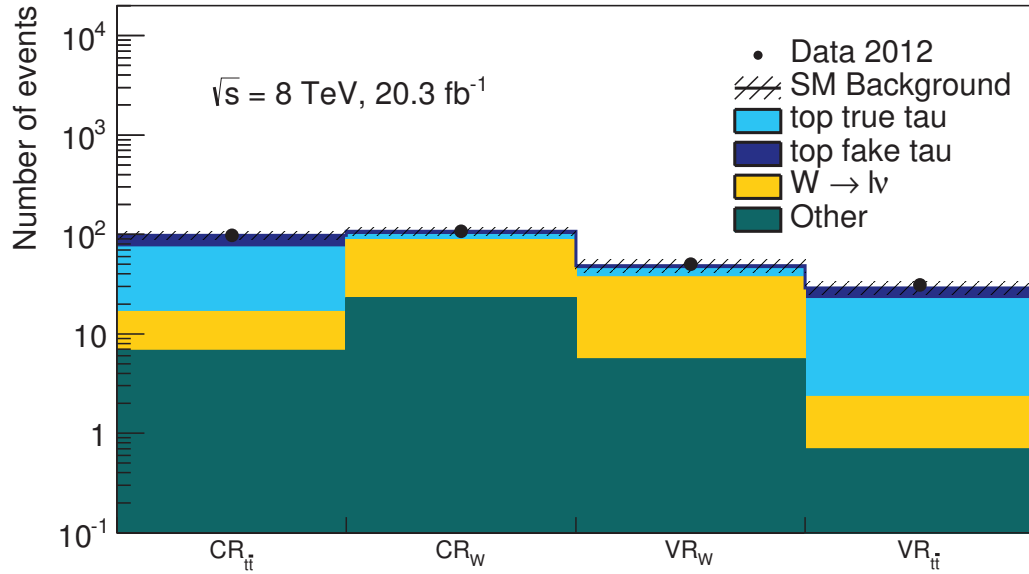
Figure 7.14: Background yields and composition after the fit for the two CRs and the two VRs in the *had-had* channel. Combined statistical and systematic uncertainties after the Likelihood fit are shown in shaded bands. The observed number of events and the background estimate in the CRs are the same by construction.
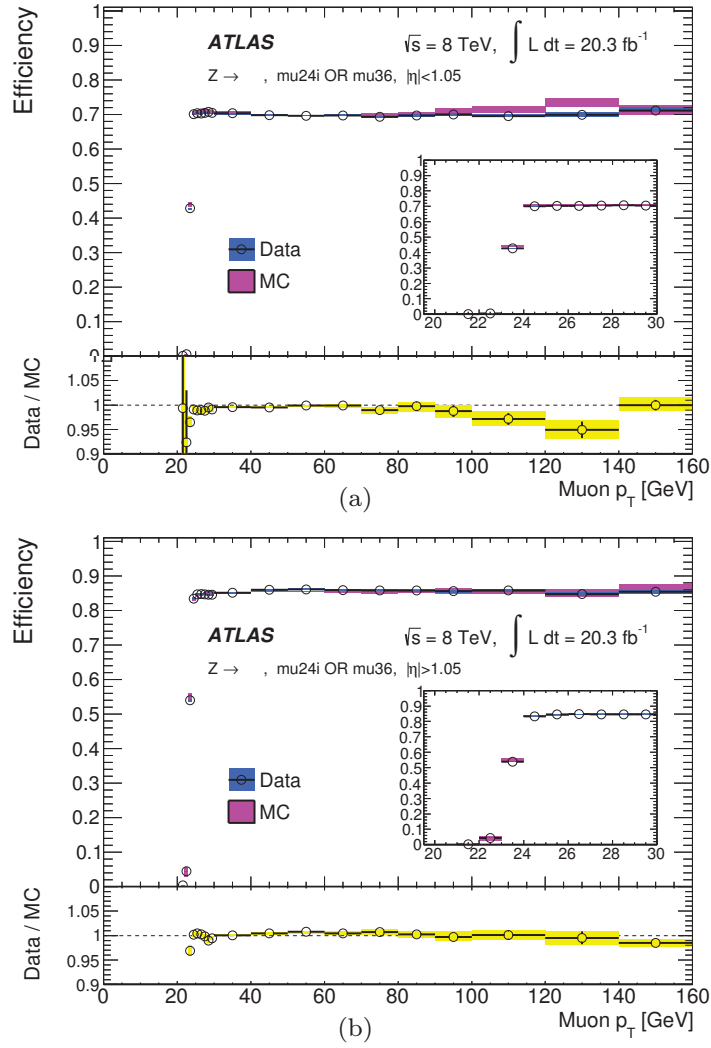
Figure 7.15: Efficiency of passing the logical `OR` between the two single muon triggers used in the *lep-had* channel for both the barrel (a) and the endcap (b) regions, for both both data (dots) and MC simulation (bands). The error bars include both statistical and systematic uncertainties. Figure taken from [241].

7.2 Lepton-Hadron Channel

As mentioned before, the *lep-had* channel targets final states where one τ-lepton decayed leptonically into an electron or muon, while the other decayed hadronically. The following sections give an overview of the procedures followed during the search for the event selection, signal regions optimisation and background estimate and validation.

7.2.1 Trigger selection

The *lep-had* channel analysis uses single lepton triggers to select data events. For the electron channel, a single isolated electron trigger is used in logical `OR` combination with

a single non-isolated electron trigger, with transverse energy threshold of $E_T > 24$ GeV and $E_T > 60$ GeV at event filter level, respectively. Similarly, the muon channel exploits a logical `OR` between a single isolated muon trigger with $p_\mathrm{T} > 24$ GeV and a single non-isolated muon trigger with $p_\mathrm{T} > 36$ GeV is required. The turn-on curve of the logical `OR` between the two single μ triggers used by the *lep-had* channel is shown in Fig. 7.15.The differences in trigger efficiency between data and MC are accounted for using a per-event weight.These multiplicative trigger scale factors differ from unity only at the $\sim 1\%$ level and are applied only to the events where the offline lepton is matched within a $\Delta R < 0.2$ with the online lepton that fired the trigger.

7.2.2 Discriminating variables and Signal Regions

The events that pass the trigger requirements described above are filtered by a set of *Preselection* criteria asking for exactly one electron or exactly one muon with $p_\mathrm{T} > 25$ GeV to ensure the trigger plateau. In Tab. 7.9 the preselection cuts are summarised. Starting from the Preselection, two independent optimisation procedures are performed in order to target different signal models. Two signal regions are defined for the *low-mass* scalar tops (SR_{LM}) and for the *high-mass* scalar tops (SR_{HM}) and their optimisation is performed using the $(m_{\tilde{t}}, m_{\tilde{\tau}}) = (195, 87)$ GeV and $(m_{\tilde{t}}, m_{\tilde{\tau}}) = (391, 148)$ GeV signal models, respectively. In the case of the *low-mass* search, the preselection is modified requiring at least two b-jets in the final state.

Similar to the *had-had* channel, the discrimination between signal and background relies on the use of the *stransverse mass* variable, introduced in Sec. 7.1.2. Three m_T2 variables are used in the selections, with different choices of the two visible momenta used in Eq. 7.3:

- $m_\mathrm{T2}(\ell, \tau_\mathrm{had})$ which is similar to $m_\mathrm{T2}(\tau_\mathrm{had}, \tau_\mathrm{had})$ where a light lepton is used instead of a τ_had.

- $m_\mathrm{T2}(b\ell, b\tau_\mathrm{had})$ uses as visible momenta the light lepton, the τ_had and the two jets with the highest `MV1` weight, while the invisible momentum is built assuming massless particles. There is a two-fold ambiguity in the pairing of the jets with the leptons which is resolved considering the invariant masses $m(b\ell)$ and $m(b\tau_\mathrm{had})$. Only the pairings for which the invariant masses are below m_t are considered[6]. If only one pairing satisfies the condition, that pairing is chosen. If both pairings satisfy the condition, the stransverse mass is calculated for both cases and the smaller value is taken. In the case none of the pairings satisfies the condition, the event is accepted in the case of the SR_{HM}, while it is rejected in the case of SR_{LM}. This variable is bound from above for $t\bar{t}$ events.

- $m_\mathrm{T2}(b\ell, b)$ uses the light lepton and the two bjets as visible momenta, a massless invisible particles hypothesis and tries to target $t\bar{t}$ events where the W boson decay in τ_had has not been identified. Again, a two-fold ambiguity is present, and it's solved

---

[6]In the case of $t\bar{t}$ processes, when the lepton and the jet come from the same top quark, their invariant mass has an upper limit at $\sqrt{m_t^2 - m_W^2} \approx 152$ GeV. Due to detector resolution, this requirement is loosened to be lower than the mass of the top quark.

using the same algorithm described for $m_{\text{T2}}(b\ell, b\tau_{\text{had}})$, with the difference that if no pairing satisfies the condition, the event is rejected.

The distributions for $m_{\text{T2}}(\ell, \tau_{\text{had}})$ and $m_{\text{T2}}(b\ell, b\tau_{\text{had}})$ are shown in Fig. 7.16 after applying the preselection criteria.

Two additional variables are used in this channel in order to provide further discrimination between signal and background:

- The ratio of the scalar sum of the transverse momenta of the two leading jets (H_{T}) to the effective mass m_{eff}, defined in this case as $m_{\text{eff}} = E_{\text{T}}^{\text{miss}} + H_{\text{T}} + p_{\text{T}}^{\ell} + p_{\text{T}}^{\tau_{\text{had}}}$.

- The ratio of the scalar sum of the transverse momenta of the light lepton and the τ_{had} to the effective mass m_{eff} is used as discriminating variable in the *low mass* selection in order to reject $t\bar{t}$ events.

The summary of the signal regions definitions after the optimisation procedure is shown in Tab. 7.9.

Variable	Preselection	
Number of leptons ($p_T > 10$ GeV)	$=1$	
Leading lepton momentum	≥ 25 GeV	
Number of τ ($p_T > 20$ GeV)	$=1$	
Number of jets ($p_T > 20$ GeV)	≥ 2	
Number of jets ($p_T > 50$ GeV)	≥ 1	
Sign of the lepton and τ_{had} charge	Opposite Sign (OS)	
	SR_{LM}	SR_{HM}
$N_{b-\text{jets}}$	≥ 2	≥ 1
$m_{\text{T2}}(\ell, \tau_{\text{had}})$	$-$	> 120 GeV
$m_{\text{T2}}(b\ell, b\tau_{\text{had}})$	< 60 GeV	> 180 GeV
$m_{\text{T2}}(b\ell, b)$	< 100 GeV	$-$
$E_{\text{T}}^{\text{miss}}$	$-$	> 150 GeV
$H_{\text{T}}/m_{\text{eff}}$	< 0.5	< 0.5
$(p_{\text{T}}^{\ell} + p_{\text{T}}^{\tau_{\text{had}}})/m_{\text{eff}}$	> 0.2	$-$
m_{eff}	$-$	> 400 GeV

Table 7.9: Criteria defining the *lep-had* Preselection, the *low-mass* Signal Region SR_{LM} and the *high-mass* Signal Region SR_{HM}. A dash indicates that the cut is not applied.

7.2.3 Background estimate and validation

The *lep-had* channel background can be divided in two components indicated by *real*, when both the light lepton and the τ_{had} are matched to a true electron or muon and τ in simulation, and *fakes* when either the light lepton or the τ_{had} are not matched to the correspondent truth object. The contributions of top pair events and single top events in both *real* and *fake* categories have been merged together forming the *top background*. The
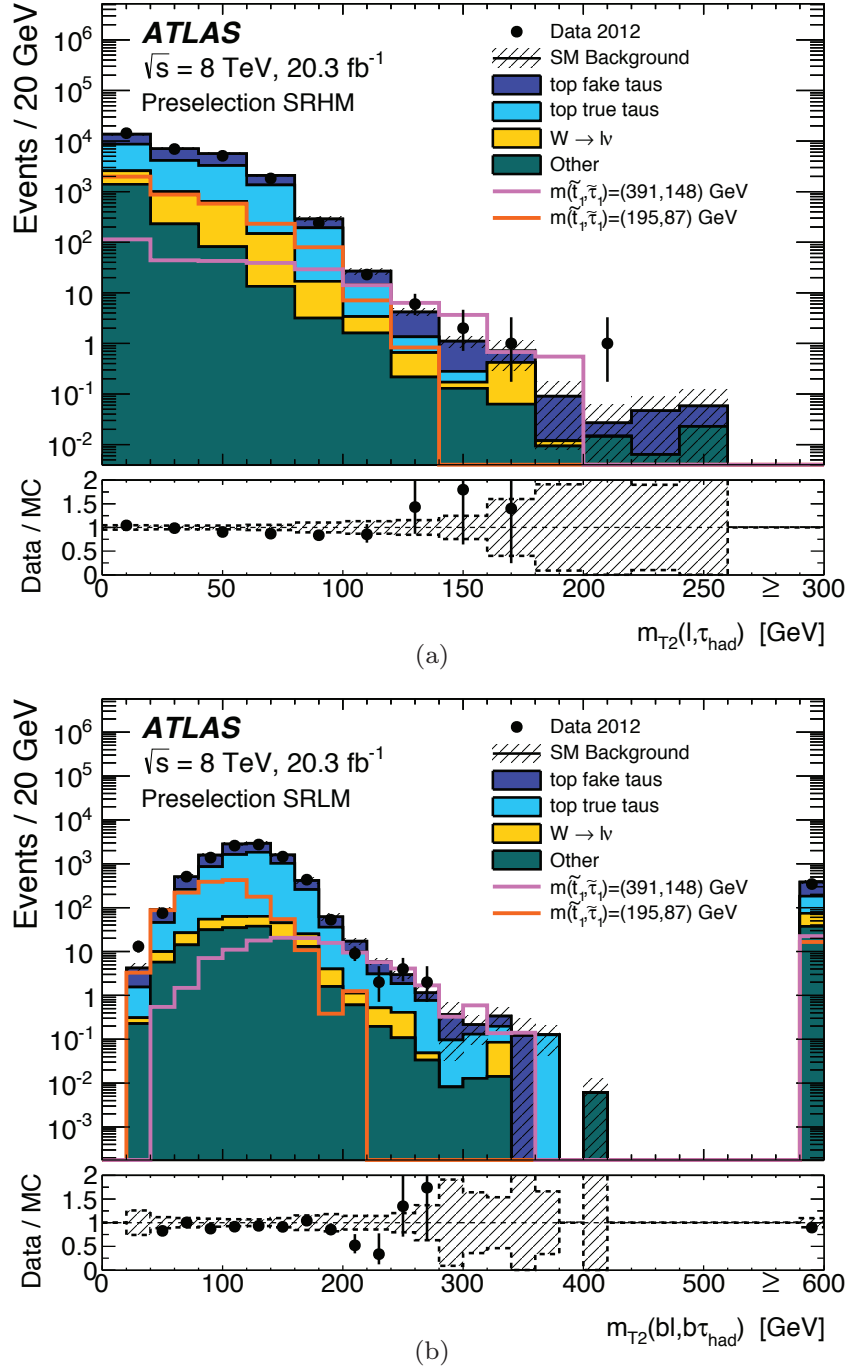
Figure 7.16: Distribution of the $m_{\mathrm{T2}}(\ell, \tau_{\mathrm{had}})$ (a) for the events passing the *lep-had* preselection criteria and of the $m_{\mathrm{T2}}(b\ell, b\tau_{\mathrm{had}})$ (b) for the events passing the *lep-had* preselection criteria with the additional requirement of a second b-tagged jet. The error band includes both statistical and systematic uncertainties. The overflow bin in the $m_{\mathrm{T2}}(b\ell, b\tau_{\mathrm{had}})$ is populated by the events that do not satisfy the $m(bl), m(b\tau_{\mathrm{had}}) < m_t$ pairing, as described in the text. Figures taken from [1].

MC expected SM events	SR_{HM}	SR_{LM}
Total	2.18	25.8
Top *real*	0.18	11.49
Top *fakes*	1.06	10.06
W+jets	0.65	2.45
Z+jets	−	1.87
Dibosons	0.01	−
$t\bar{t} + V$	0.27	0.03

Table 7.10: Relative contribution of the various SM background processes to the *lep-had* signal regions. A dash indicates a negligible background contribution. The uncertainties on the pre-fit MC estimate are not reported.

real component is modelled using MC simulation, but the contribution due to top processes is normalised to the data observed in a dedicated Control Region. The *fakes* component is estimated with a method very similar to the one described for the *had-had* channel and uses MC simulation to model the *fakes* distribution and a normalisation fit constrained to a control region. The relative contribution of the various SM processes is shown in Tab. 7.10 for both the *lep-had* selections, where it is possible to notice that the background events in the *high-mass* region are mostly due to *fakes* while in the *low-mass* region the background is equally distributed among *real* and *fakes* contributions. A summary of the selection cuts defining the two signal regions is given in Tab. 7.11.

Lepton-hadron channel background estimate

Similarly to the *had-had* channel, a shape discrepancy in the τ_{had} p_{T} spectrum in W+jets events is observed in both the electron and muon channel and therefore corrected with the same technique described in Sec. 7.1.4. The weights defined by Eq. 7.8 have been extracted for both the electron and the muon channel separately and for the two channels together. The weights from the former method are applied to correct for the shape disagreement, while the latter method has been used as systematic uncertainty. Similar to the *had-had* case, the weights have been extracted in a region where all the Preselection cuts are applied but a b-jet veto is used instead, in order to enrich the sample in W+jets sample, and an additional requirement of $m_{\mathrm{T}}(\ell, E_{\mathrm{T}}^{\mathrm{miss}}) > 40$ GeV is applied in order to reject potential multijet contribution and to remove Z+jets contamination. Additional studies on the τ_{had} p_{T} spectrum in a $t\bar{t}$ enriched region did not show any shape mis-modelling, therefore no weights have been derived for the top sample.

For each signal region, three control regions are defined targeting the contributions arising from W+jet, top background with *real* leptons and top background with *fakes*. For the top control regions, a cut on the $m_{\mathrm{T}}(\ell, E_{\mathrm{T}}^{\mathrm{miss}})$ has been used to separate the contributions from the *real* and *fake* leptons in the final state. The normalisation scale factors are extracted through a simultaneous likelihood fit on the three control regions, separately for the *high-* and *low-mass*. The results of the fit are checked in two validation

Region	$N_{b-\mathrm{jet}}$	$H_\mathrm{T}/m_\mathrm{eff}$	$\frac{p_\mathrm{T}^\ell + p_\mathrm{T}^{\tau_\mathrm{had}}}{m_\mathrm{eff}}$	$m_\mathrm{T2}(b\ell, b)$	$m_\mathrm{T2}(b\ell, b\tau_\mathrm{had})$	$m_\mathrm{T}(\ell, E_\mathrm{T}^\mathrm{miss})$	m_eff
$\mathrm{CR}_{LM}^{T,\mathrm{real}}$	≥ 2	-	> 0.2	< 100 GeV	$110 - 160$ GeV	> 100 GeV	-
$\mathrm{CR}_{LM}^{T,\mathrm{fakes}}$	≥ 2	-	> 0.2	< 100 GeV	$110 - 160$ GeV	< 100 GeV	-
CR_{LM}^{W}	0	< 0.5	> 0.2	-	-	> 40 GeV	< 400 GeV
VR_{LM}	≥ 2	> 0.5	> 0.2	< 100 GeV	$60 - 110$ GeV	-	-

Region	$N_{b-\mathrm{jet}}$	$E_\mathrm{T}^\mathrm{miss}$	m_eff	$H_\mathrm{T}/m_\mathrm{eff}$	$m_\mathrm{T2}(b\ell, b\tau_\mathrm{had})$	$m_\mathrm{T2}(\ell, \tau_\mathrm{had})$	$m_\mathrm{T}(\ell, E_\mathrm{T}^\mathrm{miss})$
$\mathrm{CR}_{HM}^{T,\mathrm{real}}$	≥ 1	> 150 GeV	> 400 GeV	< 0.5	> 180 GeV	20-80 GeV	> 120 GeV
$\mathrm{CR}_{HM}^{T,\mathrm{fakes}}$	≥ 1	> 150 GeV	> 400 GeV	< 0.5	> 180 GeV	20-80 GeV	< 120 GeV
CR_{HM}^{W}	0	> 150 GeV	> 400 GeV	< 0.5	-	20-80 GeV	40-100 GeV
VR_{HM}	≥ 1	< 150 GeV	> 400 GeV	< 0.5	> 180 GeV	> 80 GeV	-

Table 7.11: Selection criteria defining the *high-mass* and *low-mass* control regions for top background with *real* leptons ($\mathrm{CR}_{LM}^{T,\mathrm{real}}$, $\mathrm{CR}_{HM}^{T,\mathrm{real}}$), top background with *fakes* ($\mathrm{CR}_{LM}^{T,\mathrm{fakes}}$, $\mathrm{CR}_{HM}^{T,\mathrm{fakes}}$) and W+jets (CR_{LM}^{W}, CR_{HM}^{W}) and the validation region (VR_{LM}, VR_{HM}), respectively. A dash indicates that the cut is not applied.

regions, one for each mass selection, that are kinematically closer to the corresponding signal region. The selection criteria of the CRs and the VR for the *low-mass* and *high-mass* selections are reported in Tab. 7.11. The event yields after the likelihood fit are reported in Tab. 7.12 and Tab. 7.13, together with the scale factors obtained during the procedure. The tables show a good agreement between the data observed in the Validation Regions with the yields expected from MC simulation after applying the normalisation scale factors, which justifies the extrapolation of the fit results to the signal regions.

7.3 Lepton-Lepton Channel

As mentioned before, the *lep-lep* channel has not been directly studied in the $\tilde{t} \to \tilde{\tau}$ search, but has been covered by applying the selections of a search for direct scalar top production in dileptonic final states [190]. As will be presented in Ch. 8, the interpretation of the dilepton search in this model provides a good coverage of the compressed phase space hence making it unnecessary to design a dedicated search for the $\tilde{t} \to \tilde{\tau}$ model in this channel. The dilepton search focuses on two decay modes, leading to three possible scenarios. The first decay mode is $\tilde{t} \to b + \tilde{\chi}^\pm$ where $\Delta(m_{\tilde{t}}, m_{\tilde{\chi}^\pm}) > m_b$, where the $\tilde{\chi}^\pm$ decays into a $\tilde{\chi}^0$ LSP through a W boson, which can be on-shell or off-shell depending on the $\Delta(m_{\tilde{\chi}^\pm}, m_{\tilde{\chi}^0})$. The second decay mode is $\tilde{t} \to t + \tilde{\chi}^0$, focusing on the on-shell top quark mode. Since $\tilde{t} \to \tilde{\tau}$ was not the main focus of this analysis, only a very brief overview of the *lep-lep* analysis is given in this section.

7.3.1 Discriminating variables and Signal Regions

Three analysis strategies are followed in the dilepton search, all starting from the same preselection requiring exactly two oppositely charged leptons (electrons, muons or one of

high-mass Region	$\mathrm{CR}_{HM}^{T,\mathrm{real}}$	$\mathrm{CR}_{HM}^{T,\mathrm{fakes}}$	CR_{HM}^{W}	VR_{HM}
Observed events	39	45	101	17
Pre-fit bkg events	33	42	132	20
Post-fit bkg events	39 ± 6	45 ± 7	101 ± 10	22 ± 5
top *real* τ_{had}	36 ± 7	16 ± 4	12 ± 3	9 ± 7
top *fake* τ_{had}	1.9 ± 0.8	24 ± 9	25 ± 11	10 ± 6
W+jets	$0.1_{-0.1}^{+0.2}$	4 ± 2	56 ± 15	2 ± 1
Z+jets	-	-	1 ± 1	0.5 ± 0.3
Other bkgs	0.9 ± 0.2	0.8 ± 0.1	6.8 ± 0.6	0.4 ± 0.1
$\mu_{t\bar{t}}^{\mathrm{real}} = 1.20 \pm 0.22$		$\mu_{t\bar{t}}^{\mathrm{fake}} = 1.13 \pm 0.41$		$\mu_{W} = 0.61 \pm 0.17$

Table 7.12: Event yields in the $\mathrm{CR}_{HM}^{T,\mathrm{real}}$, $\mathrm{CR}_{HM}^{T,\mathrm{fakes}}$, CR_{HM}^{W} and VR_{HM} for observed data and MC estimate before and after normalisation fit. The post-fit results for various SM processes are reported, together with the scale factors obtained from the likelihood fit. The *other bkgs* category includes $t\bar{t} + V$, dibosons and Drell-Yan processes. The uncertainties quoted include both statistical and systematic effects and correlations between different sources of systematics are taken into account for the uncertainty on the post-fit total number of background events. A dash indicates a negligible background contribution.
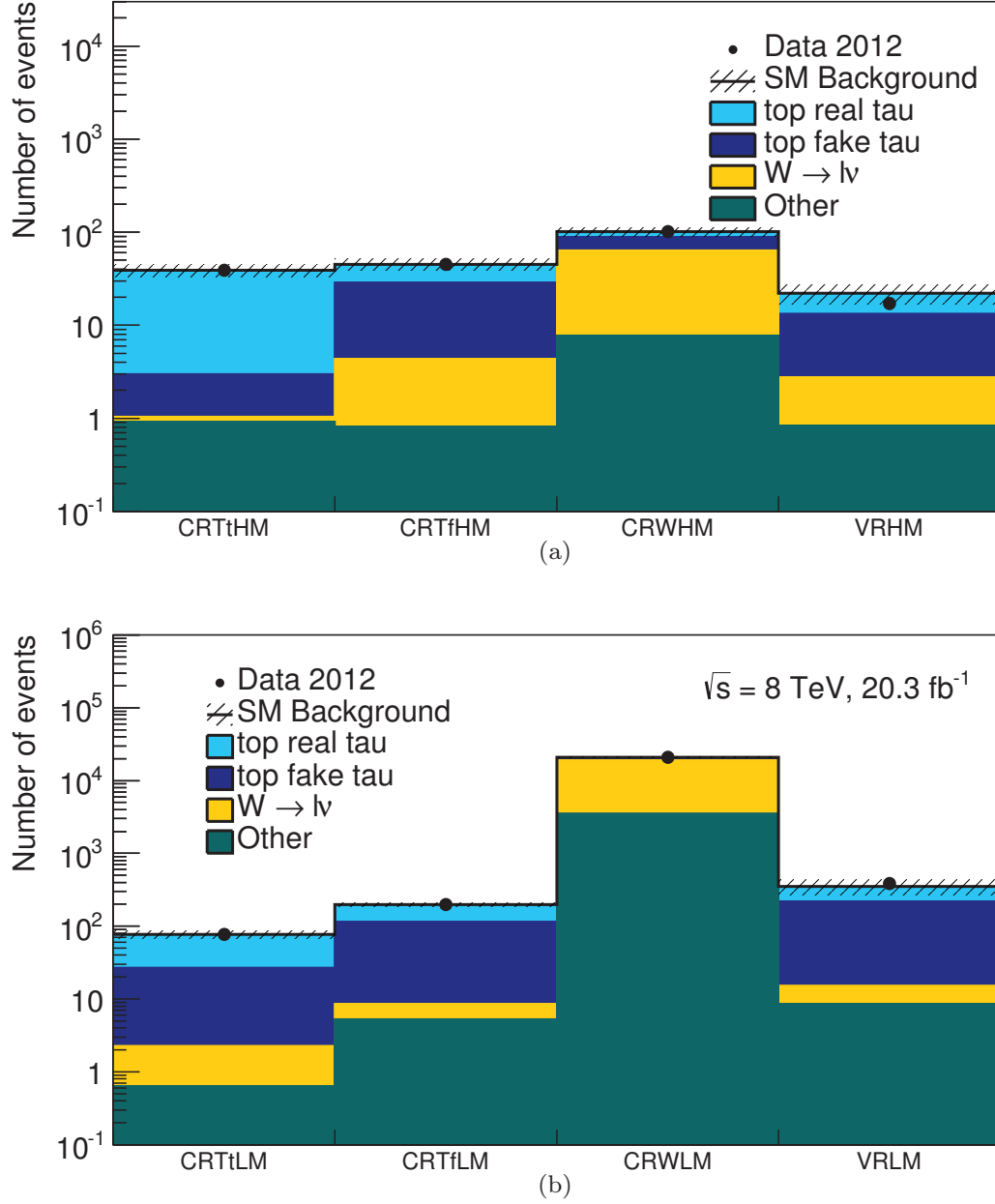
Figure 7.17: Background yields and composition after the fit for the three CRs and the VRs in the *lep-had* channel for the *high-mass* (a) and *low-mass* (b) selection. Combined statistical and systematic uncertainties after the Likelihood fit are shown in shaded bands. The observed number of events and the background estimate in the CRs are the same by construction.

low-mass Region	$\mathrm{CR}_{LM}^{T,\mathrm{real}}$	$\mathrm{CR}_{LM}^{T,\mathrm{fakes}}$	CR_{LM}^{W}	VR_{LM}
Observed events	77	198	20929	386
Pre-fit bkg events	98	235	22282	409
Post-fit bkg events	77 ± 9	198 ± 14	20929 ± 144	351 ± 84
top *real* τ_{had}	50 ± 17	83 ± 29	783 ± 350	129.06 ± 50.04
top *fake* τ_{had}	25 ± 10	106 ± 36	1132 ± 478	206 ± 107
W+jets	1.7 ± 0.5	3 ± 2	15480 ± 641	7 ± 3
Z+jets	0.3 ± 0.2	5 ± 1	3268 ± 259	8 ± 2
Other bkgs	0.4 ± 0.1	0.5 ± 0.2	267 ± 23	0.9 ± 0.3
$\mu_{t\bar{t}}^{\mathrm{real}} = 0.71 \pm 0.24$		$\mu_{t\bar{t}}^{\mathrm{fake}} = 0.98 \pm 0.33$	$\mu_W = 0.94 \pm 0.04$	

Table 7.13: Event yields in the $\mathrm{CR}_{LM}^{T,\mathrm{real}}$, $\mathrm{CR}_{LM}^{T,\mathrm{fakes}}$, CR_{LM}^{W} and VR_{LM} for observed data and MC estimate before and after normalisation fit. The post-fit results for various SM processes are reported, together with the scale factors obtained from the likelihood fit. The *other bkgs* category includes $t\bar{t} + V$, dibosons and Drell-Yan processes. The uncertainties quoted include both statistical and systematic effects and correlations between different sources of systematics are taken into account for the uncertainty on the post-fit total number of background events.

each) with at least one of them having $p_{\mathrm{T}} \geq 25$ GeV and with invariant mass $m_{\ell\ell} > 20$ GeV. The strategies use different main discriminating variables and are introduced below:

- **Leptonic m_{T2} analysis**: this strategy uses $m_{\mathrm{T2}}(\ell, \ell)$ as main discriminating variable. As discussed in Sec. 7.1.2, this variable has a kinematic endpoint at the mass of the W boson for $t\bar{t}$ or WW events. In particular, in the $\tilde{t} \to b + \tilde{\chi}^{\pm}$ the upper bound strongly depends on $\Delta(m_{\tilde{\chi}^{\pm}}, m_{\tilde{\chi}^0})$ value. Four non exclusive Signal Regions are defined in this strategy.

- **Hadronic m_{T2} analysis**: this strategy uses $m_{\mathrm{T2}}^{b-\mathrm{jet}} \equiv m_{\mathrm{T2}}(b, b, \ell + \ell + E_{\mathrm{T}}^{\mathrm{miss}})$, where the leptons are added vectorially to the missing transverse momentum. This variable is bounded from above by m_t for top-quark events, while for stop events it strongly depends on $\Delta(m_{\tilde{t}}, m_{\tilde{\chi}^{\pm}})$. This strategy optimises for one Signal Region.

- **Multivariate analysis (MVA)**: this strategy tries to reconstruct the on-shell top decay in the $\tilde{t} \to t + \tilde{\chi}^0$ decay using a multivariate technique based on a BDT using a gradient-boosting algorithm [242]. The orthogonality with the other two strategies is ensured by a cut on the *stransverse mass*. In total nine Signal Regions are defined, five targeting different-flavour and four targeting same-flavour leptons in the final state.

The three strategies are then combined in order to maximise the coverage of the search for the models considered.

Signal Region	L90	L100	L110	L120
leading lepton p_T [GeV]		> 25		
$\Delta\phi_j$		> 1.0		
$\Delta\phi_b$		< 1.5		
$m_\text{T2}(\ell,\ell)$ [GeV]	>90	> 100	> 110	>120
Leading jet p_T [GeV]	−	> 100	> 20	−
Sub leading jet p_T [GeV]	−	> 50	> 20	−

Table 7.14: Selection criteria used in the leptonic $m_\text{T2}(\ell,\ell)$ analysis. The dash indicates that the particular cut is not applied. The table is taken from [190].

7.3.2 Background estimate and validation

The background determination follows a procedure similar to the one already described for the $\tilde{t} \to \tilde{\tau}$ search, with the addition of a dedicated data-driven method for the evaluation of the number of events due to non-prompt and *fake* leptons. The dominant SM backgrounds are top quark pair production for all the analyses and dibosons and single top Wt for the m_T2 based analyses, respectively. These backgrounds are normalised to data in dedicated CRs and then extrapolated to the SRs using MC simulation after a crosscheck performed in predefined VRs. The Z^*/γ+jets background has been constrained to data in a CR in the hadronic m_T2 analysis although its contamination to the SR selection is subdominant. Minor backgrounds containing prompt leptons from W, Z and H bosons are estimated directly from MC simulation.

The events arising from fake and non-prompt lepton background are due to semileptonic $t\bar{t}$, s- and t-channel single top, W+jets and multijet processes. The contribution from this background, indicated as *reducible*, is estimated by a *matrix-method* technique, similar to the one described in [243, 244]. The detailed description of the method applied to this search can be found in [190]. In the CRs likelihood fit, the non-prompt leptons contribution is set to the estimated yields but its normalisation is allowed to vary within its uncertainty, which is parametrised as a function of the leptons p_T and η and ranges between 10% and 50%.

A good agreement between observed data and post-fit MC simulation event yields is found in each VR for the three analyses, validating in this way the background estimation procedure adopted.

7.3.3 Reinterpretation of the analysis

The leptonic $m_\text{T2}(\ell,\ell)$ analysis is sensitive to the $\tilde{t} \to \tilde{\tau}$ search in the phase space characterised by low mass difference between the scalar top and the scalar tau, with the exception of low scalar top and low scalar tau masses. The selection criteria for the four non-exclusive signal regions that have been used for the reinterpretation are outlined in Tab. 7.14. All the selections are characterised by a lower cut on the $m_\text{T2}(\ell,\ell)$ and two angular variables cuts defined as:

- $\Delta\phi_j$: the azimuthal angular opening between the $\mathbf{E}_T^{\mathrm{miss}}$ and the direction of the closest jet.

- $\Delta\phi_b$: is the azimuthal angular opening between the $\mathbf{E}_T^{\mathrm{miss}}$ and $\mathbf{p}_{\mathrm{Tb}}^{\ell\ell} = \mathbf{E}_T^{\mathrm{miss}} + \mathbf{p}_{\mathrm{T}}^{\ell_1} + \mathbf{p}_{\mathrm{T}}^{\ell_2}$

8 Results and Interpretation

This chapter presents the results of the search for pair production of scalar top quarks with two tau leptons in the final state with particular focus on the *lep-had* and *had-had* channels, described in the previous chapters. The number of observed events in the signal regions are reported and compared to the SM expectation. The sources of systematic uncertainties are discussed and investigated. Since the event yields observed in the signal region are compatible with the SM-only hypothesis, the results are interpreted in terms of exclusion limits on the cross section of the $\tilde{t} \to \tilde{\tau}$ process. The exclusion limits are determined for the *lep-lep* , *lep-had* and *had-had* channels singularly and combined.

8.1 Observed events in the SRs and Discovery test

The observed data in the Signal Regions for the $\tilde{t} \to \tilde{\tau}$ search are presented in Tab. 8.1 along with the background yields before and after the background-only likelihood fit described in Sec. 6.5, for all the three channels investigated in this analysis. In the table, the total uncertainties, containing both the statistical and systematic sources, are reported. The sources of systematics are described in Sec. 8.3. A 3D reconstruction of the topology of one of the three candidate events that enter the SR_{HH} is shown in this section. In the *event display* the reconstructed objects such as tracks, calorimeter clusters and missing transverse momentum are shown. The distributions of $m_{T2}(\tau_{\mathrm{had}}, \tau_{\mathrm{had}})$, $m_{T}^{\mathrm{sum}}(\tau_{\mathrm{had}}, \tau_{\mathrm{had}})$, $m_{T2}(b\ell, b\tau_{\mathrm{had}})$ and $m_{T2}(\ell, \tau_{\mathrm{had}})$ for the events satisfying all the SR criteria except the one on the variable reported in the figure are shown in Fig. 8.1 for the *had-had* , *lep-had low-mass* and *lep-had high-mass* selections, respectively. A hypothesis test is performed on the collected data using a likelihood fit for each SR separately, with the observed data yields, the expected background and its uncertainty as input to the calculation. In each signal region, the data observed is compatible with the SM-only hypothesis. The observed and expected upper limits at 95% Confidence Level (CL) on the number of BSM events S^{95} and on the visible non-SM signal cross section $\sigma_{\mathrm{vis}} = A \times \epsilon \times \sigma_{\mathrm{prod}}$ where A is the detector acceptance, ϵ is the reconstruction efficiency and σ_{prod} is the BSM signal production cross section, are shown in Tab. 8.1. The detector acceptance is defined as the fraction of the number of events passing the geometric and kinematic cuts at truth generator level and it is calculated from MC simulation. The reconstruction efficiency is also calculated with simulated data and is defined as the fraction of events passing the trigger requirement, the object identification criteria and the event reconstruction efficiency for events in the detector acceptance. The values of the product of the detector acceptance times the reconstruction efficiency for a few selected signal hypotheses are shown in Tab. 8.2. The σ_{vis} is then obtained dividing the limit on the number of BSM events by the luminosity of the data sample. The MC expectation total error includes both statistical and systematic uncertainties.

Channel	SRHH	SRLM	SRHM
Observed events	3	20	3
Pre-fit bkg events	3.7	25.8	2.2
Post-fit bkg events	3.1 ± 1.2	22.1 ± 4.7	2.1 ± 1.5
Limit on BSM events $S^{95}_{\mathrm{obs}}(S^{95}_{\mathrm{exp}})$	$5.5\ (5.5^{+2.1}_{-1.3})$	$12.4\ (13.2^{+4.9}_{-3.5})$	$6.4\ (5.2^{+2.6}_{-0.9})$
Limit on $(A\epsilon\sigma)^{95}_{\mathrm{obs}}((A\epsilon\sigma)^{95}_{\mathrm{exp}})$ [fb]	$0.27\ (0.27^{+0.11}_{-0.06})$	$0.61\ (0.65^{+0.24}_{-0.17})$	$0.31\ (0.26^{+0.13}_{-0.04})$
top only *real* τ_{had}	2.0 ± 1.1	8.2 ± 3.9	$0.2^{+0.3}_{-0.2}$
top ≥ 1 *fake* τ_{had}	0.9 ± 0.5	9.8 ± 4.5	$1.2^{+1.4}_{-1.2}$
W+jets	$0.01^{+0.02}_{-0.01}$	2.2 ± 0.6	0.4 ± 0.4
Z/γ^*+jets	$0.04^{+0.15}_{-0.04}$	1.9 ± 1.1	–
$t\bar{t} + V$	0.04 ± 0.02	–	0.3 ± 0.1
Diboson	0.14 ± 0.02	–	–

Table 8.1: Observed number of events and background fit results for the *had-had* and *lep-had* channels of the $\tilde{t} \rightarrow \tilde{\tau}$ search. The total uncertainties include both statistical and systematic sources. Since the systematics can be correlated between different background components, they do not necessarily add up in square sum to the total uncertainty. A dash indicates negligible background contribution. The observed (expected) upper limit on the BSM signal events $S^{95}_{\mathrm{obs}}(S^{95}_{\mathrm{exp}})$ and on the visible cross section $(A\epsilon\sigma)^{95}_{\mathrm{obs}}((A\epsilon\sigma)^{95}_{\mathrm{exp}})$ are also given.

$\tilde{t}$ mass [GeV]	$\tilde{t}$ mass [GeV]	lepton–lepton $A \times \epsilon$	lepton–hadron $A \times \epsilon$ (SRLM)	lepton–hadron $A \times \epsilon$ (SRHM)	hadron–hadron $A \times \epsilon$
153	87	-	1.29×10^{-4}	-	2.27×10^{-4}
195	87	-	1.36×10^{-4}	-	4.46×10^{-4}
195	148	1.71×10^{-4}	7.80×10^{-5}	-	7.00×10^{-4}
195	185	8.01×10^{-4}	-	-	-
391	148	7.32×10^{-4}	-	9.44×10^{-4}	3.40×10^{-3}
503	493	1.03×10^{-2}	-	-	-
561	87	-	-	1.74×10^{-3}	6.70×10^{-3}
561	337	-	-	1.30×10^{-2}	9.90×10^{-3}
561	500	-	-	8.68×10^{-3}	2.50×10^{-3}

Table 8.2: Geometrical acceptance times reconstruction efficiency for the various signal regions, for a few selected $(m_{\tilde{t}}, m_{\tilde{\tau}})$ signal mass hypotheses. For each signal model, values are shown only for the channels targeting that point. The *lep-lep* results are taken from the reinterpretation of Ref. [190].

Run: 209736
Event: 180956915
2012-09-04 05:56:10 CEST
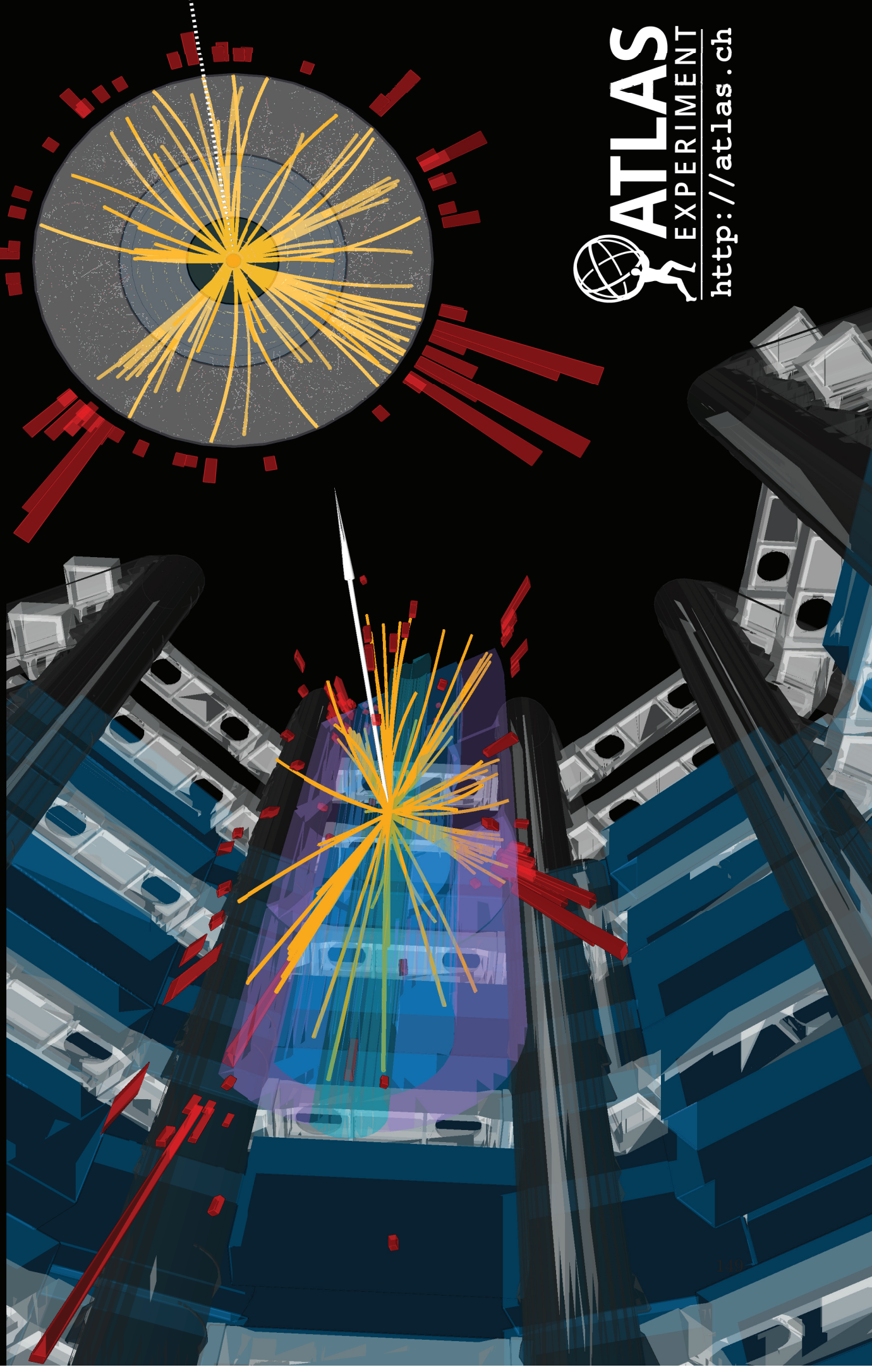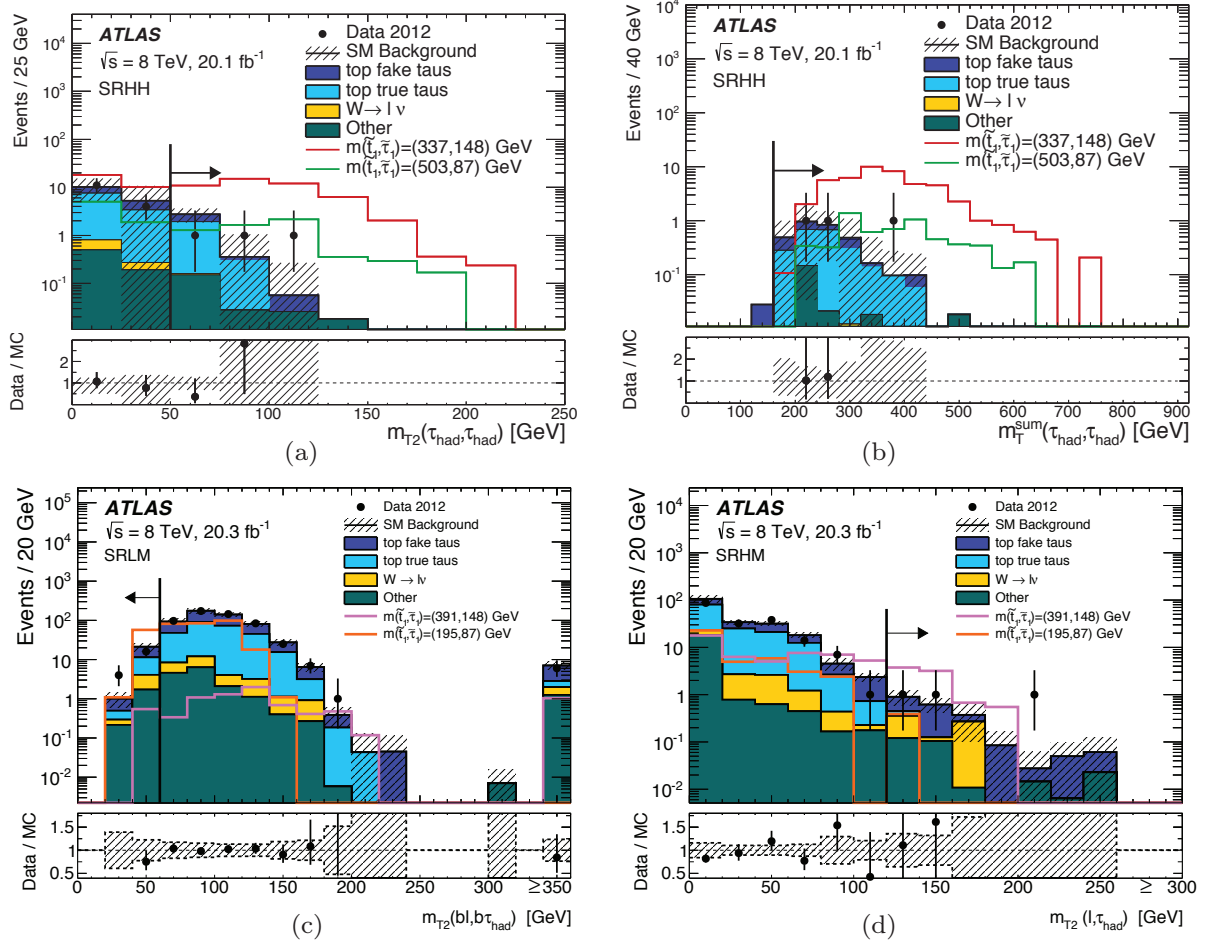
Figure 8.1: Distribution of $m_{\mathrm{T2}}(\tau_{\mathrm{had}}, \tau_{\mathrm{had}})$ (a), $m_{\mathrm{T}}^{\mathrm{sum}}(\tau_{\mathrm{had}}, \tau_{\mathrm{had}})$ (b), $m_{\mathrm{T2}}(b\ell, b\tau_{\mathrm{had}})$ (c) and $m_{\mathrm{T2}}(\ell, \tau_{\mathrm{had}})$ (d) for all events passing the SRs criteria minus the one on the variable shown for the *had-had* (a,b), *lep-had low-mass* (c) and *lep-had high-mass* (d) selections, respectively. The contribution of the SM processes are stacked and the shaded area represents the total uncertainty on the prediction. The background yields have been rescaled by the post-fit normalisation scale factors. The arrows mark the cut values used to define the SR. For each distribution, two signal models are shown. Figures taken from [].

Figure 8.2: The dashed and solid lines show the expected and observed exclusion limits at 95% CL in the $(m_{\tilde{t}}, m_{\tilde{\tau}})$ plane from the *had-had* (a), *lep-had low-mass* selection (b), *lep-had high-mass* selection (c) and the *lep-lep* selections (d), respectively. The LEP limit of $m_{\tilde{\tau}} \geq 87$ GeV is indicated by a green band. The solid red line and the dashed red lines indicate the observed exclusion limit and the $\pm 1\sigma$ variation on the theoretical signal production cross section, respectively. The dashed black line and the yellow band indicate the expected exclusion limit and its $\pm 1\sigma$ variation of the total uncertainty. The areas bounded by the red line, ore the red line and green band, are excluded.

8.2 Exclusion limits on top squark production

Since no excess over the SM expectation has been found, the results of the analysis can be interpreted as cross section exclusion limits on the $\tilde{t} \rightarrow \tilde{\tau}$ simplified model for each mass hypothesis in the $(m_{\tilde{t}}, m_{\tilde{\tau}})$ plane. The exclusion limits are derived using a likelihood fit similar to the one used for the background normalisation method, described in Sec. 6.5 and Sec. 7.1.4, with the addition of an overall signal-strength parameter constrained to assume only positive values. The likelihood fit is performed simultaneously on the CRs and the SRs, taking into account the sources of systematics and their cross-correlations in the different regions through the introduction of nuisance parameters and the amount of signal contamination in the CRs. For each mass hypothesis, the expected limits are calculated for
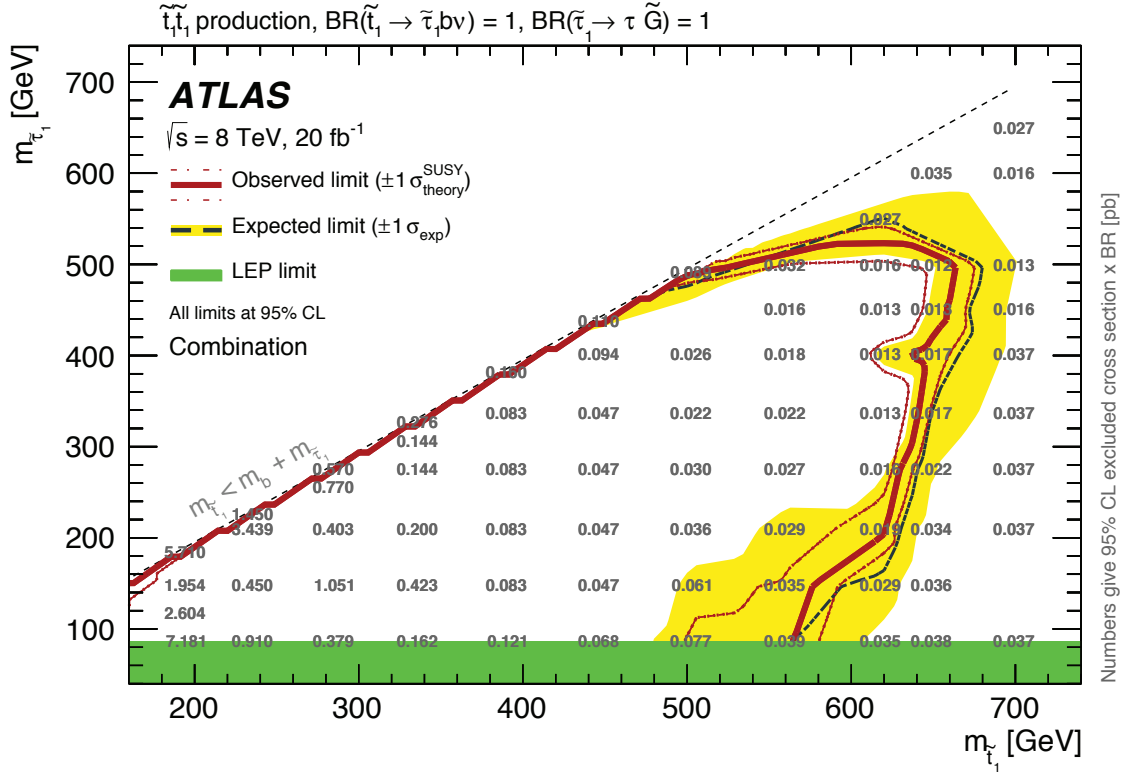
Figure 8.3: The dashed and solid lines show the expected and observed exclusion limit at 95% CL in the $(m_{\tilde{t}}, m_{\tilde{\tau}})$ plane for the three channels combined. The LEP limit of $m_{\tilde{\tau}} \geq 87$ GeV is indicated by a green band. The limits on the $\tilde{t} \to \tilde{\tau}$ production cross section in pb are reported for each signal hypothesis. The solid red line and the dashed red lines indicate the observed exclusion limit and the $\pm 1\sigma$ variation on the theoretical signal production cross section, respectively. The dashed black line and the yellow band indicate the expected exclusion limit and its $\pm 1\sigma$ variation of the total uncertainty.

the *had-had* selection, the two *lep-had* selections and the statistical combination of the *lep-lep* selections. The results for the single channels are shown in Fig. 8.2. The black dashed and the red solid line represent the 95% CL expected and observed limit, respectively. The *had-had* channel observed limit seems to coincide with the expected limit. This effect is due the fact that the observed number of events is very similar to the SM expectation. All the sources of systematics have been included apart from the the theoretical signal cross section uncertainty. The yellow band around the expected limit shows the effect of the $\pm 1\sigma$ variation of the total uncertainty on the limit. The two dotted red lines around the observed limit correspond to the $\pm 1\sigma$ variation on the theoretical signal production cross section. The three channels show a good complementarity in covering the parameter space of this simplified model. From Fig. 8.2 it is possible to observe that the *lep-lep* channel provides a good exclusion in the compressed scenario, the two *lep-had* selections provide a good coverage of the low stop and low stau masses as well as the bulk area of the phase space up to large stop and stau masses. The *had-had* channel provides good coverage

at low stau masses in a wide range of stop masses up to medium stop and stau masses. The single channels are merged choosing at each grid point the selection giving the best expected sensitivity in order to compute the combined expected and observed exclusion limits. The results are reported in Fig. 8.3, showing that models with scalar top mass below 490 GeV are excluded at 95% CL. Signal hypotheses with a scalar top mass up to 650 GeV are excluded depending on the scalar tau mass. The numerical results quoted on the particle masses are taken from the -1σ theoretical lines in order to provide more conservative results. The upper limit on the $\tilde{t} \rightarrow \tilde{\tau}$ production cross section is shown for each signal hypothesis. The scalar top masses below 150 GeV are not considered in this search but are implausible because the production cross section times the branching fraction for the process $\tilde{t}\tilde{t} \rightarrow bb\tau\tau + X$ is ~ 25 times larger than the same quantity for the $t\bar{t}$ process in the same final state. Since measurements of the $t\bar{t}$ cross section in various final states [245–248] are in good agreement with SM expectations, these signal hypotheses are considered as excluded.

8.3 Systematic uncertainties of the analysis

Various sources of systematic uncertainty affect the predicted background event yields in the SRs and CRs. The uncertainties are either evaluated directly from MC simulation or propagated through the likelihood fit for backgrounds that are normalised to the data observed in CRs. It is possible to divide the systematic sources in two classes. The first class consists of all the systematics affecting the reconstructed objects and these are estimated by varying the calibrations described in Ch. 3 within their uncertainties. The experimental uncertainties considered in the search are the following:

- **Jet energy scale and resolution.** The uncertainty on the jet energy scale (JES) and jet energy resolution (JER) is derived using a combination of MC simulated samples and data driven techniques. The impact on the background expected yields is estimated smearing the jet transverse momenta in the MC simulated samples. In addition, the impact of the variation of the JES and JER is propagated to the $E_{\mathrm{T}}^{\mathrm{miss}}$ [155, 249].

- **Un-associated clusters in the calorimeter energy scale and resolution.** These uncertainties are related to the contributions to the $E_{\mathrm{T}}^{\mathrm{miss}}$ from calorimeter clusters that are not associated to any reconstructed object, as well as low momentum ($7 < p_{\mathrm{T}} < 20$ GeV) jets and modelling of the pile-up.

- **Pile-up.** The uncertainty on the number of pile-up events is evaluated scaling the mean of the distribution of the number of interaction per bunch crossing by a 10%.

- **Integrated luminosity.** The uncertainty on the integrated luminosity recorded by ATLAS for the 2012 sample is 2.8% [250].

- **Lepton identification and reconstruction.** In the MC simulation, all selected electrons, muons or taus contribute with a multiplicative weight to the overall event weight in order to account for differences in efficiency with respect to data [138, 145].

These uncertainties arise from the variations of the identification and trigger scale factors, for a total impact at the level of a few percent.

- **Electron energy scale and muon momentum scale.** The impact of these uncertainties is obtained smearing the energy (momentum) of the reconstructed electron (muon) within the calorimeter (ID and MS systems) resolution [138, 145].

- **Hadronic tau energy scale (TES).** Systematic uncertainties for the TES are evaluated by varying the parameters acting on the energy reconstruction in MC and depend on the τ p_T, η and prong type for a contribution up to 4% [150].

- **B-tagging efficiency.** This uncertainty is evaluated propagating the uncertainties on the b-tagging algorithm calibration, which consist of b-jets and c-jets identification efficiency and light flavour *mistag* rate [161, 162].

- **Fake and non-prompt lepton background uncertainties.** This uncertainty only applies to the *lep-lep* analysis. The uncertainty mostly arises from the limited statistics of the sample used for the matrix method technique.

The second class is composed by theoretical uncertainties that affect the MC estimate and are evaluated with different MC samples with respect to the nominal ones. These uncertainties are described in the following list:

- **Production cross section.** The uncertainties on the production cross sections are $\sim 6\%$ for $t\bar{t}$, 6%, 5% and 7% for WW, ZZ and WZ respectively [251, 252]. For single top (Wt channel) the uncertainty on the cross section is 7%, while for $t\bar{t} + W$ and $t\bar{t} + Z$ uncertainties of 30% and 29% are used.

- **Top pair production uncertainties**. Since the $t\bar{t}$ contribution represents the major background in the SRs, the analysis dedicates particular attention to the modelling of this process. The following sources of systematics related to the top pair background are considered:

  1. **Generator modelling:** The predictions of `POWHEG-BOX` are compared with those of `MC@NLO` in order to asses the impact of a particular choice of MC generator.

  2. **Hadronisation and showering modelling:** The difference of the predictions between `POWHEG-BOX` interfaced to `PYTHIA` and `POWHEG-BOX` interfaced to `HERWIG` is used to evaluate the systematic uncertainty due to parton showering and hadronisation.

  3. **Initial (ISR) and final state radiation (FSR):** In order to account for uncertainties in the modelling of initial or final state QCD radiation, the predictions have been compared to the ones obtained using `ACERMC-3.8` samples generated with different tuning parameters.

- **NLO interference between single top and top pair production.** At next-to-leading order, contributions with an additional b quark in the final state lead to

ambiguities in distinguishing the single top Wt-channel and top pair production. This effect becomes significant in the *lep-had* analysis that uses b-jets in the computation of $m_{\text{T2}}(b\ell, b\tau_{\text{had}})$, selecting a region where these ambiguities are important. The Wt samples are generated using `MC@NLO-4.06` and `POWHEG-1.0` using the diagram removal scheme [253]. The difference with the LO prediction on WWb and $WWbb$ final states, including $t\bar{t}$ and Wt processes, obtained with `ACERMC-3.8` is used to evaluate the impact of this systematics source.

- **W+jets and Z+jets modelling.** The uncertainties on these processes production have been evaluated by re-weighting the `SHERPA` predictions to `ALPGEN-2.14` with various numbers of partons in the final state and different choices of factorisation and renormalisation scales.

- **Parton density functions (PDF).** These uncertainties are determined in the MC predictions following the prescription described in [254] comparing different PDF sets and are found to be negligible compared to the other systematic sources.

- **Diboson generation.** This uncertainty, important only for the *lep-lep* channel, is evaluated by comparing the predictions of `POWHEG-1.0` and `SHERPA-1.4.1`, which includes also the impact of choice of a different parton showering scheme.

The systematic uncertainties, both experimental and theoretical, are evaluated in each selection and are included in the likelihood fit through the insertion of gaussian constrained nuisance parameters. The relative contribution of the relevant systematics to the total uncertainty in the *lep-had* and *had-had* selections is shown in Tab. 8.3. Since the individual uncertainties are correlated, they do not add up in square sum to the total relative uncertainty. Some of the sources of systematics can be merged under the same table entry, taking into account the correlation matrix. For example, *Top normalisation* includes the uncertainties on the normalisation factors for both the fake tau and true tau components of the top background and the *Top-quark theory uncertainty* merges the top quark generator, the ISR and FSR, the parton showering and the $t\bar{t} - Wt$ interference systematic uncertainties together.

A similar table for the *lep-lep* analysis can be found in [190] and is not reported here.

The uncertainty on the signal production cross sections is estimated from an envelope of cross section predictions obtained using the 68% CL ranges of the `CTEQ` and `MSTW` PDF sets, together with variations of the renormalisation and factorisation parameters, following the procedure described in [207]. The total uncertainty associated to the NLO+NLL signal production cross section is between 14% to 16% for scalar top masses ranging between 150 GeV and 560 GeV.

8.4 Searches for stop decaying to stau in Run-2

The $\tilde{t} \to \tilde{\tau}$ analysis discussed in this thesis rose considerable interest within the ATLAS experiment community and the analysis has been updated using data collected at $\sqrt{s} = 13$ TeV in 2015 and early 2016, with a total integrated luminosity of 13.2 fb^{-1}. The Run-2 analysis considers the same GMSB benchmark model in the final state where one of the

	SR$_{HH}$	SR$_{LM}$	SR$_{HM}$
Background events	3.1 ± 1.2	22.1 ± 4.7	2.1 ± 1.5
Uncertainty Breakdown [%]:			
Jet energy scale and resolution	17	13	2
Tau energy scale	9	4	3
Cluster energy scale and resolution	1	2	4
b-tagging	2	4	2
Top-quark theory uncertainty	37	11	64
W+jets theory and normalisation	-	1	19
Simulation statistics	20	6	21
Top normalisation	18	6	20

Table 8.3: Summary of the background yields in the *lep-had* and *had-had* analyses and the associated total uncertainties. Only the relevant sources of systematics have been quoted as a relative uncertainty on the total background. Various sources of systematics can be merged under the same table entry, taking into account the correlation matrix. A dash indicates a negligible contribution.

two tau leptons decays hadronically and the other into a light lepton, but focusing on the un-excluded higher mass range of the scalar top quark. A complete overview of the analysis is given in [255] and only a summary of the results is discussed here.

The analysis selects only events with exactly one identified τ_{had} and exactly one electron or muon, missing transverse momentum $E_{\mathrm{T}}^{\mathrm{miss}} > 180$ GeV, hadronic tau transverse momentum $p_{\mathrm{T}}^{\tau} > 70$ GeV and at least one b-jet in the signal region. The most discriminant variable in the analysis is the stransverse mass $m_{\mathrm{T2}}(\ell, \tau)$, see Sec. 7.1.2, while the invariant mass between the reconstructed hadronic tau and the light lepton $m(\ell, \tau)$ is used for the definition of control regions. The SM background estimate in the signal region is based on Monte Carlo simulation together with the extraction of data-driven normalisation for $t\bar{t}$ and W+jets expected yields from dedicated control regions, using a procedure similar to the one described in Sec. 7.2.3.

The extrapolation of the normalisation factors calculated in the control region to the signal region is checked using a set of validation regions defined by kinematic cuts between those of the control regions and the signal region. A good agreement between data and modelling is observed in those regions. Similar to what is described in Sec. 8.3, systematic uncertainties are divided in detector-related and theoretical uncertainties. The main sources of experimental uncertainties are due to jet and tau lepton energy calibration and resolution, the missing transverse momentum measurement and b-jet and tau identification. The sources of theoretical uncertainties include uncertainties on $t\bar{t}$ modelling, production cross section and PDF sets. The dominant systematics of the analysis are the $t\bar{t}$ modelling (53%) and the normalisation of $t\bar{t}$ events with a fake tau lepton (49%). The analysis observes four events in the signal region to be compared to a SM expected background of 3.4 ± 1.9 events, leading to the conclusion that no statistically significant excess has been found. In Fig. 8.4 the exclusion limits on the mass parameters of the $\tilde{t} \rightarrow \tilde{\tau}$ simplified model are shown. The search performed using 13.2 fb^{-1} of $p-p$ collision data at $\sqrt{s} = 13$
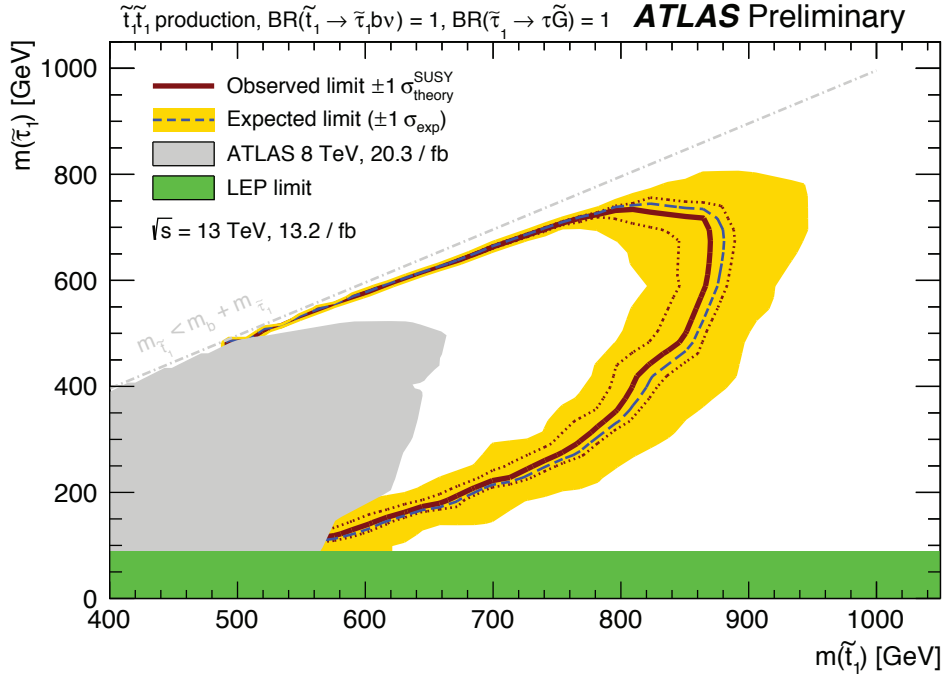
Figure 8.4: The expected (dashed blue line) and observed (red line) exclusion limits at 95% CL in the $(m_{\tilde{t}}, m_{\tilde{\tau}})$ plane for the $\tilde{t} \to \tilde{\tau}$ simplified model and for 13.2 fb^{-1} of integrated luminosity at $\sqrt{s} = 13$ TeV. The plot includes the Run-1 ATLAS exclusion contour [1] and the limit on the mass of the tau slepton set by the LEP experiments [224]. The yellow band indicates the $\pm 1\sigma$ uncertainty band on the expected limit, while the dotted red line indicate the uncertainty due to the signal cross section.

TeV shows that masses of the top squark up to 870 GeV and tau slepton masses up to 730 GeV are excluded at 95% CL in this model.

8.5 Conclusions

The work presented in this thesis focused on the search for direct production of scalar top quark pairs in final states with tau leptons, jets and missing transverse momentum. This search is motivated by a set of possible SUSY scenarios arising from the GMSB mechanism. The search discussed in this thesis increases the coverage of the direct production of top squark searches performed by the ATLAS experiment since it covers a final state that would not be otherwise considered as discussed in Sec. 1.3.2. The analysis is performed using the $\sqrt{s} = 8$ TeV $p-p$ collisions data from the full 2012 dataset, for a total integrated luminosity of 20 fb^{-1} recorded by ATLAS detector at the LHC. The search is subdivided in three independent analysis channels depending on the τ-lepton decay mode:

- The **Dilepton channel** targets final states where both the τ-leptons decay leptonically. The channel has been covered by the reinterpretation of a previous and more general search with similar final state [190].

- The **Lepton-Hadron channel** targets final states where one τ-lepton decayed hadronically and the other leptonically.

- The **Hadron-Hadron channel** targets final states where both τ-leptons decay hadronically.

The search is optimised for the scalar top decay mode $\tilde{t} \to b\tilde{\tau}\nu_\tau$ followed by $\tilde{\tau} \to \tilde{G}$, assuming 100% branching ratio for each decay step. The observed data in all selections has been observed to be compatible with the SM-only hypothesis. The results have been interpreted as upper limits on different signal hypotheses depending on the scalar top and scalar τ masses. The three channels show good complementarity in covering the simplified model parameter space. Lower limits on the scalar top mass are set at 95% confidence level and found to be between 490 GeV and 650 GeV for scalar tau masses between the LEP limit and the scalar top mass.

The search for direct production of scalar top quarks has been updated using $p-p$ collision data recorded at $\sqrt{s} = 13$ TeV, recorded by the ATLAS experiment during 2015 and 2016. The Run-2 search was performed using only the lepton-hadron channel. Considering $\tilde{t} \to \tilde{\tau}$ simplified models, top squark masses up to 870 GeV and tau slepton masses up to 730 GeV are excluded at 95% Confidence Level.

Summary

The Standard Model (SM) describes the properties of the all known elementary particles and their electromagnetic, weak and strong quantum interactions. Matter is composed of half-integer spin particles, called *fermions*, which are divided into six *quarks* (u, d, c, s, t, b), which can only be found confined into hadrons, and six *leptons* $(\nu_e, e, \nu_\mu, \mu, \nu_\tau, \tau)$. The interactions between these particles are mediated by spin-1 *bosons*: the weak force is carried by the massive Z and $W^\pm$ bosons, while the photon γ and the gluons g are responsible for the electromagnetic and strong forces, respectively. The particles of the theory gain their mass through the spontaneous electroweak symmetry breaking described by the Higgs mechanism, which has been confirmed by the observation of the Higgs boson in 2012.

In the last decades the Standard Model has revealed itself very successful in predicting the behaviour of subatomic particles. However, the SM is a theory far from being complete since it does not include gravity and does not provide any explanation of the nature of Dark Matter and Dark Energy, which together compose about 95% of the Universe. Physicists have worked on possible extensions of the SM in order to solve these shortcomings. One promising theory is Supersymmetry (SUSY), which extends the SM allowing symmetry transformations that interchange fermions with bosons and predicts a super partner for each SM particle.

Since no supersymmetric particle has been experimentally observed yet, SUSY, if it exists, must be a broken symmetry and the masses of the superpartners are thought to be much larger than those of the SM particles. The mechanism behind the supersymmetry breaking is not known at the moment and in some models all the SUSY breaking terms are added directly to the Lagrangian. In contrast to this approach, other supersymmetric models assume the existence of a *hidden sector* where the SUSY breaking is generated and it is then transmitted to the *visible sector* composed by the SM particles and their superpartners. In particular, in the *Gauge Mediated Supersymmetry Breaking* (GMSB) model, a set of supersymmetric fields that couple directly to the *hidden sector* transmits the SUSY breaking to the *visible sector* through quantum loops in gauge interactions.

If Supersymmetric particles exist, they can be produced in very energetic proton collisions. The production cross section for supersymmetric particles is larger for those that couple strongly to the matter constituents, such as gluinos and squarks, with the scalar top quark pair cross section of an order of magnitude smaller than the other two generations of squarks. However, the requirement of a low level of fine tuning necessary for Supersymmetry to provide a solution for the *hierarchy problem*, together with a large Yukawa coupling and large off-diagonal terms in the mass mixing matrix, constrains the masses of top squarks below the TeV scale in many SUSY models and so these particles may be produced at the Large Hadron Collider (LHC).

The LHC is a two-ring superconducting, circular proton or heavy-ion collider located at CERN in Geneva. While the LHC is designed to operate at a proton-proton centre-of-mass

energy of $\sqrt{s} = 14$ TeV, the delivered energy was $\sqrt{s} = 7$ TeV during 2010 and 2011, $\sqrt{s} = 8$ TeV during 2012 and $\sqrt{s} = 13$ TeV in 2015 and 2016. The proton beams cross each other in four sections of the LHC, where particle detectors are placed in order to study the products of the collisions. The "A Toroidal LHC ApparatuS" (ATLAS) is one of these experiments and it is designed to primarily study the Electroweak Symmetry Breaking and the Higgs Mechanism, precisely measure the SM parameters and look for new physics beyond the SM.

This thesis presents a SUSY analysis in a particular scenario arising from the GMSB mechanism that assumes a massless gravitino $\tilde{G}$ as lightest supersymmetric particle, a stau lepton $\tilde{\tau}$ as next-to-lightest supersymmetric particle and the top squark $\tilde{t}$ as the lightest among the quark superpartners. The analysis is performed using the data collected by ATLAS at a centre-of-mass energy $\sqrt{s} = 8$ TeV during 2012 data taking, for a total of 20.3 fb^{-1} of integrated luminosity of $p-p$ collisions. In the model considered, the only open decay channel of the top squark is the three body decay $\tilde{t} \rightarrow b\tilde{\tau}\nu_\tau$, followed by the decay $\tilde{\tau} \rightarrow \tau\tilde{G}$, while the other supersymmetric particles are assumed to have very large masses and they do not contribute to the top squark decay chain.

The final state of this search is characterised by the presence of two tau leptons, two jets that contain a b-hadron and particles that escape detection such as neutrinos and gravitinos. The analysis is split into three orthogonal sub-channels that consider the cases with both taus decayed leptonically (*lep-lep*), with one hadronically decaying tau and a muon or an electron in the final state (*lep-had*) or two hadronically decaying tau leptons (*had-had*), respectively. Such final states can be realised also by Standard Model processes that represent the backgrounds to this search..

Figure S.1: Diagram showing the top squark pair production in $p - p$ collisions followed by the decay $\tilde{t} \rightarrow \tilde{\tau} b \nu_\tau$ and $\tilde{\tau} \rightarrow \tau \tilde{G}$.

Monte Carlo simulations are used to model the kinematics of the $\tilde{t} \rightarrow \tilde{\tau}$ signal, which depend on the unknown top squark mass $m_{\tilde{t}}$ and tau slepton mass $m_{\tilde{\tau}}$, and of the Standard Model processes. For each channel, a number of statistically independent *Signal regions* is defined by applying specific kinematic cuts on the physics objects in the final states in order to achieve good discrimination between the signal and background. Among several kinematic variable, the *stransverse mass* m_{T2}, provides the best discrimination power as shown in Fig. S.2. The presence of physics beyond the Standard Model would manifest itself via an excess of observed events with respect to the SM-only expectation. In order to precisely estimate the number of expected SM events in the signal regions, a normalisation fit to the major background sources is performed in *control regions*, which are designed to enhance the selection of single particular SM background processes and reduce to a negligible fraction the signal acceptance. For each channel, a simultaneous fit of the major background processes normalisation, which takes into account the associated systematic uncertainties,

$\tilde{t}_1\tilde{t}_1$ production, BR($\tilde{t}_1 \to \tilde{\tau}_1 b\nu$) = 1, BR($\tilde{\tau}_1 \to \tau \tilde{G}$) = 1

Figure S.3: Exclusion limits on the top squark production with direct decay $\tilde{t} \to \tilde{\tau}b\nu_\tau$ and $\tilde{\tau} \to \tau\tilde{G}$ at $\sqrt{s} = 8$ TeV. The limits on the $\tilde{t} \to \tilde{\tau}$ production cross section in pb are reported for each signal hypothesis.

is performed and the resulting estimates are validated in dedicated *validation regions*, designed to be enriched in SM background processes and kinematically similar, but still orthogonal, to the signal regions. The number of observed data events in the signal regions is found to be compatible with the SM-only hypothesis, hence the results of the search are interpreted as exclusion limits on the production cross section of the $\tilde{t} \to \tilde{\tau}$ model considered. In Figure S.3, the solid red line shows the observed exclusion limit at 95% CL in the $(m_{\tilde{t}}, m_{\tilde{\tau}})$ plane and for each signal hypothesis, the upper limit on the production cross section in picobarns is reported. The three channels have good complementarity in covering the simplified model parameter space and top squark masses up to 650 GeV are excluded depending on the scalar tau lepton mass.
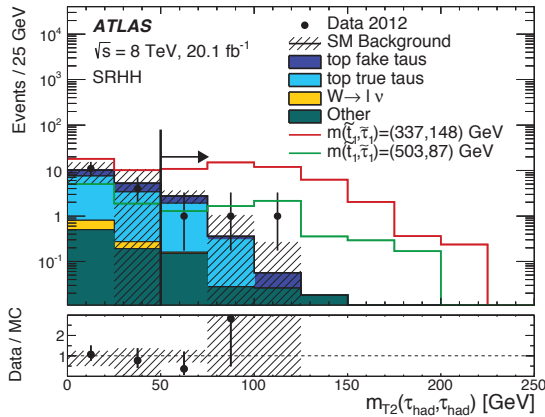
Figure S.2: Distribution of m_{T2} in the *had-had* signal region for the observed data, SM expectation and a $\tilde{t} \to \tilde{\tau}$ model at $\sqrt{s} = 8$ TeV.

At the end of Run-1, a long technical stop, known as the *Long Shutdown 1* (LS1), took place in order to prepare LHC and its experiments to record $p - p$ collisions at a centre-of-mass energy of $\sqrt{s} = 13$ TeV. The ATLAS experiment underwent several upgrades, modifications and refurbishment of detector elements with the aim to improve the acceptance, efficiency and performance in recording high quality data during Run-2. One of the major upgrades of the ATLAS Inner Detector (ID) consisted in the insertion of a new layer of the Pixel detector, the Insertable B-Layer (IBL), designed to significantly improve the tracking performance. The
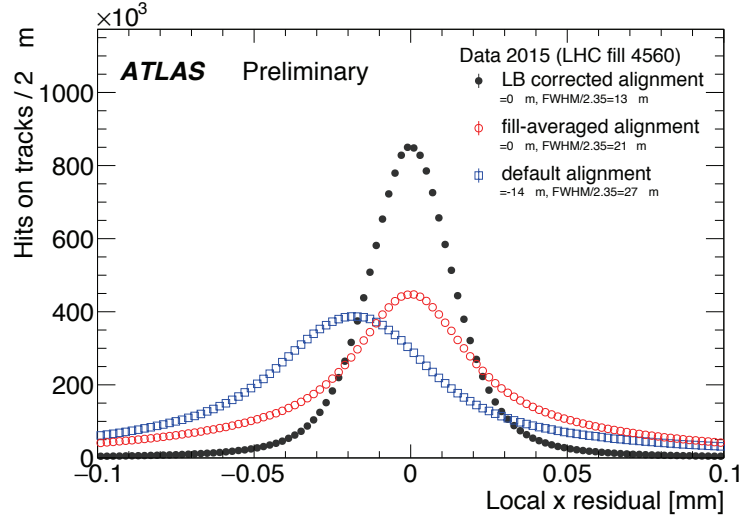
Figure S.4: The IBL local-x ($r\phi$) track-to-hit unbiased residual distributions obtained with a baseline alignment corrections (blue), with run-by-run corrections (red) and with within-run dynamic corrections (black).

insertion of a new detector causes a major change in the geometry of the experiment, which needs to be precisely assessed in order to reconstruct tracks at the design resolution.

The technique used in the ATLAS ID to measure the position of the sensitive elements is the *track-based Inner Detector Alignment*. Such method consists of calculating the corrections to an assumed ATLAS ID geometry by minimising a χ^2 function which depends on the tracks parameters and on the position and orientation of the ID sensitive elements. This thesis presents the alignment of the ATLAS Inner Detector during the LS1, using cosmic ray data for the first commissioning, and for early Run-2 data taking, showing the final alignment performed at the end of 2015 campaign. During the ATLAS commissioning period with cosmic ray data, it has been observed that the IBL detector structure deforms assuming a parabolic shape whose magnitude M depends linearly on the operating temperature T with a slope $dM/dT = -10.6 \pm 0.7$ μm/K. Since small changes in temperature can cause sizeable displacements of the active elements that would undermine the quality of reconstructed tracks, the framework of the ID Alignment has been improved to include an additional degree of freedom that models such deformation, together with the possibility to calculate the corrections at a much smaller time granularity to correct for distortions happening during the data taking. The effect of such time-dependent correction is shown in Fig. S.4, where it is shown that the track-to-hit residual distribution gets significantly narrower, indicating the recovery of the IBL design resolution. This novel approach changes the computation of the ATLAS Inner Detector geometry which is not anymore fixed during the collection of data originating from $p - p$ collisions in Run-2, but is dynamically computed to account for smaller time-scale detector deformations.

Samenvatting

Het Standaard Model (SM) beschrijft de eigenschappen van alle bekende elementaire deeltjes en hun elektromagnetische, zwakke en sterke quantum interacties. Materie bestaat uit half-integer spin deeltjes, *fermionen*. Deze zijn verdeeld in zes *quarks* (u, d, c, s, t, b), die gebonden zijn in hadrons, en zes *leptonen* $(\nu_e, e, \nu_\mu, \mu, \nu_\tau, \tau)$. De interacties vinden plaats door middel van spin-1 *bosonen*: de massieve Z en $W^\pm$ bosonen zijn verantwoordelijk voor de zwakke kernkracht, terwijl het foton γ en de gluonen g verantwoordelijk zijn voor respectievelijk de elektromagnetische kracht en sterke kernkracht. De deeltjes verkrijgen hun massa door spontane elektrozwakke symmetrie breking beschreven in het Higgs mechanisme. Dit mechanisme is bevestigd door de observatie van het Higgs boson in 2012.

Het Standaard model is in de laatste decennia zeer succesvol gebleken in het beschrijven van het gedrag van sub atomische deeltjes. Het SM is echter ver van compleet omdat het geen gravitatie bevat en geen uitleg voor de oorsprong van Donkere Materie en Donkere Energie, wat bij elkaar ongeveer 95% van het universum behelst. Natuurkundigen hebben gewerkt aan mogelijke uitbreidingen van het SM om deze tekortkomingen op te lossen. Een veel belovende theorie is Supersymmetrie (SUSY), dit breidt het SM uit met symmetrische transformaties die fermionen en bosonen met elkaar omwisselen en voorspelt een super partner voor elk SM deeltje.

Omdat er nog nooit experimenteel een supersymmetrisch deeltje is geobserveerd, moet SUSY, als het bestaat, een gebroken symmetrie zijn. De massa's van de superpartners worden dan verwacht veel hoger te liggen dan die van de SM deeltjes. Het mechanisme achter supersymmetrie breking is niet bekend. In sommige modellen worden alle symmetrie brekings termen toegevoegd aan de Lagrangiaan, in tegenstelling tot deze aanpak zijn er ook SUSY modellen die een *verbogen sector* aannemen, waar symmetrie brekings termen gegenereerd worden. Deze brekings termen komen vervolgens weer naar boven in de *zichtbare sector*, die opgemaakt wordt door SM deeltjes en hun superpartners. Dit is het geval in het *Ijk bemiddelde Supersymmetrie breking* (GMSB) model, een set van supersymmetrische velden die direct koppelt aan de *verborgen sector* en vervolgens de symmetrie brekings termen doorspeelt naar de *zichtbare sector* doormiddel van quantum lussen in ijk interacties.

Als Supersymmetrische deeltjes bestaan, kunnen ze geproduceerd worden in energetische proton-proton botsingen. De productie doorsnede is het grootst voor supersymmetrische deeltjes die koppelen doormiddel van de sterke kernkracht, zoals gluinos en squarks. De werkzame doorsnede van het scalaire top quark is dan twee orde groottes kleiner dan die van de andere twee generatie squarks. Een kleine hoeveelheid afstemming is nodig voor Supersymmetrie om een oplossing te zijn voor het *hiërarchie probleem*. In veel SUSY modellen wordt door een grote Yukawa koppeling samen met grote niet-diagonale termen in de massa mixing matrix, de massa van de top squarks beperkt tot onder de TeV schaal,

waardoor de deeltjes geproduceerd kunnen worden in de Large Hadron Collider (LHC).

De LHC bestaat uit twee supergeleidende ringen voor proton-proton botsingen of botsingen met zware ionen en bevindt zich bij CERN in Geneve. De LHC is ontworpen voor een proton-proton massamiddelpunts energie van $\sqrt{s} = 14$ TeV, de geleverde energie was $\sqrt{s} = 7$ TeV tijdens 2010 en 2011, $\sqrt{s} = 8$ TeV tijdens 2012 en $\sqrt{s} = 13$ TeV in 2015 en 2016. De protonen botsen op vier punten in de LHC, hieromheen zijn detectoren gebouwd om de botsingen te bestuderen. De "A Toroidal LHC ApparatuS" (ATLAS) detector is een van de ontworpen experimenten om Elektrozwakke Symmetrie Breking en het Higgs mechanisme te bestuderen, voor precisie metingen aan SM parameters en om te zoeken naar natuurkunde voorbij het SM.

Deze thesis bevat een SUSY analyse van een specifiek scenario van het GMSB mechanisme. Het model bevat een massaloze gravitino $\tilde{G}$ als lichtste supersymmetrische deeltjes, een stau lepton $\tilde{\tau}$ als een-na-lichtste supersymmetrische deeltjes en de top squark $\tilde{t}$ als lichtste van de quark superpartners. De analyse is uitgevoerd met behulp van de data van ATLAS met een massamiddelpunts energie van $\sqrt{s} = 8$ TeV tijdens de 2012 data neming, met een totaal van 20.3 fb^{-1} geÃ¯ntegreerde luminositeit van $p - p$ botsingen. In het onderzochte model is het enige open kanaal het drie lichaams verval van het top squark $\tilde{t} \rightarrow b\tilde{\tau}\nu_\tau$, gevolgd door het verval $\tilde{\tau} \rightarrow \tau\tilde{G}$. De andere supersymmetrische deeltjes hebben een dergelijk hoge massa dat ze niet voorkomen in het top squark verval.

De uiteindelijke toestand in deze zoektocht wordt gekarakteriseerd door de aanwezigheid van twee tau leptonen, twee jets die een b-hadron bevatten en deeltjes die aan de detector ontsnappen zoals neutrinos en gravitinos. De analyse is opgesplitst in drie orthogonale sub kanalen die het geval bekijken wanneer beide taus leptonisch vervallen (*lep-lep*), wanneer een tau hadronisch vervalt en de andere leptonisch (*lep-had*) of wanneer beide taus hadronische vervallen (*had-had*).

Figure S.1: Diagram met top squark paar productie in een $p-p$ botsing gevolgd door het verval $\tilde{t} \rightarrow \tilde{\tau}b\nu_\tau$ and $\tilde{\tau} \rightarrow \tau\tilde{G}$.

Zulke uiteindelijke toestanden worden ook veroorzaakt door het Standaard Model, wat de achtergrond veroorzaakt in deze zoektocht. Monte Carlo simulaties zijn gebruikt om een model te vormen van de kinematica van het $\tilde{t} \rightarrow \tilde{\tau}$ signaal. Dit model hangt af van de onbekende top squark massa $m_{\tilde{t}}$ en de tau slepton massa $m_{\tilde{\tau}}$ en SM processen. Voor elk kanaal bestaat er een statistisch onafhankelijke *Signaal regio* door specifieke kinematische snedes toe te passen op de botsings producten die aanwezig zijn in uiteindelijke toestand om zo een goed onderscheid te kunnen maken tussen signaal en achtergrond. De *transversale massa* m_{T2} maakt als beste onderscheid, zoals te zien in Fig. S.2. De aanwezigheid van natuurkunde voorbij het Standaard Model zou zichtbaar zijn doormiddel van een overschot aan geobserveerde events ten opzichte van alleen het SM. Om het aantal verwachte SM events te kunnen schatten wordt er een normalisatie fit toegepast op de dominante

$\widetilde{t}_1\widetilde{t}_1$ production, BR($\widetilde{t}_1 \to \widetilde{\tau}_1 b\nu$) = 1, BR($\widetilde{\tau}_1 \to \tau \widetilde{G}$) = 1

Figure S.3: Uitsluitings limieten voor de top squark productie in het directe verval $\tilde{t} \to \tilde{\tau} b\nu_\tau$ en $\tilde{\tau} \to \tau\tilde{G}$ bij $\sqrt{s} = 8$ TeV. De limieten op de $\tilde{t} \to \tilde{\tau}$ productie werkzame doorsnede worden vermeld in pb voor elke signaal hypothese.

achtergronden in *controle regio's*, die zo gekozen zijn om een specifieke SM achtergrond te isoleren met weinig signaal. Voor elk kanaal wordt tegelijktijdig een fit van de achtergrond normalisatie gedaan, hierin worden ook systematische fouten meegenomen. De resulterende achtergrond schattingen worden gevalideerd in *validatie regio's*, speciaal ontworpen voor de specifieke SM achtergrond en kinematich vergelijkbaar, maar orthogonaal aan de signaal regio's.
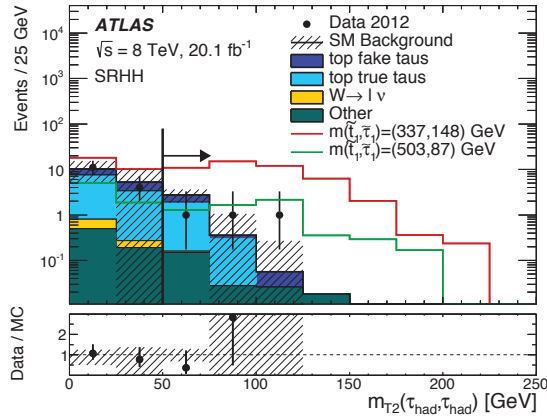
Figure S.2: Distributie van $m_{\mathrm{T}2}$ in de *had-had* signaal regio voor de geobserveerde data, de SM verwachting en een $\tilde{t} \to \tilde{\tau}$ model bij $\sqrt{s} = 8$ TeV.

Het aantal geobserveerde data events in de signaal regio's is compatibel met de alleen SM hypothese, vandaar dat de resultaten van de zoektocht worden geÃ¯nterpreteerd door middel van uitsluitings limieten met 95% zekerheid in het $(m_{\tilde{t}}, m_{\tilde{\tau}})$ vlak en voor elke signaal hypothese, het bovenste limiet op de productie werkzame doorsnede wordt vermeld in picobarns. De drie kanalen vullen elkaar goed aan in het beschrijven van de parameters van het gesimplificeerde model en een top squark massa lager dan 650 GeV wordt uitgesloten afhankelijk van de scalaire tau lepton massa. Op het einde van Run-1 heeft er een lange technische stop plaats gevonden, bekend als de *Long Shutdown 1* (LS1), om de LHC klaar te maken voor proton-proton botsingen met een massamiddelpunts energie van $\sqrt{s} = 13$ TeV. Het ATLAS experiment is toen op bepaalde punten verbeterd, onder andere door aangepaste en gerenoveerde detector elementen voor
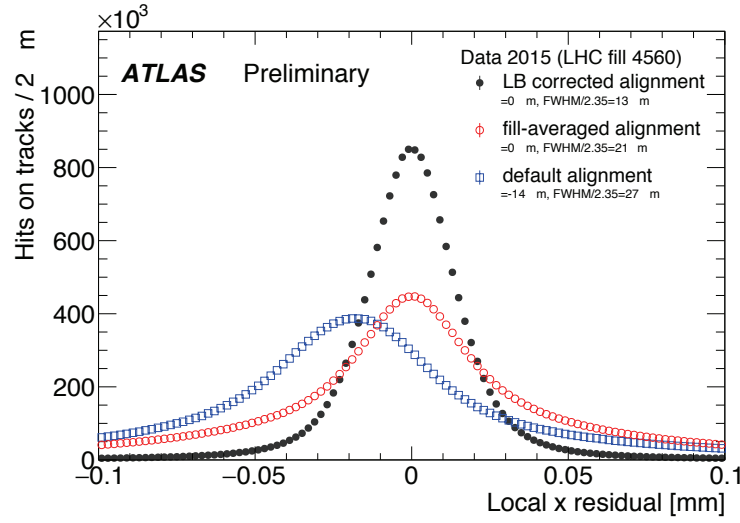
Figure S.4: The IBL local-x ($r\phi$) track-to-hit unbiased residual distributions obtained with a baseline alignment corrections (blue), with run-by-run corrections (red) and with within-run dynamic corrections (black).

verbeterde acceptatie, efficiÃ«ntie en prestatie om de hoge data kwaliteit van Run-2 aan te kunnen. Een van de grote verbeteringen aan de ATLAS Inner Detector (ID) is de invoeging van de Insertable B-Layer (IBL), ontworpen om deeltjes sporen nog beter te kunnen meten.

De invoeging van deze detector is een grote verandering in de geometrie van het experiment, die precies bekend moet zijn om de sporen goed te kunnen reconstrueren volgens de ontwerp resolutie. De gebruikte techniek in de ATLAS ID is om de positie van de gevoelige elementen te meten is de *track-based Inner Detector Alignment*. Deze methode bestaat uit het bereken van de correcties op de verwachte ATLAS ID geometrie door de χ^2 functie te minimaliseren. De χ^2 functie hangt af van de spoor parameters en de posities van de ID gevoelige elementen. Deze thesis laat de uitlijning van de ATLAS ID zien tijdens de LS1, met gebruik van kosmische stralings data, en het begin van Run-2 data verzameling, met de uiteindelijk uitgevoerde uitlijning op het einde van de 2015 campagne. Tijdens de ATLAS inbedrijfsstelling periode met kosmische stralings data, is het opgevallen dat de IBL detector structuur afhangt van een parabolische vorm waarbij de grootte M lineair afhangt van de operationele temperatuur T met een helling $dM/dT = -10.6 \pm 0.7$ μm/K. Omdat een klein verschil in temperatuur een grote verplaatsing van actieve elementen kan veroorzaken komt dit de kwaliteit van de geconstrueerde sporen niet ten goede. Hierdoor is aan het raamwerk van de ID uitlijning een additionele vrijheidsgraad toegevoegd die deze deformatie behelst. Ook is de mogelijkheid toegevoegd om de correcties op een korter tijdsbestek te kunnen doen waardoor de track-to-hit residuele distributie significant smaller te wordt, wat een herstel aangeeft van de IBL ontwerp resolutie. Deze nieuwe aanpak verandert de berekening van de ATLAS ID geometrie waardoor deze niet meer vaststaat in een data collectie van $p-p$ botsingen in Run-2, maar dynamisch berekend wordt om correcties op kleine tijdsschaal uit te kunnen voeren.

Bibliography

[1] The ATLAS Collaboration, "Search for direct top squark pair production in final states with two tau leptons in pp collisions at $\sqrt{s} = 8$ TeV with the ATLAS detector," *Eur. Phys. J.*, vol. C76, no. 2, p. 81, 2016.

[2] S. L. Glashow, J. Iliopoulos, and L. Maiani, "Weak Interactions with Lepton-Hadron Symmetry," *Phys. Rev.*, vol. D2, pp. 1285–1292, 1970.

[3] S. Weinberg, "A model of leptons," *Phys. Rev. Lett.*, vol. 19, pp. 1264–1266, Nov 1967.

[4] A. Salam, "Weak and Electromagnetic Interactions," *Conf. Proc.*, vol. C680519, pp. 367–377, 1968.

[5] S. L. Glashow, "Partial Symmetries of Weak Interactions," *Nucl. Phys.*, vol. 22, pp. 579–588, 1961.

[6] C. N. Yang and R. L. Mills, "Conservation of isotopic spin and isotopic gauge invariance," *Phys. Rev.*, vol. 96, pp. 191–195, Oct 1954.

[7] C. Patrignani et al. (Particle Data Group), "Review of particle physics," *Chin.Phys. C*, vol. 40, no. 100001, 2016.

[8] M. E. Peskin and D. V. Schroeder, *An introduction to quantum field theory*. Advanced book program, Boulder (Colo.): Westview Press Reading (Mass.), 1995. Autre tirage : 1997.

[9] P. W. Higgs, "Broken symmetries and the masses of gauge bosons," *Phys. Rev. Lett.*, vol. 13, pp. 508–509, Oct 1964.

[10] P. W. Higgs, "Broken symmetries, massless particles and gauge fields," *Phys. Lett.*, vol. 12, pp. 132–133, 1964.

[11] P. W. Higgs, "Spontaneous symmetry breakdown without massless bosons," *Phys. Rev.*, vol. 145, pp. 1156–1163, May 1966.

[12] F. Englert and R. Brout, "Broken Symmetry and the Mass of Gauge Vector Mesons," *Phys. Rev. Lett.*, vol. 13, pp. 321–323, 1964.

[13] G. S. Guralnik, C. R. Hagen, and T. W. B. Kibble, "Global conservation laws and massless particles," *Phys. Rev. Lett.*, vol. 13, pp. 585–587, Nov 1964.

[14] T. W. B. Kibble, "Symmetry breaking in non-abelian gauge theories," *Phys. Rev.*, vol. 155, pp. 1554–1561, Mar 1967.

[15] J. Bernstein, "Spontaneous symmetry breaking, gauge theories, the higgs mechanism and all that," *Rev. Mod. Phys.*, vol. 46, pp. 7–48, Jan 1974.

[16] The ATLAS Collaboration, "Observation of a new particle in the search for the Standard Model Higgs boson with the ATLAS detector at the LHC," *Physics Letters B*, vol. 716, no. 1, pp. 1 – 29, 2012.

[17] The CMS Collaboration, "Observation of a new boson at a mass of 125 GeV with the CMS experiment at the LHC," *Physics Letters B*, vol. 716, no. 1, pp. 30 – 61, 2012.

[18] The CMS Collaboration, "Observation of a new boson with mass near 125 GeV in pp collisions at $\sqrt{s} = 7$ and 8 TeV," *Journal of High Energy Physics*, vol. 2013, no. 6, p. 81, 2013.

[19] D. J. Gross and F. Wilczek, "Ultraviolet behavior of non-abelian gauge theories," *Phys. Rev. Lett.*, vol. 30, pp. 1343–1346, Jun 1973.

Bibliography

[20] J. H. Oort, "The force exerted by the stellar system in the direction perpendicular to the galactic plane and some related problems," *Bull. Astron. Inst. Netherlands*, vol. 6, pp. 249–287, 1932.

[21] F. Zwicky, "Die Rotverschiebung von extragalaktischen Nebeln," *Helv. Phys. Acta*, vol. 6, pp. 110–127, 1933.

[22] P. A. R. Ade *et al.*, "Planck 2015 results. XIII. Cosmological parameters," *Astron. Astrophys.*, vol. 594, p. A13, 2016.

[23] G. Hinshaw, D. Larson, E. Komatsu, D. N. Spergel, C. L. Bennett, J. Dunkley, M. R. Nolta, M. Halpern, R. S. Hill, N. Odegard, L. Page, K. M. Smith, J. L. Weiland, B. Gold, N. Jarosik, A. Kogut, M. Limon, S. S. Meyer, G. S. Tucker, E. Wollack, and E. L. Wright, "Nine-year Wilkinson Microwave Anisotropy Probe (WMAP) Observations: Cosmological Parameter Results," *The Astrophysical Journal Supplement Series*, vol. 208, p. 19, Oct. 2013.

[24] V. C. Rubin and W. K. Ford, Jr., "Rotation of the Andromeda Nebula from a Spectroscopic Survey of Emission Regions," *Astrophysical Journal*, vol. 159, p. 379, Feb. 1970.

[25] D. Clowe, M. Bradac, A. H. Gonzalez, M. Markevitch, S. W. Randall, C. Jones, and D. Zaritsky, "A direct empirical proof of the existence of dark matter," *Astrophys. J.*, vol. 648, pp. L109–L113, 2006.

[26] J. R. Primack, "Dark matter and structure formation," in *Midrasha Mathematicae in Jerusalem: Winter School in Dynamical Systems Jerusalem, Israel, January 12-17, 1997*, 1997.

[27] F. Wilczek, "Unification of force and substance," *Philosophical Transactions of the Royal Society of London A: Mathematical, Physical and Engineering Sciences*, vol. 374, no. 2075, 2016.

[28] H. Miyazawa, "Baryon Number Changing Currents," *Progress of Theoretical Physics*, vol. 36, pp. 1266–1276, Dec. 1966.

[29] P. Ramond, "Dual Theory for Free Fermions," *Phys. Rev.*, vol. D3, pp. 2415–2418, 1971.

[30] Yu. A. Golfand and E. P. Likhtman, "Extension of the Algebra of Poincare Group Generators and Violation of p Invariance," *JETP Lett.*, vol. 13, pp. 323–326, 1971. [Pisma Zh. Eksp. Teor. Fiz.13,452(1971)].

[31] A. Neveu and J. H. Schwarz, "Factorizable dual model of pions," *Nucl. Phys.*, vol. B31, pp. 86–112, 1971.

[32] A. Neveu and J. H. Schwarz, "Quark model of dual pions," *Phys. Rev. D*, vol. 4, pp. 1109–1111, Aug 1971.

[33] J.-L. Gervais and B. Sakita, "Field theory interpretation of supergauges in dual models," *Nuclear Physics B*, vol. 34, no. 2, pp. 632 – 639, 1971.

[34] D. Volkov and V. Akulov, "Is the neutrino a goldstone particle?," *Physics Letters B*, vol. 46, no. 1, pp. 109 – 110, 1973.

[35] J. Wess and B. Zumino, "A lagrangian model invariant under supergauge transformations," *Physics Letters B*, vol. 49, no. 1, pp. 52 – 54, 1974.

[36] J. Wess and B. Zumino, "Supergauge transformations in four dimensions," *Nuclear Physics B*, vol. 70, no. 1, pp. 39 – 50, 1974.

[37] S. Coleman and J. Mandula, "All possible symmetries of the *s* matrix," *Phys. Rev.*, vol. 159, pp. 1251–1256, Jul 1967.

[38] R. Haag, J. T. Lopuszanski, and M. Sohnius, "All possible generators of supersymmetries of the s-matrix," *Nuclear Physics B*, vol. 88, no. 2, pp. 257 – 274, 1975.

[39] S. P. Martin, "A Supersymmetry primer," 1997. [Adv. Ser. Direct. High Energy Phys.18,1(1998)].

[40] R. Barbieri and G. F. Giudice, "Upper Bounds on Supersymmetric Particle Masses," *Nucl. Phys.*, vol. B306, pp. 63–76, 1988.

[41] J. R. Ellis, J. S. Hagelin, D. V. Nanopoulos, K. A. Olive, and M. Srednicki, "Supersymmetric Relics from the Big Bang," *Nucl. Phys.*, vol. B238, pp. 453–476, 1984.

[42] S. Dimopoulos, S. Raby, and F. Wilczek, "Supersymmetry and the scale of unification," *Phys. Rev. D*, vol. 24, pp. 1681–1683, Sep 1981.

[43] I. J. R. Aitchison, "Supersymmetry and the MSSM: An Elementary introduction," *arXiv:hep-ph/0505105*, 2005.

[44] M. Drees, R. Godbole, and P. Roy, *Theory and phenomenology of Sparticles: an account of four-dimensional N=1 supersymmetry in high-energy physics*. Singapore: World Scientific, 2004.

[45] D. J. Gross and R. Jackiw, "Effect of anomalies on quasi-renormalizable theories," *Phys. Rev. D*, vol. 6, pp. 477–493, Jul 1972.

[46] P. Fayet, "Spontaneously broken supersymmetric theories of weak, electromagnetic and strong interactions," *Physics Letters B*, vol. 69, no. 4, pp. 489 – 494, 1977.

[47] G. R. Farrar and P. Fayet, "Phenomenology of the production, decay, and detection of new hadronic states associated with supersymmetry," *Physics Letters B*, vol. 76, no. 5, pp. 575 – 579, 1978.

[48] L. Girardello and M. Grisaru, "Soft breaking of supersymmetry," *Nuclear Physics B*, vol. 194, no. 1, pp. 65 – 76, 1982.

[49] L. O'Raifeartaigh, "Spontaneous Symmetry Breaking for Chiral Scalar Superfields," *Nucl. Phys.*, vol. B96, pp. 331–352, 1975.

[50] G. F. Giudice and R. Rattazzi, "Theories with gauge mediated supersymmetry breaking," *Phys. Rept.*, vol. 322, pp. 419–499, 1999.

[51] M. Dine and W. Fischler, "A phenomenological model of particle physics based on supersymmetry," *Physics Letters B*, vol. 110, no. 3, pp. 227 – 231, 1982.

[52] L. Alvarez-Gaumé, M. Claudson, and M. B. Wise, "Low-energy supersymmetry," *Nuclear Physics B*, vol. 207, no. 1, pp. 96 – 110, 1982.

[53] C. R. Nappi and B. A. Ovrut, "Supersymmetric extension of the $SU(3) \times SU(2) \times U(1)$ model," *Physics Letters B*, vol. 113, no. 2, pp. 175 – 179, 1982.

[54] M. Dine and A. E. Nelson, "Dynamical supersymmetry breaking at low energies," *Phys. Rev. D*, vol. 48, pp. 1277–1287, Aug 1993.

[55] M. Dine, A. E. Nelson, and Y. Shirman, "Low energy dynamical supersymmetry breaking simplified," *Phys. Rev. D*, vol. 51, pp. 1362–1370, Feb 1995.

[56] M. Dine, A. E. Nelson, Y. Nir, and Y. Shirman, "New tools for low energy dynamical supersymmetry breaking," *Phys. Rev. D*, vol. 53, pp. 2658–2669, Mar 1996.

[57] P. van Nieuwenhuizen, "Supergravity," *Physics Reports*, vol. 68, no. 4, pp. 189 – 398, 1981.

[58] S. Deser and B. Zumino, "Broken supersymmetry and supergravity," *Phys. Rev. Lett.*, vol. 38, pp. 1433–1436, Jun 1977.

[59] E. Cremmer, B. Julia, J. Scherk, P. van Nieuwenhuizen, S. Ferrara, and L. Girardello, "Super-higgs effect in supergravity with general scalar interactions," *Phys. Lett.*, vol. B79, pp. 231–234, 1978.

[60] S. Dimopoulos, S. Thomas, and J. D. Wells, "Sparticle spectroscopy and electroweak symmetry breaking with gauge-mediated supersymmetry breaking," *Nuclear Physics B*, vol. 488, no. 1, pp. 39 – 91, 1997.

Bibliography

[61] A. Buckley, "PySLHA: a Pythonic interface to SUSY Les Houches Accord data," *Eur. Phys. J.*, vol. C75, no. 10, p. 467, 2015.

[62] R. Barbieri and G. Giudice, "Upper bounds on supersymmetric particle masses," *Nuclear Physics B*, vol. 306, no. 1, pp. 63 – 76, 1988.

[63] A. Arbey, M. Battaglia, A. Djouadi, F. Mahmoudi, and J. Quevillon, "Implications of a 125 GeV Higgs for supersymmetric models," *Phys. Lett.*, vol. B708, pp. 162–169, 2012.

[64] The ATLAS and CMS Collaborations, "Combined Measurement of the Higgs Boson Mass in *pp* Collisions at $\sqrt{s} = 7$ and 8 TeV with the ATLAS and CMS Experiments," *Phys. Rev. Lett.*, vol. 114, p. 191803, 2015.

[65] N. Craig, D. Green, and A. Katz, "(De)Constructing a Natural and Flavorful Supersymmetric Standard Model," *JHEP*, vol. 07, p. 045, 2011.

[66] C. Csaki, L. Randall, and J. Terning, "Light Stops from Seiberg Duality," *Phys. Rev.*, vol. D86, p. 075009, 2012.

[67] G. Larsen, Y. Nomura, and H. L. L. Roberts, "Supersymmetry with Light Stops," *JHEP*, vol. 06, p. 032, 2012.

[68] J. Gao, M. Guzzi, J. Huston, H.-L. Lai, Z. Li, P. Nadolsky, J. Pumplin, D. Stump, and C. P. Yuan, "CT10 next-to-next-to-leading order global analysis of QCD," *Phys. Rev.*, vol. D89, no. 3, p. 033009, 2014.

[69] J. C. Collins, D. E. Soper, and G. F. Sterman, "Factorization of Hard Processes in QCD," *Adv. Ser. Direct. High Energy Phys.*, vol. 5, pp. 1–91, 1989.

[70] D. Mason *et al.*, "Measurement of the Nucleon Strange-Antistrange Asymmetry at Next-to-Leading Order in QCD from NuTeV Dimuon Data," *Phys. Rev. Lett.*, vol. 99, p. 192001, 2007.

[71] A. Cooper-Sarkar, "What did HERA teach us about the structure of the proton?," *J. Phys.*, vol. G39, p. 093001, 2012.

[72] S. Alekhin, K. Melnikov, and F. Petriello, "Fixed target Drell-Yan data and NNLO QCD fits of parton distribution functions," *Phys. Rev.*, vol. D74, p. 054033, 2006.

[73] S. Alekhin *et al.*, "The PDF4LHC Working Group Interim Report," *arXiv:1101.0536*, 2011.

[74] A. D. Martin, W. J. Stirling, R. S. Thorne, and G. Watt, "Parton distributions for the LHC," *Eur. Phys. J.*, vol. C63, pp. 189–285, 2009.

[75] F. D. Aaron *et al.*, "Combined Measurement and QCD Analysis of the Inclusive e+- p Scattering Cross Sections at HERA," *JHEP*, vol. 01, p. 109, 2010.

[76] R. D. Ball *et al.*, "Parton distributions for the LHC Run II," *JHEP*, vol. 04, p. 040, 2015.

[77] P. M. Nadolsky, H.-L. Lai, Q.-H. Cao, J. Huston, J. Pumplin, D. Stump, W.-K. Tung, and C. P. Yuan, "Implications of CTEQ global analysis for collider observables," *Phys. Rev.*, vol. D78, p. 013004, 2008.

[78] W. Beenakker, R. Höpker, M. Krämer, M. Spira, and P. Zerwas, "Prospino2 cross sections." http://www.thphys.uni-heidelberg.de/~plehn/index.php?show=prospino&visible=tools.

[79] W. Beenakker, R. Hopker, and M. Spira, "PROSPINO: A Program for the production of supersymmetric particles in next-to-leading order QCD," *arXiv:hep-ph/9611232*, 1996.

[80] The ATLAS Collaboration, "Search for new phenomena in final states with large jet multiplicities and missing transverse momentum at $\sqrt{s} = 8$ TeV proton-proton collisions using the ATLAS experiment," *Journal of High Energy Physics*, vol. 2013, no. 10, p. 130, 2013.

[81] The ATLAS Collaboration, "Search for supersymmetry at $\sqrt{s} = 8$ TeV in final states with jets and two same-sign leptons or three leptons with the ATLAS detector," *Journal of High Energy Physics*, vol. 2014, no. 6, p. 35, 2014.

[82] The ATLAS Collaboration, "Search for squarks and gluinos with the ATLAS detector in final states with jets and missing transverse momentum using $\sqrt{s} = 8$ TeV proton-proton collision data," *Journal of High Energy Physics*, vol. 2014, no. 9, p. 176, 2014.

[83] The ATLAS Collaboration, "Search for supersymmetry in events containing a same-flavour opposite-sign dilepton pair, jets, and large missing transverse momentum in $\sqrt{s} = 8$ TeV pp collisions with the ATLAS detector," *The European Physical Journal C*, vol. 75, no. 7, p. 318, 2015.

[84] W. Beenakker, M. Kramer, T. Plehn, M. Spira, and P. M. Zerwas, "Stop production at hadron colliders," *Nucl. Phys.*, vol. B515, pp. 3–14, 1998.

[85] The ATLAS Collaboration, "ATLAS Run-1 searches for direct pair production of third-generation squarks at the Large Hadron Collider," *The European Physical Journal C*, vol. 75, no. 10, p. 510, 2015.

[86] G. L. Kane, C. Kolda, L. Roszkowski, and J. D. Wells, "Study of constrained minimal supersymmetry," *Phys. Rev. D*, vol. 49, pp. 6173–6210, Jun 1994.

[87] N. Ohta, "Grand unified theories based on local supersymmetry," *Progress of Theoretical Physics*, vol. 70, no. 2, pp. 542–549, 1983.

[88] L. Hall, J. Lykken, and S. Weinberg, "Supergravity as the messenger of supersymmetry breaking," *Phys. Rev. D*, vol. 27, pp. 2359–2378, May 1983.

[89] R. Barbieri, S. Ferrara, and C. Savoy, "Gauge models with spontaneously broken local supersymmetry," *Physics Letters B*, vol. 119, no. 4, pp. 343 – 347, 1982.

[90] The ATLAS Collaboration, "Search for direct top squark pair production in events with a Z boson, b-jets and missing transverse momentum in $\sqrt{s} = 8$ TeV pp with the ATLAS detector," *The European Physical Journal C*, vol. 74, no. 6, p. 2883, 2014.

[91] S. Myers and E. Picasso, "The Design, construction and commissioning of the CERN Large Electron Positron collider," *Contemp. Phys.*, vol. 31, pp. 387–403, 1990.

[92] The ATLAS Collaboration, "The ATLAS Experiment at the CERN Large Hadron Collider," *Journal of Instrumentation*, vol. 3, no. 08, p. S08003, 2008.

[93] L. Evans and P. Bryant, "LHC Machine," *Journal of Instrumentation*, vol. 3, no. 08, p. S08001, 2008.

[94] T. Sjöstrand, S. Mrenna, and P. Z. Skands, "PYTHIA 6.4 Physics and Manual," *JHEP*, vol. 05, p. 026, 2006.

[95] T. Sjöstrand, S. Ask, J. R. Christiansen, R. Corke, N. Desai, P. Ilten, S. Mrenna, S. Prestel, C. O. Rasmussen, and P. Z. Skands, "An Introduction to PYTHIA 8.2," *Comput. Phys. Commun.*, vol. 191, pp. 159–177, 2015.

[96] The TOTEM Collaboration, "Luminosity-independent measurement of the proton-proton total cross section at $\sqrt{s} = 8$ TeV," *Phys. Rev. Lett.*, vol. 111, p. 012001, Jul 2013.

[97] The ATLAS Collaboration, "Measurement of the Inelastic Proton-Proton Cross Section at $\sqrt{s} = 13$ TeV with the ATLAS Detector at the LHC," Tech. Rep. ATLAS-CONF-2015-038, CERN, Geneva, Aug 2015.

[98] The ATLAS Collaboration, "Atlas data summary." https://atlas.web.cern.ch/Atlas/GROUPS/DATAPREPARATION/DataSummary, 2015.

[99] O. S. Bruning, P. Collier, P. Lebrun, S. Myers, R. Ostojic, J. Poole, and P. Proudlock, "LHC Design Report Vol.1: The LHC Main Ring," 2004.

[100] The ATLAS Collaboration, "ATLAS Inner Detector Alignment Performance with February 2015 Cosmic Rays Data," Tech. Rep. ATL-PHYS-PUB-2015-009, CERN, Geneva, Apr 2015.

[101] The ATLAS Collaboration, "ATLAS inner detector: Technical design report. Vol. 1," tech. rep., CERN, 1997.

Bibliography

[102] The ATLAS Collaboration, "ATLAS inner detector: Technical design report. Vol. 2," tech. rep., CERN, 1997.

[103] M. Capeans, G. Darbo, K. Einsweiller, M. Elsing, T. Flick, M. Garcia-Sciveres, C. Gemme, H. Pernegger, O. Rohne, and R. Vuillermet, "ATLAS Insertable B-Layer Technical Design Report," Tech. Rep. CERN-LHCC-2010-013. ATLAS-TDR-19, CERN, Geneva, Sep 2010.

[104] Y. Takubo, "The Pixel Detector of the ATLAS experiment for the Run-2 at the Large Hadron Collider," *JINST*, vol. 10, no. 02, p. C02001, 2015.

[105] H. Pernegger, "The Pixel Detector of the ATLAS experiment for LHC Run-2," *Journal of Instrumentation*, vol. 10, no. 15, p. C06012, 2015.

[106] N. Barlow. Personal Communication, 2016.

[107] F. Djama, "Overview of the atlas insertable b-layer project," *Journal of Instrumentation*, vol. 8, no. 01, p. C01034, 2013.

[108] The ATLAS IBL collaboration, "Prototype ATLAS IBL modules using the FE-I4A front-end readout chip," *Journal of Instrumentation*, vol. 7, no. 11, p. P11010, 2012.

[109] L. Zwalinski *et al.*, "CO_2 cooling system for Insertable B Layer detector into the ATLAS experiment," *PoS*, vol. TIPP2014, p. 224, 2015.

[110] J. Bilbao de Mendizabal, "The ATLAS Insertable B-Layer (IBL) design, production and engineer challenges." Proceedings of IWADC 2014, Benevento, ITALY, 15-17 Semptember, 2014.

[111] The ATLAS Collaboration, "Study of the mechanical stability of the ATLAS Insertable B-Layer," Tech. Rep. ATL-INDET-PUB-2015-001, CERN, Geneva, Jun 2015.

[112] A. B. Poy, H. Boterenbrood, H. J. Burckhart, J. Cook, V. Filimonov, S. Franz, O. Gutzwiller, B. Hallgren, V. Khomutnikov, S. Schlenker, and F. Varela, "The detector control system of the ATLAS experiment," *Journal of Instrumentation*, vol. 3, no. 05, p. P05006, 2008.

[113] The ATLAS Collaboration, "ATLAS liquid-argon calorimeter: Technical Design Report," tech. rep., CERN, Geneva, 1996.

[114] The ATLAS Collaboration, "ATLAS tile calorimeter: Technical Design Report," tech. rep., CERN, Geneva, 1996.

[115] M.L. Andrieux et al., "Construction and test of the first two sectors of the ATLAS barrel liquid argon presampler," *Nucl. Instrum. Meth. A*, vol. 479, no. 2-3, pp. 316 – 333, 2002.

[116] The ATLAS Collaboration, "ATLAS muon spectrometer: Technical Design Report," tech. rep., CERN, Geneva, 1997.

[117] The ATLAS Collaboration, "Technical Design Report for the Phase-I Upgrade of the ATLAS TDAQ System," Tech. Rep. CERN-LHCC-2013-018. ATLAS-TDR-023, CERN, Geneva, Sep 2013. Final version presented to December 2013 LHCC.

[118] T. Cornelissen, M. Elsing, S. Fleischmann, W. Liebig, E. Moyse, and A. Salzburger, "Concepts, Design and Implementation of the ATLAS New Tracking (NEWT)," Tech. Rep. ATL-SOFT-PUB-2007-007. ATL-COM-SOFT-2007-002, CERN, Geneva, Mar 2007.

[119] A. Salzburger, "Tracking tutorial," Tech. Rep. Artemis School on Calibration and performance of ATLAS detectors, MPI, 2008.

[120] R. E. Kalman, "A new approach to linear filtering and prediction problems," *Transactions of the ASME–Journal of Basic Engineering*, vol. 82, no. Series D, pp. 35–45, 1960.

[121] R. Fruhwirth, "Application of Kalman filtering to track and vertex fitting," *Nucl. Instrum. Meth.*, vol. A262, pp. 444–450, 1987.

[122] D. Wicke, "A New algorithm for solving tracking ambiguities," *LC Public notes*, pp. 219–228, 1999.

[123] The ATLAS collaboration, "A neural network clustering algorithm for the ATLAS silicon pixel detector," *JINST*, vol. 9, p. P09009, 2014.

[124] The ATLAS Collaboration, "Performance of the atlas inner detector track and vertex reconstruction in the high pile-up lhc environment," Tech. Rep. ATLAS-CONF-2012-042, CERN, Geneva, Mar 2012.

[125] The ATLAS Collaboration, "Early Inner Detector Tracking Performance in the 2015 data at $\sqrt{s} = 13$ TeV," Tech. Rep. ATL-PHYS-PUB-2015-051, CERN, Geneva, Dec 2015.

[126] T. Sjöstrand, S. Mrenna, and P. Skands, "A brief introduction to pythia 8.1," *Computer Physics Communications*, vol. 178, no. 11, pp. 852 – 867, 2008.

[127] A. Sidoti, "Minimum Bias Trigger Scintillators in ATLAS Run-2," *Journal of Instrumentation*, vol. 9, no. 10, p. C10020, 2014.

[128] The ATLAS Collaboration, "Summary of ATLAS Pythia 8 tunes," Tech. Rep. ATL-PHYS-PUB-2012-003, CERN, Geneva, Aug 2012.

[129] The ATLAS Collaboration, "Performance of primary vertex reconstruction in proton-proton collisions at $\sqrt{s} =7$ TeV in the ATLAS experiment," Tech. Rep. ATLAS-CONF-2010-069, CERN, Geneva, Jul 2010.

[130] W. Waltenberger, R. Frühwirth, and P. Vanlaer, "Adaptive vertex fitting," *Journal of Physics G: Nuclear and Particle Physics*, vol. 34, no. 12, p. N343, 2007.

[131] The ATLAS Collaboration, "Vertex reconstruction plots." http://atlas.web.cern.ch/Atlas/GROUPS/PHYSICS/IDTRACKING/PublicPlots/ATL-COM-PHYS-2012-474/, 2012.

[132] The ATLAS Collaboration, "Vertex Reconstruction Performance of the ATLAS Detector at $\sqrt{s} =13$ TeV"," Tech. Rep. ATL-PHYS-PUB-2015-026, CERN, Geneva, Jul 2015.

[133] The ATLAS Collaboriation, "Characterization of Interaction-Point Beam Parameters Using the pp Event-Vertex Distribution Reconstructed in the ATLAS Detector at the LHC," Tech. Rep. ATLAS-CONF-2010-027, CERN, Geneva, May 2010.

[134] The ATLAS Collaboration, "Impact parameter resolution." https://atlas.web.cern.ch/Atlas/GROUPS/PHYSICS/PLOTS/IDTR-2015-007, 2012.

[135] The ATLAS Collaboration, "Tracking Studies for *b*-tagging with 7 TeV Collision Data with the ATLAS Detector," Tech. Rep. ATLAS-CONF-2010-070, CERN, Geneva, Jul 2010.

[136] The ATLAS Collaboration, "Alignment of the ATLAS Inner Detector and its Performance in 2012," Tech. Rep. ATLAS-CONF-2014-047, CERN, Geneva, Jul 2014.

[137] The ATLAS Collaboration, "Muon reconstruction performance of the ATLAS detector in proton-proton collision data at $\sqrt{s} = 13$ TeV," *The European Physical Journal C*, vol. 76, no. 5, pp. 1–30, 2016.

[138] The ATLAS Collaboration, "Electron efficiency measurements with the ATLAS detector using the 2012 LHC proton-proton collision data," Tech. Rep. ATLAS-CONF-2014-032, CERN, Geneva, Jun 2014.

[139] The ATLAS Collaboration, "Topological cell clustering in the ATLAS calorimeters and its performance in LHC Run 1," *arXiv:1603.02934*, 2016.

[140] The ATLAS Collaboration, "Electron performance measurements with the ATLAS detector using the 2010 LHC proton-proton collision data," *Eur. Phys. J.*, vol. C72, p. 1909, 2012.

[141] T. G. Cornelissen, M. Elsing, I. Gavrilenko, J. F. Laporte, W. Liebig, M. Limper, K. Nikolopoulos, A. Poppleton, and A. Salzburger, "The global χ^2 track fitter in ATLAS," *J. Phys. Conf. Ser.*, vol. 119, p. 032013, 2008.

[142] The ATLAS Collaboration, "Improved electron reconstruction in ATLAS using the Gaussian Sum Filter-based model for bremsstrahlung," Tech. Rep. ATLAS-CONF-2012-047, CERN, Geneva, May 2012.

Bibliography

[143] The ATLAS Collaboration, "Electron efficiency measurements in 2015 data." https://atlas.web.cern.ch/Atlas/GROUPS/PHYSICS/PLOTS/EGAM-2015-006/index.html, 2015.

[144] The ATLAS Collaboration, "Electron identification measurements in ATLAS using $\sqrt{s} = 13$ TeV data with 50 ns bunch spacing," Tech. Rep. ATL-PHYS-PUB-2015-041, CERN, Geneva, Sep 2015.

[145] The ATLAS Collaboration, "Measurement of the muon reconstruction performance of the ATLAS detector using 2011 and 2012 LHC proton-proton collision data," *Eur. Phys. J.*, vol. C74, no. 11, p. 3130, 2014.

[146] S. Hassani, L. Chevalier, E. Lancon, J. F. Laporte, R. Nicolaidou, and A. Ouraou, "A muon identification and combined reconstruction procedure for the ATLAS detector at the LHC using the (MUONBOY, STACO, MuTag) reconstruction packages," *Nucl. Instrum. Meth.*, vol. A572, pp. 77–79, 2007.

[147] T. Lagouri, "Muon Identification and Combined Reconstruction Study in Higgs to Four Muons Physics Events with the ATLAS Detector at the LHC at CERN," *ATL-PHYS-CONF-2006-016*, 2004.

[148] R. O. Duda and P. E. Hart, "Use of the hough transformation to detect lines and curves in pictures," *Commun. ACM*, vol. 15, pp. 11–15, Jan. 1972.

[149] K. A. Olive *et al.*, "Review of Particle Physics," *Chin. Phys.*, vol. C38, p. 090001, 2014.

[150] The ATLAS Collaboration, "Identification and energy calibration of hadronically decaying tau leptons with the ATLAS experiment in pp collisions at $\sqrt{s} = 8$ TeV," *The European Physical Journal C*, vol. 75, no. 7, pp. 1–33, 2015.

[151] The ATLAS Collaboration, "Tagging and suppression of pileup jets with the ATLAS detector," Tech. Rep. ATLAS-CONF-2014-018, CERN, Geneva, May 2014.

[152] A. Hocker et al., "TMVA - Toolkit for Multivariate Data Analysis," *arXiv:physics/0703039*, Mar. 2007.

[153] M. Cacciari, G. P. Salam, and G. Soyez, "The anti-k_t jet clustering algorithm," *Journal of High Energy Physics*, vol. 2008, no. 04, p. 063, 2008.

[154] M. Cacciari and G. P. Salam, "Dispelling the N^3 myth for the k_t jet-finder," *Phys. Lett.*, vol. B641, pp. 57–61, 2006.

[155] The ATLAS Collaboration, "Jet energy measurement with the ATLAS detector in proton-proton collisions at $\sqrt{s} = 7$ TeV," *Eur. Phys. J.*, vol. C73, no. 3, p. 2304, 2013.

[156] The ATLAS Collaboration, "Jet energy measurement and its systematic uncertainty in proton-proton collisions at $\sqrt{s} = 7$ TeV with the ATLAS detector," *Eur. Phys. J.*, vol. C75, p. 17, 2015.

[157] The ATLAS Collaboration, "Jet energy measurement and its systematic uncertainty in proton–proton collisions at $\sqrt{s} = 7$TeV with the ATLAS detector," *The European Physical Journal C*, vol. 75, no. 1, pp. 1–101, 2015.

[158] The ATLAS Collaboration, "Performance of pile-up mitigation techniques for jets in *pp* collisions at $\sqrt{s} = 8$ TeV using the ATLAS detector," *Nucl. Instrum. Meth.*, vol. A824, pp. 367–370, 2016.

[159] The ATLAS Collaboration, "Approved jes uncertainty public plots." https://twiki.cern.ch/twiki/bin/view/AtlasPublic/JetEtmissApproved2013JESUncertainty, 2013.

[160] The ATLAS Collaboration, "Commissioning of the ATLAS high-performance b-tagging algorithms in the 7 TeV collision data," Tech. Rep. ATLAS-CONF-2011-102, CERN, Geneva, Jul 2011.

[161] The ATLAS Collaboration, "Calibration of the performance of *b*-tagging for *c* and light-flavour jets in the 2012 ATLAS data," Tech. Rep. ATLAS-CONF-2014-046, CERN, Geneva, Jul 2014.

[162] The ATLAS Collaboration, "Performance of b-jet identification in the ATLAS experiment," *Journal of Instrumentation*, vol. 11, no. 04, p. P04008, 2016.

[163] The ATLAS Collaboration, "Impact parameter-based b-tagging algorithms in the 7 TeV collision data with the ATLAS detector: the TrackCounting and JetProb algorithms," Tech. Rep. ATLAS-CONF-2010-041, CERN, Geneva, Jul 2010.

[164] The ATLAS Collaboration, "Performance of the ATLAS Secondary Vertex b-tagging Algorithm in 7 TeV Collision Data," Tech. Rep. ATLAS-CONF-2010-042, CERN, Geneva, Jul 2010.

[165] The ATLAS Collaboration, "Calibration of *b*-tagging using dileptonic top pair events in a combinatorial likelihood approach with the ATLAS experiment," Tech. Rep. ATLAS-CONF-2014-004, CERN, Geneva, Feb 2014.

[166] The ATLAS Collaboration, "Performance of missing transverse momentum reconstruction in proton-proton collisions at $\sqrt{s} = 7$ tev with atlas," *The European Physical Journal C*, vol. 72, no. 1, pp. 1–35, 2012.

[167] The ATLAS Collaboration, "Performance of Missing Transverse Momentum Reconstruction in ATLAS studied in Proton-Proton Collisions recorded in 2012 at 8 TeV," Tech. Rep. ATLAS-CONF-2013-082, CERN, Geneva, Aug 2013.

[168] M. Cacciari, G. P. Salam, and G. Soyez, "The Catchment Area of Jets," *JHEP*, vol. 04, p. 005, 2008.

[169] T. Golling, "Alignment of the Silicon Tracking Detector using Survey Constraints," Tech. Rep. ATL-INDET-PUB-2006-001. ATL-COM-INDET-2006-002. CERN-ATL-INDET-PUB-2006-001, CERN, Geneva, Mar 2006.

[170] The ATLAS Collaboration, "The ATLAS Inner Detector commissioning and calibration," *The European Physical Journal C*, vol. 70, no. 3, pp. 787–821, 2010.

[171] J. Boudreau and V. Tsulaia, "The GeoModel Toolkit for Detector Description," *Computing in High Energy Physics and Nuclear Physics 2004*, p. 353, 2005.

[172] P. Brückman, A. Hicheur, and S. J. Haywood, "Global chi2 approach to the Alignment of the ATLAS Silicon Tracking Detectors," Tech. Rep. ATL-INDET-PUB-2005-002. ATL-COM-INDET-2005-004. CERN-ATL-INDET-PUB-2005-002, CERN, Geneva, 2005.

[173] A. Bocci and W. Hulsbergen, "TRT Alignment For SR1 Cosmics and Beyond," Tech. Rep. ATL-INDET-PUB-2007-009. ATL-COM-INDET-2007-011. CERN-ATL-COM-INDET-2007-011, CERN, Geneva, Jun 2007.

[174] V. Lacuesta Miquel, S. Martí i García, and S. García Navarro, "Alignment of the ATLAS Inner Detector and Single Top studies," PhD Thesis, Valencia U., 2015. Presented 20 Jan 2016.

[175] R.Härtel, "Iterative Local χ^2 alignment approach for the ATLAS SCT detector," Diploma Thesis, TU München, 2005.

[176] T. Göttfert, "Iterative Local χ^2 alignment approach for the ATLAS Pixel detector," Diploma Thesis, Universität Würzburg, 2006.

[177] The ATLAS Collaboration, "Study of alignment-related systematic effects on the ATLAS Inner Detector tracking," Tech. Rep. ATLAS-CONF-2012-141, CERN, Geneva, Oct 2012.

[178] A. Keith Morley, *Electron Bremsstrahlung Studies and Track Based Alignment of the ATLAS Detector*. PhD thesis, Melbourne U., 2010.

[179] The ATLAS Collaboration, "Study of alignment-related systematic effects on the ATLAS Inner Detector tracking," Tech. Rep. ATLAS-CONF-2012-141, CERN, Geneva, Oct 2012.

[180] T. Sjöstrand, S. Mrenna, and P. Z. Skands, "A Brief Introduction to PYTHIA 8.1," *Comput. Phys. Commun.*, vol. 178, pp. 852–867, 2008.

[181] S. Fratina, M. Hance, M. Newcomer, D. Olivito, R. Van Berg, P. Wagner, H. Williams, B. Auerbach, D. Dobos, and P. Lichard, "The TRT Fast-OR Trigger," Tech. Rep. ATL-INDET-PUB-2009-002, CERN, Geneva, Dec 2009.

[182] The ATLAS Pixel Collaboration, "Drift of the ibl lv current and its consequence in ibl distortion." https://atlas.web.cern.ch/Atlas/GROUPS/PHYSICS/PLOTS/PIX-2015-007, 2015.

[183] The ATLAS Pixel Collaboration, "Results from the atlas ibl low voltage current task force x-ray irradiation campaigns." https://atlas.web.cern.ch/Atlas/GROUPS/PHYSICS/PLOTS/PIX-2015-008, 2015.

[184] L. Gonella, F. Faccio, M. Silvestri, S. Gerardin, D. Pantano, V. Re, M. Manghisoni, L. Ratti, and A. Ranieri, "Total Ionizing Dose effects in 130-nm commercial CMOS technologies for HEP experiments," *Nucl. Instrum. Methods Phys. Res., A*, vol. 582, pp. 750–754, 2007.

[185] The ATLAS Collaboration, "Expected performance of the ATLAS b-tagging algorithms in Run-2," Tech. Rep. ATL-PHYS-PUB-2015-022, CERN, Geneva, Jul 2015.

[186] The ATLAS Collaboration, "Commissioning of the ATLAS b-tagging algorithms using $t\bar{t}$ events in early Run-2 data," Tech. Rep. ATL-PHYS-PUB-2015-039, CERN, Geneva, Aug 2015.

[187] The ATLAS Collaboration, "Alignment of the ATLAS Inner Detector with the initial LHC data at $\sqrt{s} = 13$ TeV," Tech. Rep. ATL-COM-PHYS-2015-581, CERN, Geneva, Jun 2015.

[188] The ATLAS Collaboration, "Common Framework Implementation for the Track-Based Alignment of the ATLAS Detector," Tech. Rep. ATL-SOFT-PUB-2014-003, CERN, Geneva, Mar 2014.

[189] The ATLAS collaboration, "A neural network clustering algorithm for the atlas silicon pixel detector," *Journal of Instrumentation*, vol. 9, no. 09, p. P09009, 2014.

[190] The ATLAS Collaboration, "Search for direct top-squark pair production in final states with two leptons in pp collisions at $\sqrt{s} = 8$ tev with the atlas detector," *Journal of High Energy Physics*, vol. 2014, no. 6, pp. 1–66, 2014.

[191] The ATLAS Collaboration, "Standard model results." https://twiki.cern.ch/twiki/bin/view/AtlasPublic/StandardModelPublicResults, 2015.

[192] K. Kröninger, A. B. Meyer, and P. Uwer, "Top-Quark Physics at the LHC," in *The Large Hadron Collider: Harvest of Run 1* (T. Schörner-Sadenius, ed.), pp. 259–300, 2015.

[193] M. Cacciari, M. Czakon, M. Mangano, A. Mitov, and P. Nason, "Top-pair production at hadron colliders with next-to-next-to-leading logarithmic soft-gluon resummation," *Physics Letters B*, vol. 710, no. 4-5, pp. 612 – 622, 2012.

[194] P. Bärnreuther, M. Czakon, and A. Mitov, "Percent-level-precision physics at the tevatron: Next-to-next-to-leading order qcd corrections to $q\bar{q} \to t\bar{t}+x$," *Phys. Rev. Lett.*, vol. 109, p. 132001, Sep 2012.

[195] M. Czakon and A. Mitov, "Nnlo corrections to top-pair production at hadron colliders: the all-fermionic scattering channels," *Journal of High Energy Physics*, vol. 2012, no. 12, pp. 1–18, 2012.

[196] M. Czakon and A. Mitov, "Nnlo corrections to top pair production at hadron colliders: the quark-gluon reaction," *Journal of High Energy Physics*, vol. 2013, no. 1, pp. 1–19, 2013.

[197] M. Czakon and A. Mitov, "Top++: A Program for the Calculation of the Top-Pair Cross-Section at Hadron Colliders," *Comput. Phys. Commun.*, vol. 185, p. 2930, 2014.

[198] M. Czakon, P. Fiedler, and A. Mitov, "Total top-quark pair-production cross section at hadron colliders through $\mathcal{O}(\alpha_S^4)$," *Phys. Rev. Lett.*, vol. 110, p. 252004, Jun 2013.

[199] N. Kidonakis, "Next-to-next-to-leading-order collinear and soft gluon corrections for t-channel single top quark production," *Phys. Rev.*, vol. D83, p. 091503, 2011.

[200] N. Kidonakis, "Two-loop soft anomalous dimensions for single top quark associated production with a W- or H-," *Phys. Rev.*, vol. D82, p. 054018, 2010.

[201] N. Kidonakis, "Next-to-next-to-leading logarithm resummation for *s*-channel single top quark production," *Phys. Rev. D*, vol. 81, p. 054028, Mar 2010.

[202] T. Binoth, M. Ciccolini, N. Kauer, and M. Krämer, "Gluon-induced W-boson pair production at the LHC," *JHEP*, vol. 0612, p. 046, 2006.

[203] M. Garzelli, A. Kardos, C. Papadopoulos, and Z. Trocsanyi, "$t\bar{t} + W^{+-}$ and $t\bar{t} + Z$ Hadroproduction at NLO accuracy in QCD with Parton Shower and Hadronization effects," *JHEP*, vol. 11, p. 056, 2012.

[204] The ATLAS Collaboration, "The atlas simulation infrastructure," *The European Physical Journal C*, vol. 70, no. 3, pp. 823–874, 2010.

[205] S. Agostinelli et al., "Geant4 - a simulation toolkit," *Nuclear Instruments and Methods in Physics Research Section A: Accelerators, Spectrometers, Detectors and Associated Equipment*, vol. 506, no. 3, pp. 250 – 303, 2003.

[206] The ATLAS Collaboration, "The simulation principle and performance of the ATLAS fast calorimeter simulation FastCaloSim," Tech. Rep. ATL-PHYS-PUB-2010-013, CERN, Geneva, Oct 2010.

[207] M. Krämer, A. Kulesza, R. van der Leeuw, M. Mangano, S. Padhi, T. Plehn, and X. Portell, "Supersymmetry production cross sections in *pp* collisions at $\sqrt{s} = 7$ TeV," 2012.

[208] S. Alioli, P. Nason, C. Oleari, and E. Re, "A general framework for implementing NLO calculations in shower Monte Carlo programs: the POWHEG BOX," *JHEP*, vol. 1006, p. 043, 2010.

[209] J. M. Campbell, R. K. Ellis, P. Nason, and E. Re, "Top-pair production and decay at NLO matched with parton showers," *JHEP*, vol. 1504, p. 114, 2015.

[210] B. Cooper, J. Katzy, M. Mangano, A. Messina, L. Mijovic, *et al.*, "Importance of a consistent choice of alpha(s) in the matching of AlpGen and Pythia," *Eur. Phys. J.*, vol. C72, p. 2078, 2012.

[211] E. Re, "Single-top Wt-channel production matched with parton showers using the POWHEG method," *Eur. Phys. J.*, vol. C71, p. 1547, 2011.

[212] S. Alioli, P. Nason, C. Oleari, and E. Re, "NLO single-top production matched with shower in POWHEG: s- and t-channel contributions," *JHEP*, vol. 0909, p. 111, 2009.

[213] B. P. Kersevan and E. Richter-Was, "The Monte Carlo event generator AcerMC version 2.0 with interfaces to PYTHIA 6.2 and HERWIG 6.5," 2004.

[214] J. Alwall, M. Herquet, F. Maltoni, O. Mattelaer, and T. Stelzer, "MadGraph 5: Going Beyond," *JHEP*, vol. 06, p. 128, 2011.

[215] The ATLAS Collaboration, "New ATLAS event generator tunes to 2010 data," http://cdsweb.cern.ch/record/1345343.

[216] T. Gleisberg *et al.*, "Event generation with SHERPA 1.1," *JHEP*, vol. 0902, p. 007, 2009.

[217] M. L. Mangano, M. Moretti, F. Piccinini, R. Pittau, and A. D. Polosa, "ALPGEN, a generator for hard multiparton processes in hadronic collisions," *JHEP*, vol. 0307, p. 001, 2003.

[218] G. Corcella, I. G. Knowles, G. Marchesini, S. Moretti, K. Odagiri, P. Richardson, M. H. Seymour, and B. R. Webber, "HERWIG 6: An Event generator for hadron emission reactions with interfering gluons (including supersymmetric processes)," *JHEP*, vol. 0101, p. 010, 2001.

[219] S. Catani *et al.*, "Vector boson production at hadron colliders: A Fully exclusive QCD calculation at NNLO," *Phys. Rev. Lett.*, vol. 103, p. 082001, 2009.

Bibliography

[220] M. Bähr *et al.*, "Herwig++ Physics and Manual," *Eur. Phys. J.*, vol. C58, pp. 639–707, 2008. 143 pages, program and additional information available from http://projects.hepforge.org/herwig.

[221] W. Beenakker *et al.*, "Supersymmetric top and bottom squark production at hadron colliders," *JHEP*, vol. 1008, p. 098, 2010.

[222] W. Beenakker *et al.*, "Squark and gluino hadroproduction," *Int. J. Mod. Phys.*, vol. A26, pp. 2637–2664, 2011.

[223] S. Gieseke, C. Rohr, and A. Siodmok, "Colour reconnections in Herwig++," *Eur. Phys. J.*, vol. C72, p. 2225, 2012.

[224] The LEP SUSY Working Group and ALEPH, DELPHI, L3, OPAL experiments, "Combined LEP selectron/smuon/stau results, 183-208 GeV," 2004. http://lepsusy.web.cern.ch/lepsusy/ www/sleptons_summer04/slep_final.html.

[225] G. Abbiendi et al., (OPAL collaboration), "Searches for gauge-mediated supersymmetry breaking topologies in e+ e- collisions at LEP2," *Eur. Phys. J.*, vol. C46, pp. 307–341, 2006.

[226] A. Heister et al., (ALEPH collaboration), "Search for scalar leptons in e+ e- collisions at center-of-mass energies up to 209 GeV," *Phys. Lett.*, vol. B526, pp. 206–220, 2002.

[227] J. Abdallah et al., (DELPHI collaboration), "Searches for supersymmetric particles in e+ e-collisions up to 208 GeV and interpretation of the results within the MSSM," *Eur. Phys. J.*, vol. C31, pp. 421–479, 2003.

[228] P. Achard et al., (L3 Collaboration), "Search for scalar leptons and scalar quarks at LEP," *Phys. Lett.*, vol. B580, pp. 37–49, 2004.

[229] K. Cranmer, G. Lewis, L. Moneta, A. Shibata, and W. Verkerke, "HistFactory: A tool for creating statistical models for use with RooFit and RooStats," 2012.

[230] M. Baak, G. J. Besjes, D. Côte, A. Koutsman, J. Lorenz, and D. Short, "HistFitter software framework for statistical data analysis," *Eur. Phys. J.*, vol. C75, p. 153, 2015.

[231] W. Verkerke and D. Kirkby, "The RooFit toolkit for data modeling," *ArXiv Physics e-prints*, June 2003.

[232] L. Moneta, K. Cranmer, G. Schott, and W. Verkerke, "The RooStats project," in *Proceedings of the 13th International Workshop on Advanced Computing and Analysis Techniques in Physics Research. February 22-27, 2010, Jaipur, India. http://acat2010.cern.ch/. Published online at <A href="http://pos.sissa.it/cgi-bin/reader/conf.cgi?confid=93">http://pos.sissa.it/cgi-bin/reader/conf.cgi?confid=93</A>, p.57*, p. 57, 2010.

[233] G. Cowan, K. Cranmer, E. Gross, and O. Vitells, "Asymptotic formulae for likelihood-based tests of new physics," *Eur. Phys. J.*, vol. C71, p. 1554, 2011. [Erratum: Eur. Phys. J.C73,2501(2013)].

[234] A. L. Read, "Presentation of search results: the cl s technique," *Journal of Physics G: Nuclear and Particle Physics*, vol. 28, no. 10, p. 2693, 2002.

[235] C. Lester and D. Summers, "Measuring masses of semi-invisibly decaying particle pairs produced at hadron colliders," *Physics Letters B*, vol. 463, no. 1, pp. 99 – 103, 1999.

[236] A. Barr, C. Lester, and P. Stephens, "A variable for measuring masses at hadron colliders when missing energy is expected; m t 2 : the truth behind the glamour," *Journal of Physics G: Nuclear and Particle Physics*, vol. 29, no. 10, p. 2343, 2003.

[237] M. Burns, K. Kong, K. T. Matchev, and M. Park, "Using Subsystem MT2 for Complete Mass Determinations in Decay Chains with Missing Energy at Hadron Colliders," *JHEP*, vol. 03, p. 143, 2009.

[238] W. S. Cho, K. Choi, Y. G. Kim, and C. B. Park, "Measuring superparticle masses at hadron collider using the transverse mass kink," *JHEP*, vol. 02, p. 035, 2008.

[239] The ATLAS Collaboration, "Search for squarks and gluinos with the atlas detector in final states with jets and missing transverse momentum using 4.7 fb^{-1} of $\sqrt{s}$=7 TeV proton-proton collision data," *Phys. Rev. D*, vol. 87, p. 012008, Jan 2013.

[240] The ATLAS Collaboration, "Search for supersymmetry in events with large missing transverse momentum, jets, and at least one tau lepton in 20 fb^{-1} of $\sqrt{s} = 8$ TeV proton-proton collision data with the ATLAS detector," *JHEP*, vol. 09, p. 103, 2014.

[241] The ATLAS Collaboration, "Performance of the atlas muon trigger in pp collisions at $\sqrt{s} = 8$ tev," *The European Physical Journal C*, vol. 75, no. 3, pp. 1–31, 2015.

[242] J. H. Friedman, "Stochastic Gradient Boosting," *Comput. Stat. & Data Anal.*, vol. 38, p. 367, 1999.

[243] The ATLAS Collaboration, "Measurement of the top quark pair production cross section in pp collisions at $\sqrt{s} = 7$ TeV in dilepton final states with ATLAS," *Phys. Lett.*, vol. B707, pp. 459–477, 2012.

[244] The ATLAS Collaboration, "Measurement of the top quark-pair production cross section with ATLAS in pp collisions at $\sqrt{s} = 7$ TeV," *Eur. Phys. J.*, vol. C71, p. 1577, 2011.

[245] The ATLAS Collaboration, "Measurement of the top quark pair cross section with atlas in pp collisions at using final states with an electron or a muon and a hadronically decaying τ lepton," *Physics Letters B*, vol. 717, no. 1-3, pp. 89 – 108, 2012.

[246] The CMS Collaboration, "Measurement of the production cross section in pp collisions at in dilepton final states containing one τ lepton," *Physics Letters B*, vol. 739, pp. 23–43, 2014.

[247] The ATLAS Collaboration, "Measurement of the $t\bar{t}$ production cross section in the τ + jets channel using the atlas detector," *The European Physical Journal C*, vol. 73, no. 3, pp. 1–18, 2013.

[248] The CMS Collaboration, "Measurement of the $t\bar{t}$ production cross section in the τ+jets channel in pp collisions at $\sqrt{s} = 7$ tev," *The European Physical Journal C*, vol. 73, no. 4, pp. 1–18, 2013.

[249] The ATLAS Collaboration, "Jet energy resolution in proton-proton collisions at $\sqrt{s} = 7$ TeV recorded in 2010 with the ATLAS detector," *Eur. Phys. J.*, vol. C73, no. 3, p. 2306, 2013.

[250] The ATLAS Collaboration, "Improved luminosity determination in pp collisions at $\sqrt{s} = 7$ TeV using the ATLAS detector at the LHC," *Eur. Phys. J.*, vol. C73, no. 8, p. 2518, 2013.

[251] S. Frixione and B. R. Webber, "Matching NLO QCD computations and parton shower simulations," *JHEP*, vol. 06, p. 029, 2002.

[252] T. Binoth, M. Ciccolini, N. Kauer, and M. Krämer, "Gluon-induced w -boson pair production at the lhc," *Journal of High Energy Physics*, vol. 2006, no. 12, p. 046, 2006.

[253] S. Frixione, E. Laenen, P. Motylinski, B. R. Webber, and C. D. White, "Single-top hadroproduction in association with a W boson," *JHEP*, vol. 07, p. 029, 2008.

[254] Botje, Michiel et al., "The PDF4LHC Working Group Interim Recommendations," *arXiv:1101.0538*, 2011.

[255] The ATLAS Collaboration, "Search for top-squark pair production in final states with two tau leptons, jets, and missing transverse momentum in $\sqrt{s} = 13$ TeV pp-collisions with the ATLAS detector," Tech. Rep. ATLAS-CONF-2016-048, CERN, Geneva, Aug 2016.

Acknowledgements